

AD-A154 269

THERMODYNAMICS OF HIGH TEMPERATURE MATERIALS(U)  
NATIONAL BUREAU OF STANDARDS GAITHERSBURG MD CENTER FOR  
CHEMICAL PHYSICS S ABRAMOWITZ 15 MAR 85

1/3

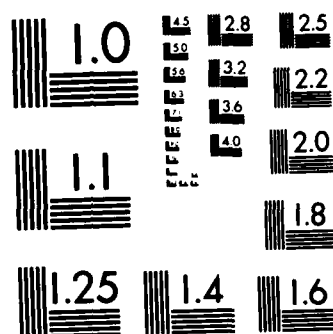
UNCLASSIFIED

AFOSR-TR-85-0394 AFOSR-ISSA-84-00034

F/G 11/2

NL





MICROCOPY RESOLUTION TEST CHART  
NATIONAL BUREAU OF STANDARDS-1963-A

3

AD-A154 269

DTIC FILE COPY

DISTRIBUTION STATEMENT A  
Approved for public release  
Distribution Unlimited

DTIC  
ELECTE  
S MAY 29 1985  
B

2.5 2 11.5

UNCLASSIFIED

SECURITY CLASSIFICATION OF THIS PAGE

AD A 154 269

## REPORT DOCUMENTATION PAGE

1a. REPORT SECURITY CLASSIFICATION UNCLASSIFIED		1b. RESTRICTIVE MARKINGS													
2a. SECURITY CLASSIFICATION AUTHORITY		3. DISTRIBUTION/AVAILABILITY OF REPORT Approved for public release; distribution unlimited.													
2b. DECLASSIFICATION/DOWNGRADING SCHEDULE															
4. PERFORMING ORGANIZATION REPORT NUMBER		5. MONITORING ORGANIZATION REPORT NUMBER <b>AFOSR-TR- 85 - 0394</b>													
6a. NAME OF PERFORMING ORGANIZATION National Bureau of Standards	6b. OFFICE SYMBOL (If applicable)	7a. NAME OF MONITORING ORGANIZATION Air Force Office of Scientific Research													
6c. ADDRESS (City, State and ZIP Code) Gaithersburg, MD 20899		7b. ADDRESS (City, State and ZIP Code) Bldg 410 Bolling AFB DC 20332-6448													
8a. NAME OF FUNDING/SPONSORING ORGANIZATION AFOSR	8b. OFFICE SYMBOL (If applicable) NE	9. PROCUREMENT INSTRUMENT IDENTIFICATION NUMBER AFOSR-ISSA-84-00034													
8c. ADDRESS (City, State and ZIP Code) Bldg 410 Bolling AFB DC 20332-6448		10. SOURCE OF FUNDING NOS <table border="1"><tr><td>PROGRAM ELEMENT NO. 61102F</td><td>PROJECT NO. 2306 2306</td><td>TASK NO. C4 NO. A2</td><td>WORK UNIT NO.</td></tr></table>		PROGRAM ELEMENT NO. 61102F	PROJECT NO. 2306 2306	TASK NO. C4 NO. A2	WORK UNIT NO.								
PROGRAM ELEMENT NO. 61102F	PROJECT NO. 2306 2306	TASK NO. C4 NO. A2	WORK UNIT NO.												
11. TITLE (Include Security Classification) Thermodynamics of High Temperature Materials															
PERSONAL AUTHOR(S) S. Abramowitz, ed.															
13a. TYPE OF REPORT Annual	13b. TIME COVERED FROM 10/1/83 TO 9/30/84	14. DATE OF REPORT (Yr., Mo., Day) 85/3/15	15. PAGE COUNT 243 + IV												
16. SUPPLEMENTARY NOTATION															
17. COSATI CODES <table border="1"><tr><th>FIELD</th><th>GROUP</th><th>SUB. GR.</th></tr><tr><td></td><td></td><td></td></tr><tr><td></td><td></td><td></td></tr><tr><td></td><td></td><td></td></tr></table>		FIELD	GROUP	SUB. GR.										18. SUBJECT TERMS (Continue on reverse if necessary and identify by block number) High Temperature, Thermophysics, Thermodynamics, Materials <i>This report</i>	
FIELD	GROUP	SUB. GR.													
19. ABSTRACT (Continue on reverse if necessary and identify by block number) <p>The research described encompasses six tasks each of which treats, from either an experimental or theoretical base, the measurement or interpretation of the high-temperature thermophysical behavior of model systems which show potential applications to the environmental resistant materials and the spacecraft survivability programs. While there is significant overlap between these tasks, the first two chapters are addressed to the environmental resistant materials program, while the later four chapters are addressed to the spacecraft survivability program.</p> <p>The heat capacity, electrical resistivity and hemispherical total emittance of graphite has been measured in the range of 1500-3000 K. The heat capacity and electrical resistivity of nickel has been measured in the range 1300-1700 K. The melting point of nickel has also been determined. The specific heat of both hexagonal and cubic boron nitride has been determined in the range of 273.15-1200 K. The heat capacity of Aluminum has been calculated using several theoretical models. The results are to be compared with (cont.)</p>															
20. DISTRIBUTION/AVAILABILITY OF ABSTRACT UNCLASSIFIED/UNLIMITED <input checked="" type="checkbox"/> SAME AS RPT. <input type="checkbox"/> DTIC USERS <input type="checkbox"/>		21. ABSTRACT SECURITY CLASSIFICATION UNCLASSIFIED													
22a. NAME OF RESPONSIBLE INDIVIDUAL JOSEPH W HAGER, Maj, USAF		22b. TELEPHONE NUMBER (Include Area Code) (202) 767-4933	22c. OFFICE SYMBOL NE												



## 19. Conti

experimental determinations, new nearing completion.

The thermodynamic effects of elastic and inelastic collisions have been determined. The problem of how to treat polyatomic molecules having highly distorted vibrational states, as can be expected after laser irradiation, has been addressed. High temperature equilibria have been modelled using a square well potential. A program for evaluation of the classical partition function and resultant thermodynamic quantities for molecules at high temperatures has been developed and made available to the thermodynamics community including the JANAF group. An efficient computer code has been developed which allows calculation of the equilibrium configuration of the symmetric carbon structures present in graphite-like layers. Experiments have been initiated to test the predictions of this code. The gas phase ionic reactions leading to the build up of unsaturated hydrogen deficient carbon chain hydrocarbons has been studied using precursors such as diacetylene, cyanoacetylene, cyanogen and 1,3,7 hexatriene. Theoretical and experimental determinations have been made of the proton affinities of some relevant species. Studies have been continued to determine the kinetics and molecular mechanisms of laser induced vaporization of carbonaceous materials. A study to determine the mechanism of formation of metal-containing particulates, which lead to aerosol formation, has been continued. Temperature dependency of the ionization cross sections has been observed in simple molecular model systems in order to explain disparate literature results.

Thermodynamics of High Temperature Materials

Annual Report for the Period

1 October 1983 - 30 September 1984

AIR FORCE OFFICE OF SCIENTIFIC RESEARCH

AFOSR-ISSA-84-00034

AIR FORCE OFFICE OF SCIENTIFIC RESEARCH (AFOSR)  
NOTICE OF TRANSMITTAL TO DTIC

This technical report has been reviewed and is  
approved for public release IAW AFR 190-12.  
Distribution is unlimited.

MATTHEW J. KNEUER

Chief, Technical Information Division

Approved for public release;  
distribution unlimited.

## TABLE OF CONTENTS

CHAPTER	PAGE
ABSTRACT	III
1. Research on Thermophysical Properties	
a. Heat Capacity, Electrical Resistivity and Hemispherical Total Emittance of AXM -5Q1 POCO Graphite in the Range of 1500-3000 K.	2
b. Thermophysical Properties of Nickel above 1300 K.	13
2. High Temperature Enthalpy Measurements	28
a. Relative Enthalpy of Hexagonal and Cubic Boron Nitride Between 273.15 and 1200 K.	29
b. Aluminum: Derivation of $C_{VO}$ from $C_p$ and Comparison to $C_{VO}$ Calculated from Anharmonic Potentials.	38
3. Critique of Thermodynamic Functions Evaluated at High Temperatures	63
a. Adiabatic Analysis of Distant Perturbations: Applications to Herzberg-Teller Vibronic Coupling Theory.	69
4. Stability and Growth of Graphitic Layers	97
a. Counting of Resonance Structure for Large Benzenoid Polynuclear Molecules. A Chemical Theory of Graphite - Like Molecule	102

Accession For	
NTIS GRA&I	<input checked="" type="checkbox"/>
DTIC TAB	<input type="checkbox"/>
Unannounced	<input type="checkbox"/>
Justification	
By <b>PER CALL JC</b>	
Distribution/	
Availability Codes	
Dist	Avail and/or Special
<b>A-1</b>	



5.	Build Up and Irradiation of Obscuring Clouds Under Near Vacuum Conditions: Applicability to Spacecraft Survivability	128
a.	Consecutive Ion Molecule Condensations Reactions and Photodissociation Mechanisms of Condensation Ions in Polyacetylenic Compounds.	134
b.	Structure of $C_6H_7^+$ Ions Formed in Unimolecular and Biomolecular Reactions.	162
6.	Molecular Basis for Laser Induced Vaporization of Refractory Materials.	203

## ABSTRACT

The research described encompasses six tasks each of which treats, from either an experimental or theoretical base, the measurement or interpretation of the high-temperature thermophysical behavior of model systems which show potential applications to the environmental resistant materials and the spacecraft survivability programs. While there is significant overlap between these tasks, the first two chapters are addressed to the environmental resistant materials program, while the later four chapters are addressed to the spacecraft survivability program.

The heat capacity, electrical resistivity and hemispherical total emittance of graphite has been measured in the range of 1500-3000 K. The heat capacity and electrical resistivity of nickel has been measured in the range 1300-1700 K. The melting point of nickel has also been determined. The specific heat of both hexagonal and cubic boron nitride has been determined in the range of 273.15-1200 K. The heat capacity of Aluminum has been calculated using several theoretical models. The results are to be compared with experimental determinations, now nearing completion.

The thermodynamic effects of elastic and inelastic collisions have been determined. The problem of how to treat polyatomic molecules having highly distorted vibrational states, as can be expected after laser irradiation, has been addressed. High temperature equilibria have been modelled using a square well potential. A program for evaluation of the classical partition function and resultant thermodynamic quantities for

molecules at high temperatures has been developed and made available to the thermodynamics community including the JANAF group. An efficient computer code has been developed which allows calculation of the equilibrium configuration of the symmetric carbon structures present in graphite-like layers. Experiments have been initiated to test the predictions of this code. The gas phase ionic reactions leading to the build up of unsaturated hydrogen deficient carbon chain hydrocarbons has been studied using precursors such as diacetylene, cyanoacetylene, cyanogen and 1,3,7 hexatriene. Theoretical and experimental determinations have been made of the proton affinities of some relevant species. Studies have been continued to determine the kinetics and molecular mechanisms of laser induced vaporization of carbonaceous materials. A study to determine the mechanism of formation of metal containing particulars, which lead to aerosol formation, has been continued. Temperature dependency of the ionization cross sections has been observed in simple molecular model systems in order to explain disparate literature results.

1. Research on Thermophysical Properties

A. Cezairliyan, Principal Investigator.

- a. Heat Capacity, Electrical Resistivity and Hemispherical Total Emittance of AXM-5Q1 POCO Graphite in the Range of 1500-3000 K.
- b. Thermophysical Properties of Nickel Above 1300 K.

a, Heat Capacity, Electrical Resistivity and Hemispherical Total  
Emittance of AXM-5Q1 POCO Graphite in the Range 1500-3000 K<sup>1</sup>

A. Cezairliyan, A.P. Miiller and M.S. Morse

In recent years, graphite has become one of the most important refractory materials in the development of high-temperature technologies, finding applications both as a component in structural composites and as a standard reference material for thermal property measurements. As a result, there has been an increasing need for accurate data on various thermophysical properties of graphite, particularly at temperatures above 2000 K where significant disagreement exists among the relatively few investigations reported in the literature.

In the present work, accurate measurements of heat capacity, electrical resistivity and hemispherical total emittance of AXM-5Q1 POCO graphite were performed in the temperature range 1500-3000 K by means of a rapid pulse-heating technique [1, 2]. This study, which was conducted as part of the CODATA program on high-temperature materials, was motivated in part by the difference (~3%) between heat capacity values obtained recently at IMGC<sup>2</sup> [3] for AXM-5Q1<sup>3</sup> and results obtained earlier at NBS [4] for similar graphite (AXM-5Q)<sup>3</sup>. This difference is considerably larger than the measurement resolution (~0.5%) of the pulse-heating systems

---

<sup>1</sup> To appear in Int. J. Thermophysics 6....(1985).

<sup>2</sup> Istituto di Metrologia "G. Colonetti".

<sup>3</sup> The additional "1" in the grade designation refers to graphite of greater purity.



(identical in principle) used at the two laboratories. The aim therefore is two-fold: (1) to resolve the difference between results obtained at IMGC and NBS, and (2) to obtain final definitive values for the above properties of graphite.

Two specimens were fabricated into the form of thin-walled tubes from a cylindrical rod sample of AXM-5Q1 graphite supplied by the Office of Standard Reference Materials at NBS. The dimensions of the tubes were, nominally: length, 76 mm; outside diameter, 6.3 mm; wall thickness, 0.5 mm. A small rectangular hole (0.5 x 1.0 mm) was fabricated through the wall at the center of each tube, thereby approximating black-body conditions for the pyrometric temperature measurements. In order to compensate for the cross-sectional nonuniformity created by the hole, a portion of the specimen was removed by grinding a flat along the length of the tube excluding the 1 mm length of the hole.

Each specimen was pulse-heated in a vacuum environment of about 1.3 mPa ( $\sim 10^{-5}$  torr), successively from room temperature through six overlapping temperature ranges between 1500 and 3000 K. The duration of the electrical current pulse used to resistively heat the specimen ranged between 400 and 500 ms. The heating rates varied, depending upon the temperature range, between 3000 and 5000 K·s<sup>-1</sup>. During each pulse experiment, simultaneous measurements of specimen temperature, and voltage across and current through the specimen were recorded with millisecond resolution.

Heat capacity was computed using the data taken during the heating period by means of the relation  $C_p = (eI - P_r)/nT'$

where  $e$  is the voltage drop across the specimen,  $i$  the current,  $P_r$  the power loss due to thermal radiation,  $n$  the number of moles, and  $T'$  the heating rate of the specimen. On the basis of data taken during the initial cooling period of the specimen, the correction for radiative heat loss was calculated to be about 4% at 1500 K and as much as 35% at 3000 K. The results in the six temperature ranges for the two specimens were combined and fitted by a quadratic function in temperature by means of the least-squares method. The function that represents the final results (standard deviation = 0.3%) for the heat capacity of AXM-5Q1 graphite at temperatures between 1500 and 3000 K is

$$C_p = 19.438 + 3.6688 \times 10^{-3} T - 4.6624 \times 10^{-7} T^2 \quad (1)$$

where  $C_p$  is in  $J \cdot mol^{-1} \cdot K^{-1}$  and  $T$  is in K. In the computations of heat capacity, the atomic weight of graphite was taken as 12.011. The deviation of the heat capacity values for the two specimens from the smooth function defined by Eq. (1) is shown in Fig. 1. As may be seen, the deviations are about 0.5% or less at all but the highest temperatures where the deviations become as large as 1% for one of the specimens.

The electrical resistivity of the specimen was computed<sup>4</sup> by means of the relation  $\rho = RA/L$  where  $R$  is the resistance,  $A$  the cross-sectional area, and  $L$  the length of specimen between the voltage probes. The cross-sectional area was obtained from the density of the graphite material and the measurement of specimen

---

<sup>4</sup> In all computations, the geometrical quantities of the specimens were based on their room temperature (295 K) dimensions.

values of resistivity. Powell et al. did not give details concerning the heat treatment and purity of the specimen used in their measurements.

Results for the melting point of nickel as reported in the literature are presented in Table III, along with corresponding values based on IPTS-68 for comparison with the present work. Prior to the gas-thermometer work by Day and Sosman [15], most of the early determinations of the nickel melting point were made by means of thermocouples (for a summary see Refs. [16,17]). All subsequent investigations, with the exception of our work, have utilized visual optical pyrometry for the measurement of temperature.

In experiments by Wensel and Roeser [16], and by Van Dusen and Dahl [17], melting temperatures were determined by measuring the relative brightness of blackbodies at the melting points of gold and nickel, and then calculating the upper temperatures by means of Planck's law (based on accepted values for the gold point and the second radiation constant). Their results form the basis for the secondary reference point value of 1728 K assigned to the melting temperature of nickel [2,18]. In subsequent work by Schofield and Bacon [19] and by Oriani and Jones [20], the radiation temperature measurements were referenced indirectly to the gold point by means of calibrated tungsten-filament lamps.

As may be seen in Table III, these investigations yield somewhat lower melting point values than the present result, 1729 K. However, the differences are within the measurement uncertainties reported by the investigators. With the exception of the work by Oriani and Jones, the specimens used in the

those reported in the literature in Figs. 2 and 3, respectively.

Heat capacity data at temperatures in the present range have also been obtained by Krauss and Warncke [8] and by Vollmer et al. [9], using adiabatic calorimetry, and by Kollie [10] using a slow pulse heating method. The results of Vollmer et al. are in good agreement (better than 1%) with the present work whereas the data obtained in the other two investigations are about 4% higher. Measurements by Novikov [11] using an adiabatic method and by Ewert [12] using drop calorimetry have yielded heat capacity data at temperatures up to about 1250 and 1275 K, respectively. The trend of these data with increasing temperature is different than that of the present work, though extrapolations to 1300 K yield respective values which are only about 2 and 3% lower than the present value for heat capacity.

The electrical resistivity results reported by Kollie [10] and by Powell et al. [13] are respectively about 1 and 1.5% lower than our results whereas the data reported by Laubitz et al. [14] when extrapolated to 1300 K is about 2% lower. However, the differences are within the combined experimental (and extrapolation) errors. The lower values of resistivity obtained in the earlier investigations may be partially due to extensive annealing of the specimens used in the measurements: the specimen (>99.89% pure) used by Kollie was annealed at 1100 K for 24 h and Laubitz et al. annealed their specimen (99.99<sup>+</sup>% pure) at 1400 K for 2 h whereas the present specimens (99.98<sup>+</sup>% pure) were each subjected to a pulse heating to about 1500 K, prior to the measurements. Specimens of higher purity should also yield lower

The final values for heat capacity and electrical resistivity are presented at 50 K temperature intervals in Table I. It should be noted that in all computations the geometrical quantities of the specimens are based on their room temperature (298 K) dimensions.

The melting temperature for each specimen was obtained by averaging the temperatures measured during the melting period; the solid to liquid transition is indicated by a plateau in the temperature versus time function, as shown in Fig. 1. (Suitable melting plateaus were obtained only for two specimens.) A summary of results for the specimens is given in Table II. The average melting temperature for the two specimens is 1729.4 K with an absolute deviation of 0.5 K. It may be concluded that the melting temperature of nickel is 1729 K.

A detailed analysis of the sources and magnitudes of errors involved in the measurement of various thermophysical properties with the NBS pulse heating system has been given in an earlier publication [5]. More recently, errors in temperature measurements with the same system were discussed in connection with the measurement of the melting temperature of palladium [7], which is about 100 K above that of nickel. In the present work, specific items in the error analyses were recomputed whenever conditions differed from those in the earlier publications. The maximum uncertainties in the measured properties are estimated to be as follows: heat capacity, 3%; electrical resistivity, 1%; melting temperature,  $\pm 4$ K.

The heat capacity and electrical resistivity of nickel measured in this work are presented and compared graphically with

of least-squares yielding a polynomial in temperature. The function that represents the results for heat capacity (standard deviation = 0.6%) at temperatures between 1300 and 1700 K is

$$C_p = 21.735 + 9.8200 \times 10^{-3}T \quad (1)$$

where  $C_p$  is in  $\text{J}\cdot\text{mol}^{-1}\cdot\text{K}^{-1}$  and  $T$  is in K. In the computation of heat capacity, the atomic weight of nickel was taken as 58.71.

The electrical resistivity was determined from the same data on voltage, current and temperature that were used to calculate heat capacity. The cross-sectional area of the specimen, which is needed in the computation of resistivity, was obtained from the density of nickel ( $8.902 \text{ g}\cdot\text{cm}^{-3}$ ) and a measurement of the specimen weight. The final values for resistivity were obtained by fitting a polynomial in temperature to the combined results for the three temperature ranges, by means of the least-squares method. The function that represents the results for electrical resistivity (standard deviation = 0.1%) at temperatures between 1300 and 1700 K is

$$\rho = 18.908 + 2.3947 \times 10^{-2}T \quad (2)$$

where  $\rho$  is in  $\mu\Omega\cdot\text{cm}$  and  $T$  is in K. Prior to the pulse experiments, a Kelvin bridge was used to measure the electrical resistivity of the specimens at "room temperature", yielding an average value of  $7.54 \mu\Omega\cdot\text{cm}$  at 295 K, with an average absolute deviation of 0.3% and a maximum absolute deviation of 0.4%.

detected elements was less than 20 ppm, each element being below the 1 ppm limit.

The response of the high-speed photoelectric pyrometer [6] was optimized by dividing the temperature interval of the measurements (1300-1700 K) into three ranges. One experiment per specimen was performed in each temperature range. The heating rate was varied depending on the temperature range by adjusting the value of a resistance in series with the specimen; typically, the heating rate was in the range  $2400\text{--}3400\text{ K}\cdot\text{s}^{-1}$ . Duration of the current pulse was in the range 500-600 ms.

All measurements of heat capacity and electrical resistivity were performed with the specimens in a vacuum environment of about 1.3 mPa ( $\sim 10^{-5}$  torr). For the melting experiments, the specimens were pulse-heated in an argon environment at about 0.2 MPa ( $\sim 2$  atm).

Upon completion of the experiments, the high-speed pyrometer was calibrated against a tungsten filament reference lamp which, in turn, had been calibrated against the NBS Photoelectric Pyrometer by the Radiometric Physics Division at NBS. All temperatures reported in this work, except where explicitly noted otherwise, are based on IPTS-68.

The heat capacity was computed using the data on voltage, current, and temperature taken during the heating period of each experiment. A correction was made for the radiative heat loss from the specimen based on data taken during the initial cooling period of the specimen. This correction amounted to about 1% at 1300 K and about 2% at 1700 K. Heat capacity data for the three temperature ranges were combined and then smoothed by the method

b. Thermophysical Properties of Nickel above 1300 K

A. Cezairliyan, A.P. Miiller and M.S. Morse

On the basis of a suggestion made by the Air Force, measurements of the heat capacity and electrical resistivity of nickel were performed in the temperature range 1300 to 1700 K [1]. In addition the melting temperature of nickel, which is a secondary reference point on the International Practical Temperature Scale of 1968 (IPTS-68) [2], was also measured [3]. This work was carried out by means of a rapid pulse-heating technique [4,5] which involves resistively heating the specimen from room temperature to temperatures of interest by passing a subsecond electrical current pulse through it; and simultaneously measuring (with millisecond resolution) pertinent experimental quantities such as specimen temperature, voltage across and current through the specimen. The short heating time (less than 1s) of this technique tends to minimize problems associated with quasi steady-state experiments at high temperatures, especially, specimen contamination and evaporation.

The measurements were performed on three tubular specimens fabricated from cylindrical rods by an electroerosion technique. Nominal dimensions of the tubes were: length, 75 mm; outside diameter, 6.4 mm; wall thickness, 0.5 mm. The results of a typical analysis furnished by the manufacturer indicate that the material was 99.98% pure with the following impurities in ppm by mass: Fe, 30; O, 20; N, 13; C, 8; Sn<15; In<6; Sr<5; Cl, Ge, Nd, S, Se, Sm, Ta, Te, <3 each; the total amount of all other



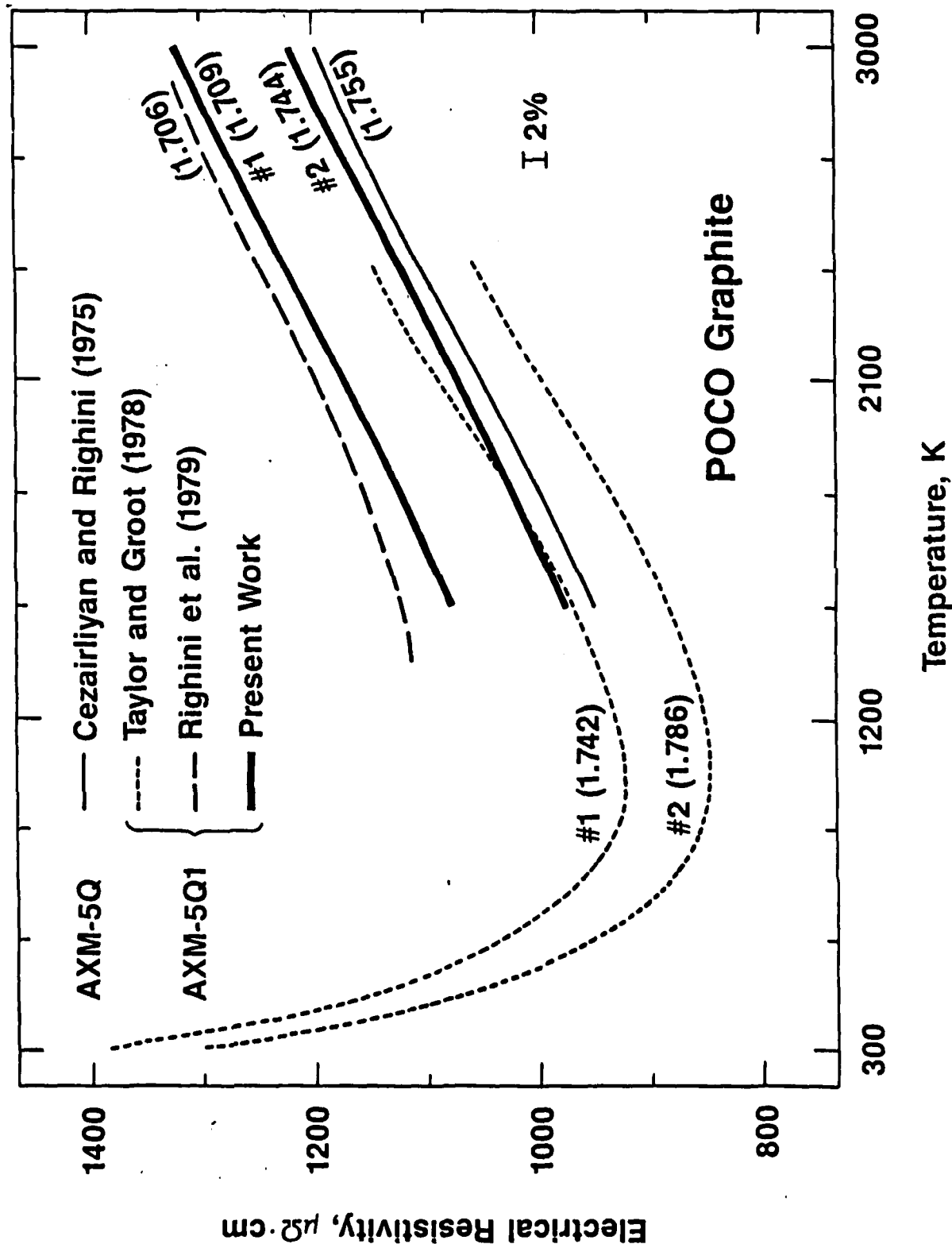


Fig. 3. Comparison of the present work with electrical resistivity data reported in the literature for AXM-5Q and AXM-5Q1 POCO graphite. The numbers in brackets refer to the density (in  $\text{g}\cdot\text{cm}^{-3}$ ) of the specimens at room temperature.

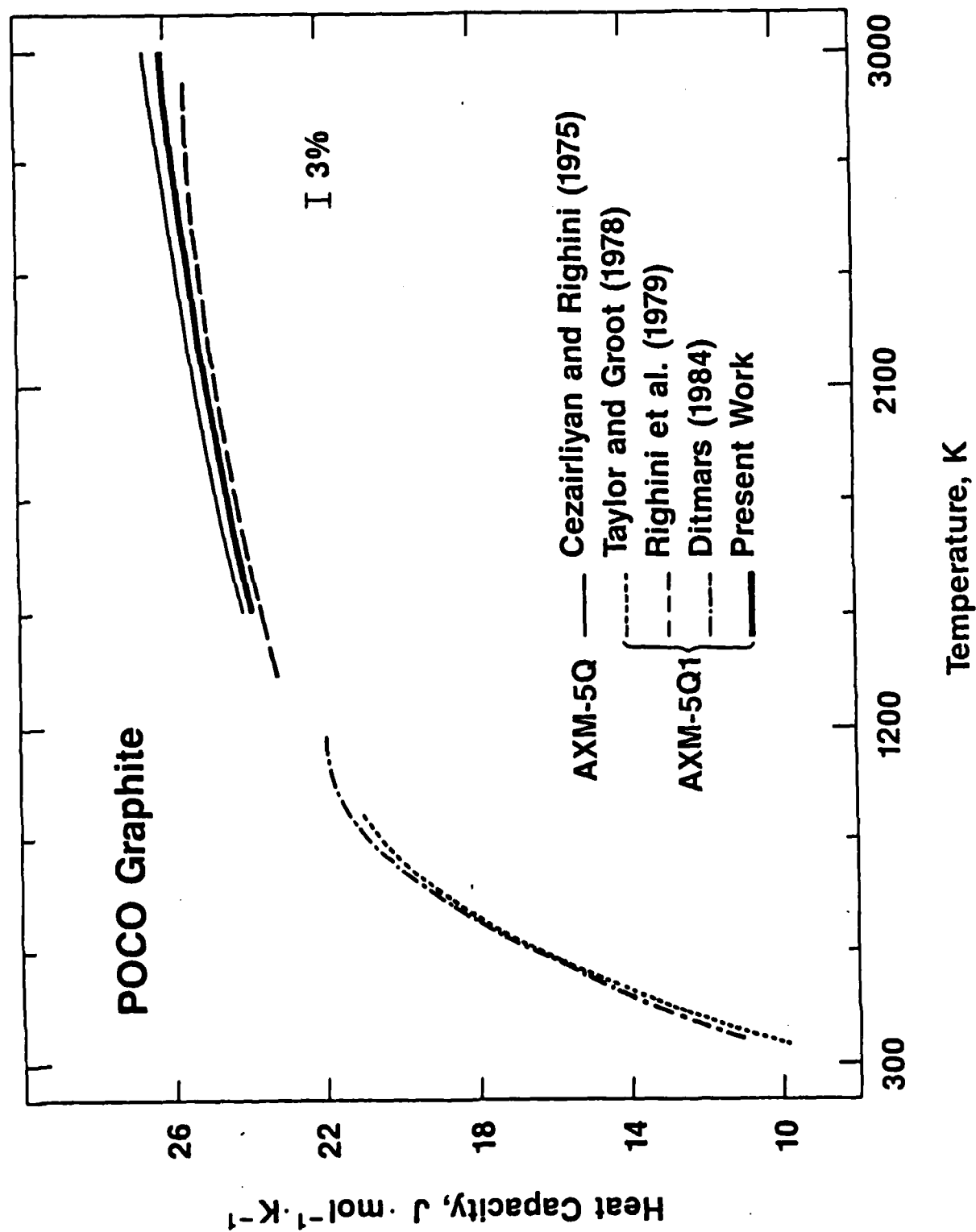


Fig. 2. Comparison of the present work with heat capacity data reported in the literature for AXM-5Q and AXM-5Q1 POCO graphite.

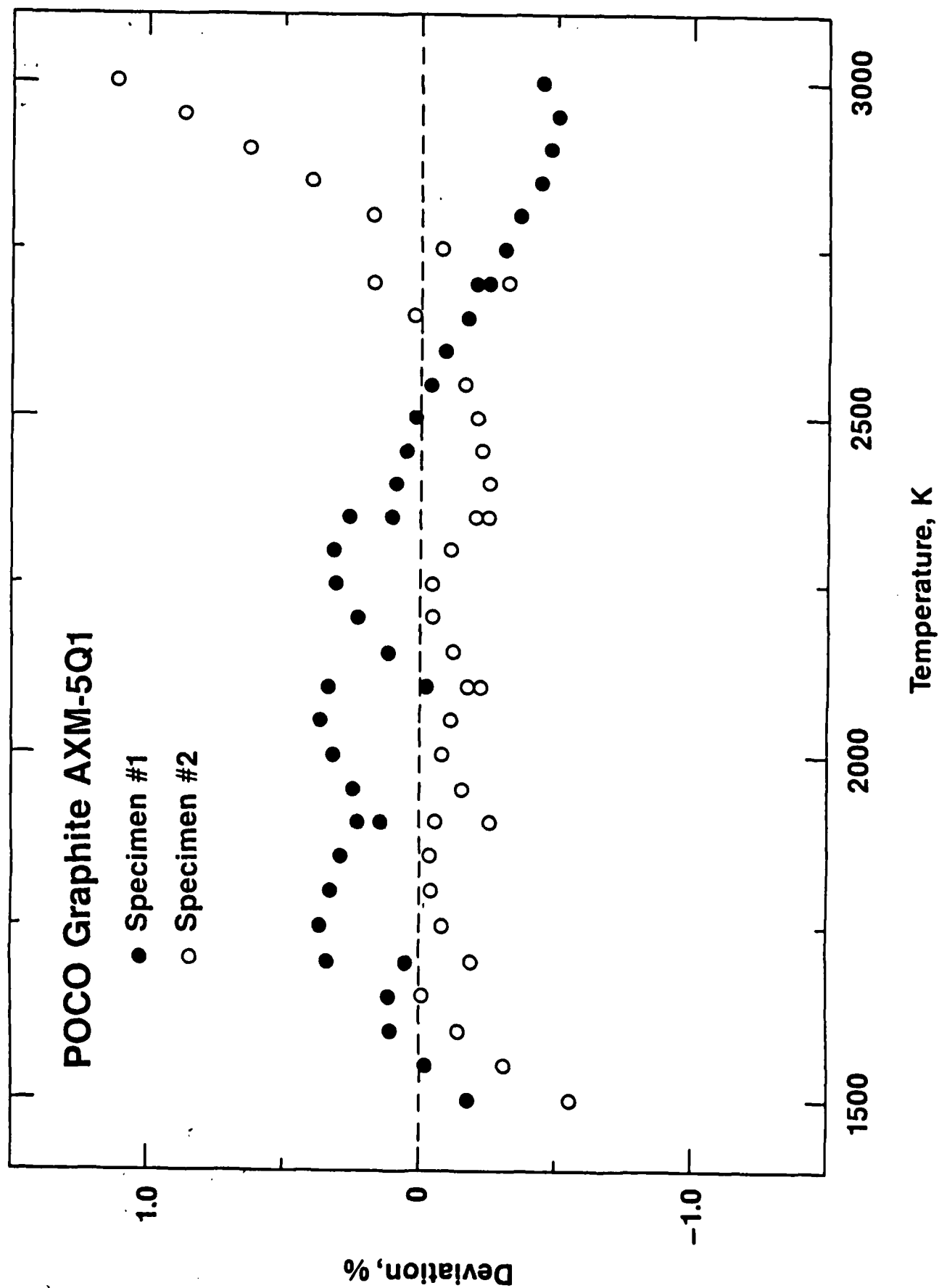


Fig. 1. Deviation of the heat capacity results for the individual specimens from Eq. (1), which represents the least-squares fit to the combined data for the two specimens.

Table I. Smoothed Values for Heat Capacity, Electrical Resistivity and Hemispherical Total Emittance of AXM-5Q1 POCO Graphite.

T (K)	$C_p$ (J·mol <sup>-1</sup> ·K <sup>-1</sup> )	$\rho$ ( $\mu\Omega\cdot\text{cm}$ )		$\epsilon$
		Specimen 1	Specimen 2	
1500	23.89	1078.6	975.0	-
1600	24.11	1092.6	989.5	-
1700	24.33	1107.7	1004.7	0.813
1800	24.53	1123.5	1020.6	0.815
1900	24.73	1140.0	1037.0	0.817
2000	24.91	1157.0	1053.9	0.820
2100	25.09	1174.4	1071.0	0.822
2200	25.25	1192.0	1088.3	0.825
2300	25.41	1209.7	1105.7	0.827
2400	25.56	1227.2	1123.0	0.829
2500	25.70	1244.6	1140.1	0.832
2600	25.83	1261.6	1157.0	0.834
2700	25.94	1278.0	1173.4	0.837
2800	26.06	1293.8	1189.4	0.839
2900	26.16	1308.7	1204.6	0.841
3000	26.25	1322.6	1219.2	-

would make a less-than-ideal standard for the measurement of transport properties.

#### References

1. A. Cezairliyan, J. Res. Nat. Bur. Stand. (U.S.) 75C: 7(1971).
2. A. Cezairliyan, M.S. Morse, H.A. Berman, and C.W. Beckett, J. Res. Nat. Bur. Stand. (U.S.) 74A: 65 (1970).
3. F. Righini, A. Cibrario, and A. Rosso, Rappporto Interno 5/173, Istituto di Metrologia "G. Colonetti", (1979).
4. A. Cezairliyan and F. Righini, Rev. Int. Htes. Temp. et Refract. 12: 124 (1975).
5. International Committee for Weights and Measures, "The International Practical Temperature Scale of 1968," Metrologia 5: 35 (1969).
6. A. Cezairliyan, A.P. Miiller, and M.S. Morse, "Thermodynamics of High Temperature Materials" AFOSR-ISSA-83-00038: 8 (1983).
7. R.E. Taylor and H. Groot, High Temp.-High Press. 12: 147 (1980).
8. D.A. Ditmars, to be published.

differences are probably due to systematic measurement errors rather than any real dependence of results on differences in specimen material. Below about 1200 K, there is good agreement between the data of Taylor and Groot [7], obtained by scanning calorimetry, and the heat capacity values derived from the relative enthalpy measurements by Ditmars [8].

Considerable differences exist among the values of electrical resistivity for graphite reported in the literature, and these appear to be related to rather large variations in the density. For comparison, the curves in Fig. 3 have been labelled with the room temperature density (in  $\text{g}\cdot\text{cm}^{-3}$ ) of the specimen material used in each case. As expected, there is an inverse relationship between resistivity and density, i.e., the highest resistivities are associated with the lowest densities and vice-versa. It may be seen that the resistivity values for our specimen #2 and Taylor and Groot's specimen #1, which have essentially the same density, are in good agreement.

Other measurements of hemispherical total emittance of POCO graphite, such as those by Righini et al. [3] and by Cezairliyan and Righini [4], yield values which are within 3% of the present results. However the trends (emittance versus temperature) are somewhat different.

In summary, the present study shows that the heat capacity of AXM-5Q1 POCO graphite is well characterized at temperatures up to 3000 K, and therefore, this material would be a suitable high-temperature standard for heat capacity measurements. The large variations observed in electrical resistivity (as well as in thermal conductivity [7]), however, suggest that this material

Final values for the measured properties, as derived from Eqs. (1)-(4), are presented at 100 K intervals in Table I. The values are based on the International Practical Temperature Scale of 1968 [5].

Details concerning the estimates of errors in the measured and computed quantities in experiments with the present measurement system are given in a previous publication [2]. Specific items in the error analyses were recomputed whenever the present conditions differed from those in the earlier publication. The maximum uncertainties are estimated to be as follows: heat capacity, 3%; electrical resistivity, 1%; hemispherical total emittance, 5%.

Comparisons of our results for heat capacity and electrical resistivity with other data on graphites of the same grade as reported in the literature are presented in Figs. 2 and 3, respectively. It should be noted that all investigations labelled by AXM-5Q1 involved specimens fabricated from samples taken from the same lot of POCO graphite.

As may be seen in Fig. 2, heat capacity data obtained by Righini et al. [3] at IMGC are about 1 to 2% lower than the present results which, in turn, are approximately 1% lower than values for AXM-5Q graphite reported by Cezairliyan and Righini [4] at NBS. Limited measurements (described in the previous report [6]) have also been performed at NBS on the same specimen used by Righini et al., and have yielded results (not shown) that are about 0.5% lower than the AXM-5Q data. The agreement among the measurements at NBS therefore suggests that the observed

weight. Rather large differences (~10%) in resistivity values, which seem to be related to the difference in density for the two specimens (see below), were found to exist. Therefore, the results for each specimen were fitted separately by the least-squares method. The functions which represent the final results (standard deviation = 0.1%) for electrical resistivity of specimens 1 and 2 in the range 1500 to 3000 K are

$$\rho = 1084.6 - 1.9940 \times 10^{-1} T + 1.6760 \times 10^{-4} T^2 - 2.4896 \times 10^{-8} T^3 \quad (2)$$

$$\text{and } \rho = 931.02 - 1.2587 \times 10^{-1} T + 1.3299 \times 10^{-4} T^2 - 1.9673 \times 10^{-8} T^3 \quad (3)$$

respectively, where  $\rho$  is in  $\mu\Omega\cdot\text{cm}$  and  $T$  is in K. The respective densities used in the computations were 1.706 and 1.744  $\text{g}\cdot\text{cm}^{-3}$ . Prior to the pulse experiments, a Kelvin bridge was used to measure the electrical resistivity at "room temperature" (292 K) yielding values of 1,738 and 1,538  $\mu\Omega\cdot\text{cm}$  for specimens 1 and 2, respectively.

The hemispherical total emittance was computed for each specimen from data taken during both heating and cooling periods. The function which represents the final results (standard deviation = 0.3%) for hemispherical total emittance of AXM-5Q1 POCO graphite in the range 1700 to 2900 K is

$$\epsilon = 0.7718 + 2.397 \times 10^{-5} T \quad (4)$$

where  $T$  is in K.



earlier measurements were less pure than those used in the present study, which may account partially for the lower melting points obtained earlier. The depression of the melting point due to the premelting effects of impurities in the present specimens is estimated to be not more than 1 K.

Of the seventeen secondary reference points above the freezing point of gold given in a recent extended list [18], seven are based solely on measurements by Cezairliyan and co-workers using a rapid pulse-heating technique. The agreement of the present result with the assigned value for the nickel melting point (1728 K), which is based on quasi-steady state experiments, strengthens the foundation for secondary reference points at higher temperatures determined by dynamic techniques.

## References

1. A. Cezairliyan and A.P. Miiller, Int. J. Thermophysics 4: 389 (1983).
2. The International Committee for Weights and Measures, Metrologia 5: 35 (1969).
3. A. Cezairliyan and A.P. Miiller, Int. J. Thermophysics 5: 315 (1984).
4. A. Cezairliyan, M.S. Morse, H.A. Berman, and C.W. Beckett, J. Res. Nat. Bur. Stand. (U.S.) 74A: 65 (1970).
5. A. Cezairliyan, J. Res. Nat. Bur. Stand. (U.S.) 75C: 7 (1971).
6. G.M. Foley, Rev. Sci. Instrum. 41: 827 (1970).
7. A.P. Miiller and A. Cezairliyan, Int. J. Thermophysics 2: 63 (1981).
8. V.F. Krauss and H. Warncke, Z. Metallkunde 46: 61 (1955).
9. O. Vollmer, R. Kohlhaas, and M. Brauer, Z. Naturforsch. 21a: 181 (1966).
10. T.G. Kollie, Ph.D. dissertation, University of Tennessee, 1969 (Oak Ridge National Laboratory Technical Memo ORNL-TM-2649).
11. I.I. Novikov, V.V. Roshchupkin, A.G. Mozgovoi, and N.A. Semashko, High Temp. 19: 694 (1981).
12. M. Ewert, Proc. Akad. Wetenschappen Amsterdam 39: 833 (1936).
13. R.W. Powell, R.P. Tye, and M.J. Hickman, Int. J. Heat Mass Transfer 8: 679 (1965).
14. M.J. Laubitz, T. Matsumura, and P.J. Kelley, Can. J. Phys.

- 54: 92 (1976).
15. A.L. Day and R.B. Sosman, High Temperature Gas Thermometry,  
Publ. 157 (Carnegie Inst. Washington, 1911).
16. H.T. Wensel and W.F. Roeser, J. Res. Nat. Bur. Stand. (U.S.)  
5: 1309 (1930).
17. M.S. VanDusen and A.I. Dahl, J. Res. Nat. Bur. Stand. (U.S.)  
39: 291 (1947).
18. L. Crovini, R.E. Bedford, and A. Moser, Metrologia 13: 197  
(1977).
19. T.H. Schofield and A.E. Bacon, J. Inst. Metals 82: 167  
(1953).
20. R.A. Oriani and T.S. Jones, Rev. Sci. Instrum. 25: 248

TABLE I. Smoothed Heat Capacity and Electrical Resistivity of Nickel According to Eqs. (1) and (2).

T (K)	$C_p$ (J·mol <sup>-1</sup> ·K <sup>-1</sup> )	$\rho$ ( $\mu\Omega\cdot\text{cm}$ )
1300	34.50	50.04
1350	34.99	51.24
1400	35.48	52.43
1450	35.97	53.63
1500	36.46	54.83
1550	36.96	56.03
1600	37.45	57.22
1650	37.94	58.42
1700	38.43	59.62

TABLE II. Experimental Results for the Melting Temperature of Nickel

Specimen number	Heating rate <sup>a</sup> (K·s <sup>-1</sup> )	Number of temp. at plateau	Melting temp. (K)	Stand. dev. (K)
1	2570	84	1729.9	0.4
2	2560	68	1728.9	0.4

<sup>a</sup>Derivative of the temperature versus time functions (at approximately 30 K below the melting plateau) obtained by fitting the temperature data before melting to a quadratic function in time with the least squares method.

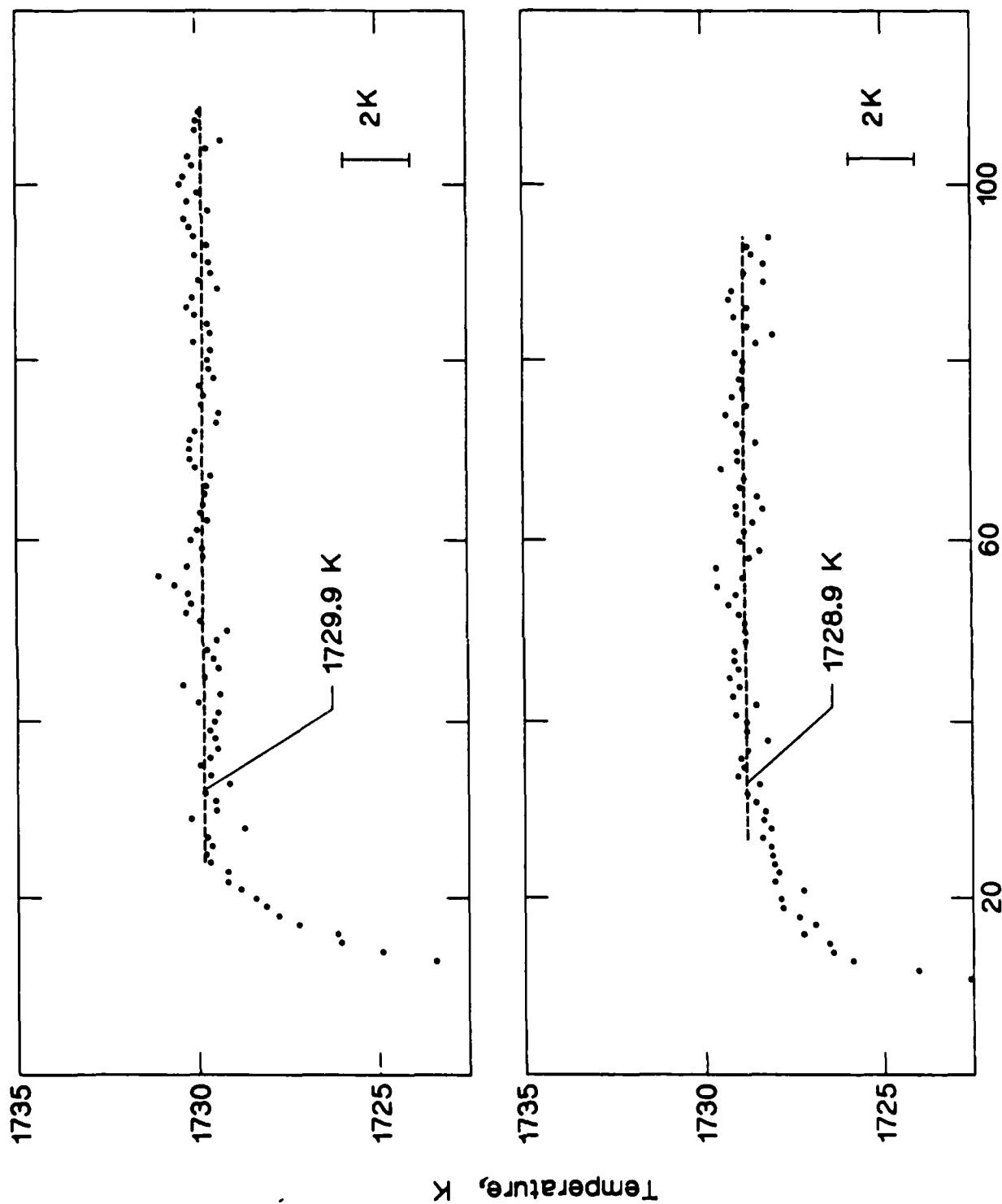
TABLE III. Values for the Melting Point of Nickel Reported in the Literature

Investigator	Ref.	Year	Specimen purity (%)	Constants <sup>a</sup>		Melting Point (K)	
				T <sub>Au</sub> (K)	c <sub>2</sub> (cm.K)	As reported <sup>b</sup>	On IPTS-68
Day and Sosman	[15]	1911	99.84			1725	
Wensel and Roeser	[16]	1930	99.94	1336	1.432	1728+1	1728 <sup>c</sup>
van Dusen and Dahl	[17]	1947	99.84	1336	1.432	1728+1	1728 <sup>c</sup>
Schofield and Bacon	[19]	1953	99.86	1336.15	1.438	1724+10	1726
Oriani and Jones	[20]	1954	99.999	1336.15	1.438	1725+4	1727
Present work			99.98 <sup>+</sup>	1337.58	1.4388	1729+4	1729

<sup>a</sup>Values of T<sub>Au</sub> (gold point) and c<sub>2</sub> (second radiation constant) used by the investigator.

<sup>b</sup>Except for the melting point reported by Day and Sosman [15], which was obtained by gas thermometry, all others were obtained by pyrometry based on the given values of T<sub>Au</sub> and c<sub>2</sub>.

<sup>c</sup>Basis for the secondary reference point value of 1728 K given in the extended list of IPTS-68 [18].



Time , 1 unit = 0.833 ms

Fig. 1. Variation of the temperature of specimen 1 (upper) and specimen 2 (lower) near and at the melting point of nickel.

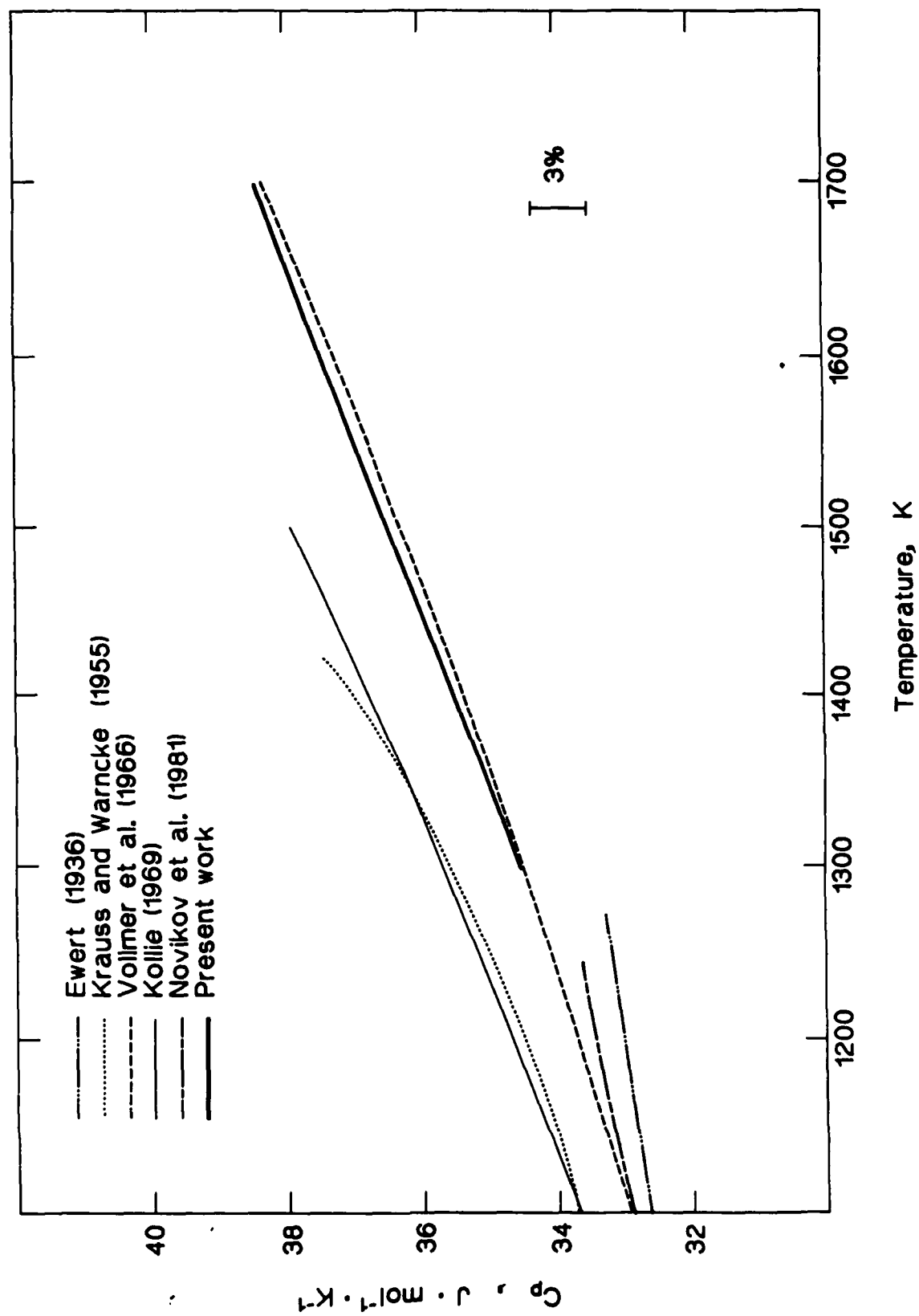


Fig. 2. Heat capacity of nickel: present work and data reported in the literature.



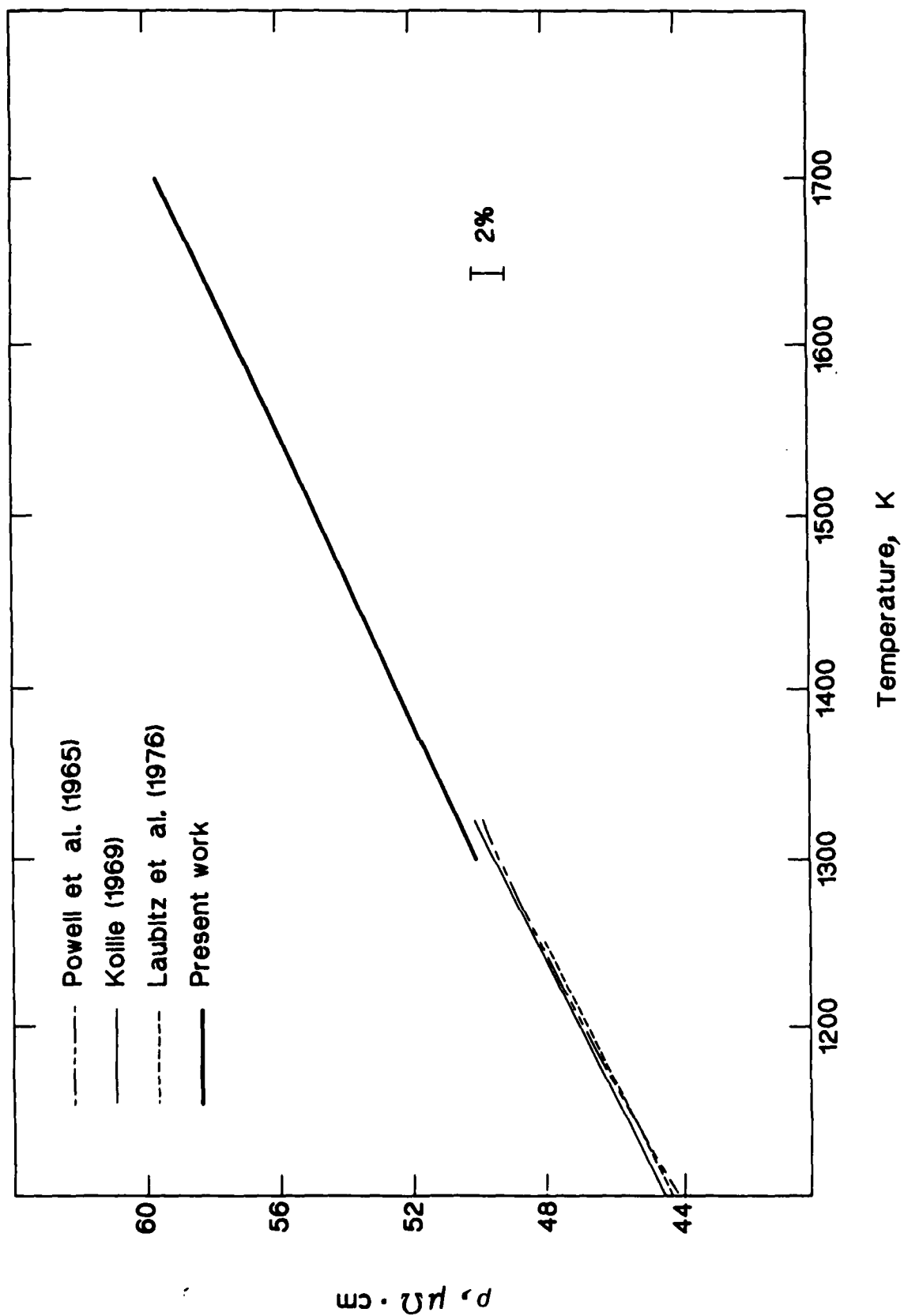


Fig. 3. Electrical resistivity of nickel: present work and data reported in the literature.

2. High Temperature Enthalpy Measurements

D. A. Ditmars, Principal Investigator

- a. Relative Enthalpy of Hexagonal and Cubic Boron Nitride Between 273.15 and 1200 K.
- b. Aluminum: Derivation of  $C_{vO}$  from  $C_p$  and Comparison to  $C_{vO}$  Calculated from Anharmonic Potentials.

a.

## Relative Enthalpy of Hexagonal and Cubic Boron

Nitride Between 273.15 K and 1200 K

by

David A. Ditmars

### Abstract

The relative enthalpy of the hexagonal ("graphitic") and cubic ("diamond-like") polymorphs of boron nitride has been measured between 273.15 K and 1173.15 K. The enthalpy data have been fitted with polynomial functions by a least-squares method. The derived specific heat functions agree well with the literature low-temperature data on boron nitride.

### Introduction

Boron nitride is a refractory compound which finds application in high-temperature technology in pure form as a structural material. It also shows promise for development as an additive in the thermal toughening of ceramic composites. It exhibits two principal polymorphs, a layered hexagonal phase isomorphic to the graphite structure and two so-called cubic phases roughly isomorphic to the diamond structure, stable at high temperatures and pressures and existing, like diamond, in a metastable state under ordinary conditions. The current status of our knowledge of the BN phase diagram is apparently still that presented by Bundy and Wentorf [1], the first investigators to synthesize cubic BN. Specific heat data on any of the BN phases is scanty, the low-temperature region being represented for the hex and cubic phases by single data sets on samples of ill-documented purity [2,3]. No heat capacity data for the cubic phase above 1000 K was found. We have undertaken the present

measurements in order to more adequately define the high-temperature thermodynamic functions of the BN phases. This is a preliminary report on our measurements up to 1200 K.

### Samples

A sample of dense, pressure, annealed, pyrolytic hexagonal BN in solid disc form was obtained from the Union Carbide Corporation through the courtesy of Dr. A.W. Moore. The cubic BN was obtained from the Van Itallie Corporation, N.Y., in the form of a high-quality industrial abrasive, 60/80 mesh "Borazon." Both samples were examined by semi quantitative spectrographic analysis and both showed the following impurity concentrations (wt percent): < 0.01%: (Be), < 0.02%: (Ag, Cu, K, Li, Mg, Na, Ti), < 0.05%: Al, Ba, Ca, Cr, Fe, Mn, Mo, Ni, Sn, Sr, V, Zr). The "hex" sample showed < 0.05% Si, but the cubic sample was unusually high at 0.2% Si. Structural analyses on the samples are not yet complete. The hex sample was machined in wafers of 0.5 in. diameter and 0.06 in thickness. Several of these wafers and a quantity of the crushed cubic BN were sealed in separate Pt-10Rh capsules of nearly identical mass under 13 kP helium gas pressure.

### Method

The enthalpy, relative to 273.15 K, of each sample (plus encapsulation) was measured in a precise isothermal, phase-change calorimeter over the temperature range 373-1173 K. The method has been well-documented previously [4,5]. Two or three measurements were made at each of nine temperatures distributed at equal temperature intervals to check the precision of measurement. In addition, an earlier series of enthalpy measurements on an empty Pt-10Rh capsule nearly identical to those used to encapsulate the BN samples was available [6]. The sample enthalpy data

were obtained by subtracting from the measured sample plus capsule enthalpy, that of the encapsulation alone. Small corrections ( $< 0.05\%$ ) were made to the measured enthalpies of the encapsulated samples to account for the small mass differences between the capsules used and the empty capsule. The following sample masses were used: hex, 8.88584 g (0.3580589 mole); cubic, 10.19105 g (0.4106529 mole).

Table 1. Enthalpy Data for Hexagonal BN<sup>1</sup>

T/K	$(H_T - H_{273.15})/\text{J mol}^{-1}$
372.812	2122.57
372.770	2122.55
372.741	2119.03
423.482	3446.71
423.481	3443.08
423.466	3443.50
473.601	4899.32
473.364	4890.22
473.305	4885.42
573.297	8140.30
572.986	8129.86
572.980	8128.23
673.361	11772.80
673.241	11767.41
673.235	11767.35
873.03	19818.89
873.20	19820.50
973.74	24167.78
1073.52	28602.34
1074.15	28634.84
1174.28	33182.82

<sup>1</sup> M.W. = 24.8167

Table 2. Enthalpy Data for Cubic BN<sup>1</sup>

<u>T/K</u>	<u>(H<sub>T</sub> - H<sub>273.15</sub>)/J mol<sup>-1</sup></u>
372.186	1785.53
473.056	4418.12
472.882	4409.13
571.385	7571.79
673.296	11292.95
673.211	11294.05
773.374	15266.30
872.97	19468.13
873.44	19496.40
973.72	23908.10
1073.52	28430.45
1073.56	28428.13
1174.35	33097.86

<sup>1</sup> M.W. = 24.8176

### Results

The net measured enthalpy data for the hex and cubic phases are presented in tables 1 and 2, respectively. These were fitted with the following model:

$$(H_T - H_{273.15}) = At^3 + Bt^2 + Ct + D(t/T) \quad (1)$$

where H = enthalpy in J mol<sup>-1</sup>

t = Celsius temperature

T = Kelvin temperature.

The coefficients and the residual standard deviation (σ) of the fits are given in table 3.

which is obtained from the second rank tensor  $\phi_{\alpha\beta}$  derived from the Morse potential.

The closed loops appearing in diagrams 2(a), 3(a), 3(b), 3(c), and 3(d) involve a single BZ sum which has been evaluated with 108,000 points in the whole zone. The other diagrams [2(b), 3(c), 3(d), 3(f)] in which the phonon lines connect the different vertices have been evaluated with 500 wave vectors in the whole zone. We have used a combination of 215 odd and even wave vectors in the calculation of diagrams 3(g) and 3(h), and finally the diagram 3(e) has been evaluated by the plane-wave method as given in Shukla and Wilk [22]. We will omit presenting the rest of the details of the calculation of the diagrams as they can be obtained from Shukla and Wilk [22].

The harmonic contribution to  $C_{v_0}$  is calculated from the well-known formula

$$C_{v_0}^h = k_B \sum_{\vec{q}j} \left( \frac{\hbar \omega(\vec{q}j)}{2k_B T} \right)^2 \text{Cosech}^2 \left( \frac{\hbar \omega(\vec{q}j)}{k_B T} \right) \quad (11)$$

where  $\omega(\vec{q}j)$  is the phonon frequency for the wave vector  $\vec{q}$  and branch index  $j$ . In the work of Shukla and Plint [1] the above expression was evaluated numerically by performing the  $\vec{q}$  summation for a large number of points in the Brillouin zone. It was noted by Shukla and Plint that the three term high temperature expansion ( $T > \theta_D$ ) gave the same results as Eq. (11) in the temperature range 550-900 K. In the present work we are able to evaluate

$$\begin{aligned}
& \Phi(\lambda_1, \dots, \lambda_n) \\
&= \frac{1}{2M^{n/2}} \sum_{\ell}' \sum_{\alpha\beta\gamma} \phi_{\alpha\beta\gamma}(|\vec{R}_{\ell}|) e_{\alpha}(\lambda_1) e_{\beta}(\lambda_2) \dots e_{\gamma}(\lambda_n) \\
&\times \prod_{i=1}^n [1 - \exp(i\vec{q}_i \cdot \vec{R}_{\ell})] \quad (9)
\end{aligned}$$

where  $M$  is the atomic mass,  $\vec{R}_{\ell}$  a vector of the direct lattice and  $e_{\alpha}(\lambda_i)$  ( $i=1, \dots, n$ ) are the components of the eigen-vector  $\vec{e}(\lambda_i)$ . The prime over the  $\ell$  summation indicates the omission of the origin point.

The calculation of the diagrams presented in Fig. 3 is extremely complicated because of the multiple Brillouin zone (BZ) sums as well as the summation over the neighbours and the tensors  $\phi_{\alpha\beta\gamma}$ . So far, they have been evaluated only for the Lennard-Jones nearest neighbour interaction potential for the fcc crystal by Shukla and Cowley [10] and Shukla and Wilk [22].

To get some idea of the magnitude of  $F$  to  $O(\lambda^4)$  in  $Al$ , here, we have chosen to calculate the above eight contributions for the Morse potential. Recently the nearest neighbour interaction Morse potential has been used successfully in the calculation of the thermal expansion and other thermodynamic properties by Shukla and MacDonald [23] and MacDonald and MacDonald [24].

The Morse potential with its parameters  $D$ ,  $\alpha$ , and  $r_0$  for  $Al$  is defined by [23]

$$\phi(r) = D \{ \exp[-2\alpha(r-r_0)] - 2\exp[-\alpha(r-r_0)] \} \quad (10)$$

$$D = 0.6369 \times 10^{-12} \text{ erg}, \quad \alpha = 1.1611 (\text{\AA})^{-1}, \quad r_0 = 2.8485 \text{\AA}.$$

The tensors  $\phi_{\alpha\beta\gamma}$  needed in the above calculation of the diagrams of  $O(\lambda^2)$  and  $O(\lambda^4)$  are obtained by differentiating the above potential. The  $\omega(\vec{q})$  and  $\vec{e}(\vec{q})$  are obtained by diagonalizing the dynamical matrix  $D_{\alpha\beta}(\vec{q})$



$$H_A = \lambda V_3 + \lambda^2 V_4 + \lambda^3 V_5 + \lambda^4 V_6 \quad (7)$$

which is obtained by expanding the potential energy in powers of the atomic displacement and truncating the expansion after the sixth degree term. The eight contributions to  $F$  of  $O(\lambda^4)$  arise from the  $V_6$ ,  $V_4-V_4$ ,  $V_3-V_5$ ,  $V_3-V_3-V_4$ , and  $V_3-V_3-V_3-V_3$  interactions in the first, second, third and the fourth order perturbation theory, respectively. In the diagrammatic language, these contributions to  $F$  have been derived by Shukla and Cowley [10]. It should be noted that there are two distinct contributions or diagrams for each of the  $V_4-V_4$ ,  $V_3-V_3-V_4$  and  $V_3-V_3-V_3-V_3$  interactions, whereas there is only one distinct diagram for the  $V_6$  and  $V_3-V_5$  interaction. We present these diagrams and the two lowest order  $\lambda^2$  diagrams in Figs.(2) and (3), respectively.

Symbolically they represent the various phonon lines connecting the different vertices  $V_n$  ( $n=1,2,\dots,6$ ) for the different combinations listed above. In the high temperature limit, their contributions to  $F$  are listed in Table II, where the meaning of the various symbols is as follows:  $\hbar$  is the Planck's constant divided by  $2\pi$ ,  $\beta=(k_B T)^{-1}$ ,  $k_B$  is the Boltzmann constant,  $\omega(\lambda_i)$  is the phonon-frequency for the mode  $\lambda_i=(\vec{q}_i, j_i)$ ,  $\vec{q}_i$  is the wave vector and  $j_i$  is the branch index, and in general the  $V$  function is defined by

$$V(\lambda_1, \dots, \lambda_n) = \left(\frac{1}{n!}\right) N^{1-n/2} \Delta(\vec{q}_1 + \dots + \vec{q}_n) \times \left(\frac{\hbar^n}{2^n \omega(\lambda_1) \dots \omega(\lambda_n)}\right)^{\frac{1}{2}} \phi(\lambda_1, \dots, \lambda_n) \quad (8)$$

where  $N$  denotes the number of unit cells in the crystal and  $\Delta(\vec{q}_1 + \vec{q}_2 + \dots + \vec{q}_n) = 1$  if the argument of the  $\Delta$  function is a vector of the reciprocal lattice (including zero) and zero otherwise. The  $\phi$  function is defined by

For any of these curves the portion above  $3R$  must be accounted for by invoking the anharmonic and vacancy contributions to  $C_{V_0}$ . To separate these two contributions we need to calculate all the anharmonic contributions to  $C_{V_0}$  and then the remainder is the vacancy contribution because there are no other excitations which contribute to  $C_{V_0}$  in the temperature range 700-950 K.

First let us examine the anharmonic effect which can be evaluated either by the lattice dynamics method (i.e. the perturbation theory (PT) or the self consistent phonon theory) which is valid for all temperatures or by computer simulation techniques such as the Monte Carlo or Molecular Dynamics methods which are usually applicable in the classical high temperature limit ( $T > \theta_D$ , where  $\theta_D$  is the Debye temperature). Among these methods so far, only the perturbation method has been applied in the calculation of  $C_{V_0}$  for Al by Shukla and Plint[1]. Their calculation was carried out employing the lowest order perturbation theory which requires the numerical evaluation of two terms in the Helmholtz function ( $F$ ). These terms arise from the cubic and quartic terms of the Taylor expansion of the crystal potential energy ( $V(r)$ ).

If we denote the perturbation expansion parameter by  $\lambda$ , defined by the ratio of a typical root mean square atomic displacement and the nearest neighbour distance, the lowest order PT contributions to  $F$  are of  $O(\lambda^2)$  and their contribution to  $C_{V_0}$  is proportional to  $T$  in the high temperature limit ( $T > \theta_D$ ). Since our "experimental"  $C_{V_0}$  indicates an upward curvature, it is necessary to look for additional anharmonic contributions to  $C_{V_0}$  which vary as  $T^2$ . In fact it has been shown by Shukla and Cowley [10] that all the  $T^2$  contributions are given by the PT of  $O(\lambda^4)$  which requires the numerical evaluation of eight terms in  $F$ . The anharmonic Hamiltonian ( $H_A$ ) is given by

The resultant entropy,  $S_{V_0}$ , was subjected to a smoothing procedure. Finally the specific heat at the 0 K volume,  $C_{V_0} = T(dS_{V_0}/dT)$ , was obtained by four point differentiation and smoothing of the results.

The difference quantity  $C_p - C_{V_0}$  was then determined as a function of temperature and used to obtain reduced values of  $C_{V_0}$  from literature  $C_p$  data for comparison purposes. The  $C_{V_0}$  values are summarised in Table I.

Figure(1) shows the values of  $C_{V_0}$  reduced from the new experimental data [2] and the values reduced from literature  $C_p$  data [3,4,5]. The results of the present work show a steadily increasing specific heat with upward curvature from 550 K that reaches 3R near 775 K. As found in previous work [1], there is a wide discrepancy between the  $C_{V_0}$  values obtained from the  $C_p$  results given in refs [3,4]. The Brooks and Bingham data give a  $C_{V_0}$  that reaches 3R near 625 K and shows a marked upward curvature for  $T > 700$  K. Leadbetter's data give a  $C_{V_0}$  that never reaches 3R. The apparent decrease in this  $C_{V_0}$  after reaching  $5.82 \text{ cal mol}^{-1} \text{ K}^{-1}$  at 700 K may be a consequence of errors arising from the end point of the range of specific heat measurements near 750 K.

The results from Takahashi's data are similar to those obtained from Leadbetter's data to 650 K but increase steadily with increasing temperature above 650 K. The graph does not reach 3R by 850 K. The  $C_{V_0}$  curve from Takahashi's data is essentially parallel to that obtained from the new data but consistently lower over the entire temperature range shown in Fig. 1.

The isochores were almost straight lines. The slope of each isochore for the temperature range  $400 \leq T \leq 900$  K was obtained by a linear regression. The set of values of  $(\partial p / \partial T)_V$  thus found was used to evaluate the integral in Eq. (1) to obtain  $S_0$ .

As a second step the electronic contribution [18] to the entropy at the 0 K volume was subtracted. Here we have not followed the customary approach of representing the electronic specific heat,  $C_e$ , by  $C_e = \gamma T$  where the coefficient  $\gamma$  is obtained from the low temperature heat capacity measurements. For Al,  $\gamma$  is known from the low temperature specific heat measurements of Phillips [19]. However, whether one should use this value of  $\gamma$  in the analysis of the high temperature ( $T > \theta_D$ ) heat capacity is questionable because of the temperature dependence of the electron-phonon contribution to  $\gamma$ .

There are several contributions to  $\gamma$  arising from the free-electrons ( $\gamma_0$ ), the electron-phonon interaction ( $\gamma_1(T)$ ), the electron-electron interaction ( $\gamma_{ee}$ ) and finally the band structure effects ( $\gamma_B(T)$ ). The sum total of these contributions to  $C_e$  is given as

$$C_e = [\gamma_0 + \gamma_1(T) + \gamma_{ee} + \gamma_B(T)]T \quad (6)$$

The theoretical calculation of  $\gamma_1(T)$  by Grimvall [20] indicates that in the high temperature limit ( $T > \theta_D$ ),  $\gamma_1(T)$  does not contribute. In detail the temperature dependence of  $\gamma_B(T)$  is not known at this time. However, we can have some estimate of  $\gamma_B$  and  $\gamma_{ee}$  (a small contribution) from the work of Ashcroft and Wilkins [21].

Since the harmonic and anharmonic calculations reported in this paper have been performed in the high temperature limit, we represent  $C_e$  by  $(\gamma_0 + \gamma_B)T$  with  $\gamma_B = .06 \gamma_0$  [21], so that  $C_e/T = 2.438 \times 10^{-4} \text{ cal mol}^{-1} \text{ K}^{-2}$ .

## II. Reduction of $C_p$ to $C_{v_0}$ and anharmonic calculations of order $\lambda^2$ and $\lambda^4$

The correction from  $C_p$  to  $C_{v_0}$  was made by, first, obtaining the entropy  $S_0 = S(V_0, T)$  at the 0 K volume from the experimental entropy  $S_v = S(V, T)$  [2] measured at constant pressure  $p_1$  using the relation

$$S_0 = S_v - \int_{V_0}^V \left( \frac{\partial p}{\partial T} \right)_V dv \quad (1)$$

The isochores required for the evaluation of the integrand were generated from the Murnaghan equation [9]

$$p_2 - p_1 = \frac{B}{W} \left[ \left( \frac{v_1}{v_2} \right)^W - 1 \right] \quad (2)$$

in which  $v_1$  and  $v_2$  are the volumes in the states  $(p_1, T)$  and  $(p_2, T)$  respectively,  $B$  is the isothermal bulk modulus in state  $(p_1, T)$  and  $W = (\partial B / \partial p)_T$  at  $T$ . In making the calculations the isothermal quantities  $B$  and  $W$  were derived from the corresponding adiabatic quantities  $B_s$  and  $W_s$  by the standard formula

$$1/B = 1/B_s + TV\beta^2/C_p \quad (3)$$

and the result of Overton [11]

$$W = W_s + Z (1 - 2B'/B\beta - 2W_s) + Z^2 (W_s - 1 - \beta'/\beta^2) \quad (4)$$

$$Z = TV\beta^2 B/C_p \quad (5)$$

in which  $\beta = \left( \frac{1}{V} \right) \left( \frac{\partial V}{\partial T} \right)_p$  and the prime denotes differentiation with respect to temperature.

The data sources used for the quantities  $\beta, V, B_s$  and  $W_s$  were:

$\beta, V(T < 300)$ , Fraser and Hollis Hallett [12] and Gibbons [13]

$\beta, V(T > 300)$ , Simmons and Balluffi [14]

$B_s(T < 300)$ , Kamm and Alers [15]

$B_s(T > 300)$ , Gerlich and Fisher [16]

$W_s$ , Schmunk and Smith [17]

for finding  $E(T)$  always produces a positive correction term [8]. To avoid the difficulty mentioned above in Al we have converted  $C_v$  to  $C_{v_0}$  by an alternative method using the Murnaghan equation [9]. This procedure yields satisfactory results.

Our earlier theoretical calculation [1] of  $C_{v_0}$  was carried out employing the lowest order (cubic and quartic) anharmonic perturbation theory [ $O(\lambda^2)$ ]. It was not known if the contributions from the higher order perturbation theory, i.e. of  $O(\lambda^4)$  are significant in Al. In this paper, in addition to the  $\lambda^2$  contributions to  $C_{v_0}$ , we will also calculate the higher order perturbation ( $\lambda^4$ ) contributions to  $C_{v_0}$  [10] from an effective Morse potential. We hope from this calculation to find the relative importance of the  $\lambda^2$  and  $\lambda^4$  contributions to  $C_{v_0}$ .

A summary of the theoretical calculations and the reduction of the new experimental data is presented in Sec. II where we note a sharp contrast in the behaviour of  $C_{v_0}$  for Al determined in Ref. 1 in comparison with the previous measurements [3,4]. The agreement between the theoretical and the new experimental values of  $C_{v_0}(T)$  is more than satisfactory in the range 400-900 K. The calculation of the  $\lambda^4$  contributions to  $C_{v_0}$  is also presented in Sec. II. The numerical results and discussion are contained in Sec. III and the conclusions of this work are presented in Sec. IV.

b. Aluminum (II): Derivation of  $C_{V_0}$  from  $C_p$  and comparison to  $C_{V_0}$  calculated from anharmonic models

R.C. Shukla<sup>1</sup>, C.A. Plint<sup>1</sup>, and D.A. Ditmars<sup>2</sup>

## I. INTRODUCTION

Ample justification to have a definitive measurement of the specific heat at constant pressure ( $C_p$ ) of Al in the temperature range 273 K to 933 K came from the recent work of Shukla and Plint [1]. The preceding paper [2] presents just such a  $C_p$  measurement. In this paper, we present a theoretical analysis of these specific heat results, as well as those of Leadbetter [3], Brooks and Bingham [4], and Takahashi [5]. There are several steps in the theoretical analysis that must be completed before the new  $C_p$  data can be compared with theory. In fact the theoretical calculations are carried out for  $C_{V_0} \equiv C_{V_0}(V_0, T)$  which represents the specific heat at constant volume reduced to the volume  $V_0$  appropriate for 0 K. In the previous work of Shukla and Plint [1] the reduction from  $C_p$  to  $C_{V_0}$  was carried out by the Slater-Overton [6,7] procedure.

The reduction of the present experimental  $C_p(T)$  data together with those of Brooks and Bingham [4], Leadbetter [3], and Takahashi [5] to  $C_{V_0}(T)$  has been modified from that described previously [1]. For aluminum the Slater-Overton procedure [6,7], when extended to 900 K, produced an oscillation of the correction term  $E(T) = C_V - C_{V_0}$  where  $C_V \equiv C_V(V, T)$  from positive to negative (500-600 K) and back to positive above 600 K. The anharmonic correction  $E(T)$  is small for aluminum and the unphysical oscillation may represent the effects of the approximations of the Slater-Overton procedure and of the uncertainties arising from the assumed thermal expansion and compressibility data. For the alkali metals, which have a much larger anharmonic correction, the Slater-Overton procedure

---

1. Physics Department, Brock University, St. Catharines, Ontario,  
L2S 3A1, Canada.

2. National Bureau of Standards, Gaithersburg, MD 20899

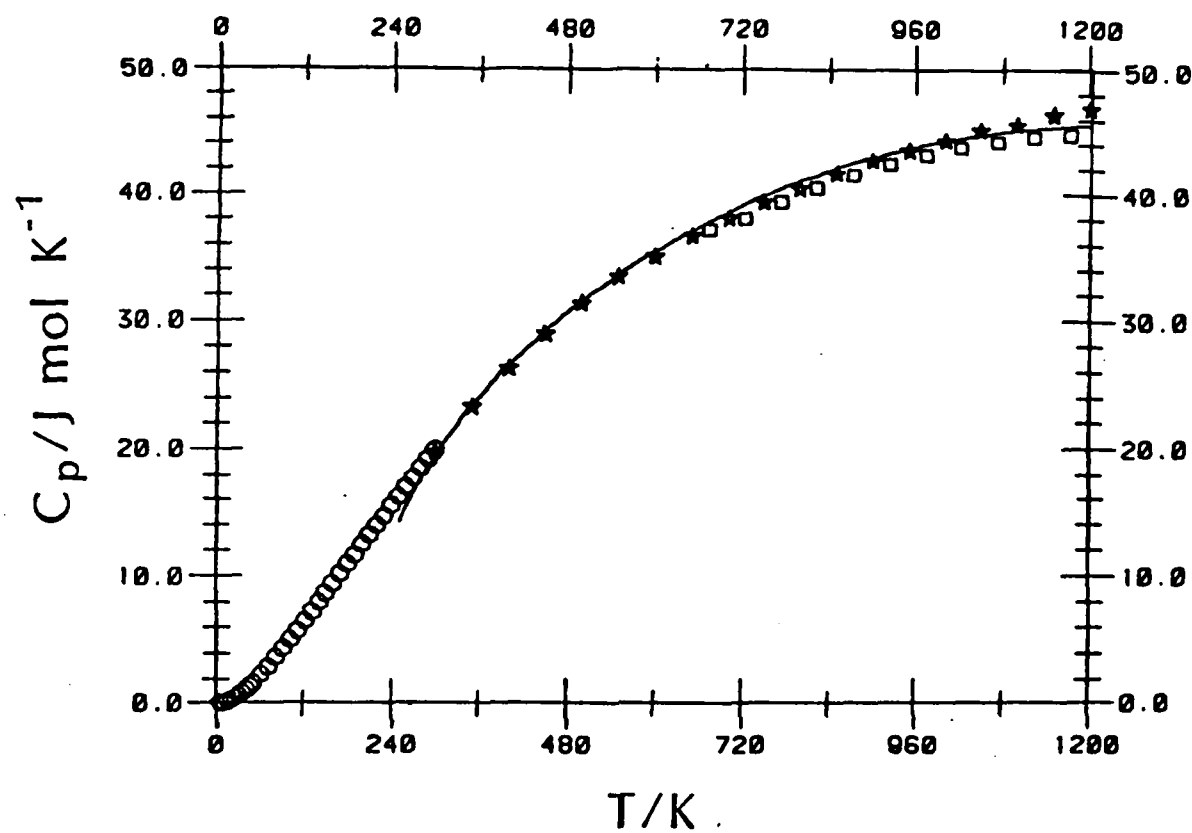


Figure 3. Specific heat of hexagonal BN:  $\circ$  : Westrum (1960) [2],  $\star$  : McDonald (1961) [8],  $\square$  : Magnus (1926) [9], — (present work).



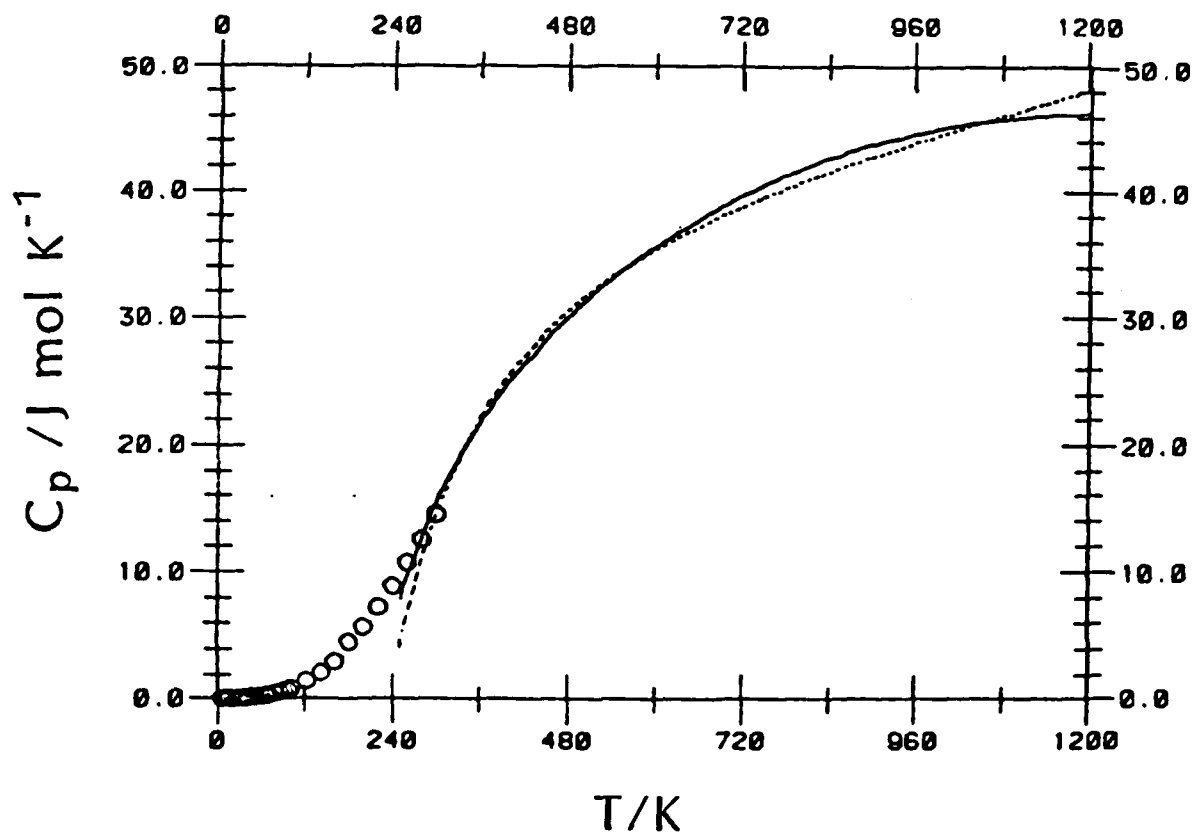


Figure 2. Specific heat of cubic BN ○ : Sirota (1976) [3], ..... : Kiselva (1973) [7], — : (present work).

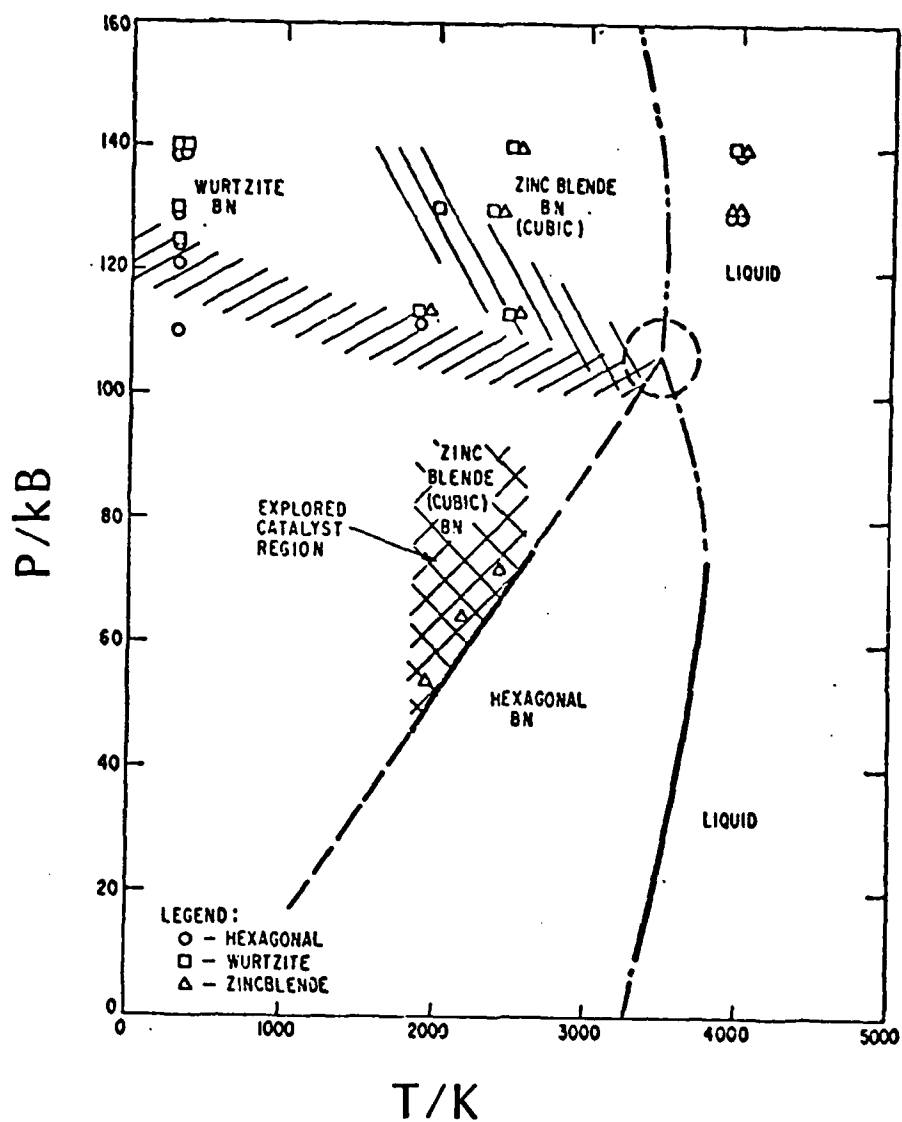


Figure 1. Tentative P-T phase diagram of BN; (Bundy and Wentorf (1963)

[1].

### Bibliography

- [1] Bundy, F.P. and Wentorf, R.H., Jr., J. Chem. Phys. 38 (5), 1144-1149 (1963).
- [2] Westrum, E.F., Jr., priv. comm. (1960).
- [3] Sirota, N.N. and Kofman, N.A., Sov. Phys. Dokl. 20(12), 861-862 (1976)
- [4] Douglas, T.B. and King, E.G., Chap. 8 in Experimental Thermodynamics. Vol. I, Calorimetry of Non-Reacting Systems, pp. 293-318, J.P. McCullough and D.W. Scott, Eds., (Butterworths, London, 1968).
- [5] Ditmars, D.A., Cezairliyan, A., Ishihara, S., and Douglas, T.B., NBS Special Publication 260-55 (1977).
- [6] Ditmars, D.A. and Douglas, T.B., J. Res. Nat. Bur. Stand. (U.S.) 75A (Phys. and Chem.) (5), 401-420 (1971).
- [7] Kiseleva, I.A., Mel'chakova, L.V., and Topor, N.D., Izvest. Akad. Nauk SSSR, Neorg. Mat. 9 (3), 494-495 (1973).
- [8] McDonald, R.A. and Stull, D.R., J. Phys. Chem., 65, 1918 (1961).
- [9] Magnus, A. and Danz, H., Ann. der Physik, 386 4. Folge 81, 407-424 (1926).

Table 3

Coefficients of fit to hex and cubic BN enthalpy data

	hex BN	cubic BN
A	-7.953294E-06	-8.364759E-06
B	+2.229104E-02	+2.278997E- 02
C	+2.511515E+01	+2.637653E+01
D	-2.267366E+03	-4.000692E+03
$\sigma/J \text{ mol}^{-1}$	8.60	12.25

The specific heats derived from these functions have been compared with some existing literature data in figures 2 and 3 and indicate a reasonable agreement with the low-temperature data. Smooth-merging of the present and the low-temperature data as well as extension of the measurements to higher temperatures in another calorimeter are in progress.

this expression analytically for the central force nearest neighbour model of the fcc crystal.

The high temperature  $(\frac{\hbar\omega(\vec{q}j)}{2k_B T} < 1)$  three term expansion of  $C_{v_0}^h$  is

$$C_{v_0}^h = k_B \sum_{\vec{q}j} \left[ 1 - \frac{1}{3} \left( \frac{\hbar\omega(\vec{q}j)}{2k_B T} \right)^2 + \frac{1}{15} \left( \frac{\hbar\omega(\vec{q}j)}{2k_B T} \right)^4 + \dots \right] \quad (12)$$

Therefore to evaluate this expression analytically we need to evaluate the sums  $\sum_{\vec{q}j} \omega^2(\vec{q}j)$  and  $\sum_{\vec{q}j} \omega^4(\vec{q}j)$ . These sums can be evaluated from the following eigenvalue equation

$$\sum_{\beta} D_{\alpha\beta}(\vec{q}) e_{\beta}(\vec{q}j) = \omega^2(\vec{q}j) e_{\alpha}(\vec{q}j) \quad (13)$$

where  $D_{\alpha\beta}(\vec{q})$  are the elements of the dynamical matrix and  $\vec{e}(\vec{q}j)$  is the eigenvector for the mode  $\vec{q}j$ . Omitting the details we find the following

$$C_{v_0}^h = 3Nk_B \left[ 1 - \frac{1}{3M} \left( \frac{\hbar}{k_B T} \right)^2 (\phi'' + \frac{2}{r} \phi') + \frac{1}{12M^2} \left( \frac{\hbar}{k_B T} \right)^4 (\phi'' + \frac{2}{r} \phi')^2 \right] \quad (14)$$

where  $\phi'$  and  $\phi''$  are the first and second derivatives of  $\phi(r)$  which are evaluated from equation (10).

### III. RESULTS AND DISCUSSION

The numerical results for all the diagrams of  $O(\lambda^2)$  and  $O(\lambda^4)$  for the nearest neighbour Morse potential are presented in Table III. It is interesting to note that among the  $\lambda^4$  diagrams the contribution from 3(b) is close to that of the total  $F(\lambda^4)$ . In fact the sum total of 3(a) and 3(b) is only 2.5% lower than the total  $F(\lambda^4)$ .

A detailed calculation of the harmonic and anharmonic  $(\lambda^2)$   $C_{V_0}$  indicates that although the contribution to  $C_{V_0}$  from  $F(\lambda^4)$  is three times larger than that of  $F(\lambda^2)$ , it is not sufficient to account for the upward curvature in  $C_{V_0}$ . The total contribution  $(\lambda^2 \text{ and } \lambda^4)$  from the Morse potential is very similar to that of the two other pseudopotentials (Ashcroft and Harrison point ion).

We present in Table IV and Fig. 4 the values of the total  $C_{V_0}$ , harmonic plus anharmonic, to  $O(\lambda^2)$  calculated for the three pseudopotentials used in ref [1] curves 1,2,3) and for the Morse potential, with the anharmonic contribution to  $O(\lambda^2)$  (curve 4) and to  $O(\lambda^2)$  plus  $O(\lambda^4)$  (curve 2). Only the DRT potential gives a  $C_{V_0}$  that rises above 3R while, at best, the Harrison and Morse (to  $O(\lambda^2) + O(\lambda^4)$ ) potentials give a  $C_{V_0}$  that approaches 3R at 900 K.

From the results presented in Table IV it is interesting to see the results of  $C_{V_0}$  obtained from the nearest neighbour (harmonic as well as the anharmonic) Morse potential being so close to the Ashcroft (a sixth neighbour harmonic and anharmonic interaction) and Harrison point ion (13 neighbours harmonic and 8 neighbours anharmonic interaction) pseudopotentials. The latter two potentials have a much more sound theoretical basis than the Morse potential and involve a large number of neighbours

in the harmonic and anharmonic calculations.

In Fig. 4 we also present the reduced  $C_{v_0}$  values obtained from the new experimental data (curve 5) which exhibits an upward curvature for  $T > 550$  K and rises above  $3R$  near 800 K. Since none of the calculated curves show any upward curvature we have corrected the experimental  $C_{v_0}$  for a vacancy contribution  $C_v^{vac}$  using the expression

$$C_v^{vac} = (Nk_B) \exp(\Delta S/k_B) (E/k_B T)^2 \exp - (E/k_B T)$$

where  $E$  and  $\Delta S$  are the energy and entropy of formation of a single vacancy, respectively. We use  $E = 0.66$  eV [25] and estimate that  $(\Delta S/k_B) = 1.8$  on the ground that the corrected  $C_{v_0} - C_v^{vac}$  should not exhibit a negative temperature derivative. Curve 6 in Fig. 4 was obtained with  $(\Delta S/k_B) = 1.4$ . The vacancy contribution is evident at 600 K. The agreement between this curve and the calculated values for curves 2 and 3 is very satisfactory. While curve 6 lies below the curves 2, 3 over the entire temperature range  $500 \leq T \leq 900$  K the difference between them is only about .5%. After correction for vacancies the experimental  $C_{v_0}$  does not reach  $3R$  by 900 K.

It should be noted that variation of the quantity  $W$ , Eq. (3), by 10% to allow for experimental uncertainty in its value makes a change of less than 0.2% in the reduced values of  $C_{v_0}$ .

A comparison of the sets of values of the reduced  $C_{v_0}$  obtained from previous experimental data [3,4,5] with the calculated values does not alter previous conclusions [1]. The results of Leadbetter [3] and of Takahashi [5] gives curves of  $C_{v_0}$  that fall below the lowest of the calculated curves, even without correction for vacancy effects from 600 K. The results of Brooks and Bingham [4] give a curve that lies well above the DRT curve for most of the temperature range and for which a reasonable

vacancy correction does not bring about significantly improved agreement with any of the calculated curves.



#### IV. CONCLUSION

The new  $C_p$  data reported in the preceding paper [2] has been reduced to  $C_{v_0}$  using the Murnaghan equation. The lowest order anharmonic contributions are evaluated from a nearest-neighbour phenomenological Morse potential and several pseudopotentials. The contributions of the higher order perturbation theory anharmonic terms to  $C_{v_0}$  are evaluated for the nearest neighbour Morse potential. It is concluded that the vacancy contributions to  $C_{v_0}$  are more important than the higher order anharmonic terms. After removal of the vacancy contribution from  $C_{v_0}$ , obtained from the new  $C_p$  data, excellent agreement is achieved between the theory and experiment. Also it is shown that the Morse potential results for  $C_{v_0}$  are just about the same as those from the more sophisticated Ashcroft and the Harrison modified point ion pseudopotentials.

---

The new experimental research which the present work interprets was supported in part by the U.S. Air Force Office of Scientific Research.

## References

1. R.C. Shukla and C.A. Plint, Int. J. Thermophys. 1: 299 (1980).
2. D.A. Ditmars, C.A. Plint, and R.C. Shukla, Int. J. Thermophys. (to be published).
3. A.J. Leadbetter, J. Phys. C (Proc. Phys. Soc.) 1: 1481 (1968).
4. C.R. Brooks and R.E. Bingham, J. Phys. Chem. Solids 29: 1553 (1968).
5. Y. Takahashi, Private Communication.
6. J.C. Slater, Introduction to Chemical Physics (McGraw-Hill, New York, 1939), Chapter XIII.
7. W.C. Overton, J. Chem. Phys. 37: 2975 (1962).
8. R.C. Shukla and C.A. Plint in "Proceedings of the Eighth Symposium on Thermophysical Properties of Solids and of Selected Fluids for Energy Technology", edited by J.V. Sengers (A.S.M.E., New York, 1982) p. 77.
9. F.D. Murnaghan, "Finite Deformations of an Elastic Solid" (John Wiley and Sons, New York, 1951).
10. R.C. Shukla and E.R. Cowley, Phys. Rev. B 3: 4055 (1971).
11. W.C. Overton, J. Chem. Phys. 37: 116 (1962).
12. D.B. Fraser and A.C. Hollis-Hallett, Can. J. Phys. 43: 193 (1965).
13. D.F. Gibbons, Phys. Rev. 112: 136 (1958).
14. R.O. Simmons and R.W. Balluffi, Phys. Rev. 117: 52 (1960).
15. G.N. Kamm and G.A. Alers, J. Appl. Phys. 35: 327 (1964).
16. D. Gerlich and E.S. Fisher, J. Phys. Chem. Solids 30: 1197 (1969).
17. R.E. Schmunk and C.S. Smith, J. Phys. Chem. Solids 9: 100 (1959).
18. A.J. Leadbetter, J. Phys. C (Proc. Phys. Soc.) 1: 1489 (1968).
19. N.E. Phillips, Phys. Rev. 114: 676 (1959).

20. G. Grimvall, J. Phys. Chem. Solids 29: 1221 (1968)
21. N.W. Ashcroft and J.W. Wilkins, Phys. Lett. 14: 285 (1965)
22. R.C. Shukla and L. Wilk, Phys. Rev. B10: 3660 (1974)
23. R.C. Shukla and R.A. MacDonald, High Temp. High Pressures 12: 291 (1980)
24. R.A. MacDonald and W.M. MacDonald, Phys. Rev. B24: 1715 (1981)
25. W. Triftshäuser, Phys. Rev. B12: 4634 (1975)
26. W.A. Harrison, Pseudopotentials in the Theory of Metals,  
(Benjamin, New York, (1966)).
27. N.W. Ashcroft, Phys. Lett. 23: 48 (1966).
28. L. Dagens, M. Rasolt, and R. Taylor, Phys. Rev. B11: 2726 (1975).

Table I.

Temp. (K)	$C_{v_0}$ (cal mol <sup>-1</sup> K <sup>-1</sup> )			
	DPS	L	B	T
400	5.665	5.598	5.664	5.580
450	5.735	5.655	5.752	5.648
500	5.780	5.732	5.814	5.703
550	5.814	5.762	5.868	5.756
600	5.839	5.798	5.922	5.794
650	5.870	5.814	5.979	5.815
700	5.900	5.824	6.052	5.826
750	5.936	5.798	6.123	5.866
800	5.974		6.206	5.904
850	6.013		6.320	5.931
900	6.060			

DPS - this work, L Ref [2], B Ref [1], T Ref [3].

TABLE II.

High temperature limits for the various contributions to the free energy.

Diagram

High Temperature Limit

$$2a \quad \left(\frac{3}{8}\right) \left(\frac{2}{\pi}\right)^2 \sum_{\lambda_1, \lambda_2} \frac{V(\lambda_1, -\lambda_1, \lambda_2, -\lambda_2)}{\omega(\lambda_1)\omega(\lambda_2)}$$

$$2b \quad -\frac{3}{8^2} \left(\frac{2}{\pi}\right)^3 \sum_{\lambda_1, \lambda_2, \lambda_3} \frac{|V(\lambda_1, \lambda_2, \lambda_3)|^2}{\omega(\lambda_1)\omega(\lambda_2)\omega(\lambda_3)}$$

$$3a \quad \frac{15}{8^3} \left(\frac{2}{\pi}\right)^3 \sum_{\lambda_1, \lambda_2, \lambda_3} \frac{V(\lambda_1, -\lambda_1, \lambda_2, -\lambda_2, \lambda_3, -\lambda_3)}{\omega(\lambda_1)\omega(\lambda_2)\omega(\lambda_3)}$$

$$3b \quad -\frac{36}{8^3} \left(\frac{2}{\pi}\right)^4 \sum_{\lambda_1, \lambda_2, \lambda_3, \lambda_4} \frac{V(\lambda_1, -\lambda_1, \lambda_2, \lambda_3)V(-\lambda_2, -\lambda_3, \lambda_4, -\lambda_4)}{\omega(\lambda_1)\omega(\lambda_2)\omega(\lambda_3)\omega(\lambda_4)}$$

$$3c \quad -\frac{60}{8^3} \left(\frac{2}{\pi}\right)^4 \sum_{\lambda_1, \lambda_2, \lambda_3, \lambda_4} \frac{V(\lambda_1, \lambda_2, \lambda_3)V(-\lambda_1, -\lambda_2, -\lambda_3, \lambda_4, -\lambda_4)}{\omega(\lambda_1)\omega(\lambda_2)\omega(\lambda_3)\omega(\lambda_4)}$$

$$3d \quad \frac{108}{8^3} \left(\frac{2}{\pi}\right)^5 \sum_{\lambda_1, \lambda_2, \lambda_3, \lambda_4, \lambda_5} \frac{V(\lambda_1, \lambda_3, \lambda_4)V(-\lambda_2, -\lambda_3, -\lambda_4)V(-\lambda_1, \lambda_2, \lambda_5, -\lambda_5)}{\omega(\lambda_1)\omega(\lambda_2)\omega(\lambda_3)\omega(\lambda_4)\omega(\lambda_5)}$$

$$3e \quad -\frac{12}{8^3} \left(\frac{2}{\pi}\right)^4 \sum_{\lambda_1, \lambda_2, \lambda_3, \lambda_4} \frac{|V(\lambda_1, \lambda_2, \lambda_3, \lambda_4)|^2}{\omega(\lambda_1)\omega(\lambda_2)\omega(\lambda_3)\omega(\lambda_4)}$$

Diagram

High Temperature Limit

$$3f \quad -\frac{81}{\beta^3} \left(\frac{2}{\pi}\right)^6 \sum_{\lambda_1, \lambda_2, \lambda_3, \lambda_4, \lambda_5, \lambda_6} \frac{V(\lambda_1, \lambda_3, \lambda_4) V(-\lambda_1, \lambda_5, \lambda_6) V(\lambda_2, -\lambda_3, -\lambda_4) V(-\lambda_2, -\lambda_5, -\lambda_6)}{\omega(\lambda_1) \omega(\lambda_2) \omega(\lambda_3) \omega(\lambda_4) \omega(\lambda_5) \omega(\lambda_6)}$$

$$3g \quad \frac{108}{\beta^3} \left(\frac{2}{\pi}\right)^5 \sum_{\lambda_1, \lambda_2, \lambda_3, \lambda_4, \lambda_5} \frac{V(\lambda_1, \lambda_2, \lambda_4, \lambda_5) V(-\lambda_1, -\lambda_2, \lambda_3) V(-\lambda_3, -\lambda_4, -\lambda_5)}{\omega(\lambda_1) \omega(\lambda_2) \omega(\lambda_3) \omega(\lambda_4) \omega(\lambda_5)}$$

$$3h \quad -\frac{54}{\beta^3} \left(\frac{2}{\pi}\right)^6 \sum_{\lambda_1, \lambda_2, \lambda_3, \lambda_4, \lambda_5, \lambda_6} \frac{V(\lambda_1, \lambda_2, \lambda_3) V(-\lambda_1, \lambda_4, \lambda_5) V(-\lambda_2, -\lambda_5, \lambda_6) V(-\lambda_3, -\lambda_4, -\lambda_6)}{\omega(\lambda_1) \omega(\lambda_2) \omega(\lambda_3) \omega(\lambda_4) \omega(\lambda_5) \omega(\lambda_6)}$$

Table III. Anharmonic contributions to the Helmholtz free energy. Diagrams 2(a) and 2(b) are in units of  $N(k_B T)^2 \times 10^{12} \text{erg}^{-1}$  and the diagrams 3(a)...3(h) in units of  $N(k_B T)^3 \times 10^{24} \text{erg}^{-2}$ .

---

<u>Diagram</u>	<u>Contribution</u>
F(2(a))	0.38012
F(2(b))	-0.40767
Total $F(\lambda^2) = -.02755 N(k_B T)^2 \times 10^{12} \text{erg}^{-1}$	
F(3(a))	0.01742
F(3(b))	-0.21506
F(3(c))	-0.38556
F(3(d))	0.60435
F(3(e))	-0.34431
F(3(f))	-0.50573
F(3(g))	0.74463
F(3(h))	-0.11823
Total $F(\lambda^4) = -0.20249 N(k_B T)^3 \times 10^{24} \text{erg}^{-2}$	

---

TABLE IV

T(K)	Harrison	Ashcroft	$C_v$ (cal.mol <sup>-1</sup> K <sup>-1</sup> ) DRT	Morse ( $\lambda^2$ )	Morse ( $\lambda^2 + \lambda^4$ )
400	5.68707	5.70620	5.73119	5.69960	5.70757
450	5.75109	5.75849	5.79524	5.75499	5.76507
500	5.79842	5.80303	5.84347	5.79536	5.80781
550	5.83460	5.83689	5.88116	5.82570	5.84076
600	5.86307	5.86349	5.91155	5.84912	5.86704
650	5.88605	5.88483	5.93676	5.86761	5.88865
700	5.90500	5.90237	5.95818	5.88250	5.90690
750	5.92095	5.91704	5.97676	5.89470	5.92271
800	5.93461	5.92956	5.99317	5.90484	5.93670
850	5.94649	5.94042	6.00792	5.91340	5.94938
900	5.95697	5.94990	6.02134	5.92070	5.96103



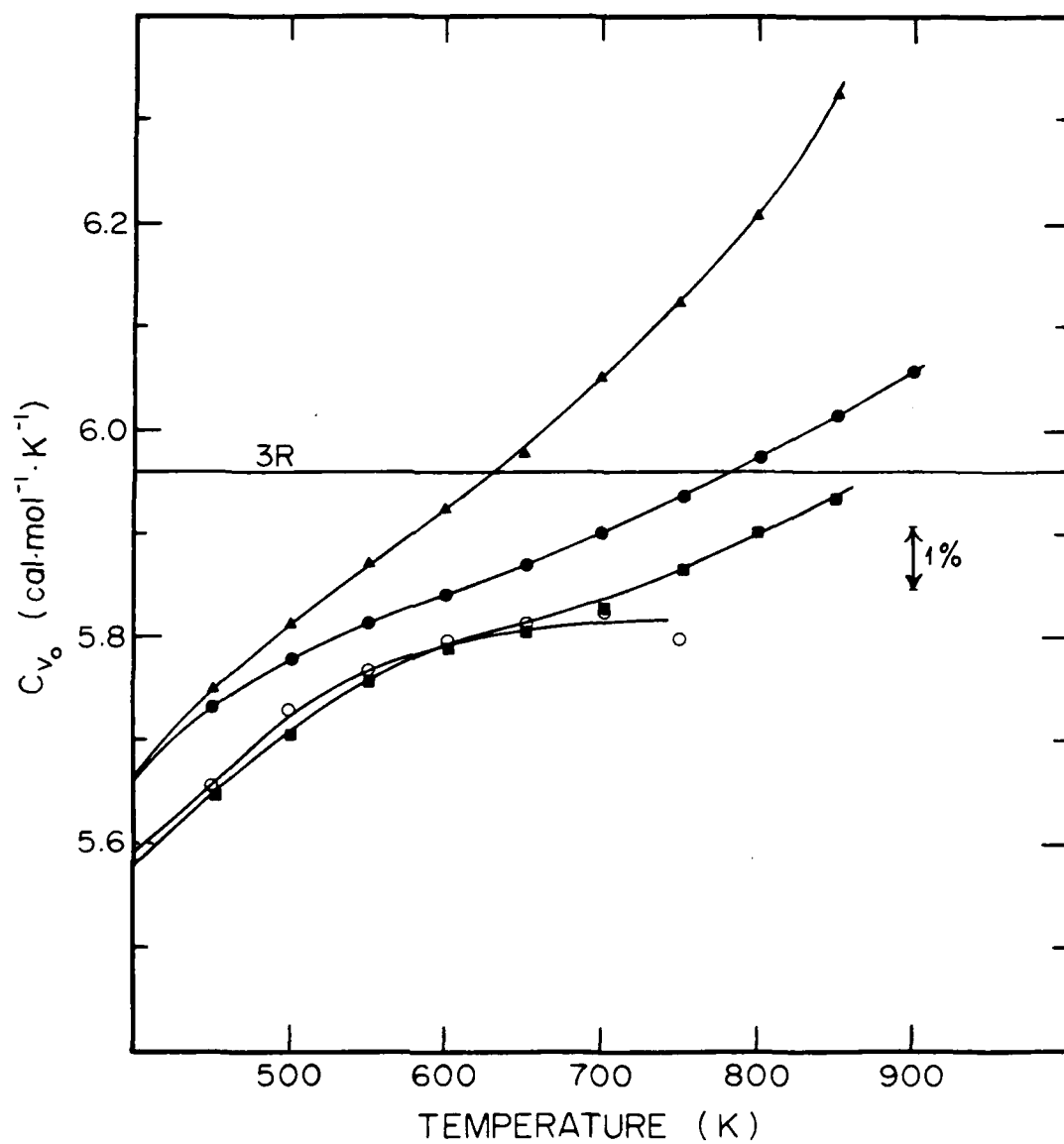


Figure 1. Reduced specific heat of Al at 0 K volume ( $C_{v_0}$ ) versus temperature (T). ▲: from smoothed data of Brooks and Bingham [4]; ●: from smoothed new data [2]; ■: from smoothed data of Takahashi [5]; ○: from smoothed data of Leadbetter [3].

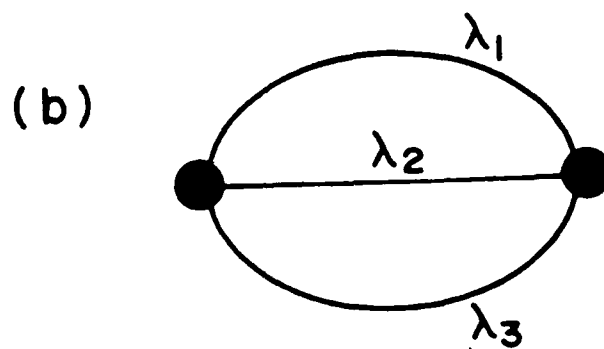
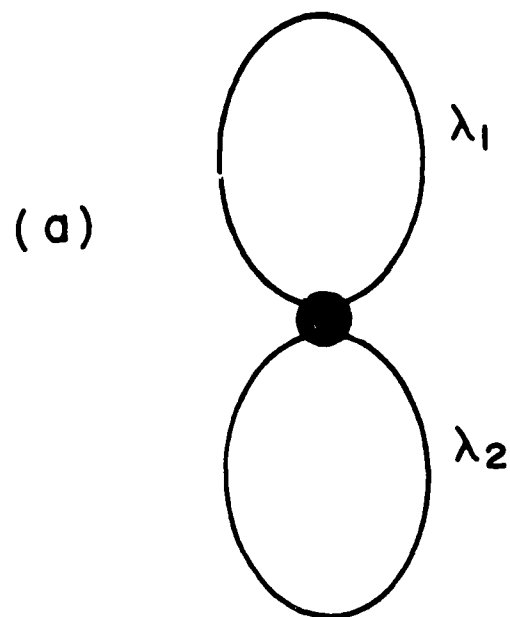


Figure 2. Diagrams of order  $\lambda^2$  (cf. text).

The adiabatic vibrational wavefunctions  $a_n^\alpha(R)$  and eigenvalues  $E_n^\alpha$  in Eq. (9) are obtained as solutions of the following equation,

$$[T + (\phi')^2 + V_{\alpha\alpha}] a_n^\alpha = E_n^\alpha a_n^\alpha, \quad (13)$$

and to lowest order in  $y(R)$  Eq. (9) is found to reproduce the perturbative results in Eq. (6) and (7). However, our numerical results will demonstrate the validity of the adiabatic theory to much higher order. Ultimately the utility of Eq. (9) is determined by the smallness of the phase-derivative,

$$\phi'(R) = \frac{\Delta(R)\Delta V'_{01}(R) - \Delta'(R)V_{01}(R)}{[\Delta(R)]^2 + 4[V_{01}(R)]^2}. \quad (14)$$

which, to first-order, determines the adiabatic off-diagonal coupling. This also appears as a second-order correction (radial Born-Oppenheimer term!) in Eq. (13) and introduces small but quantitatively significant, always positive, corrections to the adiabatic eigenvalues  $E_n^\alpha$ . In this study we have applied the adiabatic theory to the models postulated by Innes [8] to explain vibronic couplings in Formaldehyde and Propynal. As implied in Eq. (1) we are only allowing a single active vibrational mode, with displacement  $R$ , to couple the two states. Both  $\psi_0$  and  $\psi_1$  now contain a common set of frozen vibrational wavefunctions with identical quantum numbers and we have merely treated the polyatom as a pseudo-diatom. We could of course unfreeze two coordinates, say  $R_1$  and  $R_2$ , and postulate a set of interaction potentials  $V_{00}(R_1, R_2)$ ,  $V_{11}(R_1, R_2)$  and  $V_{01}(R_1, R_2)$ , together with a pair of kinetic energy operators  $T_1(R_1)$  and  $T_2(R_2)$ . This would give rise to the Duschinsky effect [9] and we believe the adiabatic

where  $f_n^0$  belongs to the set of vibrational wavefunctions generated by the attractive potential  $V_{00}(R)$ ,

$$[T + V_{00}(R)] f_n^0 = E_n^0 f_n^0 . \quad (5)$$

To first-order in  $V_{01}$  the radial function  $G$  for the distant state in Eq. (1) is approximated by [6,7],

$$G(E_n^0, R) \approx -(V_{10}/\Delta) f_n^0 \quad (6)$$

and the second-order eigenvalue is given by

$$E_n^0(2^{nd}) \approx E_n^0 - \langle f_n^0 | V_{01}^2 / \Delta | f_n^0 \rangle . \quad (7)$$

Unfortunately, unless the ratio

$$y(R) \equiv 2V_{01}/\Delta \quad (8)$$

is very much less than one, the zero-order Born-Oppenheimer function  $f_n^0$  gives a very poor description of the exact  $F$  function in Eq. (1) and hence Eqs. (6) and (7) will be in substantial error. We will show how this can be vastly improved by using adiabatic theory.

Basically we will replace Eq. (4) with the approximation,

$$|E\rangle \approx |E_n^\alpha\rangle = \xi_\alpha a_n^\alpha(R) \quad (9)$$

where the adiabatic eigenstate

$$\xi_\alpha = \cos\phi(R) \psi_0 - \sin\phi(R) \psi_1 \quad (10)$$

is defined by the  $R$ -dependent eigenphase  $\phi(R)$  where,

$$\tan 2 \phi(R) = y(R) . \quad (11)$$

This is of course the eigenphase which diagonalizes the diabatic interaction matrix  $V(R)$  and yields the adiabatic potential

$$V_{\alpha\alpha}(R) = V_{00} - V_{01} \tan \phi(R) . \quad (12)$$

given, and we shall use this system to demonstrate the usefulness of adiabatic theory in describing distant perturbations in molecular spectroscopy.

We have previously discussed [3] the role of adiabatic electronic-rotational (AER) states in diatomic spectroscopy, where  $\psi_0$  and  $\psi_1$  represent pure electronic-rotational states constructed in some appropriate Hund's coupling scheme. Further we have already made explicit application of AER theory to describe the effects of distant perturbations in inelastic atomic scattering [4]. In that case  $E$  was continuous because it exceeded the dissociation energy limit  $E > V_{00}(\infty)$ . Actually the  $\psi_0$  and  $\psi_1$  states were constructed in pure Hund's case (e) since these are equivalent to proper atomic scattering channels [3]. We also treated predissociation where channel  $\psi_0$  was open and channel  $\psi_1$  was closed [5]. Here we want to explicitly apply AER theory to pure bound state spectroscopy where  $E < V_{00}(\infty)$  and both channels are closed. Also we shall remove any restriction to diatomic molecules and actually apply AER theory to vibronic coupling in polyatomic systems.

By a distant perturbation we imply that the state  $\psi_1$  remains classically inaccessible for all intermolecular displacements  $R$  which can possibly contribute to the radial function  $G(E, R)$  at the total energy  $E$ . This requires  $V_{11}(R) > E$  in Eq. (3), or equivalently,

$$\Delta(R) \equiv V_{11}(R) - V_{00}(R) > E - V_{00}(R) \quad \text{all } R \quad (3)$$

This means that, in the absence of any  $V_{01}$  coupling, we would be permitted to replace Eq. (1) with a pure Born-Oppenheimer wavefunction,

$$|E\rangle \approx |E_n^0\rangle = \psi_0 f_n^0(R), \quad (4)$$

## 1. INTRODUCTION

We consider the strong coupling of a given molecular state  $\psi_0(r,R)$  to an energetically distant state  $\psi_1(r,R)$  such that the total wavefunction at total energy  $E$  must be represented as follows,

$$|E\rangle = \psi_0(r,R) F(E,R) + \psi_1(r,R) G(E,R) . \quad (1)$$

A particular radial coordinate  $R$  in the molecular Hamiltonian  $H(r,R)$  has been isolated for special consideration, and  $r$  is meant to represent the composite of all remaining degrees of freedom. Thus  $\psi_0$  and  $\psi_1$  are but two of an infinite set of states which span the space of  $r$ . We generate a pair of coupled equations for  $F$  and  $G$  by imposing the condition  $(H-E)|E\rangle = 0$  and operating from the left with  $\psi_0$  and  $\psi_1$  followed by an integration over  $r$ ,

$$[T + V_{00}(R) - E]F + V_{01}(R)G = 0 \quad (2a)$$

$$[T + V_{11}(R) - E]G + V_{10}(R)F = 0 \quad (2b)$$

Note that the functions  $\psi_0$  and  $\psi_1$  may contain an implicit dependence on  $R$  and will not in general commute with the radial kinetic energy operator  $T = -\partial^2/\partial R^2$ . Thus the 'potentials' may actually contain momentum operators which are required to operate on the  $F$  and  $G$  functions. For present purposes it is adequate to assume that we can neglect such radial Born-Oppenheimer couplings [1], and thus we can also assume that the off-diagonal coupling  $V_{01}=V_{10}$  is both real and symmetric. By implication our two state basis might be considered to be 'diabatic' although it would probably be less confusing to avoid all the polemics such a designation might generate [2]. Rather we are content to postulate Eqs. (1)-(3) as

Adiabatic Analysis of Distant Perturbations: Application to  
Herzberg-Teller Vibronic Coupling Theory

Frederick H. Mies

Molecular Spectroscopy Division

National Bureau of Standards

Gaithersburg, MD 20899

ABSTRACT

The simplest form of Herzberg-Teller theory involves the vibronic coupling of a single mode between two energetically separated molecular states. An adiabatic analysis of this system is presented which incorporates the effect of the distant state without recourse to direct summation over distant energy levels. The theory is compared to exact numerical results for vibronic-coupling in Propynal and Formaldehyde. The adiabatic eigenvalues are exceptionally accurate, especially if proper radial Born-Oppenheimer terms are added to the adiabatic potential for the ground state. The quality of the resultant amplitudes associated with the distant state are adequate to represent any intensity borrowing effects in the molecular spectra to well within 5%. The adiabatic theory is quite general and can be used with equal force to represent distant perturbations due to repulsive as well as attractive states, and without any commitment to linear vibronic coupling models.

a.

ADIABATIC ANALYSIS OF DISTANT PERTURBATIONS: APPLICATION TO  
HERZBERG-TELLER VIBRONIC COUPLING THEORY<sup>1</sup>

Frederick H. Mies  
Molecular Spectroscopy Division  
National Bureau of Standards  
Gaithersburg, MD 20899

<sup>1</sup> Molecular Physics in press

\*Acknowledgement: This work is supported in part by the Air Force Office of  
Scientific Research, Contract No. AFOSR-ISSA-83-00038.



## ABSTRACT

The accurate evaluation of thermodynamic properties at elevated temperatures requires proper analysis of the dissociated states of molecules. These continuum states make substantial contributions to the molecular partition function  $Q$  and result in significant modification of the equation of state and equilibrium constants for high temperature gases. Using formal scattering theory to characterize the continuum wavefunctions associated with molecular fragmentation we can derive rigorous expressions for  $Q$ . In particular this analysis includes the effect of inelastic collisions among the internal states of the fragments.

The inelastic effects are introduced by the off-diagonal elements of the scattering matrix  $S(E)$  evaluated at each total microcanonical energy  $E$ . Expressions are reduced to a simple form by using the eigenphases of the unitary matrix  $S$  to define the density of continuum states required in the evaluation of  $Q$ . Further, if we employ the exact multichannel quantum defect type (MCQDT) representation of the scattering wavefunctions we can arrive at a simple separation of the elastic and inelastic contributions to  $Q = Q_{el} + Q_{inel}$ . This MCQDT analysis also yields an unambiguous thermodynamic interpretation of any predissociation levels that may lie imbedded in the dissociation continua.

Employing previously calculated  $S$  matrix elements for various two-state couplings we conclude that the inelastic contributions to  $Q$  are negligible. However, this is predicated on having made a proper analysis of the elastic scattering potential as prescribed by the MCQDT analysis. Also the two channel examples have special features which may not persist for more complicated inelastic couplings.

THE THERMODYNAMIC EFFECTS OF INELASTIC AND STATE CHANGING COLLISIONS\*

Frederick H. Mies  
Molecular Spectroscopy Division  
National Bureau of Standards  
Gaithersburg, MD 20899

To be submitted to J. Chem. Phys.

\*Acknowledgement: This work is supported in part by the Air Force Office of Scientific Research, Contract No. AFOSR-ISSA-83-00038.

This merely requires knowledge of the rotationless molecular potential  $V(R)$ . The mathematical factors  $F_B$  and  $F_C$  are simply related to the incomplete gamma function and enable us to partition the integral into separate contributions from the bound ( $\epsilon < 0$ ) and the continuum ( $\epsilon > 0$ ) portions of phase space. All the thermodynamic functions can be obtained once  $Q(AB)$  is evaluated.

As our final contribution to these studies we have written a computer code, which is available to the thermodynamic community, to numerically evaluate the classical partition function and its separate contributions from  $Q_B$  and  $Q_C$ . The code requires as input the molecular potential  $V(R)$ . Given  $V(R)$  the code also evaluates the following two integrals,

$$I^{(1)} = \int_0^{\infty} R^2 (V/kT) e^{-V/kT} dR \quad (4)$$

$$I^{(2)} = \int_0^{\infty} R^2 (V/kT)^2 e^{-V/kT} dR. \quad (5)$$

from which the first two temperature derivatives of  $Q$  can easily be constructed. The separate bound and continuum contributions to these integrals can also be isolated.

The code evaluates the equilibrium constant and  $\Delta G^0$  and  $\Delta H^0$  for the equilibrium  $AB \rightleftharpoons A + B$ . It also tabulates the internal energy, entropy, heat capacity and Gibb's energy function  $(G^0 - H_{298})/T$  for the species  $AB$ , using our consistent thermodynamic scheme in which  $A$  and  $B$  are ideal gas atoms and all molecular effects are incorporated into the bound and continuum states of  $AB$ . The individual contributions of these portions of phase space to the thermodynamic functions are tabulated.

e.g.,  $Q(AB) = Q_B(AB) + Q_C(AB)$ . At high temperatures we can use the classical expressions for  $Q$  and obtain analytic representations of  $Q$ ,  $Q_B$  and  $Q_C$ . Our analysis is being assembled in the form of a report that will be circulated in the thermodynamic community. If sufficient interest is generated we will consider organizing a computer program which can generate all the thermodynamic functions for such a system.

(4) Program for the Evaluation of the Classical Partition Function and Resultant Thermodynamic Quantities for Diatomic Molecules at High Temperatures.

Overall, our thermodynamic studies have lead to two significant conclusions which impact on the evaluation of high temperature thermodynamic data. First, we have shown that a proper definition of a partition function for a diatomic molecule AB must include both the bound and the continuum portions of the energy spectrum

$$Q(AB) = \sum_J (2J+1) \left[ \sum_{\epsilon} e^{-\epsilon(v,J)/kT} + \int_0^{\infty} d\epsilon e^{-\epsilon/kT} \frac{\partial \eta(\epsilon, J)}{\pi \partial \epsilon} \right] \quad (1)$$

The discrete sum in this rigorous quantum mechanical formula runs over the true bound states of AB,  $\epsilon(v,J) < 0$ , when the dissociation energy is taken to be at  $\epsilon = 0$ . The integral over the continuum of asymptotic kinetic energy states  $\epsilon$  associated with each total angular momentum state  $J$  encompasses both the free and the metastable dissociative states of the system as reflected in the energy-dependence of the elastic scattering phase shift  $\eta(\epsilon, J)$ . Second, we have shown that Eq. (1) is well approximated by the classical analogue of  $Q(AB)$  in the simple integral,

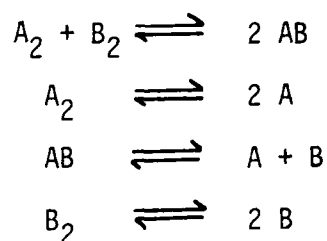
$$Q(AB) \approx 4\pi \int_0^{\infty} R^2 (e^{-V(R)/kT} - 1) dR \quad (2)$$

$$\approx 4\pi \left[ \int_0^{\infty} R^2 e^{-V/kT} F_B(R) dR + \int_0^{\infty} R^2 (e^{-V/kT} - 1) F_C(R) dR \right] \quad (3)$$

However, this convenient separation is only valid if one makes very careful and prescribed evaluations of the elastic scattering potentials consistent with the analysis presented in this new paper. The abstract of the paper is attached.

(2) Adiabatic Analysis of Distant Perturbations: Application to Herzberg-Teller Vibronic Coupling Theory. The study is somewhat peripheral to our dominant concern with dissociation continua and their contributions to high temperature thermodynamics. However this paper addresses the problem of describing the highly distorted vibrational states of polyatomic molecules which can have profound effects on the density of states, and hence on the molecular partition function. Of more likely interest in our future research is the effect of intensity borrowing of radiative oscillator strength due to vibronic coupling. This phenomenon could be of significance in assessing the interaction of molecules with intense laser fields. The abstract of this paper is attached.

(3) Modelling of High Temperature Equilibrium Using Square-Well Potentials. To allow for the qualitative assessment of the influence of dissociated states (including metastable states) on the resultant equation of state of a high temperature gas we have considered the following set of equilibria



By assigning an appropriate square-well potential to each species we can arbitrarily vary the degree of dissociation, and the relative contributions of bound  $Q_B$  and continuum  $Q_C$  components to the molecular partition functions  $Q$ ,

### 3. CRITIQUE OF CALCULATED THERMODYNAMIC FUNCTIONS EVALUATED AT HIGH TEMPERATURES

Principal Investigators:

Paul S. Julienne

Frederick H. Mies

#### Introduction

Over the past several years we have initiated several projects which addressed problems of possible interest to the Environmental Resistance Materials Program. Basically we considered the overall question as to whether there are any theoretical subtleties in the evaluation of high temperature thermodynamic data that have been overlooked by the thermodynamic communities which could significantly modify our assessment of equilibrium properties. This year we have attempted to bring these various studies to a conclusion in anticipation of the forthcoming re-direction of our efforts in support of the Spacecraft Survivability Program. For FY 85 we shall initiate a task which considers the "response of small molecules to intense laser radiation," and except for any requested applications of our thermodynamic codes to problems of immediate interest to the Electronics and Materials Science Directorate, we shall conclude our studies of high temperature thermodynamics.

#### Progress During FY 84

Four separate tasks have been completed during this period. Two of these tasks have resulted in manuscripts that are being submitted for publication.

##### (1) The Thermodynamic Effects of Inelastic and State Changing Collisions.

This work represents the refinement of our initial study of the role of continuum and metastable states in thermodynamic calculations (F. H. Mies and P. S. Julienne, J. Chem. Phys. 77, 6162-6176 (1982)) where we only considered the effects of pure elastic scattering. As intimated in previous reports, we finally conclude that the inelastic contributions to molecular partition functions are negligible compared to the dominant elastic contributions.

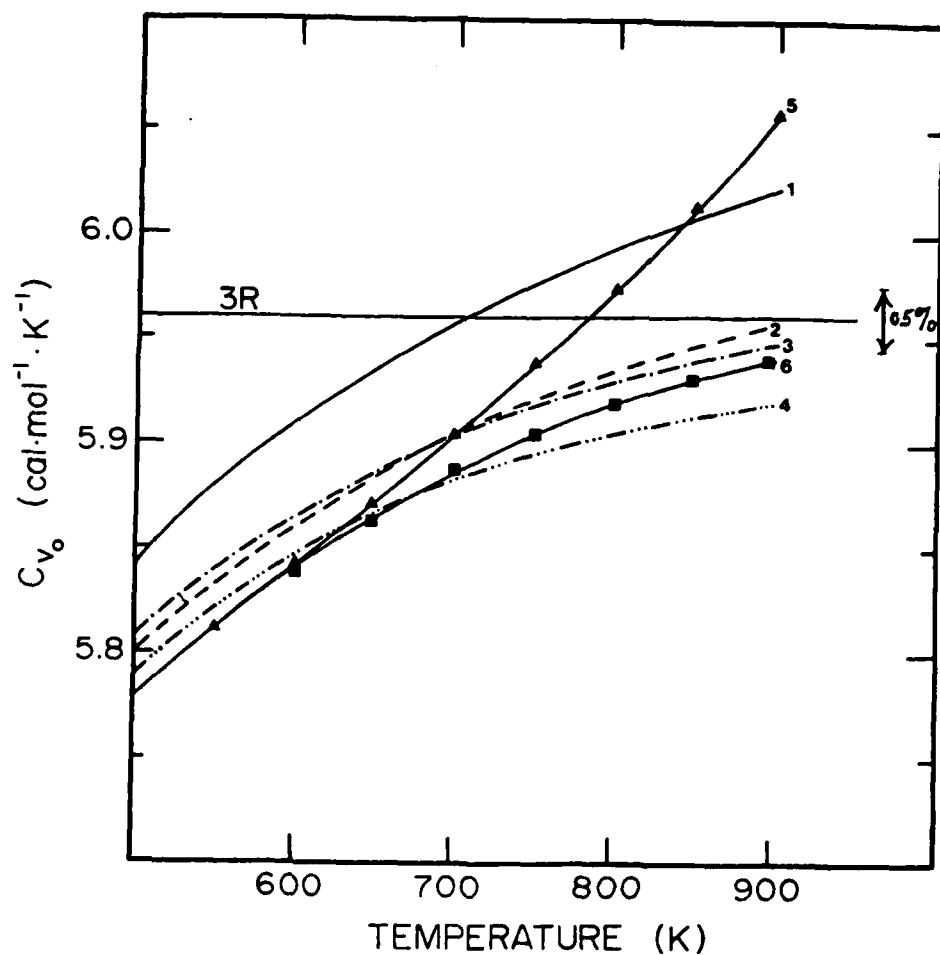


Figure 4. Calculated specific heat of Al at 0 K volume ( $C_{v_0}$ ) versus temperature (T) for four potentials (curves 1-4) and reduced specific heat for two sets of new experimental data (Curves 5,6). Curve 1 (—): from Dagens, et al. potential [28]; Curve 2 (---): from Harrison modified point ion potential [26]; Curve 3 (—•—): from Ashcroft potential [27]; Curve 4 (—...—): from effective Morse potential [23] to  $O(\lambda^2)$ ; Curve 5 ( $\blacktriangle$ ): from smoothed new data [2]; Curve 6 ( $\blacksquare$ ): Curve 5 data corrected for the vacancy contribution to the specific heat. The effective Morse potential to  $O(\lambda^2)+O(\lambda^4)$  gives results that are indistinguishable from Curve 2 at the scale of this figure.

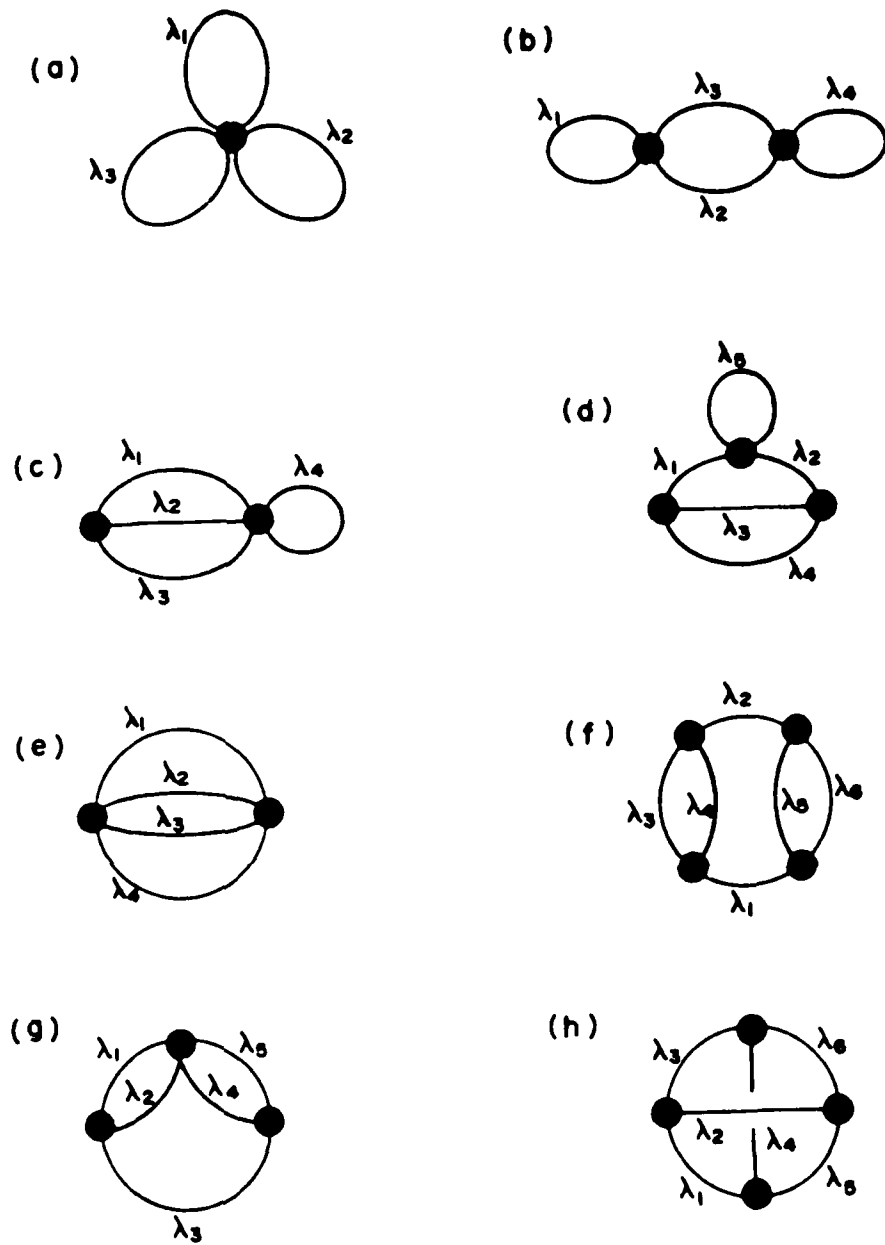


Figure 3. Diagrams of order  $\lambda^4$  (cf. text).



theory could be applied with equal force to this problem. However, in this paper we shall only consider the simple one-mode coupling represented by Eqs. (1) and (2).

In the next section we develop the adiabatic theory for two state coupling. The simple model for vibronic coupling employed by Innes [8] is solvable to arbitrary numerical accuracy following the diagonalization procedures of Chappel and Ross [10]. In section 3 we compare our adiabatic results to the exact results for Propynal and Formaldehyde. First we analyze the eigenvalues and find excellent agreement, especially if we include the adiabatic radial Born-Oppenheimer (RBO) correction  $(\phi')^2$  in Eq. (12). We then assess the quality of the wavefunctions by comparing overlaps of the exact and adiabatic radial functions and especially for the borrowed component G. We conclude that the adiabatic theory would reproduce any measurable intensity borrowing in these spectra to within 5%. Finally, in section 4 we discuss the implications and possible applications of the adiabatic theory.

## 2. ADIABATIC THEORY

Associated with  $\xi_\alpha$  in Eq. (10) is a second adiabatic eigenstate,

$$\xi_B = \sin\phi(R) \psi_0 + \cos\phi(R) \psi_1, \quad (15)$$

and together these represent an orthogonal transformation of our original 'diabatic' states. Thus we can express Eq. (1) in the equivalent form,

$$|E\rangle = \xi_\alpha(r,R) A(R) + \xi_B(r,R) B(R) \quad (16)$$

where

$$F(R) = \cos\phi(R) A(R) + \sin\phi(R) B(R) \quad (17a)$$

$$G(R) = -\sin\phi(R) A(R) + \cos\phi(R) B(R) . \quad (17b)$$

In place of Eq. (2) we obtain a set of coupled equations for the adiabatic radial functions A and B,

$$[T + V_{\alpha\alpha}(R) + (\phi')^2 - E] A + P_{\alpha\beta} B = 0 \quad (18a)$$

$$[T + V_{\beta\beta}(R) + (\phi')^2 - E] B + P_{\beta\alpha} A = 0 \quad (18b)$$

Our hope is to find a transformation which minimizes the off-diagonal coupling operator  $P_{\alpha\beta}$  in Eq. (18) such that we can neglect the contributions of B(R) in Eq. (17).

Throughout this paper we shall employ reduced energy and distance units such that the radial kinetic energy operator simply equals,

$$T = -\partial^2/\partial R^2 = -\frac{\hbar^2}{2\mu_0} \frac{\partial^2}{\partial Q^2} \quad (20)$$

Further, we will scale the displacement such that  $R=0$  coincides with the minimum in  $V_{00}(R)$  and we will scale the energy such that the zero-point energy of the  $n=0$  ground vibrational level in Eq. (5) exactly equals  $1/2$ .

Thus when we approximate  $V_{00} = R^2/4$  as a pure harmonic potential in the next section the unperturbed eigenvalues from Eq. (5) will be located at  $E_n^0 = (n+1/2)$  as shown in curve (a) of Fig. 1.

We have already assumed that the states  $\psi_0$  and  $\psi_1$  commute with the operator T, and all interchannel coupling originates from the symmetric potential matrix element  $V_{01}(R)$  in Eq. (2). At the opposite extreme we can choose the R-dependent phase  $\phi(R)$  to insure that the potential matrix  $V$  is perfectly diagonal in the new representation defined by Eqs. (10) and (15). Employing the definition of  $\phi(R)$  in Eq. (11) we obtain the pair of adiabatic potentials,

$$V_{\alpha\alpha} = V_{00}(R) - V_{01} \tan\phi(R) \quad (21a)$$

$$V_{\beta\beta} = V_{11}(R) + V_{01} \tan\phi(R) \quad (21b)$$

Since  $2\phi = \tan^{-1}(y)$  is multivalued and indeterminate by modular  $\pm\pi$  we can always choose  $V_{01}\tan\phi \geq 0$  and insure that  $V_{\alpha\alpha}$  lies below  $V_{\beta\beta}$ . This same criterion insures that  $\phi(R)$  is analytic in  $R$  and justifies the general expression for  $\phi' = d\phi/dR$  in Eq. (14). Actually this is a minor analytic subtlety which only arises when there is a curve-crossing and  $\Delta(R) = V_{11} - V_{00}$  changes sign at some distance within our range of interest. This is a very unlikely circumstance for a distant perturbation and we shall implicitly assume that  $\Delta$  remains positive for all  $R$ , such that,

$$V_{01} \tan\phi(R) \equiv V_{01}y/[(1+y^2)^{1/2} + 1] = \frac{\Delta}{2} [(1+y^2)^{1/2} - 1] \quad (22)$$

$$\underset{y \rightarrow 0}{\sim} V_{01}^2/\Delta \quad (23)$$

Thus the distant perturbation due to  $V_{01}$  causes a general lowering of the adiabatic potential  $V_{\alpha\alpha}$  relative to  $V_{00}$ .

Having eliminated any potential coupling the only remaining source of interaction between  $A(R)$  and  $B(R)$  in Eq. (18) must originate from the operator  $T$  in Eq. (2). Although we have assumed that  $\psi_0$  and  $\psi_1$  commute with  $T$  the  $R$ -dependence of the  $\sin\phi$  and  $\cos\phi$  coefficients in Eqs. (10) and (15) introduces what may be called radial Born-Oppenheimer (RBO) couplings [1,2] between the adiabatic states. The coupling operator in (18) is antisymmetric [3,4]

$$P_{\beta\alpha} = -P_{\alpha\beta} = \phi'' + 2\phi' \partial/\partial R \quad (24)$$

where  $\phi'$  is given in Eq. (14) and  $\phi''$  is the second derivative which may easily be derived from that expression. If this radial coupling is sufficiently small, then the solutions to Eq. (18) should be well approximated by  $B(R) \approx 0$  and  $A(R) \approx a_n^\alpha(R)$ , thus justifying the adiabatic

approximation in Eq. (9). Actually, by examining the magnitude of  $\phi'(R)$  in Eq. (14) for various two state systems one can develop an appreciation of the factors which most directly influence the validity of the adiabatic theory. The analysis could be put on a more rigorous basis by evaluating the Hermitian off-diagonal coupling matrix element between  $a_n^\alpha(R)$  and the corresponding vibrational wavefunctions  $b_m^\beta(R)$  defined by the distant adiabatic potential  $V_{\beta\beta}(R)$

$$\langle a_n^\alpha | P_{\alpha\beta} | b_m^\beta \rangle = \langle b_m^\beta | P_{\beta\alpha} | a_n^\alpha \rangle \quad (24)$$

and then applying appropriate perturbation theory. However, if things come to such an extreme that perturbation corrections are required, then one might be advised to abandon the adiabatic theory, except for its more qualitative insights, and to return to more rigorous procedures to derive more quantitative results. One such approach would be to use the numerical techniques presented by Hutson and Howard [7] to evaluate  $B(R)$  directly from Eq (18b), with  $A(R)$  approximated by the initial adiabatic vibrational state  $a_n^\alpha(R)$  of particular interest. A second approach would be to use the complete diagonalization technique [10] that we shall employ in the next section. However, this is probably only useful in the specialized vibronic coupling model that we will be analyzing in this paper and therefore has little general application. The third approach would be to solve the coupled equations (2) or (18) directly using various close-coupled procedures which can be gleaned from the scattering literature [11].

### 3. APPLICATION TO HERZBERG-TELLER VIBRONIC COUPLING

Using the complete set of radial functions  $\{f_n^0\}$  obtained from Eq. (5) and a comparable set of functions  $\{g_m^1\}$  with eigenvalues  $\{E_m^1\}$  defined by the diabatic potential  $V_{11}$  for the distant state, we can expand the exact radial functions  $F$  and  $G$  in these two bases,

$$F(E^*, R) = \sum_{n=0}^{n=n^*} c_n(E^*) f_n^0(R) \quad (25a)$$

$$G(E^*, R) = \sum_{m=0}^{m=m^*} d_m(E^*) g_m^1(R) \quad (25b)$$

From Eq. (2) we can generate a secular equation for the eigenvalue  $E^*$

$$(E_n^0 - E^*) c_n + \sum_m \langle f_n^0 | V_{01} | g_m^1 \rangle d_m = 0 \quad (26a)$$

$$(E_m^1 - E^*) d_m + \sum_n \langle g_m^1 | V_{10} | f_n^0 \rangle c_n = 0 \quad (26b)$$

By systematically increasing the number of basis functions  $n^*$  and  $m^*$  included in (25) we can expect to converge on an exact solution, at least for energies  $E^*$  in the vicinity of the lower  $E_n^0$  eigenvalues of the ground molecular state  $\psi_0$ . We could easily apply various layers of perturbation theory to (26) and hope to develop useful approximations to describe distant perturbations. For instance, the results in Eqs. (6) and (7) are obtained applying closure to the following sum [6], [13],

$$\sum_m |g_m^1\rangle \frac{a}{E_m^1 - E^*} \langle g_m^1| = \frac{1}{V_{11} - V_{00}} \equiv \frac{1}{\Delta} \quad (27)$$

with higher terms second-order in  $1/\Delta(R)$ . However, the converged eigenvectors resulting from (25) and (26) represent the exact solutions to the two-state problem, and it is to these that we wish to compare the adiabatic theory.

Such solutions have been developed by Innes [8] to describe vibronic coupling and intensity borrowing in Formaldehyde and Propynal. These are generated from a specialized model introduced by Chappell and Ross [10] with the following structure for the matrix elements in Eq. (2),

$$V_{00} = R^2/4 \quad (28a)$$

$$V_{11} = R^2/4 + \Delta \quad (28b)$$

$$V_{01}=V_{10} = \lambda R. \quad (28c)$$

The ground state potential is approximated as purely harmonic with unperturbed eigenvalues located at  $E_n^0 = (n+1/2)$ . These levels, and the associated quantum numbers  $n$ , are indicated in curve (a) of Fig. 1. The perturbing state is assigned an identical harmonic potential which is merely displaced by a constant energy  $\Delta$ . This model yields an equivalence between the two sets of vibrational functions  $\{f_n^0\} = \{g_m^1\}$  in (25) and greatly expedites the construction and solution of the secular equation (26). As is usual in Herzberg-Teller theory [12], the off-diagonal coupling is taken to be linear in  $R$ , which further implements the generation of Eq. (26). This simple model offers a relatively painless means of obtaining numerically exact solutions to Eq. (2) which can then be compared to the adiabatic solutions in Eqs. (9)-(13). Since the adiabatic theory is not dependent on any of the assumptions in Eq. (28) we

should obtain an adequate test of the general validity of Eq. (9) in more complicated two state situations merely by varying the parameters in this simple model.

### 3.1 Testing of Adiabatic Eigenvalues

Two parameters,  $\Delta$  and  $\lambda$ , are sufficient to completely specify the vibronic coupling in Eq. (28). First  $\Delta$ , in reduced units of the ground state vibrational energy  $h\nu_0$ , measures the distance to the perturbing excited state. For both Propynal in curve (b) and Formaldehyde in curve (c) of Fig. 1 this displacement is of the order of  $\Delta=25$ . As the coupling strength, measured by  $\lambda$ , increases the adiabatic potential  $V_{\alpha\alpha}$  in (21a) becomes increasingly attractive relative to  $V_{00}$ . To second order in the ratio  $\lambda/\Delta$  this distant interaction merely causes a reduction in the apparent force constant of the ground state harmonic potential, i.e.,

$$V_{\alpha\alpha} = [1 - 4 \frac{\lambda^2}{\Delta}] R^2/4 + (\frac{\lambda}{\Delta})^3 \quad (29a)$$

with a corresponding reduction in the adiabatic eigenvalues which we obtain from Eq. (13), i.e.,

$$E_n^\alpha \text{ (harmonic)} = [1 - 4\lambda^2/\Delta]^{1/2} E_n^0 + (\lambda/\Delta)^2 \quad (29b)$$

The radial Born-Oppenheimer correction  $(\phi')^2$  in Eq. (13) introduces the constant positive energy shift  $(\lambda/\Delta)^2$  in Eq. (29b). This approximate harmonic behavior is fairly well represented by the Propynal curve (b) in Fig. 1 where  $\lambda=2.1197$  and  $(\lambda/\Delta) = 0.083739$ . However, as can be seen in Table 1, there is already substantial deviation of the perturbative expression (29b) from both the exact and the adiabatic eigenvalues and careful examination of the adiabatic potential in Fig. 1b already shows

appreciable deviation from the pure harmonic prediction of (29a). In fact, for the Formaldehyde system, with  $\lambda = 2.7890$  and  $(\lambda/\Delta) = 0.111918$  the adiabatic potential is sufficiently lowered to cause a marked double minimum in curve (c). Obviously in this case the predictions of Eq. (29) are completely meaningless and we need to obtain precise numerical solutions for  $E_n^\alpha$  and  $a_n^\alpha(R)$  in Eq. (13).

A detailed comparison of the exact  $E_n^*$  and the adiabatic  $E_n^\alpha$  eigenvalues for these two molecules is given in Table 1. Actually the position of the levels are already shown in Fig. (1b) and (1c), and on that scale the two sets of eigenvalues are indistinguishable. For Propynal a total of  $n^*=m^*=21$  states in the expansion (25) was sufficient to insure convergence of the exact eigenvalue to the indicated precision in column two. For Formaldehyde, with the more extended and distorted adiabatic potential indicated in Fig. 1, it is not surprising that 21 states were not sufficient to insure convergence, and the eigenvalues in column 5 were obtained with  $n^*=m^*=42$ . The adiabatic eigenvalues  $E_n^\alpha$  were obtained from numerical solutions of Eq. (13) using the adiabatic potential  $V_{\alpha\alpha}$  defined by Eqs. (28), (22), (8) and (12). The code is based on the Gordon method of propagation [11] and has been well tested to insure the degree of accuracy listed in columns 3 and 6.

Noticeable differences, of the order of 0.002, only begin to occur between eigenvalues in excess of 3.0, and for the lower levels one can be quite pleased with the accuracy of the adiabatic theory. However, this degree of accuracy is achieved only if the radial Born-Oppenheimer (RBO)



term  $(\phi')^2$  is retained in Eq. (13). The eigenvalues obtained from Eq. (13) with the RBO term removed are designated as  $E_n(-RBO)$  and are listed below the complete adiabatic term values in Table 1. Actually the correction introduced by  $(\phi')^2$  is quite small, and we can certainly use the following approximation to analyze the energy differences that have been listed in Table 2.

$$E_n^\alpha - E_n^\alpha(-RBO) \approx \langle a_n^\alpha | (\phi')^2 | a_n^\alpha \rangle. \quad (30)$$

The largest correction applies to the  $n=0$  states and there is a rapid fall-off which correlates with the increasing amplitude of the vibrational wavefunction  $a_n^\alpha$  associated with each eigenvalue. This is related to the  $R$ -dependence of the phase derivative (14) that is prescribed by the potential matrix elements in (28),

$$\phi'(R^2) = \frac{\lambda}{\Delta} \frac{1}{[1+4(\lambda/\Delta)^2 R^2]}. \quad (31)$$

Neglecting the  $R$ -dependence, we would predict an upper bound of  $(\phi')^2 = (\lambda/\Delta)^2$  which is just the leading term we had previously included in the perturbative estimate (29b). As the mean square displacement  $\bar{R}_n^2 \equiv \langle a_n^\alpha | R^2 | a_n^\alpha \rangle$  increases with increasing  $n$  we expect a concomitant decrease in the expectation value of  $(\phi')^2 \approx (\lambda/\Delta)^2 [1-8(\lambda/\Delta)^2 R^2 + \dots]$  in Eq. (30). Equating  $[\phi'(\bar{R}_n^2)]^2$  to the calculated differences in Table 2 we can extract a mean  $\bar{R}_n^2$  for each level. The tabulated values of  $\bar{R}_n$  in columns 3 and 5 are qualitatively consistent with the trends we would expect when we consider the likely amplitudes of the corresponding energy levels in Fig. 1. It is interesting to note that the bimodal character of the Formaldehyde potential is reflected in these data.

### 3.2 Testing of Adiabatic Wavefunctions: Intensity Borrowing Predictions

Possibly of even more interest than the preciseness of the energy is the quality of the adiabatic wavefunction in Eq. (9). Comparing Eq. (9) to (1) we see that the exact radial components are being approximated as follows,

$$F(E_n^\alpha, R) \approx \cos\phi(R) a_n^\alpha(R) \quad (32a)$$

$$G(E_n^\alpha, R) \approx -\sin\phi(R) a_n^\alpha(R) \quad (32b)$$

These expressions measure the usefulness of the adiabatic approximation in evaluating observable properties of the molecule in the given eigenstate. Unlike  $E_n^\alpha$  which is second-order in the distant  $V_{01}$  coupling, the amplitude of the distance  $\psi_1$  state in Eq. (32b) is first-order in  $V_{01}$  and is a much more sensitive measure of the theory. As is often the case in the application of vibronic coupling theory [8,9,12], the oscillator strength to state  $\psi_0$  is considered to be much smaller than to state  $\psi_1$ . Thus the importance of the magnitude of  $G$  is greatly enhanced and plays a dominant role in determining the optical properties of these vibrationally perturbed systems.

Equation (32) offers the following prediction for the expansion coefficients in Eq. (25),

$$c_{n'}(E_n^*) \approx \bar{c}_{n'}(E_n^\alpha) \equiv \langle a_n^\alpha | \cos\phi | f_{n'}^0 \rangle \quad n' = n, n+2, n+4, \dots \quad (33a)$$

$$d_m^*(E_n^*) = \bar{d}_m(E_n^\alpha) \equiv \langle a_n^\alpha | \sin \phi | f_m^0 \rangle \quad m' = n+1, n+3, \dots \quad (33b)$$

These matrix elements have been evaluated numerically and are compared to the exact coefficients defined by the solution vectors to Eq. (26).

Recall that both  $V_{00}$  and  $V_{11}$  in Eq. (28) generate an identical set of harmonic wavefunctions  $f_n^0$ , in Eq. (5). Since the coupling in Eq. (28c) insures that  $\phi(-R) = -\phi(R)$  we obtain the rigorous selection rules for the matrix elements in (33), with alternate  $n'$  and  $m'$  coefficients identically equal to zero. The Table 3 shows a comparison for the first four  $n'=m'=0,1,2,3$  coefficients in (33). This numerical exercise should be more than enough to judge the accuracy of Eq. (32).

Since  $c_n$  is second-order in  $\phi=y/2=V_{01}/\Delta$  it is not surprising that the adiabatic approximation in Eq. (33a) is much more precise than (33b) which is linear in this parameter. Scanning through Table 3 we observe that  $|c_n - \bar{c}_n| \leq 0.0004$  which is in keeping with the quality of the adiabatic eigenvalues  $E_n^\alpha$  which are also basically second-order in  $\phi$ . When we assess the accuracy of the  $\bar{d}_n$  coefficient we only find agreement to within  $|d_n - \bar{d}_n| \leq 0.006$ . However this is still quite tolerable, and is more than adequate to insure that the adiabatic wavefunctions will reproduce any measurable vibronic intensity borrowing in the Propynal and Formaldehyde spectra to within 5%, at least for eigenvalues  $E_n^* \leq 3.0$ .

#### 4. DISCUSSION AND CONCLUSIONS

The numerical accuracies that we have achieved in applying the adiabatic theory to Herzberg-Teller vibronic coupling are very encouraging. The range of parameters we have chosen, using Propynal and

Formaldehyde as model systems, although somewhat limited, should be sufficient to judge this technique as a viable alternative to solving the pair of close-coupled equations (2) by either direct numerical integration [11] or by diagonalization procedures [8,10]. Certainly for calculation of the energy spectrum we can expect excellent results, especially if the RBO correction term is retained in Eq. (18). It also appears that the magnitude of the distant radial component  $G$  in Eq. (1) as given by Eq. (32b) is more than adequate to reproduce any intensity borrowing due to vibronic coupling. Unfavorable destructive interference between the  $F$  and  $G$  amplitudes might modify this conclusion, but such effects can easily be tested for in any given application.

The advantages of using the adiabatic theory are manifold. First, and foremost is the generality of the procedure. The Chappell and Ross [10] model system in Eq. (28) is very restrictive and probably has been developed more for its numerical convenience in constructing the secular equation (26), rather than any inherent physical qualities. Since the distant interaction potential  $V_{11}(R)$  only influences the definition of the potential difference parameter  $\Delta(R)$  in Eq. (3) this potential can be of arbitrary form. In particular we can just as well treat perturbations by distance repulsive states as have been done by Hudson and Cooper [14] using the "direct solution" [DS] method [7]. Both techniques avoid any explicit evaluation of the distant radial eigenfunctions and summations over bound and/or continuum states associated with  $V_{11}$ . In fact the two methods complement each other very nicely. Given an interaction matrix for a given physical system one can apply the adiabatic theory to Eq. (2). Actually the adiabatic solutions should be superior to the simple

first-order solution to Eq. (2a) offered by the DS method. However, given the resultant solutions to Eq. (9) and (13) further refinement can be achieved by applying the DS method to Eq. (18). Fortunately the results obtained so far for vibronic coupling hardly require this correction.

A second advantage of the adiabatic procedure is apparent in Fig. 1 where the adiabatic potentials give us instant qualitative insight into the physics of the interaction even before we begin the solution of Eq. (13). The double minimum in the Formaldehyde curve (c) is hardly apparent in Eq. (26) and was not even alluded to in the numerical study by Innes [8]. This is probably more of a curiosity than anything else but it is easy to see how in more complicated systems systematically varying input parameters in the interaction matrix  $V$ , such as in Eq. (28), and then examining the resultant adiabatic potential  $V_{\alpha\alpha}$  could avoid expensive and unnecessary calculations.

The theory is very well suited to treat isotopic effects and their influence on vibronically coupled systems. In Eq. (20) we have chosen a specific reduced coordinate  $R=R(\mu_0)$  as our independent variable. This is defined relative to some chosen reduced mass  $\mu_0$  which we associate with the displacement coordinate  $Q$ . If we change the reduced mass from  $\mu_0$  to, say  $\mu$ , on isotopic substitution, the adiabatic theory leads to the following modification of Eq. (9),

$$\left[ \left\{ T + (\phi')^2 \right\} \left( \frac{\mu_0}{\mu} \right) + V_{\alpha\alpha}(R) \right] a_n^{\alpha}(\mu, R) = E_n^{\alpha}(\mu) a_n^{\alpha}(\mu, R). \quad (34)$$

The explicit parameters  $\lambda$  and  $\Delta$  in Eq. (28) are defined with respect to  $R$ , and without changing our definition of this independent coordinate the adiabatic potential  $V_{\alpha\alpha}(R)$ , as well as  $T$  and  $(\phi')^2$  remain invariant to changes in mass. The only term in Eq. (2) which depends on  $\mu$  is the kinetic energy operator  $T$ , and we obtain the  $(\frac{\mu_0}{\mu})$  scaling of both  $T$  and the radial Born-Oppenheimer correction term  $(\phi')^2$  in Eq. (34). The solutions to Eq. (34) can then be introduced into Eqs. (9) and (32) to predict the consequences of isotopic changes.

Let us conclude with some general remarks about the validity of the adiabatic theory. Comparing Eqs. (2) and (18) we see that the net result of introducing the orthogonal transformation in Eqs. (10) and (15) is to replace the off-diagonal coupling matrix element  $V_{01}$  with the operator  $P_{\alpha\beta}$  in Eq. (24). In place of the pure Born-Openheimer approximation in Eq. (4), which entails neglecting the amplitude of the distance state  $\psi_1$  in Eq. (6), i.e.,

$$G(E_n^0, R) \approx - \frac{V_{01}}{\Delta} f_n^0(R) \approx 0 \quad (35)$$

we utilize Eq. (9), which, instead, requires neglecting the amplitude of the distant state  $\psi_\beta$  in Eq. (6), i.e.,

$$B(E_n^\alpha, R) \approx - \frac{1}{\Delta} P_{\beta\alpha} a_n^\alpha(R) \quad (36)$$

$$\approx - \frac{1}{\Delta} \frac{V_{01}}{\Delta} a_n^\alpha(R) \approx 0 \quad (37)$$

AD-A154 269

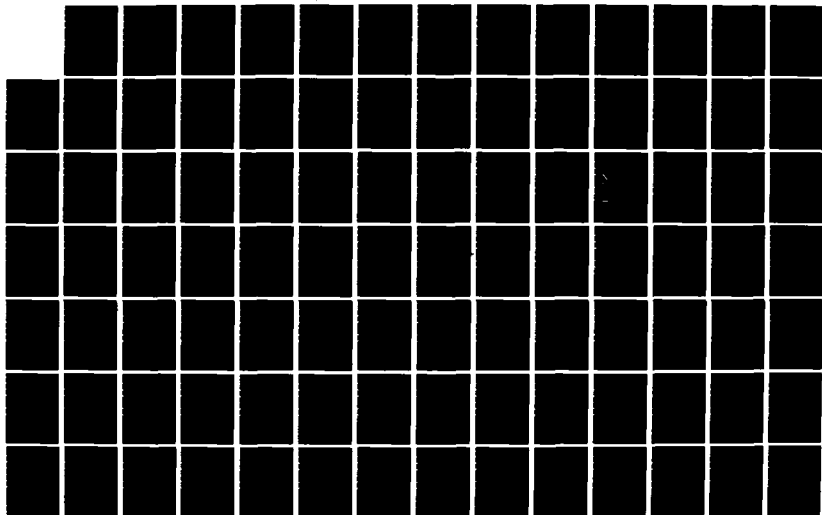
THERMODYNAMICS OF HIGH TEMPERATURE MATERIALS(U)  
NATIONAL BUREAU OF STANDARDS GAITHERSBURG MD CENTER FOR  
CHEMICAL PHYSICS S ABRAMOWITZ 15 MAR 85  
AFOSR-TR-85-0394 AFOSR-ISSA-84-00034

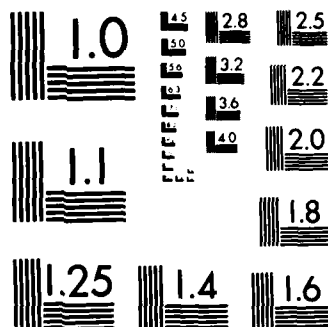
2/3

UNCLASSIFIED

F/G 11/2

NL





MICROCOPY RESOLUTION TEST CHART  
NATIONAL BUREAU OF STANDARDS-1963-A



In any given model system it is easy enough to compare the amplitudes in Eq. (35) and (36). Qualitative estimates are made available by noting the rough equality which exists between the operators  $\partial/\partial R \approx R/2$  when applied to harmonic wavefunctions. When applied to the model in Eq. (28) we obtain the approximate result in Eq. (37) which indicates that the adiabatic coupling is reduced by a factor  $1/\Delta$  compared to the original adiabatic coupling. Recall that in absolute energy units this factor represents the ratio of the vibrational spacing  $h\nu_0$  to the separation between the unperturbed states,

$$\frac{1}{\Delta} \equiv h\nu_0/(V_{11}-V_{00}). \quad (38)$$

For Propynal and Formaldehyde this factor represents a 25-fold decrease in the vibronic coupling and it might not be so surprising that the adiabatic theory is extremely quantitative in these systems.

In other systems, with large enough coupling strengths  $V_{01}$ , the reduction in Eq. (37) might not be sufficient to allow for the neglect of the  $B(E,R)$  amplitude in Eq. (17), and quantitative evaluation of the first-order amplitude (36) might be required. Alternately, the amplitude  $B$  can be extracted directly from Eq. (18b) using the superior algorithm devised by Hutson and Howard [8]. In any case, in view of the reduction factor in Eq. (38), the use of the adiabatic theory should be a powerful tool in analyzing the effects of distant perturbations.

#### ACKNOWLEDGMENTS

The author is thankful to P.S. Julianne for the use of his computer codes and his assistance in performing the adiabatic calculations presented in this paper. The author would also like to thank K.K. Innes for his valuable discussions concerning this research. This work is supported in part by the Air Force Office of Scientific Research, Contract No. AFOSR-ISSA-84-00033.

## REFERENCES

1. Bunker, P.R., and Moss, R.E., 1977, Mole. Phys. 33, 417.
2. Delos, J.B., 1981, Rev. Mod. Phys. 53, 287. Smith, F.T., 1969, Phys. Rev. 179, 111.
3. Mies, F. H., 1980, Molec. Phys 41, 953, 973.
4. Julienne, P.S., and Mies, F.H., 1981, J. Phys. B, 14, 4335.
5. Mies, F.H., and Julienne, P.S., 1984, J. Chem. Phys. 80, 2526.
6. Epstein, S.T., 1976, J. Chem. Phys. 65, 5526.
7. Hutson, J.M., and Howard, B.J., 1980, Mole. Phys. 41, 1113.
8. Innes, K.K., 1983, J. Mol. Spectrosc., 99, 294.
9. Small, G.J., 1971, J. Chem. Phys. 54, 3300. Lacey, A.R., McCoy, E.F., and Ross, I.G., 1973, Chem. Phys. Lett. 21, 233.
10. Chappell, P.J., and Ross, I.G., 1976, Chem. Phys. Lett. 43, 440.
11. Shapiro, M., and Balint-Kurti, G.G., 1979, J. Chem. Phys. 71, 1461.  
Gordon, R., 1969, J. Chem. Phys. 51, 14. Gordon, R.G., 1971 Methods Comp. Phys., 10, 81.
12. Orlando, G. and Siebrand, W., 1973, J. Chem. Phys. 58, 4513. Pople, J.A., and Sidman, J.W., 1957, J. Chem. Phys. 27, 1270. Fulton, R.L., and Gouterman, M., 1961, J. Chem. Phys. 35, 1059.
13. Mies, F.H., 1974, J. Mol. Spectrosc., 53, 150 (Appendix A)
14. Hutson, J.M., and Cooper, D.L., 1981 J. Chem. Phys. 75, 4502.

Table 1 Comparison and Exact and Adiabatic Eigenvalues for Vibronic Couplings in Propynal and Formaldehyde

quantum number	PROPYNAL			FORMALDEHYDE	
	$E_n^*$	$E_n^\alpha$	$E_n^\alpha(\text{harmonic})$	$E_n^*$	$E_n^\alpha$
		$[E_n^\alpha(-\text{RBO})]$	$E_n^O(2^{\text{nd}})$		$[E_n^\alpha(-\text{RBO})]$
n=0	0.28621 <sup>(a)</sup>	0.28630 <sup>(b)</sup> [0.27990] <sup>(c)</sup>	0.267 <sup>(d)</sup> 0.323 <sup>(e)</sup>	-0.09284 <sup>(a)</sup>	-0.09282 <sup>(b)</sup> [-0.10063] <sup>(c)</sup>
n=1	0.86238	0.86280 [0.85728]	0.813 0.968	0.01830	0.01845 [0.01279]
n=2	1.46921	1.46990 [1.46497]	1.350 1.613	0.38971	0.39012 [0.38314]
n=3	2.0990	2.09992 [2.09544]	1.887 2.257	0.75038	0.75103 [0.74543]
n=4	2.7472	2.74834 [2.74420]	2.424 2.902	1.17861	1.17950 [1.17420]
n=5	3.41073	3.41209 [2.74420]	2.962 3.547	1.64043	1.64156 [1.63665]
n=6				2.13235	2.13370 [2.12908]
n=7				2.64855	2.65013 [2.64575]
n=8				3.18550	3.18729 [3.18312]

(a) Converged exact eigenvalues obtained from solution of Eq. (26) with  $n^* = 21$  for Propynal and  $n^*=42$  for Formaldehyde.

(b) Adiabatic eigenvalues obtained from numerical solution of Eq. (13).

(c) Eigenvalues obtained from Eq. (13) with  $(\phi')^2$  term removed.

(d) Harmonic approximation to eigenvalues given by Eq. (29).

(e) Second-order energy as given by Eq. (7).

Table 2. Contribution of the Radial Born-Oppenheimer Corrections to Adiabatic Eigenvalues

Quantum number	PROPYNAL			FORMALDEHYDE		
	$E_n - E_n(-RBO)$	$\bar{R}_n^{-2}$	$\bar{R}_n$	$E_n - E_n(-RBO)$	$\bar{R}_n^{-2}$	$\bar{R}_n$
n=0	0.007012 <sup>a</sup> 0.00640	0.0 1.67	0.0 1.29	0.01252 <sup>a</sup> 0.00781	0.0 5.32	0.0 2.31
n=1	0.00552	4.54	2.13	0.00566	9.75	3.12
n=2	0.00493	6.88	2.62	0.00698	6.79	2.61
n=3	0.00448	8.97	2.99	0.00560	9.90	3.15
n=4	0.00414	10.77	3.28	0.00530	10.74	3.28
n=5	0.00387	12.35	3.51	0.00491	11.97	3.46
n=6				0.00462	12.92	3.59
n=7				0.00438	13.81	3.72
n=8				0.00417	14.65	3.83

(a) upper-bound on RBO correction based on  $(\phi')^2 = (\lambda/\Delta)^2$  with  $R=0$  in Eq. (31).

Table 3. Comparison of exact and adiabatic radial functions

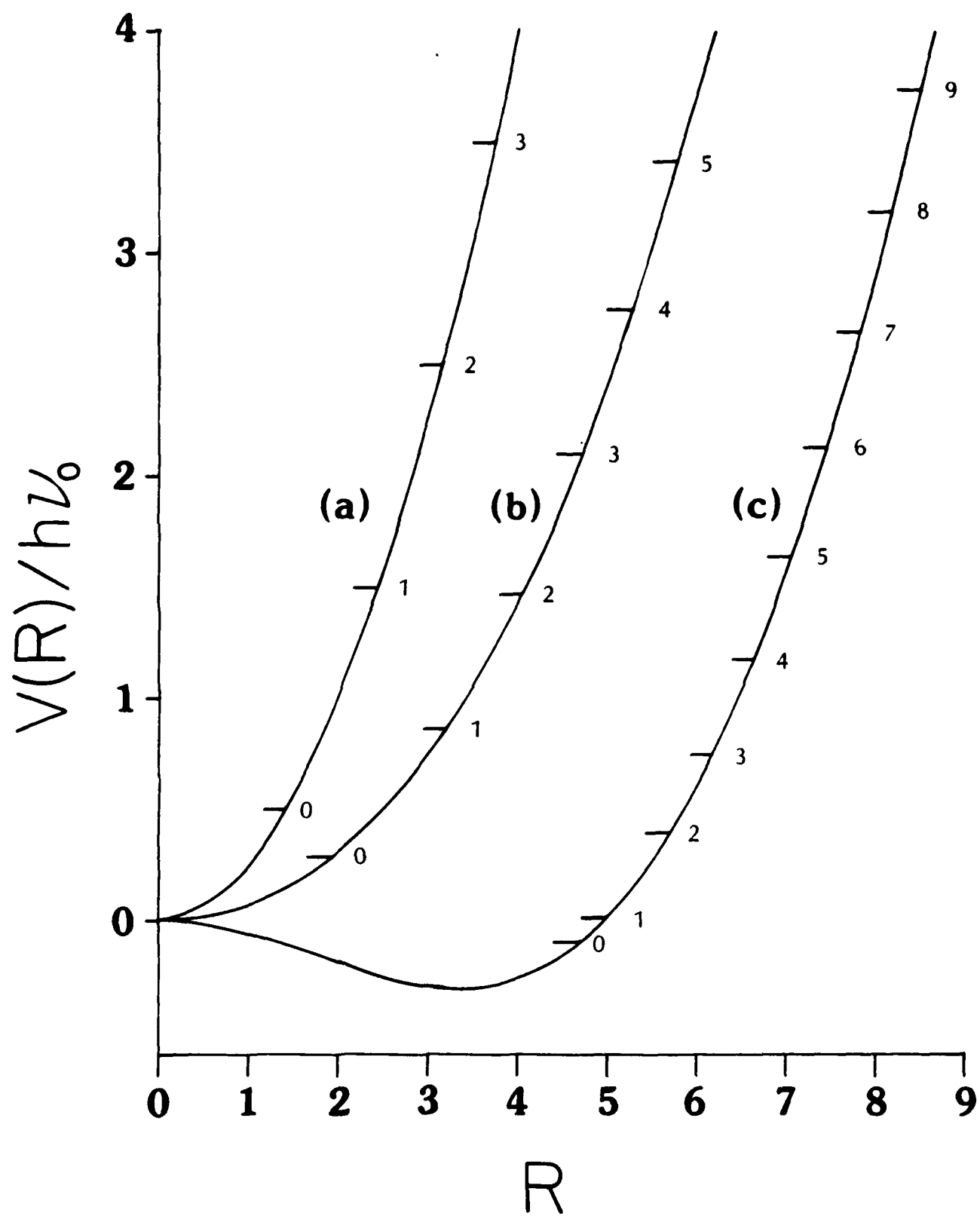
Eigenstate	n'=0	n'=1	n'=2	n'=3
<u>Propynal</u>				
n=0	0.9773 <sup>(a)</sup> 0.9771	[ 0.0986] <sup>(b)</sup> [ 0.1008]	0.1812 0.1811	[ 0.0288] [ 0.0293]
n=1	[ 0.0798] [ 0.0768]	0.9397 0.9396	[ 0.1434] [ 0.1459]	0.2856 0.2854
n=2	-0.1920 -0.1918	[ 0.0878] [ 0.0834]	0.8779 0.8779	[ 0.1748] [ 0.1771]
n=3	[-0.0270] [-0.0257]	-0.3016 -0.3014	[-0.0793] [-0.0741]	0.8020 0.8020
n=4	0.0419 0.0418	[-0.0444] [-0.0422]	-0.3864 -0.3862	[ 0.0623] [ 0.0565]
n=5	[ 0.0078] [ 0.0073]	0.0820 0.0819	[-0.0578] [-0.0548]	-0.4510 -0.4508
<u>Formaldehyde</u>				
n=0	0.7163 0.7162	[ 0.1523] [ 0.1524]	0.5170 0.5168	[ 0.1532] [ 0.1538]
n=1	[ 0.0701] [ 0.0676]	0.6386 0.6387	[ 0.1903] [ 0.1904]	0.5582 0.5580
n=2	-0.6298 -0.6293	[-0.0249] [-0.0286]	0.2810 0.2813	[ 0.1431] [ 0.1422]
n=3	[-0.0709] [-0.0681]	-0.6272 -0.6268	[-0.0691] [-0.0728]	0.1308 0.1312
n=4	0.2615 0.2612	[-0.0636] [-0.0592]	-0.5921 -0.5921	[-0.1100] [-0.1132]
n=5	[ 0.0427] [ 0.0408]	0.3641 0.3637	[-0.0432] [-0.0379]	-0.5275 -0.5276
n=6	-0.0999 -0.0998	[ 0.0585] [ 0.0551]	0.4309 0.4307	[-0.0150] [-0.0093]
n=7	[-0.0208] [-0.0197]	-0.1700 -0.1698	[ 0.0642] [ 0.0597]	0.4683 0.4682
n=8	0.0366 0.0365	[-0.0352] [-0.0331]	-0.2332 -0.2330	[ 0.0618] [ 0.0564]

(a) unbracketed coefficients correspond to  $c_{n'}(E^*_n)$ . The asymmetry of  $V_{01}(R)$  insures that  $c_{n'}(E^*_n)=0$  when  $n'=n\pm1, n\pm3, \dots$ . The upper value is the exact coefficient, the lower is the result using Eq. (33).

(b) bracketed terms give  $d_{n'}(E_n)$ , and vanish identically when  $n'=n, n\pm2, \dots$ . Upper value is exact, lower value is adiabatic prediction in Eq. (33).

# FIGURE CAPTION

- Fig. 1. curve (a) Pure harmonic potential in reduced units  $V_{00} = R^2/4$  such that eigenvalues exist at  $E_n = (n + 1/2)$ .
- curve (b) Adiabatic potential for perturbed  $v_{10}$  mode of  ${}^1A''(S_1)$  state of propynal vibronically coupled to distant  ${}^1A'(S_3)$  state. In reduced units  $\Delta = 25.313$ ,  $\lambda = 2.1197$  in Eq. (28).
- curve (c) Adiabatic potential for perturbed  $v_4$  mode of  ${}^1A_2(S_1)$  state of formaldehyde vibronically coupled to distant  ${}^1B_2(S_2)$  state. In reduced units  $\Delta = 24.920$ ,  $\lambda = 2.7890$  in Eq. (28).





4.

Stability and Growth of Graphitic Layers

Principal Investigators: S. E. Stein

R. L. Brown

Introduction

A key issue in the use of carbon as an ablation shield is the knowledge of chemical processes involved in the formation and decomposition of graphitic materials. Progress in this area has been hampered by the lack of reliable theories for treating the reactive chemical species in these substances. It is reasonable to assume that these materials consist of loosely bound layers of large planar polyaromatic molecules of varying size and having a variety of edge structures. Theories of aromatic molecules separate the bonds joining the carbon atoms into two types; the  $\sigma$ -bonds, which are localized in the region between the adjacent nuclei, and the  $\pi$ -bonds arising from the  $\pi$ -electrons which are distributed above and below the plane of the molecule. These  $\pi$ -reactions are metallic in nature and are the ones which give graphite most of its characteristic properties. There are a number of theories available which can be used to model these  $\pi$ -electron networks. In the past, however, they have been applied almost exclusively to the relatively small molecules of interest to organic chemists. Their application to very large graphitic molecules and their subsequent testing and refining by experiment are the goals of this program.

#### Progress During FY-84

Earlier in this program, we discovered that the atomic orientation at the edges of the molecules and their overall size exert a profound effect on the molecular properties, most importantly on the energy of the highest occupied molecular orbital and in the minimum electron localized energy. Some selected results which demonstrate these points are shown in Fig. 1. Most of our theoretical work over the past year was devoted to the development of efficient computer codes to adapt a sophisticated theory, namely the Pople SCF method, to very large molecules. All of the theories we have used to date require constructing a so-called bond matrix which describes how the carbon atoms are connected. For the simpler theories the key to their extension to large molecules was the discovery of a unique numbering system for the carbon atoms which resulted in a narrow banded bond matrix which greatly simplified the computations [1]. The corresponding matrix for the SCF method, however, is not banded, and in practice contains few, if any, zero elements. Calculations using this type of matrix require far more computational time than the banded cases. Furthermore, the SCF method is iterative and converges more slowly the larger the molecule. Thus the computational problems rapidly become enormous for molecules of even modest size. The only way to use this method on large molecules is to require them to have the maximum symmetry. Then, group theoretical methods can be applied to greatly simplify the computational problem. Another advantage of using symmetrical structures is that they are easily formed into homologous series each consisting of a progression of increasingly larger molecules. This facilitated the extrapolation of various electronic properties to infinite size molecules (graphite) and the development of structure/reactivity relations at the

"edges" of large polyaromatic molecules. By this means we have developed a computer code which allows us to use this SCF technique on molecules containing up to 1000 carbon atoms. For complete convergence of this iterative method, such molecules require three to six days on a high speed computer. To our knowledge, the largest molecule to which this method had previously been applied was coronene which contains 24 carbon atoms.

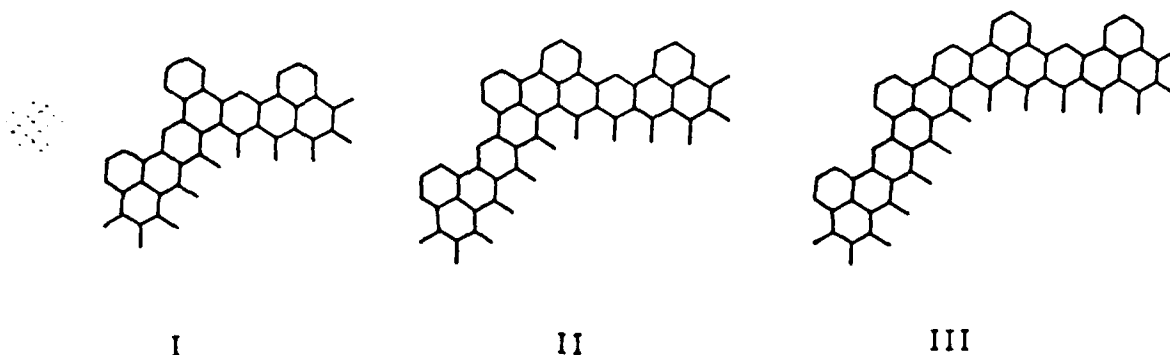
Our results so far with this more complex theory are usually in qualitative agreement with simpler theories. One critical difference, however, is that SCF methods, in accord with intuition, indicate that resonance energies per C-atom approach a unique value with increasing molecular size, independent of edge type. For the simplest theory used in previous studies, different limiting values were approached which depended on edge type. There are other general important qualitative differences whose implications we are now examining in detail.

In the past year we began experiments to test and refine our calculational models. In these experiments aromatic molecules are passed through a very-low pressure, high temperature cell. Carbon deposition reaction kinetics are measured by sampling the flow out of the reactor by mass spectrometry. We have found that even relatively reactive aromatic molecules such as anthracene are rather unreactive on pyrolytic graphite at temperatures up to 1250 K. Free radicals, on the other hand are rather reactive, and appear to be the primary agents responsible for carbon growth in our reactor. Primary results for both the relatively unreactive benzyl radical, and the reactive phenyl radical suggest the order of this reaction is between 1 and  $3/2$  and only weakly sensitive to temperature.

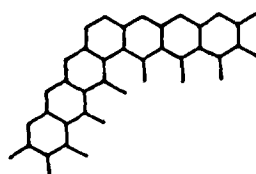
The simplest mechanism consistent with this process is that radicals deposit primarily on surface radical sites created by previous radical deposition processes.

#### References

- 1) R. L. Brown, J. Computational Chem. 4, 556 (1983).



while for all molecules with edge-type B, only a single corner type is possible, namely,

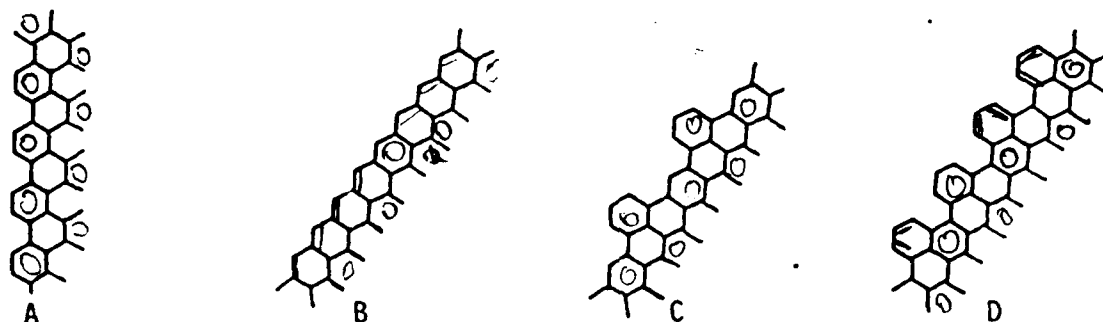


Stabilities of benzenoid layers for hexagonal series with edge-types A-D are shown in Figure 2 as a function of molecular size. Stabilities are represented as the logarithm of the number of Kekulé structures per  $\pi$ -electron ( $\equiv n_{\pi}^{-1} \ln[\# \text{ Kekulé structures}]$  where  $n_{\pi}$  is the total number of  $\pi$ -electrons). In the simplest form of SRT,  $\ln(\text{KSPE})$  is proportional to the resonance energy per  $\pi$ -electron. Molecular size is represented by  $n_{\pi}^{-1/2}$ , which is roughly proportional to the number of edge carbon atoms. This function is chosen because it was found to clearly show the behavior of  $\ln(\text{KSPE})$  as  $n_{\pi} \rightarrow \infty$ .

As shown in Figure 2, stabilities of benzenoid layers depend strongly on the nature of the edges. For each series studied, as molecular size increases,  $\ln(\text{KSPE})$  approaches an asymptotic value. Perhaps surprisingly, different series can approach distinctly different asymptotic values.

To obtain localization energies for graphite-like molecules we have employed a first-order perturbation treatment [7], and to obtain first approximations for odd-electron densities in graphite-like free radicals we have used Hückel molecular orbital (HMO) theory.

Results reported here are based on studies of a large number of highly condensed benzenoid molecules. In an effort to systematize these studies, our analysis has focused on homologous series of hexagonally-symmetric molecules. Members of a given series differed in size but had the same edge and corner construction. The following four edge structures were considered,



While it may not be evident from a cursory examination of these structures, each molecule studied was a normal Kekulé hydrocarbon. Examples of the first few members of series A and B are given in Figure 1. In general, for each edge-type a number of different corner structures are possible depending on molecular size and shape. For example, each even-sided hexagonal molecule with edge-type C has one of the following three corner structures,

Graphite is composed of very large, highly condensed benzenoid polyaromatic molecules whose electronic properties can, in principle, be examined by conventional chemical theory. Previous calculations of this nature either have been limited to molecules with less than  $\sim 50$  carbon atoms [1-3], or have treated graphite as an infinite two-dimensional crystal composed of repeating structural units [4]. Neither of these approaches has dealt thoroughly with potentially important structural features such as edges and overall size and shape. For this purpose, calculations on very large, but finite layers appear to be needed. In this work we present initial results of calculations on well-defined benzenoid molecules containing as many as 16,000 carbon atoms. Computation times are held to practical levels using theories that require as input only counts of Kekulé structures [5] along with an efficient algorithm for counting these structures in polyaromatic molecules [6].

These theories are particularly suited for these calculations since they accurately correlate a wide range of properties of polyaromatic species [7,8] and yield resonance energies and reactivity indices in good agreement with those of more sophisticated, but more time-consuming, molecular orbital calculations [9].

For estimation of resonance energy in molecules we have used the simplest form of structure-resonance theory, SRT [9], a form that relates the resonance energy of a conjugated species to the logarithm of its number of Kekulé structures. This relation is known to yield resonance energies in excellent agreement with SCFMO predictions. Other, more complex forms of SRT have been shown to yield comparable results [8].

b. A Chemical Theory of Graphite-Like Molecules

S. E. Stein and R. L. Brown

Abstract

An approach for analyzing electronic properties of large, well-defined graphite-like layers is presented. It is shown that very large structures can be examined using theories that require only counts of resonance structures as input. Stabilities are examined as a function of edge-type for four homologous series of layers containing up to 16,000 carbon atoms. Analyses of electron localization energies and  $\pi$ -electron densities are also presented. These studies provide a basis for examining effects of edge structures and relative position in the chemistry of graphite.



## REFERENCES

- 1) W. C. Herndon, *Israel J. Chem.*, 20, 270 (1980).
- 2) M. Randic, *J. C. S. Faraday Trans. II*, 232 (1975).
- 3) P. Eilfeld and W. Schmidt, *J. Electron Spectroscopy and Related Phenomena*, 24, 101 (1981).
- 4) B. Dzonova-Jerman-Blazic and N. Trinajstic, *Computers and Chemistry* 6, 121 (1982).
- 5) W. C. Herndon, *Tetrahedron*, 29, 3 (1973).
- 6) C. F. Wilcox, Jr., *Tetrahedron Lett.*, 795 (1968).
- 7) I. Gutman, N. Trinajstic, and C. F. Wilcox, Jr., *Tetrahedron*, 31 143 (1975).
- 8) G. G. Hall, *Proc. Roy. Soc. (London)* A229, 251 (1955); *Int. J. Math. Educ. Sci. Technol.*, 4, 233 (1973).
- 9) N. S. Ham, *J. Chem. Phys.*, 29, 1229 (1958).
- 10) M. J. S. Dewar, "The Molecular Orbital Theory of Organic Chemistry", McGraw-Hill, New York, 1969, p. 214.
- 11) E. Heilbronner, *Helv. Chim. Acta*, 45, 1722 (1962).
- 12) F. E. Hohn, "Elementary Matrix Algebra", MacMillan, New York, 1964, 2nd ed.
- 13) G. E. Forsythe and C. B. Moler, "Computer Solution of Linear Algebraic Systems", Prentice-Hall, New Jersey, 1967.

ML and MU are the number of rows below and above the diagonal, respectively.

For the example in Fig. 2 the bond matrix is

$$B = \begin{bmatrix} 1 & 1 & 0 & 0 & 0 & 0 & 0 & 0 & 0 & 0 \\ 1 & 0 & 1 & 0 & 0 & 0 & 0 & 0 & 0 & 0 \\ 0 & 1 & 1 & 0 & 1 & 0 & 0 & 0 & 0 & 0 \\ 0 & 0 & 1 & 1 & 0 & 1 & 0 & 0 & 0 & 0 \\ 0 & 0 & 0 & 1 & 0 & 0 & 1 & 0 & 0 & 0 \\ 0 & 0 & 0 & 0 & 1 & 1 & 0 & 1 & 0 & 0 \\ 0 & 0 & 0 & 0 & 0 & 1 & 1 & 0 & 1 & 0 \\ 0 & 0 & 0 & 0 & 0 & 0 & 1 & 0 & 0 & 1 \\ 0 & 0 & 0 & 0 & 0 & 0 & 0 & 1 & 1 & 0 \\ 0 & 0 & 0 & 0 & 0 & 0 & 0 & 0 & 1 & 1 \end{bmatrix}$$

The forth section sets up the B matrix in the form required for the LU decomposition routine SGBFA. Note that the storage required by SGBFA is  $2*ML+MU+1$ , which is larger than the actual band width.

The fifth section performs the LU factorization. On return from SGBFA, the elements of the B array having the value  $MU+ML+1$  for the first index contain factors which when multiplied together give the determinant of B. The logarithm of the absolute value of this determinant is calculated by summing the logarithms of the absolute values of these elements.

In the final section, the inverse of B is determined. On return from SGBSL, the vector array E contains the elements of the I'th row of  $B/\det(B)$ .

So far, the size of the structures we have been able to examine have been limited by the core size of our computer. For a hexagonally symmetric structure having 547 benzene rings, 1176 carbons, and a width of approximately of 65 Å, the computation time required on a Hewlett-Packard 1000 machine was only 3.5 minutes. In this particular case, the KSC for the even parent compound was  $4.8 \times 10^{66}$ .

#### Acknowledgment

I wish to thank Dr. S. E. Stein for suggesting this problem and for his critical interest and encouragement. This work was supported in part by the Gas Research Institute and by the U. S. Air Force Office of Scientific Research, under Contract ISSA-83-00038.

these two coordinate systems. The (X, Y) coordinates of each ring are shown in the parenthesis at their centers.

The numbering of the c and n-centers shown here is best explained by referring to the listing of the computer program in the Appendix. The centers of the benzene rings are contained in the array R, with  $X = R(1, NR)$ , and  $Y = R(2, NR)$ , where NR is the number of the ring. This array, along with the total number of rings NPMAX in the structure is the input to the program. Rings can be stored in R in any order. In the first section of the program, each benzene ring is examined in turn and a non-zero value (9999) placed in the array AC at the appropriate (U, V) locations to indicate the presence of three c-centers; the array AN is similarly marked to note the existence of three n-centers. The extrema (UMIN, UMAX, VMIN, VMAX) of the (U, V) values encountered, and the total number of c-centers is also determined in this section.

The numbering of the c and n-centers follows in the next section. Running through the ranges of the (U, V) values, the computer notes the presence of non-zero elements in the AC and AN arrays and numbers them. It begins with the minimum values of U and V and changes V most rapidly. This results in the numbering scheme shown in the example of Fig. 2. This method of labeling centers produces a banded matrix for B with a maximum width of  $VMAX - VMIN + 2$ . The size of the B array thus increases as the cube of the average width of the structure rather than as the forth power as it would for a non-banded configuration.

The third section of the program determines the band width of B. This is the number of rows parallel to its diagonal which are required to include all the non-zero elements. Each (U, V) cell is examined in turn, and the difference between the maximum and minimum label numbers of the c-centers in the cell noted. The biggest difference encountered gives the width of the band.

$$B = \det(B)[B^{-1}]^{\dagger} \quad (10)$$

Inversion of  $B$  may be accomplished<sup>13</sup> by solving a series of linear systems,  $Bx_1 = e_1, Bx_2 = e_2, \dots$ , where a solution  $x_i$  is the  $i$ 'th column of  $B^{-1}$  and  $e_i$  is a vector having a one in the  $i$ 'th position and zeros elsewhere. The computer program described in the next section will use the so-called LU method of factorizing  $B$  to solve these systems.

#### COMPUTER PROGRAM FOR CALCULATING THE MATRIX $B$

To minimize the computation time and maximize the size of the molecules which could be treated, it was necessary to find a numbering system for the centers which would produce a banded bond matrix. This was accomplished by using the coordinate system shown in Fig. 2. Its axes, labeled  $U$  and  $V$ , are inclined at  $60^\circ$ . The units on each are  $3^{1/2}a$ , where  $a$  is the length of the carbon-carbon bonds. The system is oriented so that the  $c$ -centers of a molecule lie at the intersections of a grid based on this unit. Each  $n$ -center is associated with a cell of this grid. An individual cell is specified by the values of the  $(U, V)$  coordinates at its lower left corner. These values will also be used to identify the cell's  $n$ -center. The sum of the NBMO coefficients for  $c$ -centers located at this corner and its two neighboring corners in the cell will be zero. The  $c$ -centers will naturally be identified by their  $(U, V)$  coordinates.

The locations of the centers of the individual benzene rings in the molecule are specified by another superimposed coordinate system. This one has orthogonal axes  $X$  and  $Y$  (not shown in Fig. 2), with the  $X$  axis parallel to the  $U$  axis of the first system. Units along the  $(X, Y)$  axes are  $3^{1/2}a$  and  $3a/2$ , respectively. The origin of the  $(U, V)$  system is at  $(0, -a)$  in the  $(X, Y)$  system. Figure 2 also gives an example of a molecule embedded in

vector  $v^{(k)}$ , and the third equality derives from the way the  $B^{(k)}$  matrices are constructed (see eqs. (2)).

Consider now the sum  $\sigma^{(k)}$  of the coefficients around the deleted n-centers. This is given by

$$\sigma^{(k)} = \sum_j b_{kj} c_j^{(k)} = (\sum_j b_{kj} \beta_{kj}) v_0 [\det(B^{(k)})]^{-1} \quad (5)$$

where the expression for the  $c_j^{(k)}$  given by eq. (4) has been used. From a theorem on determinants,<sup>12</sup> we have the equality,

$$\sum_j b_{kj} \beta_{kj} = \det(B) = \text{KSC}(\text{even parent molecule})^{8,9} \quad (6)$$

If we set the scale factor  $v_0$  equal to  $\det(B^{(k)})$  then we have

$$\sigma^{(k)} = \sum_j b_{kj} \beta_{kj} = \text{KSC}(\text{even system}) \quad (7)$$

Thus, the elements of the cofactor matrix of  $B$  are the NMO coefficients scaled so that the sum of those around the deleted n-center gives the KSC for the even parent molecule. The summation in eq. (7) is independent of which n-center is deleted. On the other hand, the summation  $s^{(k)}$  of the absolute values of the scaled coefficient  $\beta_{kj}$  over all the c-centers  $j$  gives the KSC for the odd molecule resulting from deletion of n-center  $k$ . Thus,

$$s^{(k)} = \sum_j |\beta_{kj}| \quad \text{KSC}(n\text{-center, } k \text{ deleted}) \quad (8)$$

This corresponds to calculating row sums in  $\beta$ . To get the KSC for the odd species resulting from deletion of centers from the c-set, we simply calculate column sums of  $\beta$ . This gives,

$$s^{(j)} = \sum_k |\beta_{kj}| \quad \text{KSC}(c\text{-center, } j \text{ deleted}) \quad (9)$$

The matrix  $\beta$  can be calculated<sup>12</sup> from the inverse of  $B$ . The relation is

$$B^{(1)}c^{(1)} = \begin{bmatrix} 1 & 0 & 0 \\ b_{21} & b_{22} & b_{23} \\ b_{31} & b_{32} & b_{33} \end{bmatrix} \begin{bmatrix} c_1^{(1)} \\ c_2^{(1)} \\ c_3^{(1)} \end{bmatrix} = v^{(1)} = \begin{bmatrix} v_0 \\ 0 \\ 0 \end{bmatrix}$$

$$B^{(2)}c^{(2)} = \begin{bmatrix} b_{11} & b_{12} & b_{13} \\ 0 & 1 & 0 \\ b_{31} & b_{32} & b_{33} \end{bmatrix} \begin{bmatrix} c_1^{(2)} \\ c_2^{(2)} \\ c_3^{(2)} \end{bmatrix} = v^{(2)} = \begin{bmatrix} 0 \\ v_0 \\ 0 \end{bmatrix} \quad (2)$$

$$B^{(3)}c^{(3)} = \begin{bmatrix} b_{11} & b_{12} & b_{13} \\ b_{21} & b_{22} & b_{23} \\ 0 & 0 & 1 \end{bmatrix} \begin{bmatrix} c_1^{(3)} \\ c_2^{(3)} \\ c_3^{(3)} \end{bmatrix} = v^{(3)} = \begin{bmatrix} 0 \\ 0 \\ v_0 \end{bmatrix}$$

The NBMO coefficients are denoted by  $c_j^{(k)}$  where the subscript gives the number of the c-center. The superscripts in parentheses denote the number of the deleted n-center. In our case there is always one more c-center than there are n-centers. Thus, one of the c-coefficients is arbitrarily set equal to a scale factor  $v_0$ . For this we choose  $c_k^{(k)} = v_0$ .

The solution of any set of equations  $B^{(k)}c^{(k)} = v^{(k)}$  like those shown in eqs. (2) is,<sup>12</sup>

$$c^{(k)} = (B^{(k)})^{-1}v^{(k)} = (\beta^{(k)})^+v^{(k)}[\det(B^{(k)})]^{-1} \quad (3)$$

Here,  $\beta^{(k)}$  is the cofactor matrix of  $B^{(k)}$ ; an element  $[\beta^{(k)}]_{ij}$  is  $(-1)^{i+j}$  times the determinant of the submatrix obtained by deleting the i'th row and the j'th column from  $B^{(k)}$ . Equation (3) can be written as

$$\det(B^{(k)})c_i^{(k)} = \sum_j \beta_{ji}^{(k)}v_j^{(k)} = \beta_{ki}^{(k)}v_0 = \beta_{ki}v_0 \quad (4)$$

where the quantities  $\beta_{ki}$  are the elements of the cofactor matrix of the bond matrix  $B$ . The second equality in eq. (4) follows from the definition of the

matrix B, which is a submatrix of the adjacency matrix.<sup>8,9</sup> To construct it, the carbon centers are assigned to two sets, which we label n and c, such that bonds occur only between centers belonging to different sets. Matrix elements are assigned a value of unity for centers between sets which are connected by bonds, and a value of zero otherwise. As an example, with the sets numbered as shown in Fig. 1, the bond matrix for benzene is

$$B = \begin{bmatrix} b_{11} & b_{12} & b_{13} \\ b_{21} & b_{22} & b_{23} \\ b_{31} & b_{32} & b_{33} \end{bmatrix} = \begin{matrix} & \begin{matrix} c_1 & c_2 & c_3 \end{matrix} \\ \begin{matrix} n_1 \\ n_2 \\ n_3 \end{matrix} & \begin{bmatrix} 1 & 1 & 0 \\ 1 & 0 & 1 \\ 0 & 1 & 1 \end{bmatrix} \end{matrix} \quad (1)$$

The rows of B refer to the n-centers, and the columns to the c-centers.

In Herndon's theory, the calculation of properties like reactivities and ionization potentials involves removing one of the centers from the  $\pi$ -system. In the present case this results in an odd alternate system which has a non-bonding molecular orbital (NBMO). Suppose that the center removed is taken from the n-set. Then the NBMO coefficients at the remaining n-centers are zero, and the coefficients at the c-centers sum to zero around any n-center.<sup>10</sup> They can be calculated by solving the resulting system of linear equations.<sup>11</sup> For benzene, the deletion of the centers at  $n_1$ ,  $n_2$ , and  $n_3$  results, respectively, in the following three systems of equations for the coefficients,

## INTRODUCTION

A parameterized structure-resonance theory has been developed by Herndon and co-workers<sup>1</sup> and applied to a variety of  $\pi$ -molecular systems. They have used it successfully to calculate resonance energies, bond orders, ionization potentials, and heats of formation. Our laboratory is currently engaged in a project to extend this theory to very large benzenoid molecules, the ultimate goal being its application to various aspects of soot formation and graphite chemistry. For small molecules, one of the advantages of Herndon's over other methods is the ease with which the calculations can be made without the use of a computer. For the large structures to be examined in the present work, however, a computer approach is necessary. The basic calculation involved in this theory is the enumeration of Kekulé structures. For the general type of aromatic molecule, there are several recently described<sup>2,3,4</sup> methods for dealing with this problem. None, however, is convenient for very large molecules. The purpose of the present paper is to describe an algorithm for enumerating the resonance structures of arbitrarily large benzenoid polynuclear hydrocarbons. A simple Fortran program for implementing this algorithm will also be presented. The structures to be considered will be restricted to even systems.

## METHOD

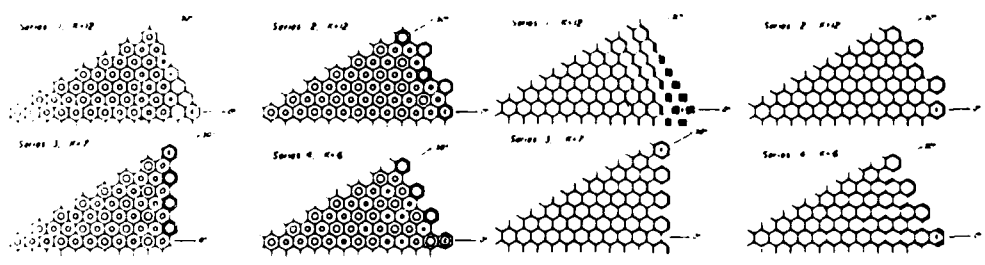
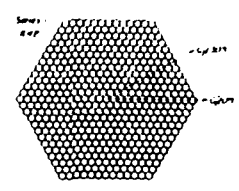
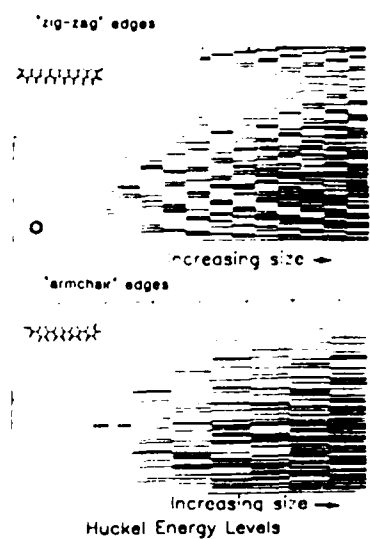
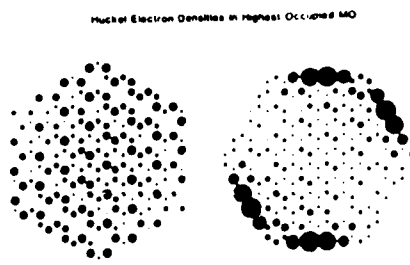
Herndon has defined<sup>5</sup> a corrected structure count. This is the number of those structures which contribute to stabilizing resonance interactions. For the even benzenoid species considered here, it is equivalent to the algebraic structure count employed by Wilcox<sup>6</sup> and is the same as the Kekulé structure count (KSC)<sup>7</sup>. It is equal to the determinant of the bond



a. COUNTING OF RESONANCE STRUCTURES FOR LARGE BENZENOID POLYNUCLEAR  
HYDROCARBONS

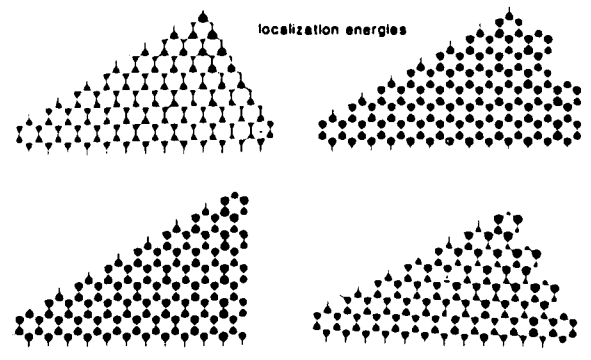
ABSTRACT

A method is presented for counting the number of resonance structures for large benzenoid polynuclear hydrocarbons. Structure counts for even systems are made and compared with those of the odd systems resulting from the removal of one of the  $\pi$ -centers from various points in the even structure. A computer program for performing the calculations is also given.



Ring Aromaticities

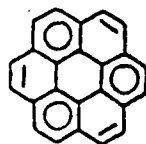
Bond Orders



Therefore, SRT predicts that even in arbitrarily large layers, average  $\pi$ -electron energies may depend on the nature of the edges. Several additional calculations using a more complex form of SRT [8] predict similar relative stabilities and asymptotic behavior.

These results differ from results of Huckel theory which suggests that all benzenoid polycyclic aromatic molecules containing more than  $\sim 30$  C-atoms have nearly the same resonance energy per C-atom [2-3]. However, for resonance energy determination Huckel calculations are clearly inferior to SCF calculations [7] and SRT theory parallels SCF theory. At this point, we expect the truth to lie between these two extreme predictions, so that in the limit of infinite size resonance energy per C-atom will not depend on edge structure; although for intermediate-sized molecules edges can have a profound effect. Preliminary calculations using SCF theory support this idea.

Qualitatively, SRT results are consistent with predictions of Clar [10], which state that the most stable benzenoid polycyclic aromatic molecules are those that can be formally represented as being entirely composed of isolated benzene rings (Clar calls these "fully benzenoid molecules"). Close inspection shows that molecules with edges A and C are fully benzenoid, while molecules with edges B and D are not. We find, for instance, that in any representation of molecules with edge-type B no more than 75% of the carbon atoms are members of a benzenoid ring. This is most easily illustrated for coronene, the second member of series B,



In Figure 2 are shown KSPE values for three series with edge-type C, but with the different corner structures shown above. As might be

expected, differences between these series are slight and diminish with increasing size. The nature of corner structures in very large molecules apparently has little influence on KSPE and is therefore ignored in the remainder of this work.

The most stable series has edges that contain only phenanthrene-like units (edge-type A, often referred to as "arm-chair" edges). These structures represent one of the two possible ways of, in effect, cutting regular hexagonal molecules out of an infinite benzenoid sheet. Each carbon-carbon bond in these structures is parallel to a pair of edges and to the  $\langle 10\bar{1}0 \rangle$  graphite crystalline directions.

The least stable series has straight, anthracene-like edges (edge-type B, often called "zig-zag" edges) and represents the second possible way of cutting a regular hexagonal structure out of an infinite benzenoid sheet. Each carbon-carbon bond in members of this series (and series C and D as well) is perpendicular to a pair of edges. Edges are aligned with the  $\langle 11\bar{2}0 \rangle$  crystal directions.

The finding that molecules with B-edges are less stable than molecules with A-edges is consistent with the general finding that "straight-edge" polyaromatic structures are less stable and have fewer Kekulé structures than do "bent" structures. For example, in the isomerization of anthracene to phenanthrene,  $\Delta H = -6 \pm 2 \text{ kcal mol}^{-1}$  [11] and the number of Kekulé structures increases from four to five.

Series C, while closely related to series B in structure, actually approaches the same asymptotic value of KSPE as does the most stable series A. This finding suggests that the relative orientation of bonds and edges, in itself, is not a factor determining resonance stability.

The stability of series D falls between that of B and C and approaches an intermediate limit for KSPE. Relative stabilities of series C and D

are opposite to predictions of group additivity [12], although as pointed out earlier, these stabilities are in accord with Clar's arguments [10].

It appears that the stability of a benzenoid layer cannot be properly rationalized in terms of separate contributions from edge structures and interior rings. The degree of coupling (conjugation) between edge and interior atoms can be a dominant factor and is directly reflected in the present determinations of KSPE.

We now consider reactivity. Reactivity will be analyzed in terms of electron localization energies, which are energies required to isolate a  $\pi$ -electron from the rest of the conjugated system. For the very large species of concern in this work, SRT was found to be inadequate for this purpose because according to SRT these values are determined as a small difference between the two very large resonance energy terms. This difference was found to slowly diverge as  $n_{\pi} \rightarrow \infty$ , even when a more complex form of SRT was used [8c]. Therefore, we have examined reactivity using a method which circumvents the above problem by treating chemical reactions as perturbations. In this method, localization energies  $\delta E_{\pi}$  for  $\pi$ -electrons are estimated by applying first-order perturbation theory to the Hückel molecular orbitals [7]. These energies can be expressed as functions of numbers of Kekulé structures,

$$\delta E_{\pi} = 2\beta \frac{KS(M)}{\sqrt{\sum_{\substack{\text{all alternant} \\ \text{C-atoms, } i}} (KS^i(R\cdot))^2}}$$

where  $KS(M)$  is the number of Kekulé structures in the reactant molecule,  $KS^i(R\cdot)$  is the number of Kekulé structures in a molecule derived from the reactant by localizing two of its electrons, one at the reaction site

and the other at position  $i$ , and  $\beta$  is the Hückel resonance integral (a semiempirical, adjustable parameter).

In Figure 3 are given representations of  $\delta E_\pi$  for two polyaromatic layers, one with edge-type A, the other with edge-type B. Activation energies for chemical reaction at the position of electron localization are often considered to be linearly related to  $\delta E_\pi$ , so that the smaller the  $\delta E_\pi$  value, the greater the reactivity.

In the more stable layer (A), reactivity is predicted to be quite uniform throughout the layer, even at the edges, although regions of alternating reactivity can be seen near the edges. For the less stable layer (B), edge atoms are far more reactive than interior atoms, and edge reactivity increases toward the center of each edge. Clearly A, which is predicted to be more thermodynamically stable than B, is also far less reactive.

Additional calculations on members of series A and B show that the average of all  $\delta E_\pi$  values approaches zero as molecules increase in size. Average reactivities are therefore predicted to increase and approach one another with increasing size and, in accord with experiment, large graphitic layers are predicted to always be highly reactive. However, relatively unreactive sites near the edges are found to approach non-zero  $\delta E_\pi$  values and the overall increase in reactivity with increasing size is particularly slow for the most stable series (A). For both molecules given in Figure 3, both the most and least reactive positions are located near the edges. In the more stable molecule (A),  $\delta E_\pi$  for these two positions are  $1.41 \beta$  and  $2.31 \beta$ , while for the less stable molecule (B) these values are  $0.484 \beta$  and  $2.28 \beta$ . For comparison,  $\delta E_\pi$  for benzene is

2.31  $\beta$  and for the most reactive position in anthracene (the 9-position) the value is 1.26  $\beta$ . It is particularly noteworthy that rather large, highly condensed polyaromatic molecules need not be any more reactive than anthracene.

The above results are consistent with the idea derived from HMO calculations that in an arbitrarily large graphite layer, the least stable occupied energy level approaches the most stable unoccupied level [2] (two-dimensional graphite is a zero-gap semi-conductor). The general finding that "zig-zag" edges are more reactive than "armchair" edges is also borne out by a good deal of experimental data [13].

The present calculations yield, as byproducts of the above reactivity calculations, HMO odd-electron densities [7]. At carbon atom  $i$  in a free radical, these densities are simply proportional to the quantity,  $[KS^i(R\cdot)]^2$ . These electron densities are shown in Figure 4 for radicals formed by localizing an electron at an interior carbon atom in each of the two molecules examined in Figure 3.

These densities are highly non-uniform even at large distances from the position of initial electron localization. Odd-electron densities are greatest at the carbon atoms nearest the position of localization and for localization at any interior site they assume the characteristic profiles shown in Figure 4. On the other hand, variations of electron density more than several C-C bonds away from the localized electron depend primarily on the detailed edge structures. Also, as the size of the graphitic plane increases, the probability of finding the odd-electron in the region nearby the localized electron is predicted to diminish to zero.

We postpone presenting a more detailed analysis of reactivity and electron density until we have parameterized the present calculations using results of more accurate theories. This work is now in progress.

In summary, we have shown that it is practical to apply reliable theories for  $\pi$ -electrons in benzenoid systems to very large, well-defined graphitic planes. Initial results of these calculations show that when viewed as members of homologous series these planes can be examined in a systematic manner. The degree of coupling between edge and interior rings can be a particularly important factor whose magnitude can not always be estimated by simple comparisons to small polyaromatic molecules.

#### Acknowledgment

Support for this work by the Gas Research Institute and the Air Force Office of Scientific Research is gratefully acknowledged.



# References and Notes

1. Younkin, J. M.; Smith, L. J.; Compton, R. N. *Theoret. Chim. Acta* 1976, 41, 157.
2. Coulson, C. A.; Schaad, L. J.; Burnelle, L. *Proc. 3rd Biennial Carbon Conf.*, 1958, p. 27.
3. Pullman, B. *ibid*, p. 3.
- 4a. Zunger, A. *Phys. Rev. B* 1978, 17, 626.
- b. Dovesi, R.; Pisani, C.; Roetti, C. *Int. J. Quantum Chem.* 1980, 17, 517.
- c. Kortela, E-K.; Maure, R., *J. Phys. C.* 1974, 7, 1749.
5. Numbers of Kekulé structures and non-bonding molecular orbital (NBMO) coefficients are closely related (see for example reference 7).
6. Brown, R. L., *J. Computational Chem.* 1983, 4, 556.
7. Heilbronner, E.; Bock, H., "The HMO Model and its Application", Wiley-Interscience, New York, 1976.
8. Herndon, W. C. *Isr. J. Chem.* 1980, 20, 270; b) *J. Org. Chem.* 1975, 40, 3583; c) *ibid* 1981, 46, 2119.
9. Swinborne-Sheldrake, R.; Herndon, W. C. *Tetrahedron Lett.* 1975, 10, 755; Herndon, W. C.; Ellzey, M. L., Jr. *J. Amer. Chem. Soc.* 1974, 96, 6631.
10. Clar, E. J., "Polycyclic Hydrocarbons", Vol. 1, Academic Press, New York, 1964, pp. 37-38.
11. Cox, J. D.; Pilcher, G., "The Thermochemistry of Organic and Organometallic Compounds", Academic Press, New York, 1970.
12. Stein, S. E.; Golden, D. M.; Benson, S. W., *J. Phys. Chem.* 1977, 81, 314.
- 13a. Lewis, I. C.; Edstrom, T. *J. Org. Chem.* 1963 28, 2050.

b. Madison, J. J.; Roberts, R. M. Ind. Eng. Chem. Fundam. 1963, 50, 237.

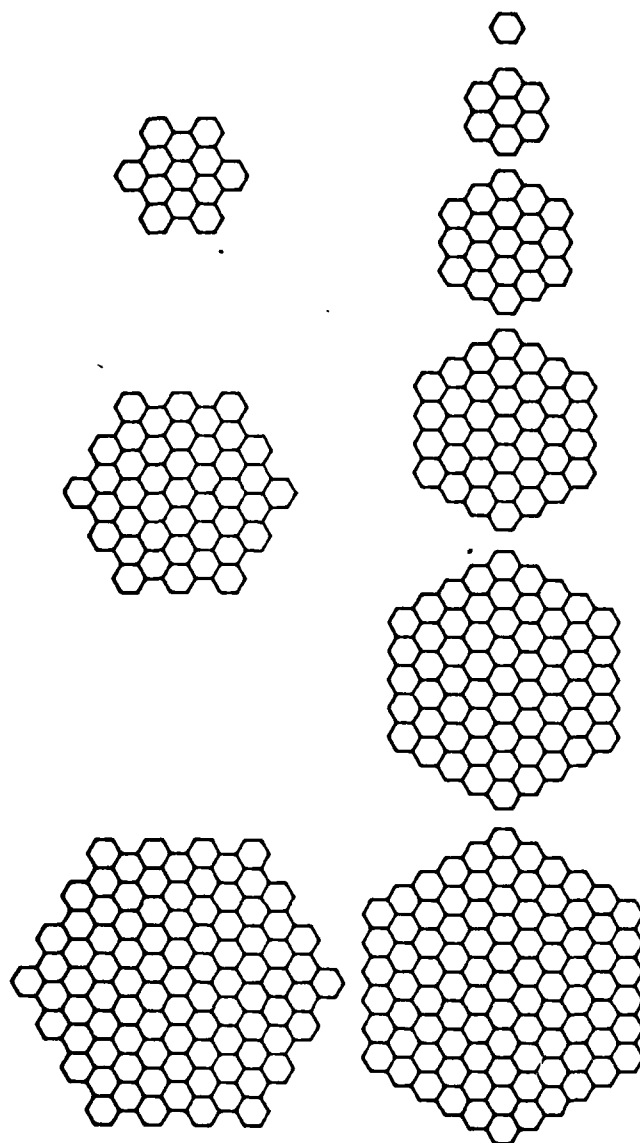
c. Herndon, W. C. Tetrahedron, 1983, 38, 1389, and references therein.

Figure 1. Two Examples of Homologous Series Studied.

Figure 2. Stabilities of Hexagonal Benzenoid Layers.  $n_\pi$  is the total number of  $\pi$ -electrons, KSPE is the number of Kekulé structures per  $\pi$ -electron (for benzene  $n_\pi = 6$ , the number of Kekulé structure is 2,  $\text{KSPE} = 2^{1/6} = 1.12$ , and  $\ln(\text{KSPE}) = 0.116$ ). Edge structures of series A-D are given in the text. The three series with edge C contain different corner structures ( $\square = \text{I}$ ;  $\nabla \equiv \text{II}$   $\circ = \text{III}$ ). For other edges, only series with the most stable corner structures are shown. Intercepts at  $n_\pi^{-1/2} = 0$  were obtained by least squares analyses of the points shown.

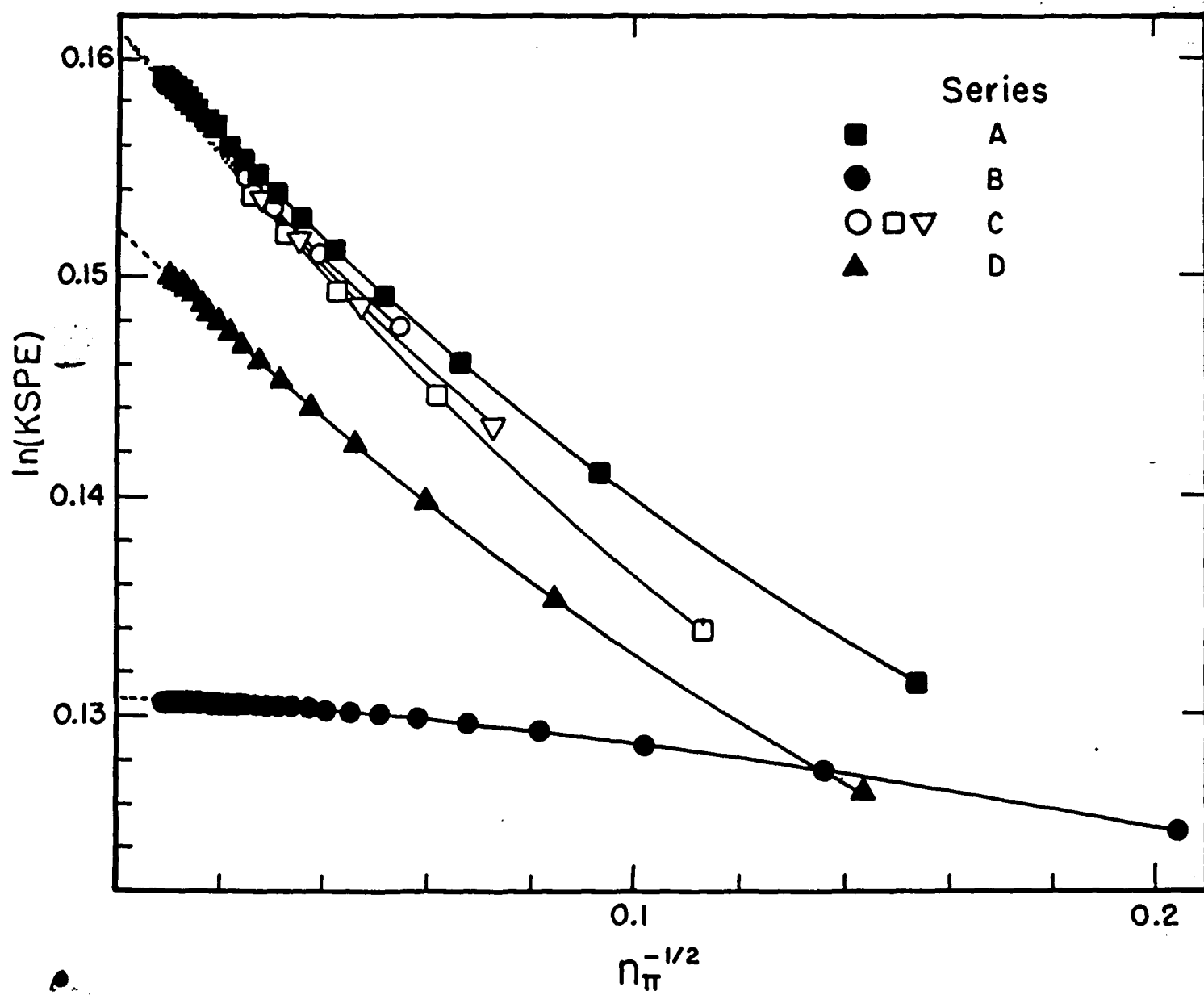
Figure 3. PMO Localization Energies. Structure A represents a member of the most stable series (series A,  $n_\pi = 222$ ) and structure B represents a member of the least stable series of comparable size (series B,  $n_\pi = 216$ ). Areas of circles are proportional to  $\delta E_\pi$ , hence the smaller the circle, the greater the reactivity.

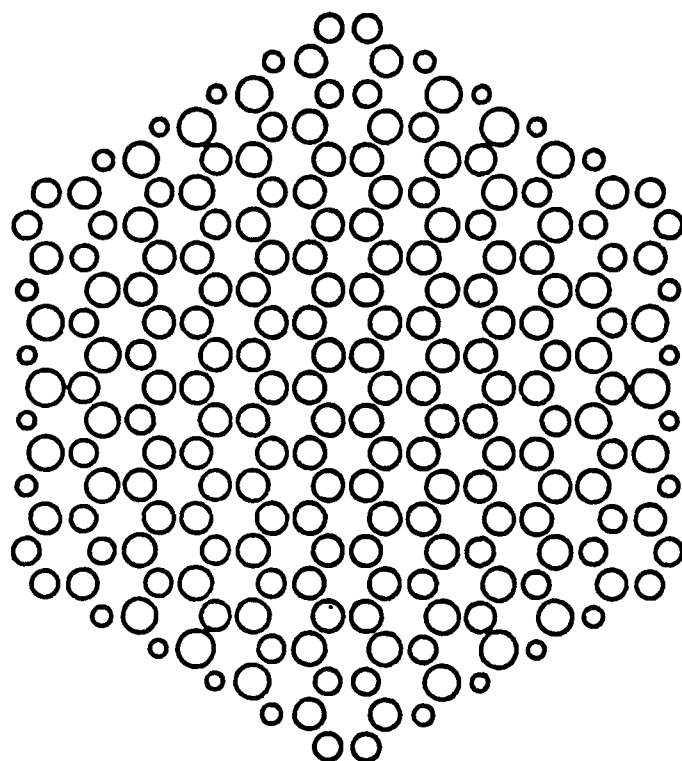
Figure 4. HMO Electron Densities. These species are the free radicals obtained by localizing an electron in the molecules represented in Figure 3 at the position denoted by the cross. Areas of circles are proportional to HMO electron densities. Note that half of the carbon atoms in these molecules, including the position of localization, have zero HMO electron densities.



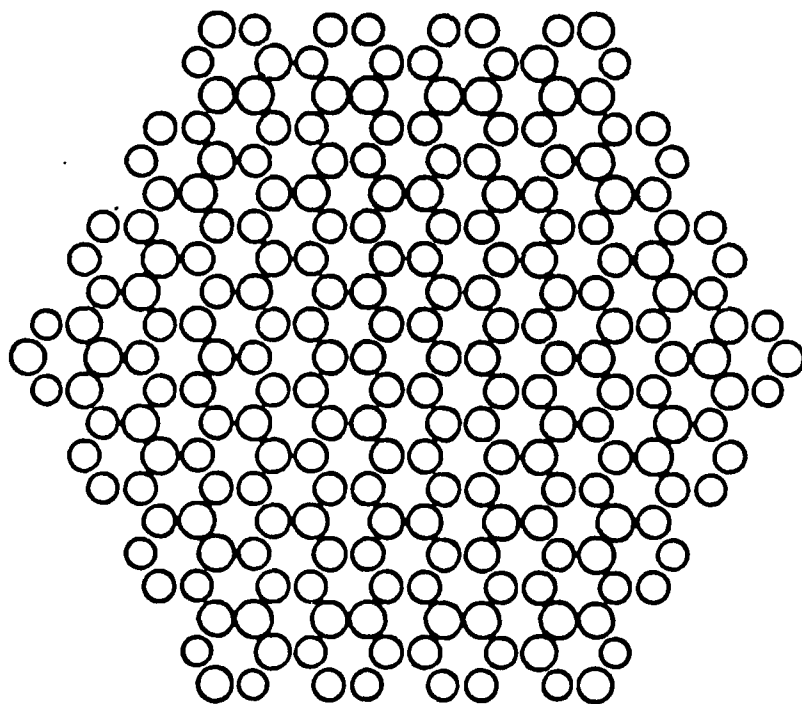
Series A

Series B





b



a

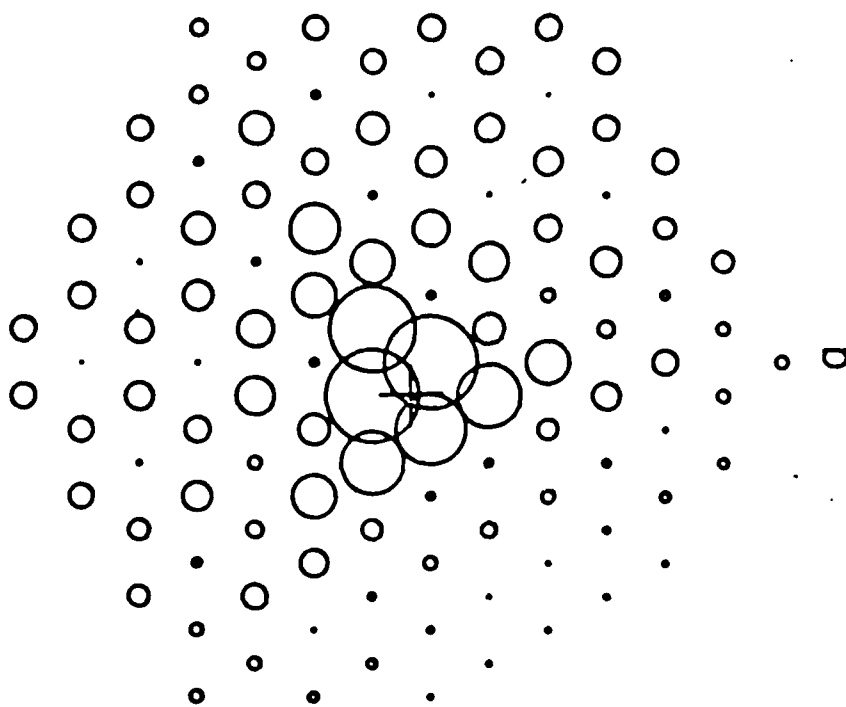
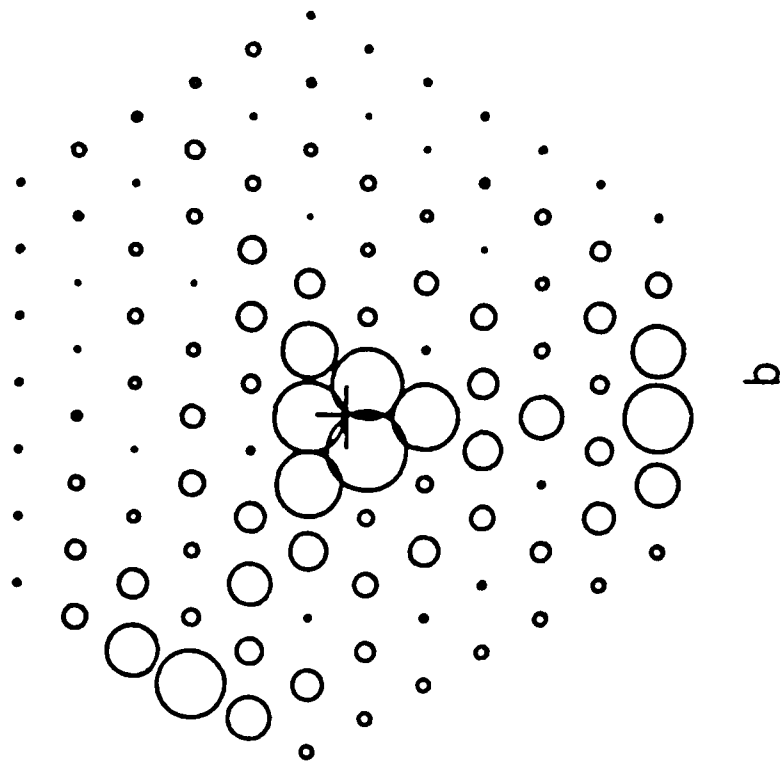


fig. 4

5. BUILD-UP AND IRRADIATION OF OBSCURING CLOUDS UNDER NEAR-VACUUM CONDITIONS:  
APPLICATION TO SPACECRAFT SURVIVABILITY

Thomas J. Buckley and Sharon G. Lias

Center for Chemical Physics  
National Bureau of Standards  
Gaithersburg, Maryland 20899



by the rate constants for the corresponding ion-molecule collisions) determined in the ICR for the initial steps of some of the sequences. Experimental or estimated heats of formation of relevant ionic and neutral species are listed in Table 2. As in previous studies of successive ionic condensation processes in unsaturated hydrocarbon systems, it is seen that the probability that a collision leads to the formation of a product ion diminishes as the size of the reactant ion is increased.

It is striking that (except for  $C_4H_2^+$ ) the  $C_{2n}H_n^+$  reactant ions of sequence 14 exhibit two populations, one reactive (leading to the formation of the next ion in the sequence) and one which does not react with diacetylene. The  $C_{2n+2}H_n^+$  ions of sequence 15, on the other hand, do not exhibit unreactive populations.

Experimentally, little independent information is available about the structures or thermochemistry of  $C_{2n}H_n^+$  ions, but it is possible from our general knowledge of ion thermochemistry to speculate about the nature of the reactive and unreactive  $C_{2n}H_n^+$  populations of ions observed in the high pressure experiments. Several possibilities exist for the structure of such ions, the simplest of which are the straight chain isomers containing triple and double bonds such that a 2:1 carbon-hydrogen ratio is achieved. For example, the formal addition of a C-H bond of one  $HC\equiv C-C\equiv CH$  entity across the triple bond of another would result in the straight chain  $C_8H_4^+$  isomer,  $HC\equiv C-C\equiv C-CH=CH-C\equiv CH^+$ . (Such  $C_{2n}H_n^+$  isomers always have two more triple bonds than double bonds.) These acyclic ions would be expected to

product ion intensities associated with sequence 14 divided by the sum of all of the product ion intensities associated with sequence 15. The ratio decreases rapidly at lower number densities, reflecting the increased probability for elimination of  $C_2H_2$  from  $[C_8H_4^+]^*$  (process 7b). This is consistent with the ICR results, since sequence 14 was not observed under the very low pressure conditions of those measurements. Since Figure 1B essentially gives the stabilization/decomposition ratio as a function of collision frequency, the curve may be used to give an order-of-magnitude approximation of the dissociative half-life of  $[C_8H_4^+]^*$ . The formulation is based on a set of conditions where the rate of  $C_2H_2$  elimination (sequence 15) is equal to the rate of stabilization (sequence 14). The assumptions are that the rate constant for collision of  $[C_8H_4^+]^*$  with  $C_4H_2$  is  $10^{-9} \text{ cm}^3 \cdot \text{molecule}^{-1} \cdot \text{s}^{-1}$  and that every collision is effective in quenching loss of  $C_2H_2$ . The equations required are quite straightforward and will not be presented here. Taking 0.008 torr as the pressure at which the stabilization /decomposition ratio is unity ((Figure 1B), the dissociative half-life for process 7b is found to be  $\sim 4 \times 10^{-6} \text{ s}$  at 300 K. In view of the second assumption, this value certainly represents only a lower limit.

At the pressures of the ICR experiments, loss of  $H_2$  from the ions of sequence 14 or loss of  $C_2H_2$  from the ions of sequence 15 leads to another sequence involving fragment ions:

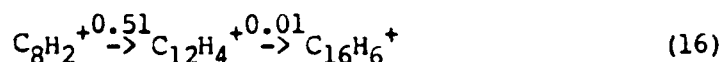
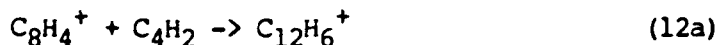
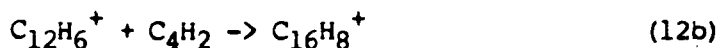


Table 1 summarizes the reaction sequences observed in diacetylene in the ICR and the high pressure mass spectrometer, and lists the thermochemistry of the initial steps of the ion-molecule reaction mechanisms, as well as the rate constants and reaction efficiencies (i.e. rate constants divided

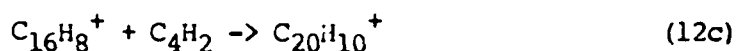
condensation ion, does occur, but the minor channel 7c, the loss of  $H_2$  which presumably requires extensive rearrangement, is entirely quenched. The  $C_8H_4^+$  ion exhibits two (or more) structures, one of which condenses with diacetylene,



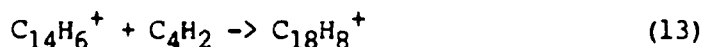
while the other isomer (or isomers) is/are unreactive. A fraction of the  $C_{12}H_6^+$  ions react to form  $C_{16}H_8^+$ :



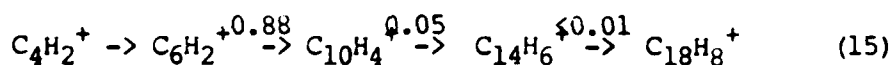
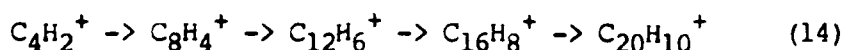
which in turn reacts to give  $C_{20}H_{10}^+$ :



Processes 8b and 8c initiated by the  $C_6H_2^+$  ion are not observed at high pressures, where all the  $C_{10}H_4^+$  condensation ions are stabilized; in the further reaction of this ion with diacetylene, the dissociation process represented in reaction 10 is not observed, but rather all the  $C_{14}H_6^+$  condensation ions are stable. These react further with diacetylene to give  $C_{18}H_8^+$ :



In reactions 7 through 13 one can recognize two parallel sequences, which can be summarized as follows from the results of Figure 1:



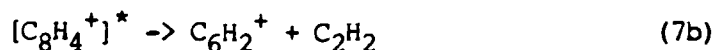
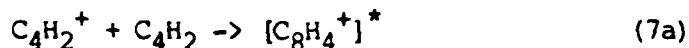
where the neutral reactant molecule is always diacetylene, and the probability of a reactive collision, based on the rate constants given in Table 1, is as indicated.

Figure 1B gives the ratio of the probabilities of sequences 14 and 15 as a function of diacetylene pressure. The points are taken from the same data used to construct Figure 1A, and are plotted as the sum of all of the

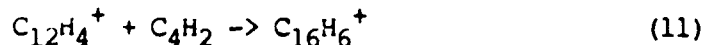
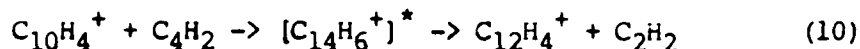
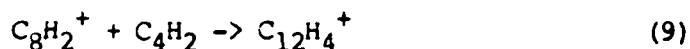
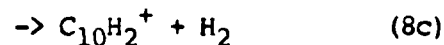
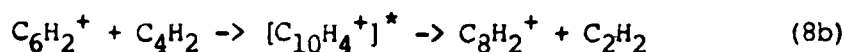
## Results and Discussion

### Diacetylene

The abundances of ions generated in diacetylene were observed as a function of time in the ICR at a total pressure of  $\sim 5 \times 10^{-6}$  torr. The results demonstrated the occurrence of the initial condensation/dissociation mechanisms:



which are followed by the sequences:



In the ICR experiments, where the collision interval lies in the range 2 ms - 5 ms and the ions are observed for 300-500 ms, the number of condensation steps which can be observed is limited by the total number of ion-molecule collisions observable on that time scale,  $\sim 50$ -200. Figure 1A shows the normalized abundances of ions observed in diacetylene in the NBS high pressure mass spectrometer as a function of the pressure of diacetylene at 300 K. In these experiments, the collision interval is approximately  $10^{-6}$  s, and the time scale of the experiment is such that charged species undergo many thousands of collisions. The results demonstrate that under these conditions, reaction 7b, the loss of acetylene from the initial

publication of earlier studies on ionic condensation processes in unsaturated hydrocarbons. Furthermore, recent photoelectron spectroscopy experiments and studies of radiative and non-radiative processes in unsaturated hydrocarbon ions have elucidated details of the excited states available to such condensation ions, as well as the relevant fluorescence lifetimes and quantum yields<sup>10</sup>.

In the present study, details of successive condensation and association reactions in two pressure regimes,  $-10^{-6}$  torr (in an ICR), and  $-10^{-2}$  torr (in a high pressure mass spectrometer) will be examined and compared. Most attention will be given to reactions occurring in diacetylene, for which reliable information about the thermochemistry, as well as the excited states and emission lifetimes of the parent radical cations and relevant condensation ions is available<sup>10</sup>. An attempt will be made to apply this new body of information to the interpretation of condensation/association processes in polyacetylenic organic compounds.

#### Experimental

The experiments were carried out on the NBS ion cyclotron resonance spectrometer (ICR) and the NBS high pressure photoionization mass spectrometer, both of which have been described before<sup>11,12</sup>. In the ICR, ionization was effected by 30 eV electrons; in the high pressure experiments, the mass spectrometer was equipped with an argon resonance lamp, which provides 11.6-11.8 eV photons.

A very high vacuum chamber equipped with a quartz window was installed on the ICR instrument to permit photodissociation studies of trapped ions. The photodissociation experiments reported here were carried out with a pulsed tunable dye laser which delivers photons of 400-700 nm.

publication of earlier studies on ionic condensation processes in unsaturated hydrocarbons. Furthermore, recent photoelectron spectroscopy experiments and studies of radiative and non-radiative processes in unsaturated hydrocarbon ions have elucidated details of the excited states available to such condensation ions, as well as the relevant fluorescence lifetimes and quantum yields<sup>10</sup>.

In the present study, details of successive condensation and association reactions in two pressure regimes,  $\sim 10^{-6}$  torr (in an ICR), and  $\sim 10^{-2}$  torr (in a high pressure mass spectrometer) will be examined and compared. Most attention will be given to reactions occurring in diacetylene, for which reliable information about the thermochemistry, as well as the excited states and emission lifetimes of the parent radical cations and relevant condensation ions is available<sup>10</sup>. An attempt will be made to apply this new body of information to the interpretation of condensation/association processes in polyacetylenic organic compounds.

#### Experimental

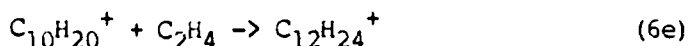
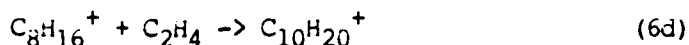
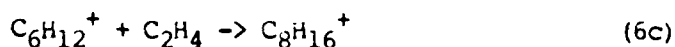
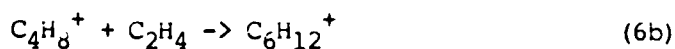
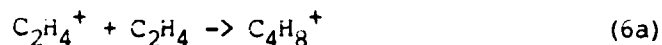
The experiments were carried out on the NBS ion cyclotron resonance spectrometer (ICR) and the NBS high pressure photoionization mass spectrometer, both of which have been described before<sup>11,12</sup>. In the ICR, ionization was effected by 30 eV electrons; in the high pressure experiments, the mass spectrometer was equipped with an argon resonance lamp, which provides 11.6-11.8 eV photons.

A very high vacuum chamber equipped with a quartz window was installed on the ICR instrument to permit photodissociation studies of trapped ions. The photodissociation experiments reported here were carried out with a pulsed tunable dye laser which delivers photons of 400-700 nm.

collision interval is very long requires that the ion have some means of energy dissipation, such as photoemission:



Little is known about emission from ions formed in condensation reactions, although a number of possibilities have been considered<sup>3</sup>. Condensation reactions have also been suggested to play an important role in the chemistry occurring in hydrocarbon flames. Specifically, a mechanism proposed for the initiation of soot formation in hydrocarbon flames<sup>4</sup>, requires that small ions, e.g.  $C_3H_3^+$ , condense with neutral hydrocarbon molecules such as acetylene to form larger ions which in turn condense, leading eventually to terminal ions with benzenoid polyaromatic structures<sup>5</sup>. A conceptual difficulty associated with the ionic condensation mechanisms which have been advanced is that, at the temperatures of 300-700 K used in mass spectrometric studies, the rate constants of successive addition steps tend to decrease as the size of the reacting condensation ion increases. For example, the rate constants for the successive condensations:

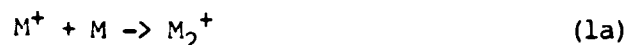


at 300 K are, respectively,  $10^{-9}$ ,  $2 \times 10^{-12}$ ,  $8 \times 10^{-13}$ ,  $2 \times 10^{-13}$ , and  $8 \times 10^{-14}$   $\text{cm}^3/\text{molecule-s}$ <sup>6</sup>. Rate constants for exothermic ion-molecule reactions show no temperature dependence or a negative temperature dependence<sup>7</sup>.

A large body of information about the thermochemistry<sup>8</sup>, structures, and isomerization mechanisms<sup>9</sup> of ions has become available since the

## Introduction

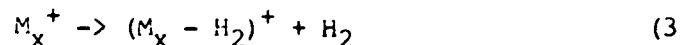
It is well known that the parent radical cations of olefins and acetylenes, or polyolefinic and polyacetylenic compounds undergo consecutive condensation reactions with the precursor compound in the gas phase, leading to higher molecular weight dimeric or polymeric ions:



It is also common that hydrocarbon condensation ions formed with excess energy dissociate by loss of H atoms:



or  $H_2$ :



or smaller unsaturated molecules:



Systematic studies<sup>1</sup> of condensation reactions in olefins have shown that the structure of the neutral molecule is the dominant factor in determining the overall reaction sequence in the system, and that 1-olefins are more reactive than 2- or 3-olefins. In some systems, particle transfer from the dimer ion to the neutral molecule has also been observed<sup>1d</sup>, e.g. H-atom transfer in 1-butene, or  $H_2$  transfer in isobutene.

Various questions of scientific and practical interest arise with regard to an examination of such condensation processes and accompanying bimolecular and unimolecular reactions. It has been suggested that ion-molecule condensation processes may be involved in the production of large molecules in interstellar media<sup>2</sup>. However, at low pressures (such as those characteristic of a space environment) the survival of a condensation ion formed in a highly exothermic process under conditions such that the



a. CONSECUTIVE ION-MOLECULE CONDENSATION REACTIONS AND PHOTODISSOCIATION  
MECHANISMS OF CONDENSATION IONS IN POLYACETYLENIC COMPOUNDS

by

Thomas J. Buckley, L. W. Sieck, Ricardo Metz and Sharon G. Lias

Center for Chemical Physics  
National Bureau of Standards  
Gaithersburg, Maryland 20899

and

Joel F. Liebman

Department of Chemistry  
University of Maryland Baltimore County  
Catonsville, Maryland

Abstract

Consecutive ion-molecule condensation and condensation/dissociation reactions in diacetylene, cyanoacetylene, and cyanogen have been examined in an ion cyclotron resonance spectrometer at pressures of  $\sim 10^{-6}$  torr, and in a high pressure photoionization mass spectrometer at pressures of  $\sim 10^{-2}$  torr.

Under the high pressure conditions in diacetylene, the initial reaction of the diacetylene radical cation with diacetylene generates  $C_6H_2^+$  and  $C_8H_4^+$  ions which then react further with neutral diacetylene, initiating the two parallel series of reactions: ( $C_6H_2^+ \rightarrow C_{10}H_4^+ \rightarrow C_{14}H_6^+ \rightarrow C_{18}H_8^+$ ) and ( $C_8H_4^+ \rightarrow C_{12}H_6^+ \rightarrow C_{16}H_8^+ \rightarrow C_{20}H_{10}^+$ ). The ions of the second sequence all show two populations, one of which is reactive, one unreactive with diacetylene. At the lower pressures of the ICR experiment, most of the  $C_8H_4^+$  ions dissociate to give ( $C_8H_2^+ + H_2$ ), so the second sequence is not seen. In its place, one sees the sequence: ( $C_8H_2^+ \rightarrow C_{12}H_4^+ \rightarrow C_{16}H_6^+$ ); both  $C_8H_2^+$  and  $C_{12}H_4^+$  are also generated in the system by loss of acetylene from the  $C_{n+2}H_n^+$  ions of the sequence initiated by reaction of  $C_6H_2^+$ . When the system is irradiated by 600 nm photons, the  $C_{12}$  and  $C_{10}$  ions dissociate by loss of acetylene or diacetylene to regenerate lower molecular weight ions; the  $C_8$ ,  $C_6$ , and  $C_4$  ions are not dissociated by photons of this energy. From these results, and similar series initiated by protonated diacetylene,  $C_4H_3^+$ , inferences are made about the heats of formation of observed ions. Rate constants are reported for the first few steps of the condensation processes; the initial condensation reaction of the parent diacetylene is efficient, but it is seen that the probability of a reactive collision decreases as the size of the reacting ion increases.

In contrast to the numerous condensation/dissociation processes observed in diacetylene, parent radical cations generated in cyanoacetylene and cyanogen mainly undergo simple consecutive addition processes with their respective parent molecules: ( $M^+ \rightarrow M_2^+ \rightarrow M_3^+ \rightarrow \text{etc.}$ ). Rate constants are reported for the first few steps of the condensation sequences, and it is seen that the reactions are slow.

PROTON AFFINITIES OF  $\text{HC}\equiv\text{C}-\text{C}\equiv\text{CH}$ ,  $\text{HC}\equiv\text{C}-\text{C}\equiv\text{N}$  and  $\text{N}\equiv\text{C}-\text{C}\equiv\text{N}$ :  
EXPERIMENTAL AND AB INITIO STUDIES

by

Michael Meot-Ner (Mautner) and Thomas J. Buckley

Center for Chemical Physics  
National Bureau of Standards  
Gaithersburg, Maryland 20899

and

Carol A. Deakyne

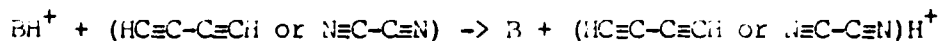
Department of Chemistry  
College of the Holy Cross  
Worcester, Massachusetts 01610

Abstract

The proton affinity of  $\text{HC}\equiv\text{C}-\text{C}\equiv\text{N}$  was determined in the NBS pulsed high pressure mass spectrometer through measurements of equilibrium constants for proton transfer reactions with bases of known gas basicity:



The proton affinity was determined to be 180 kcal/mol. Since protonated diacetylene,  $\text{C}_4\text{H}_3^+$ , and protonated cyanoacetylene,  $\text{C}_3\text{H}_2\text{N}^+$ , undergo fast reactions with the respective precursor molecules, proton transfer equilibria could not be established in these systems. Therefore, the proton affinities of  $\text{HC}\equiv\text{C}-\text{C}\equiv\text{CH}$  and  $\text{N}\equiv\text{C}-\text{C}\equiv\text{N}$  have been determined in the NBS pulsed ion cyclotron resonance spectrometer (ICR) using the technique known as "bracketing", in which one determines the occurrence or non-occurrence (and in the former case, the efficiency) of the reactions:

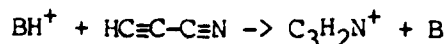


for a series of bases, B, of known gas basicity. From these results one can estimate the energy at which the protonation of the compound of interest is thermoneutral, and thereby obtain the proton affinity value. The results led to a value of 180 kcal/mol for the proton affinity of diacetylene, and 154 kcal/mol for cyanogen.

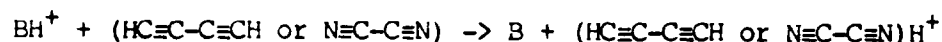
The proton affinities of these molecules reflect the stabilizing or destabilizing effects of the multiple triple bonds and the highly polar  $-\text{C}\equiv\text{N}$  groups in the relevant molecules and ions; these interactions are studied through ab initio calculations presented here.

has resulted in a paper, "Proton Affinities of  $\text{HC}\equiv\text{C}-\text{C}\equiv\text{CH}$ ,  $\text{HC}\equiv\text{C}-\text{C}\equiv\text{N}$  and  $\text{N}\equiv\text{C}-\text{C}\equiv\text{N}$ : Experimental and ab initio Studies", by Michael Meot-Ner (Mautner), Thomas J. Buckley, and Carol A. Deakyne, which is now being prepared for publication.

The proton affinity of  $\text{HC}\equiv\text{C}-\text{C}\equiv\text{N}$  was determined in the NBS pulsed high pressure mass spectrometer through measurements of equilibrium constants for proton transfer reactions with bases of known gas basicity:



The proton affinity was determined to be 180 kcal/mol. Since protonated diacetylene,  $\text{C}_4\text{H}_3^+$ , and protonated cyanoacetylene,  $\text{C}_3\text{H}_2\text{N}^+$ , undergo fast reactions with the respective precursor molecules, proton transfer equilibria could not be established in these systems. Therefore, the proton affinities of  $\text{HC}\equiv\text{C}-\text{C}\equiv\text{CH}$  and  $\text{N}\equiv\text{C}-\text{C}\equiv\text{N}$  have been determined in the NBS pulsed ion cyclotron resonance spectrometer (ICR) using the technique known as "bracketing", in which one determines the occurrence or non-occurrence (and in the former case, the efficiency) of the reactions:



for a series of bases, B, of known gas basicity. From these results one can estimate the energy at which the protonation of the compound of interest is thermoneutral, and thereby obtain the proton affinity value. The results led to a value of 180 kcal/mol for the proton affinity of diacetylene, and 154 kcal/mol for cyanogen.

The structures, isomerization mechanisms, and reaction kinetics of  $C_6H_7^+$  ions formed in the reactions ( $H_2C=C=CH_2^+ + H_2C=C=CH_2$ ) and ( $HC\equiv CCH_3^+ + HC\equiv CCH_3$ ), as well as the fragment  $C_6H_7^+$  ions in 1,3-cyclohexadiene, 1,4-cyclohexadiene, trans-1,3,5-hexatriene, 1-methylcyclopentene, 3-methylcyclopentene, and 4-methylcyclopentene have been studied. In all these systems the ions exhibit at least two structures. One isomer transfers a proton to bases with proton affinity higher than that of benzene demonstrating that this species has the benzenium (protonated benzene) structure. The remaining  $C_6H_7^+$  ions have in some systems (e.g. allene<sup>+</sup> + allene, 1- and 4-methylcyclopentene) a conjugate base having a proton affinity of 202 kcal/mol, while in other systems (e.g. 3-methylcyclopentene, trans-1,3,5-hexatriene) the conjugate base of the non-benzenium isomer has a proton affinity of 205 kcal/mol. When the  $C_6H_7^+$  ions are formed by fragmentation of a  $C_6H_8^+$  ion (in the cyclohexadienes or 1,3,5-hexatriene) which has a well-defined internal energy, it is seen that the fraction of  $C_6H_7^+$  ions exhibiting the benzenium structure decreases with increasing energy. The fraction of ions with the benzenium structure also decreases with increasing internal energy of the ( $C_3H_4^+ + C_3H_4$ ) reaction complex from 0.72 in allene (energy level of separated reactants: 315 kcal/mol) to 0.62 in propyne (energy level of separated reactants: 327 kcal/mol).

The energetics of the fragmentation process leading to  $C_6H_7^+$  formation have been examined in a photoion-photoelectron coincidence spectrometer for trans-1,3,5-hexatriene, and 1,3- and 1,4-cyclohexadiene. It is found that the transition state for the fragmentation process [ $C_6H_8^+ \rightarrow C_6H_7^+ + H$ ] is effectively the same in all three systems but lies at an energy level higher than (benzenium ion + H) products.

Rate constants for reactions of benzenium ions with a variety of organic and inorganic compounds have been determined.

An offshoot of the study of ionic mechanisms in diacetylene, cyanoacetylene, and cyanogen (described above) was a determination of the proton affinities of these molecules. Proton affinity determinations lead to information about the thermochemical properties of protonated molecules. Such data are of interest in an understanding of the ion-molecule chemistry in obscurant clouds for spacecraft protection, since  $H^+$  is present in the upper atmosphere. The experiments gave results which reflected the stabilizing or destabilizing effects of the multiple triple bonds and the highly polar  $-C\equiv N$  groups in the relevant molecules and ions, and thus are of theoretical interest. The experimental study was therefore combined with a calculation study. This

by Thomas J. Buckley, L. W. Sieck, Ricardo Metz and Sharon G. Lias (currently in NBS internal editorial review, to be submitted to the International Journal of Mass Spectrometry and Ion Processes), deals specifically with this problem area for the systems listed above.

In diacetylene, the initial reaction of the diacetylene radical cation with diacetylene generates  $C_6H_2^+$  and  $C_8H_4^+$  ions which then react further with neutral diacetylene, initiating the two parallel series of reactions: ( $C_6H_2^+ \rightarrow C_{10}H_4^+ \rightarrow C_{14}H_6^+ \rightarrow C_{18}H_8^+$ ) and ( $C_8H_4^+ \rightarrow C_{12}H_6^+ \rightarrow C_{16}H_8^+ \rightarrow C_{20}H_{12}^+$ ). The ions of the first sequence all show two populations, one of which is reactive, one unreactive with diacetylene. At lower pressures most of the  $C_8H_4^+$  ions dissociate to give ( $C_6H_2^+ + H_2$ ), and the first sequence is not seen. In its place, one sees the sequence: ( $C_8H_2^+ \rightarrow C_{12}H_4^+ \rightarrow C_{16}H_6^+$ ); both  $C_8H_2^+$  and  $C_{12}H_4^+$  are also generated in the system by loss of acetylene from the  $C_{n+2}H_n^+$  ions of the sequence initiated by reaction of  $C_6H_2^+$ . When the system is irradiated by 600 nm photons, the  $C_{12}$  and  $C_{10}$  ions dissociate by loss of acetylene or diacetylene to regenerate lower molecular weight ions; the  $C_8$ ,  $C_6$ , and  $C_4$  ions have no dissociative paths available at this energy. From these results, and similar series initiated by protonated diacetylene,  $C_4H_3^+$ , inferences are made about the heats of formation of observed ions. Rate constants are reported for the first few steps of the condensation processes; the initial condensation reaction of the parent diacetylene is efficient, but it is seen that the probability of a reactive collision diminishes as the size of the reacting ion increases.

In contrast to the numerous condensation/dissociation processes observed in diacetylene, parent radical cations generated in cyanoacetylene and diacetylene mainly undergo simple consecutive addition processes with their respective parent molecules: ( $M^+ \rightarrow M_2^+ \rightarrow M_3^+ \rightarrow$  etc.). The only fragmentation process seen is in the cyanoacetylene system where a fraction of the initially-generated dimer ions dissociate by loss of an H atom: ( $C_6H_2N_2^+ \rightarrow C_6HN_2^+ + H$ ). None of the  $M_n^+$  ions generated in cyanoacetylene or cyanogen are dissociated by 600 nm photons. Rate constants are reported for the first few steps of the condensation sequences, and it is seen that the reactions are inefficient.

An examination of analogous processes in 1,3,5-hexatriene,  $H_2C=\overset{H}{C}=\overset{H}{C}=\overset{H}{C}=CH_2$ , led to an independent study of the fragment  $C_6H_7^+$  ions formed in this compound. (These ions were found to be the only initiators of condensation sequences in 1,3,5-hexatriene.) The accompanying manuscript, "Structures of  $C_6H_7^+$  Ions Formed in Unimolecular and Bimolecular Reactions" by Sharon G. Lias and P. Ausloos (J. Chem. Phys., submitted for publication), describes this work.

BUILD-UP AND IRRADIATION OF OBSCURING CLOUDS UNDER NEAR-VACUUM CONDITIONS:  
APPLICATION TO SPACECRAFT SURVIVABILITY

Annual Report  
FY 84

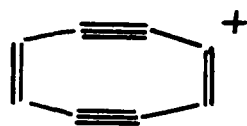
Thomas J. Buckley and Sharon G. Lias

Center for Chemical Physics  
National Bureau of Standards  
Gaithersburg, Maryland 20899

In FY 84, three related studies concerned with a molecular level understanding of processes occurring in organic systems appropriate for use as obscuring clouds have been completed and have been, or are being, prepared for publication in the archival literature. Preprints of two of these manuscripts are attached, and an abstract of the third study (manuscript in preparation) is also included.

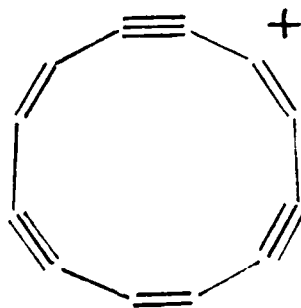
The major emphasis of this project during the past two years has been an examination of gas phase ionic reaction mechanisms leading to the build-up of long polyunsaturated carbon chain ions in hydrogen deficient systems such as diacetylene ( $\text{HC}\equiv\text{C}-\text{C}\equiv\text{CH}$ ), cyanoacetylene ( $\text{HC}\equiv\text{C}-\text{C}\equiv\text{N}$ ), and cyanogen ( $\text{N}\equiv\text{C}-\text{C}\equiv\text{N}$ ). Since carbonaceous materials are of interest as coatings for spacecraft, and laser-induced vaporization of such coating materials will generate organic gases and vapors which may undergo ionization through charge transfer processes with ions present in the ionosphere or through photoionization, the problem area addressed is that of the condensation processes occurring in a near-vacuum, as well as the photon-induced dissociation processes and the ensuing mechanisms leading to the re-building of the large condensation ions. The first manuscript, "Consecutive Ion-Molecule Condensation Reactions and Photodissociation Mechanisms of Condensation Ions in Polyacetylenic Compounds"

display a reactivity similar to that of other linear unsaturated hydrocarbon ions, such as the parent  $\text{HC}=\text{C}=\text{C}=\text{CH}^+$  cation, and therefore the reactive isomers probably correspond to such structures. The simplest cyclic structures which can be envisioned are the dehydro-[n]-annulenes of the type:  $(-\text{C}=\text{C}-\text{CH}=\text{CH}-)_{n/4}$ , a cyclic hydrocarbon with an equal number of alternating triple and double bonds (I):



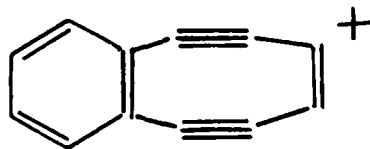
I

For the  $\text{C}_{12}$ -homologues, a structure analogous to I (II):



I'

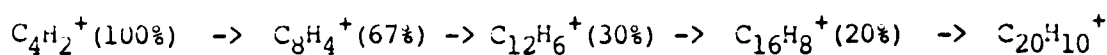
or a benzo-substituted analogue of I (III):



III

are possible cyclic structures. Although these structures may appear

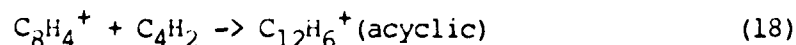
improbable, it should be noted that both  $C_{12}H_6$  isomers are known<sup>17</sup>, and the  $C_8H_4$  compound has been described as representing a "reasonable synthetic goal"<sup>17</sup>. The linear ions initially formed in the ion-molecule condensation process would presumably rearrange to form such structures only if the heats of formation were significantly lower than those of the corresponding acyclic isomers. Comparing estimated heats of formation of these cyclic  $C_{2n}H_n^+$  ions with corresponding heats of formation of the acyclic isomers (Table 2), it can be seen that the cyclic ions are expected to be more stable by 15-60 kcal/mol. This is not surprising, since a triple bond has been replaced by a single and a double bond. The relative abundance of the reactive isomers (which we assume to be the acyclic structure) diminishes as the size of the ions increases; from the results of Figure 1 one can estimate the reactive populations as follows:



This trend would be predicted from the thermochemical results summarized in Table 2. For example, while the first step in the sequence:



is exothermic by 73 kcal/mol, the second step:



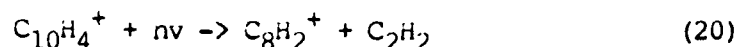
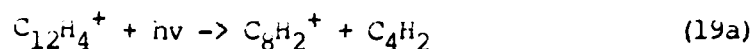
is exothermic by only approximately 53 kcal/mol, i.e. the subsequent condensation steps leading to the reactive acyclic species become less and less energetically favorable as the size of the molecules increases. On the other hand, the thermochemical estimations given in Table 2 predict that the exothermicity associated with the formation of the cyclic product ions from acyclic reactants increases slightly for succeeding steps in the series, as shown in Table 1.

The comparison of the results observed in the ICR at  $10^{-6}$  torr and



those from the high pressure mass spectrometric experiments at  $10^{-2}$  -  $10^{-1}$  torr indicates that the dissociative lifetime for the excited  $[\text{C}_8\text{H}_4^+]^*$  and  $[\text{C}_{14}\text{H}_6^+]^*$  ions is shorter than  $10^{-3}$  s but longer than  $10^{-6}$  s. The  $\text{C}_{10}\text{H}_4^+$  condensation ions survive long enough to be observed in the ion cyclotron resonance experiments, even though exothermic dissociative paths (reactions 8a and 8b) are available. If such long dissociative lifetimes seem surprising for species which originate in some cases with 50-100 kcal/mol excess energy, it should be remembered that the ions may be formed in upper electronic states; the work of Maier et al.<sup>10</sup> has shown that such polyunsaturated hydrocarbon ions usually fluoresce from upper excited levels with high quantum yields ( $>0.7$ ). The fluorescence lifetimes are usually in the ns range.

The ions formed in the diacetylene system were irradiated in the ICR with 600 nm (2.065 eV) photons, and the photodissociation mechanisms of some of the condensation ions were observed:



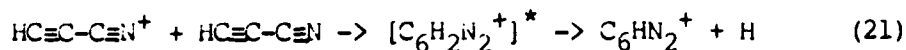
From these results, we can assign lower limits to the heats of formation of the  $\text{C}_{12}\text{H}_4^+$ ,  $\text{C}_{10}\text{H}_2^+$ , and  $\text{C}_{10}\text{H}_4^+$  condensation ions formed in diacetylene of  $>502$ ,  $>496$ , and  $>447$  kcal/mol, respectively. (The upper limits on the heats of formation of these ions given in Table 2 are based simply on the assumption that the reaction in which the ion is formed as a condensation product is exothermic.) The  $\text{C}_4\text{H}_2^+$  and  $\text{C}_6\text{H}_2^+$  ions were not dissociated by 600 nm photons. This was an expected result, since it is predicted that there are no dissociative pathways available to these ions at energies below about 6 eV.

In a related study<sup>13</sup> carried out in this laboratory, the proton

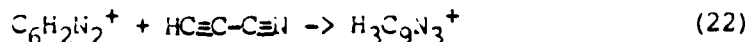
affinity of diacetylene was determined to be 180 kcal/mol, corresponding to a heat of formation for  $C_4H_3^+$  of 295 kcal/mol. The condensation/dissociation sequences initiated by this ion are entirely analogous to those initiated by reactions of the parent  $C_4H_2^+$  ion, i.e. the condensation ions dissociate by loss of  $H_2$  or acetylene. These reaction sequences, along with the corresponding exothermicities, rate constants and reaction efficiencies are listed in Table 3.

#### Cyanoacetylene and Cyanogen

Cyanoacetylene is isoelectronic to diacetylene, and has a similar conjugated triple bonded structure. However, while diacetylene has no dipole moment, cyanoacetylene is highly polar, with a dipole moment of 3.6 D. The abundances of ions were observed in cyanoacetylene in the ICR as a function of time (pressure,  $10^{-6}$  torr) and in the high pressure mass spectrometer as a function of pressure (i.e. in both cases as a function of number of ion-molecule collisions undergone). The latter results are shown in Figure 2. The major reaction channel of the parent cyanoacetylene ion with cyanoacetylene is the formation of a dimer ion, but a minor channel, observed in the ICR, is condensation followed by dissociation, in this case loss of an H atom:

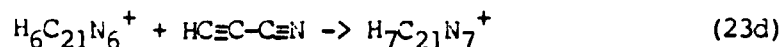
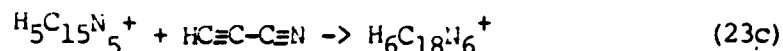
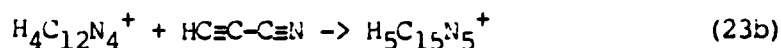
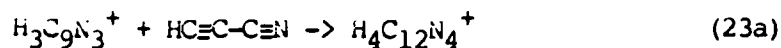


The loss of acetylene from the condensation ion is not observed, and in fact, this dissociation process is estimated to be slightly endothermic (by approximately 6 kcal/mol). The dimer ions add to cyanoacetylene:

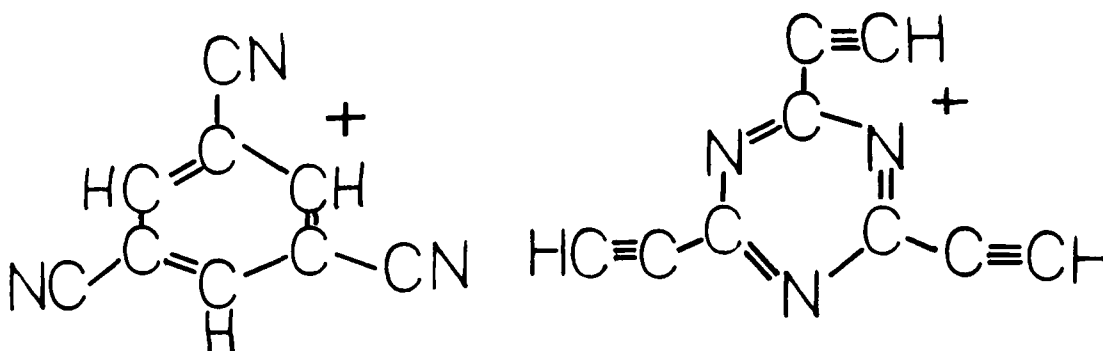


The rate constants determined in the ICR for reactions 21 and 22 are listed

in Table 4. The probability for a reactive ( $\text{HC}\equiv\text{C}-\text{C}\equiv\text{N}^+ + \text{HC}\equiv\text{C}-\text{C}\equiv\text{N}$ ) collision is much lower than for the analogous parent ion-neutral molecule collisions in the diacetylene system. The results obtained in the high pressure mass spectrometer (Figure 2) demonstrate the occurrence of the consecutive addition processes:



with the exception of the last two ions, which are still growing in at the highest pressures used in these experiments, all the ions except  $\text{H}_3\text{C}_9\text{N}_3^+$  are seen to decline in abundance due to further reaction. The  $\text{H}_3\text{C}_9\text{N}_3^+$  ions which do not react may have rearranged to some stable structure such as IV or V:



IV

V

Under the conditions of the ICR experiments, there was no evidence for an unreactive population of  $\text{H}_3\text{C}_9\text{N}_3^+$  ions.

The ion-molecule reactions observed in cyanogen, which is also isoelectronic to the other compounds studied here, are summarized in Table 5. It is seen that the parent ion adds to the neutral molecule to form a dimer, which in turn adds to form a trimer, and on the time scale of the

ICR experiments, a further addition to form a tetramer is observed. No dissociations of the product ions to form different ionic products occur, and the reactions are all inefficient.

The nature of the prevailing chemistry seen in cyanoacetylene and cyanogen, e.g. simple addition of ions to the neutral molecule, is different from that described above for diacetylene, where observed reactions include isomerizations and dissociations of the condensation ions to form new ionic species. In the hydrocarbon systems, as discussed above, excited ions may lose excess energy by emitting a photon, a mechanism which stabilizes the excited condensation ions and extends their lifetime vis-a-vis dissociation to regenerate the original reactants. In cyanoacetylene and cyanogen, the results of Maier et al<sup>10</sup> have demonstrated that radiative pathways are unavailable (that is, the fluorescence quantum yields are  $<10^{-3}$ ). These authors have suggested that the lack of detectable radiative channels in these compounds may result from the existence of close-lying doublet states which lead to a preference for internal conversion pathways. In our experiments, it appears that the ions in cyanoacetylene and cyanogen tend to dissociate to re-form the reactant species, possibly because the collision complexes retain excess vibrational energy, and therefore are short-lived.

### Conclusions

It has been shown that parent radical cations generated in diacetylene undergo a condensation reaction to generate  $C_8H_4^+$  which dissociate at pressures of  $\sim 10^{-6}$  torr to give  $C_8H_2^+$  and  $C_6H_2^+$  ions which, in turn initiate successive condensation sequences (processes 14 and 15) leading to high molecular weight polyunsaturated product ions. At pressures of  $\sim 10^{-2}$  torr, the dissociation to give  $C_8H_2^+$  is entirely quenched, and the initial

$C_8H_4^+$  condensation ions add to diacetylene generating a sequence of product ions of the formula  $C_{2n}H_n^+$ ; these ions display two populations, one of which is reactive with diacetylene and one of which is not. It is postulated that the reactive populations are acyclic isomers, while the unreactive populations represent ions which have undergone ring closure. It has been demonstrated that the latter process is a thermodynamically favorable channel, which becomes increasingly favored with increasing chain length. The initial steps in the condensation sequences have rate constants which are close to the collision rate, and succeeding steps become increasingly slow. Cyanoacetylene and cyanogen radical cations add to their respective neutral molecules predominantly to generate simple dimers, trimers, tetramers, etc., without important dissociation steps leading to other channels. In cyano-acetylene certain of the condensation ions (especially  $C_9H_3N_3^+$ ) do apparently rearrange to structures which are unreactive with the parent molecules. In these systems all the condensation reactions have a low probability of being observed upon the occurrence of an ion-molecule collision.

It is postulated that the existence of radiative pathways in the conjugated polyene-yne ions of the diacetylene system leads to stabilized condensation ions, and increases the efficiency of the reaction sequences. The lack of such pathways<sup>10</sup> in the diacetylene and cyanogen systems, on the other hand, increases the probability that a condensation ion formed with excess energy will dissociate to regenerate the original reactant species.

#### Acknowledgements

This work was supported by the Air Force Office of Scientific Research. The preliminary experiments were carried out by Dr. Pierre Ausloos.

## References

1. See for example: (a) J. M. S. Henis, *J. Chem. Phys.* **52**, 282 (1970); (b) J. M. S. Henis, *J. Chem. Phys.* **52**, 292 (1970); (c) Z. Luczynski and J. A. Herman, *Int. J. Mass Spectrom. Ion Phys.* **31**, 237 (1979); (d) A. Podgorski and J. A. Herman, *Int. J. Mass Spectrom. Ion Phys.* **34**, 125 (1980).
2. (a) A. Dalgarno and J. H. Black, *Rep. Prog. Phys.* **39**, 573 (1976); (b) E. Herbst and W. Klemperer, *Phys. Today* **29**, 32 (1976); (c) E. Herbst and W. Klemperer, *Phys. Today* **26**, 505 (1973); (d) W. T. Huntress, *Chem. Soc. Rev.* **6**, 295 (1977).
3. (a) V. G. Anicich, G. A. Blake, W. T. Huntress, and M. T. Bowers, *Chem. Phys. Lett.* **75**, 278 (1980); (c) L. M. Bass, P. R. Kemper, V. G. Anicich, and M. T. Bowers, *J. Am. Chem. Soc.* **103**, 5283 (1981).
4. (a) H. F. Calcote, *Comb. and Flame* **42**, 215 (1981); (b) D. B. Olson and H. F. Calcote in "Particulate Carbon: Formation During Combustion" (D. C. Siegla and G. W. Smith, Eds.), Plenum, New York, (1981) p. 177.
5. S. E. Stein, *Comb. and Flame* **51**, 357 (1983).
6. P. Kebarle and R. M. Haynes, *J. Chem. Phys.* **47**, 1676 (1967).
7. M. Meot-Ner (Mautner) in "Gas Phase Ion Chemistry" (M. T. Bowers, Editor), Vol II, Academic Press, Inc., (1979).
8. S. G. Lias, J. F. Liebman, J. E. Bartmess, J. L. Holmes, and R. D. Levin, *J. Phys. Chem. Ref. Data*, in preparation: The thermochemical data on ions presented in this evaluated compilation is based on experimental results summarized in (a) H. M. Rosenstock, K. Draxl, B. W. Steiner, and J. T. Herron, *J. Phys. Chem. Ref. Data* **6**, Suppl. 1 (1977); (b) R. D. Levin and S. G. Lias, *Natl. Stand. Ref. Data Ser.*, *Natl. Bur. Stand. (U. S.)*, **71** (1982); (c) S. G. Lias, J. F. Liebman, and R. D. Levin, *J. Phys. Chem. Ref. Data*, in press.
9. For a recent review, see: G. S. Groenewold and M. L. Gross in "Ionic Processes in the Gas Phase" (M. A. Almoester Ferreira, Ed.), D. Reidel Publ. Co. (1984), pp. 243-265.
10. (a) M. Allan, E. Kloster-Jensen, and J. Maier, *Chem. Phys.* **7**, 11 (1976); (b) J. P. Maier, M. Ochsner, and F. Thommen, *Faraday Disc. Chem. Soc.* **75**, 77 (1983); (c) J. P. Maier, D. Klapstein, S. Leutwyler, L. Misev, and F. Thommen in "Ionic Processes in the Gas Phase" (M. A. Almoester Ferreira, Ed.) D. Reidel Publ. Co. (1984), pp. 159-178; (d) M. Allan, E. Heilbronner, E. Kloster-Jensen, and J. P. Maier, *Chem. Phys. Letters* **41**, 29 (1976).
11. (a) S. G. Lias, J. R. Eyler, and P. Ausloos, *Int. J. Mass Spectrom. Ion Phys.* **19**, 219 (1976); (b) S. G. Lias and T. J. Buckley, *Int. J. Mass Spectrom. Ion Proc.* **56**, 123 (1984).

12. (a) L. W. Sieck, S. K. Searles and P. J. Ausloos, J. Am. Chem. Soc. 91, 7627 (1969); (b) L. W. Sieck and S. K. Searles, J. Am. Chem. Soc. 92, 2937 (1970).
13. (a) T. Su and M. T. Bowers, Int. J. Mass Spectrom. Ion Phys. 17, 309 (1975); (b) W. J. Chesnavich, T. Su, and M. T. Bowers in "Kinetics of Ion-Molecule Reactions" (P. Ausloos, Ed.), Plenum (1979), p. 165.
14. M. Meot-Ner (Mautner), T. J. Buckley, and C. A. Deakyne, J. Chem. Phys. in preparation.
15. See for example: (a) J. L. Beauchamp, Ann. Rev. Phys. Chem. 22, 5277 (1971); (b) S. G. Lias and P. Ausloos in "Ion-Molecule Reactions: Their Role in Radiation Chemistry", Am. Chem. Soc., Washington, D.C. (1975), pp. 91-95.
16. H. M. Rosenstock, J. Dannacher, and J. F. Liebman, Radiat. Phys. Chem. 20, 7 (1982).
17. T. L. Chan, N. Z. Chang, and F. Sondheimer, Tetrahedron 39, 427 (1983).
18. T. D. Gierke, H. L. Tigelaar, and W. H. Flygare, J. Am. Chem. Soc. 94, 330 (1972).

Table 1. Ion-molecule reactions in diacetylene: Thermochemistry, rate constants, and reaction efficiencies.

Reaction	$\Delta H^a$ kcal/mol	$k_{Rn}^b$	$k_{Rn}/Z^c$
<u>Condensation-Dissociation Sequences Seen in ICR</u>			
$C_4H_2^+ + C_4H_2 \rightarrow \text{Products}$ $C_4H_2^+ + C_4H_2 \rightarrow [C_8H_4^+]^* \rightarrow C_6H_2^+ + C_2H_2$ $\quad \quad \quad \rightarrow C_8H_2^+ + H_2$	-8 -12	13.9 $\pm$ 0.5	1.06
$C_6H_2^+ + C_4H_2 \rightarrow \text{Products}$ $C_6H_2^+ + C_4H_2 \rightarrow [C_{10}H_4^+]^* \rightarrow C_8H_2^+ + C_2H_2$ $\quad \quad \quad \rightarrow C_{10}H_2^+ + H_2$	-5 -2	10.6 $\pm$ 0.4	0.88
$C_{10}H_4^+ + C_4H_2 \rightarrow [C_{14}H_6^+]^* \rightarrow C_{12}H_4^+ + C_2H_2$		0.5	0.05
<u>Condensation Sequence:</u> $C_4H_2^+ \rightarrow C_8H_4^+ \rightarrow C_{12}H_6^+ \rightarrow C_{16}H_8^+ \rightarrow C_{20}H_{10}^+$			
$C_4H_2^+ + C_4H_2 \rightarrow C_8H_4^+ \text{ (Acyclic, 67\% )}$ $\quad \quad \quad \rightarrow C_8H_4^+ \text{ (Cyclic, 33\% )}$	-73 -88		
$C_8H_4^+ \text{ (Acyclic) } + C_4H_2 \rightarrow C_{12}H_6^+ \text{ (Acyclic, 30\% )}$ $\quad \quad \quad \rightarrow C_{12}H_6^+ \text{ (Cyclic, 70\% )}$	-53 -99		
$^dC_{12}H_6^+ \text{ (Acyclic) } + C_4H_2 \rightarrow C_{16}H_8^+ \text{ (Acyclic, 20\% )}$ $\quad \quad \quad \rightarrow C_{16}H_8^+ \text{ (Cyclic, 80\% )}$			
$^dC_{16}H_8^+ \text{ (Acyclic) } + C_4H_2 \rightarrow C_{20}H_{10}^+$			
<u>Condensation Sequence:</u> $C_4H_2^+ \rightarrow C_6H_2^+ \rightarrow C_{10}H_4^+ \rightarrow C_{14}H_6^+ \rightarrow C_{18}H_8^+$			
$^dC_6H_2^+ + C_4H_2 \rightarrow C_{10}H_4^+$	-24 $\pm$ 29		
$^dC_{10}H_4^+ + C_4H_2 \rightarrow C_{14}H_6^+$			
$^dC_{14}H_6^+ + C_4H_2 \rightarrow C_{18}H_8^+$			
<u>Fragment Ion Condensation Sequence:</u> $C_8H_2^+ \rightarrow C_{12}H_4^+ \rightarrow C_{16}H_6^+$			
$C_8H_2^+ + C_4H_2 \rightarrow C_{12}H_4^+$	-20 $\pm$ 24	5.8	0.51
$C_{12}H_4^+ + C_4H_2 \rightarrow C_{16}H_6^+$		<0.1	<0.01



Footnotes to Table 1.

<sup>a</sup>See Table 2.

<sup>b</sup>Rate constants in  $\text{cm}^3/\text{molecule-s} \times 10^{-10}$  determined in the ICR; cited rate constants are for loss of reactant ion (i.e. include all channels).

<sup>c</sup>Probability that a collision results in observable reaction; collision rate constants,  $Z$ , calculated from AQO formulation in reference 13a. The quadrupole moment of  $\text{C}_4\text{H}_2$  taken as  $10 \times 10^{-26}$  esu  $\text{cm}^2$  (see ref. 18).

<sup>d</sup>Observed in high pressure mass spectrometer only.

Table 2. Summary of Heats of Formation of Ions and Molecules.

Species	$\Delta H_f$ kcal/mol	Ref.
$\text{HC}\equiv\text{C}-\text{C}\equiv\text{CH}$	109	8
$\text{HC}\equiv\text{CH}$	54	8
$\text{HC}\equiv\text{C}-\text{C}\equiv\text{N}$	90	8
$\text{N}\equiv\text{C}-\text{C}\equiv\text{N}$	73	8
$\text{HC}\equiv\text{C}-\text{C}\equiv\text{CH}^+$	344	8
$\text{HC}\equiv\text{C}-\text{C}\equiv\text{C}-\text{C}\equiv\text{CH}^+$	391	8
$\text{HC}\equiv\text{C}-\text{C}\equiv\text{C}-\text{C}\equiv\text{C}-\text{C}\equiv\text{CH}^+$	-441	8
$\text{HC}\equiv\text{C}-\text{C}\equiv\text{C}-\text{CH}=\text{CH}-\text{C}\equiv\text{CH}^+$	-380	Est <sup>a</sup>
$\text{C}-\text{C}_6\text{H}_4^+$ (I)	-365	Est <sup>b</sup>
$\text{C}_{10}\text{H}_2^+$	>496, <500	See Discussion
$\text{C}_{10}\text{H}_4^+$	>447, <504	See Discussion
$\text{C}_{12}\text{H}_4^+$	>502, <554	See Discussion
$\text{C}_{12}\text{H}_6^+$ (Acyclic)	-436	Est <sup>c</sup>
(Cyclic II)	-390	Est <sup>d</sup>
(Cyclic III)	-375	Est <sup>e</sup>
$\text{C}_4\text{H}_3^+$ (Protonated diacetylene)	299	14
$\text{C}_{10}\text{H}_3^+$	302	f
$\text{C}_9\text{H}_3^+$	312	f
$\text{HC}\equiv\text{C}-\text{C}\equiv\text{N}^+$	358	8
$\text{N}\equiv\text{C}-\text{C}\equiv\text{N}^+$	382	8
$\text{N}\equiv\text{C}-\text{C}\equiv\text{C}-\text{C}\equiv\text{N}^+$	400	8

<sup>a</sup>In all cases for which data are available, the reactions  $[\text{RCH}=\text{CH}_2 + \text{R}'\text{C}\equiv\text{CH} \rightarrow \text{RCH}=\text{CHC}\equiv\text{CR}']$  are approximately thermoneutral (+2 kcal/mol). Therefore, making the assumption of thermoneutrality for  $[\text{HC}\equiv\text{CCH}=\text{CH}_2 + \text{HC}\equiv\text{C}-\text{C}\equiv\text{CH} \rightarrow \text{HC}\equiv\text{C}-\text{C}\equiv\text{C}-\text{CH}=\text{CH}-\text{C}\equiv\text{CH}]$ , the heat of formation of  $\text{HC}\equiv\text{C}-\text{C}\equiv\text{C}-\text{CH}=\text{CH}-\text{C}\equiv\text{CH}$  is estimated as -178 kcal/mol. To arrive at a value for the ionization potential, it is seen (reference 7) that when a triple bond is replaced by a double bond, the ionization potential is decreased by 0.4 kcal/mol; from the value of 9.09 eV reported for the ionization potential of  $\text{C}_8\text{H}_2$

(reference 10d), one would predict an ionization potential of 8.7 eV for octa-1,3,7-triyne-5-ene. Furthermore, acyclic  $C_8H_4$  would be expected to have an ionization potential between that of 1,3,5,7-octatetrayne (9.09 eV) and 1,3,5,7-octatetraene (7.8 eV); interpolating linearly and taking into account the number of double and triple bonds, one obtains a value of ~8.8 eV. The estimated heat of formation of the acyclic  $C_8H_4^+$  ion is thus  $178 \text{ kcal/mol} + -7.75 \times 23.06 \text{ kcal/mol}$  or  $-380 \text{ kcal/mol}$ .

<sup>D</sup>From "macroincrementation" (reference 16). The heat of formation of cycloocta-1,5-diene-3,7-diyne is taken as equal to  $\Delta H_f(1,3,5,7\text{-cyclooctatetraene}) + \Delta H_f(1,5\text{-cyclooctadiyne}) - \Delta H_f(1,5\text{-cyclooctadiene}) + \Delta E(\text{planarization of } 1,3,5,7\text{-cyclooctatetraene and cyclooctadiene, assumed to be } 14 \text{ kcal/mol})$ . The inversion or planarization energy of cyclooctatetraene and cyclooctadiene are explicitly included since these molecules are known to exist preferentially in non-planar configurations, while both cyclic  $C_8H_4$  and its benzo-analog are planar. A value of 187 kcal/mol is estimated for the cyclooctadienediyne. The ionization potential of the dibenzo-analogue of I has been measured to be 7.7 eV. From the observation of the changes in ionization potentials of cyclic molecules and their benzo-analogues, this leads to an estimate of 7.9 eV for the IP of I. The resulting heat of formation of the ion is 365 kcal/mol.

<sup>C</sup>See comment a. The heat of formation of the acyclic  $C_8H_4$  + that of vinylacetylene leads to a value of -247 kcal/mol for an acyclic  $C_{12}H_6$  molecule. By reasoning analogous to that presented in comment a, this compound would be predicted to have an ionization potential of ~8.2 eV, and the acyclic  $C_{12}H_6^+$  ion would have a heat of formation of ~436 kcal/mol.

<sup>a</sup>The heat of formation of the neutral molecule with the structure of II is estimated from the heat of formation of but-1-ene-3-yne (vinylacetylene) (69 kcal/mol); since this molecule should be relatively strain-free, a straightforward estimate would lead to a value of  $3(69)$  or 207 kcal/mol. Taking into account anti-aromaticity, and estimating this contribution as  $12/8$  that of the anti-aromaticity estimated for cyclooctatetraene, or  $12/8 \times 14 \text{ kcal/mol}$ , one obtains 228 kcal/mol. A contribution of about 4 kcal/mol planarization energy brings the value to about 232 kcal/mol.

<sup>e</sup>The heat of formation of a species is increased by about 5 kcal/mol by the benzo-annulation of a non-aromatic double bond, and one might expect a similar trend with benzo-annulation of an anti-aromatic double bond. On this basis the heat of formation of the neutral molecule corresponding to structure III can be estimated from that of the molecule of structure I (see b) to be ~192 kcal/mol. The ionization potential is estimated from that of the dibenzo-analog to be approximately 7.9 eV.

<sup>f</sup>Based on the observation that the hydrogen affinities of structurally-related molecules are the same<sup>15</sup>. From the results presented here for diacetylene, the hydrogen affinities of polyacetylenic hydrocarbon ions are estimated to be ~101 kcal/mol, and therefore the heats of formation of  $C_6H_3^+$  and  $C_8H_3^+$  can be calculated from the known heats of formation of the  $C_6H_2^+$  and  $C_8H_2^+$  ions.

Table 3. Ion-molecule reactions initiated by  $C_4H_3^+$  in diacetylene: Thermochemistry, rate constants, and reaction efficiencies.

Reaction	$\Delta H^a$ kcal/mol	$k_{Rn}^b$	$k_{Rn}/Z^c$
$C_4H_3^+ + C_4H_2 \rightarrow$ Products		13.6	1.02
$\rightarrow C_6H_3^+ + C_2H_2$	-60		
$\rightarrow C_8H_3^+ + H_2$	-100		
$\rightarrow C_8H_5^+$			
$C_6H_3^+ + C_4H_2 \rightarrow$ Products		5.4	0.45
$\rightarrow C_8H_3^+ + C_2H_2$	-49		
$\rightarrow C_{10}H_5^+$			

<sup>a</sup>See Table 2.

<sup>b</sup>Rate constants in  $cm^3/molecule-s \times 10^{-10}$  determined in the ICR; cited rate constants are for loss of reactant ion (i.e. include all channels).

<sup>c</sup>Probability that a collision results in observable reaction; collision rate constants,  $Z$ , calculated from AQO formulation in reference 13a. The quadrupole moment of  $C_4H_2$  taken as  $10 \times 10^{-26}$  esu  $cm^2$  (see ref. 18).

times could be predicted assuming either a "benzene-like" /"cyclohexadiene-like" transition state or a "fulvene-like transition state" In order to fit the observed experimental results, the assumed transition states usually had to be "tighter" or "loosened" slightly by multiplying the transition state frequencies by some arbitrarily-chosen factor. The activation energies estimated in these calculations were not significantly different for the different closed-ring transition states assumed. The results are summarized in Table 1, and the calculated breakdown plots are shown as solid lines in Figures 2, 3, and 4. (Calculated breakdown plots were sufficiently close for the two assumed transition states that only one curve is shown in each Figure.) The results are also shown as the features of an assumed potential surface in Figure 1.

The energy levels of the transition states obtained from these results (Table 1) are identical for trans-1,3,5-hexatriene and 1,4-cyclohexadiene (275 kcal/mol at absolute zero) and slightly lower (272 kcal/mol) for 1,3-cyclohexadiene. Taking a value of 209 for the 0 Kelvin heat of formation of the benzenium ion, it is evident (Figure 1) that the transition states in all three systems lie at an energy level higher than that of the most probable products ( $\text{C}_6\text{H}_7^+ + \text{H}$ ) by 13 to 16 kcal/mol.

The question arises of whether the differences in the energy levels calculated for the transition states for trans-1,3,5-hexatriene and 1,4-cyclohexadiene compared to 1,3-cyclohexadiene are real. In view of (1) the errors involved in the analysis of the raw data (because of the estimates which had to be made to analyze the shapes of the time-of-flight peaks, and the resulting uncertainties in the position of the cross-over points) and (2) the fact that the matches of the calculated breakdown curves with the experimental points at energies other than the "cross-over" points are only approximate, it is likely that the differences are not significant and

no information about the vibrational frequencies of the  $C_6H_8^+$  ions are available, so vibrational frequencies of the corresponding neutral molecules were used<sup>13,14</sup>. (A comparison of the vibrational spectrum of ground state trans-1,3,5-hexatriene cations with the spectrum of the neutral molecule demonstrates that differences are small.)

The vibrational frequencies of the transition state, and the activation energy for the dissociation are variable parameters. The calculated "rate-energy curve" is used to predict the degree of fragmentation which would be observed at any particular energy and observation time, i.e. to calculate a breakdown curve for a particular sampling time; this calculation incorporates a convolution with the ion energy sampling function of the apparatus, as well as the room temperature rotational and vibrational energy distributions of the molecules in the starting sample. As described by Rosenstock et al<sup>9</sup>, one takes that value for the activation energy which correctly predicts the cross-over energies (energies at which 50% of the parent ions have dissociated) of the experimentally determined breakdown curves at the two different sampling times as the zero Kelvin onset energy for the fragmentation process. In the interpretation of the data reported here, the calculations incorporated three different assumed transition states, that is, three sets of assumed frequencies based on the vibrational frequencies of the corresponding molecules<sup>13-16</sup>: (a) a linear or "hexatriene-like" transition state; (b) a "benzene-like" or "cyclohexadiene-like" transition state; or (c) a "fulvene-like" transition state. The decomposition rates predicted based on the open-ring structure for the transition state were sufficiently fast in every case that the observed experimental results could not be modelled. The experimentally-observed cross-over energies for the two observation

as a function of photon energy in trans-1,3,5-hexatriene, 1,3-cyclohexadiene, and 1,4-cyclohexadiene, respectively. Franklin and Carroll<sup>12</sup> reported the formation of  $C_6H_6^+$  ions in the energy range covered here. However, in this and other studies<sup>3</sup> this fragment was not seen, in spite of the fact that the fragmentation to give ( $C_6H_6^+ + H_2$ ) is thermodynamically the lowest energy dissociation process.

The time dependence of process 8 was examined by recording the relative abundances of  $C_6H_8^+$  and  $C_6H_7^+$  at two different ion residence times, 1.22 and 6.20  $\mu s$ . It can be seen in the Figures that in all three cases, the degree of fragmentation at a particular energy is much greater for the larger ion source residence time (6.20  $\mu s$ ) as compared to 1.22  $\mu s$ . That is, in trans-1,3,5-hexatriene where considerable rearrangement is necessary to form the benzenium ion, and in the cyclohexadienes, where a simple C-H bond cleavage would give a benzenium ion, the H-loss process is relatively slow, occurring with a rate slower than  $1 \times 10^7 s^{-1}$  at energies near the experimental onset in all three cases.

The "breakdown curves" generated in the photoelectron-photoion coincidence experiments were interpreted by carrying out statistical calculations to model the dissociation as described before<sup>9</sup>. Briefly, following the determination of the energy dependence of the fragmentation process, a quasi-equilibrium (QET) calculation is carried out to predict the rate constant for the dissociation as a function of energy ("rate-energy curve"). As usual<sup>9</sup>, the vibrational frequencies of the dissociating parent radical cation are taken to be the same as the vibrational frequencies of the corresponding neutral molecule. In the systems studied here, an incomplete set of vibrational frequencies for the trans-1,3,5-hexatriene cation has been published<sup>11</sup>, and was utilized along with complementary frequencies from the molecule<sup>12</sup>, but for the cyclohexadienes,

with masses differing by only one mass unit and with TOF peaks overlapping, are not known with a high accuracy. However, a re-calculation of the data using an entirely different procedure to estimate the relative abundances (namely, just taking the two peak maxima as an indication rather than carrying out a detailed deconvolution) resulted in estimates of the relative abundances which were the same within  $\pm 5$  percent.

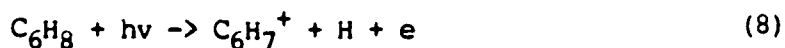
Over the energy range covered in these experiments (9.8-11.7 eV) no other fragmentation processes were observed in the systems studied. The experimental cross-over points were identified by carrying out a statistical analysis of the experimental curves traced by plotting the normalized abundances of the  $C_6H_8^+$  and  $C_6H_7^+$  ions. The relative abundances of the daughter and parent ions (masses 79 and 80) were each routinely corrected to account for  $^{13}C$ -substituted analogues (i.e. the abundance attributed to  $m/e$  79 was increased by 6.6%, and this increment was subtracted from the abundance attributed to  $m/e$  80, after which the residue at  $m/e$  80 was increased by 6.6%).

Allan, Dannacner and Maier<sup>3</sup> observed that trans-1,3,5-hexatriene polymerizes to give a dimer which dissociates to give  $C_6H_8^+$  ions at energies between 10 and 11 eV; because of this, the measurements on this compound were repeated with a fresh sample in order to verify the observed abundances of the ions.

## Results and Discussion

### Appearance Energies of $C_6H_7^+$ Ions in Selected $C_6H_8$ Compounds

Figures 2 through 4 show the relative abundances of the parent  $C_6H_8^+$  ions and the  $C_6H_7^+$  fragment ions formed in the process:





## Experimental

The experiments were performed using the NBS pulsed ion cyclotron resonance spectrometer which has been described previously<sup>8</sup>, and the photoelectron-photoion coincidence spectrometer, which has also been described<sup>9</sup>.

In the ICK experiments, two or more gases were admitted to the instrument through separate inlet systems, and the pressure was measured using an ionization gauge, which was calibrated for each gas against a capacitance manometer. Ion abundances were followed as a function of time using the detection system described elsewhere<sup>8,10</sup>. Ionization was effected by 40 eV electrons.

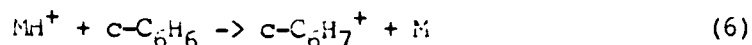
The time-of-flight peaks for the ions of masses 79 and 80 observed in the photoelectron-photoion coincidence experiments overlapped slightly. Each peak had a base width of about 90 nanoseconds (i.e. nine TOF channels), with an overlap of about 40 nanoseconds since the asymmetric daughter peak tended to tail towards the parent peak. It was therefore necessary to computationally separate the composite coincidence signal into contributions which could be attributed to the fragment and parent ions by observing the shapes of the signals which can be attributed to the individual ions, observed at energies where no fragmentation occurs ( $m/e$  80) or where all parent radical cations have dissociated ( $m/e$  79); the maxima of the two time-of-flight peaks were not in the overlap region. The shapes attributed to the TOF peaks were substantially the same in the three subject compounds, indicating that during the course of these experiments, the contributions to ions at masses 79 and 80 from the dissociation of higher molecular weight polymer impurities (as seen by Allan et al<sup>3</sup>) was not a serious problem. Obviously, the relative abundances of the two ions

(which are the precursors of the fragment ions of interest) with specific known amounts of internal energy through charge transfer reactions:



(where  $M$  is a species, such as a rare gas atom, with a well-established ionization energy). In the present study a similar approach is used to elucidate the structure(s) of the  $C_6H_7^+$  ions produced in the allene and propyne systems (reactions 1 and 2) and as a fragment ion in a variety of  $C_6H_8$  and  $C_6H_{10}$  compounds.

The kinetics and thermochemistry of the benzenium ion, assumed to be the predominant  $C_6H_7^+$  species formed in most systems<sup>1-3</sup>, are easily investigated, since ions which unequivocally have this structure can be generated by protonating benzene:



Taking a proton affinity of 179.5 kcal/mol for propylene<sup>6</sup> as the reference, the proton affinity of benzene is 181.3 kcal/mol<sup>6</sup>, and from the relationship:

$$\text{Proton affinity}(c-C_6H_6) = \Delta H_f(c-C_6H_6) + \Delta H_f(H^+) - \Delta H_f(c-C_6H_7^+) \quad (7)$$

the heat of formation of the benzenium ion at 298 K is 204 kcal/mol using the stationary electron convention (i.e. taking the 298 K heat of formation of the proton as 365.7 kcal/mol; the heat of formation of benzene is 19.3 kcal/mol). The corresponding 0 K heat of formation of the benzenium ion is 209 kcal/mol. Because appearance potential measurements of  $C_6H_7^+$  from a variety of compounds<sup>2,7</sup> led to values for the heat of formation of this ion of 220-233 kcal/mol, the appearance potentials of  $C_6H_7^+$  were redetermined in this study for various  $C_6H_8$  isomers using the photoelectron-photoion coincidence technique (PEPICO).

reactions 1 and 2 was presented in a recent photoionization mass spectrometry study<sup>1b</sup> of these systems. Since it was shown that the cross section for reaction 1 decreases when the allene ion has excess internal vibrational energy, whereas that of reaction 2 is unchanged by excess energy in the propyne ion, the authors postulated that the fragmentations of the  $[C_6H_6^+]$  ions to give  $C_6H_7^+$  involve an isomerization for which there is a barrier with a height such that the back reaction to regenerate reactants becomes competitive in the allene system, but not in the propyne system (where the initial energy level of the reactants is much higher). The suggested reaction coordinate diagram presented in that study is reproduced by the dotted line in Figure 1.

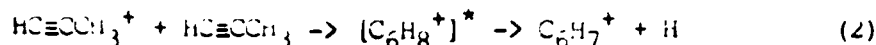
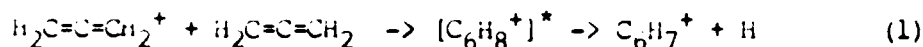
Recently<sup>5</sup>, the bimolecular reaction kinetics of ionic species have been used as a diagnostic tool for obtaining information about ion structures and isomerization mechanisms. In the simplest application, the presence of different isomers is indicated by the observation of two (or more) populations having differing reactivities with a particular neutral molecule (often the parent); in the event that one of these populations is entirely unreactive, the relative abundances of those species and the isomeric ions can be established from plots of ion abundance as a function of time. In many systems, the identities of isomeric ions can be established unambiguously through the kinetics of bimolecular reactions or through thermochemical information derived therefrom. For example, the acidity of an ion of interest can be determined in experiments in which one observes whether or not the ion transfers a proton to bases of known gas phase basicity:



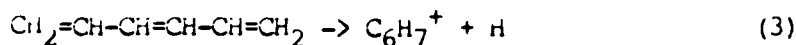
Furthermore, the effects of internal energy on isomerization mechanisms can be investigated in such experiments by forming the parent radical cations

## Introduction

A major ion formed in the fragmentation of a number of  $C_6H_8$  isomers is  $C_6H_7^+$ . Also, the formation of  $C_6H_7^+$  ions through the ion-molecule condensation-dissociation sequences:



is well known<sup>1</sup>. Although numerous structures are possible for  $C_6H_7^+$  entities, most studies to date have assumed, or presented evidence,<sup>1</sup> that the predominant  $C_6H_7^+$  formed in gas phase systems has the structure of protonated benzene, i.e. is the benzenium (or cyclonexadienyl) ion. For example, Franklin and Carroll<sup>2</sup> examined the fragmentation of trans-1,3,5-nexatriene to give  $C_6H_7^+$ :



They assigned a cyclic structure to the fragment ion, but noted that a fraction was probably acyclic. More recently, Allan, Dannacher and Maier<sup>3</sup> studied the same process for both the cis- and trans- isomers, using photoelectron-photoion coincidence spectroscopy and taking gas phase emission spectra of the cations. In a detailed analysis, they postulated that a cyclic  $C_6H_7^+$  ion is formed via a cyclic  $C_6H_8^+$  precursor, and that a second fragmentation pathway involves a linear vibrationally excited  $C_6H_8^+$  ion which cyclizes slowly prior to dissociating to give a cyclic product ion. Furthermore, recently cited collisional activation results<sup>4</sup> indicated that the fragmentation spectra of the  $C_6H_7^+$  ions produced in reactions 1 and 2 in the allene or propyne systems, respectively, were very similar and under the conditions of those experiments corresponded "to a large extent" to the spectrum of the benzenium ion.

A detailed consideration of the potential surface associated with

b. STRUCTURES OF  $C_6H_7^+$  IONS FORMED IN UNIMOLECULAR AND BIMOLECULAR REACTIONS

by

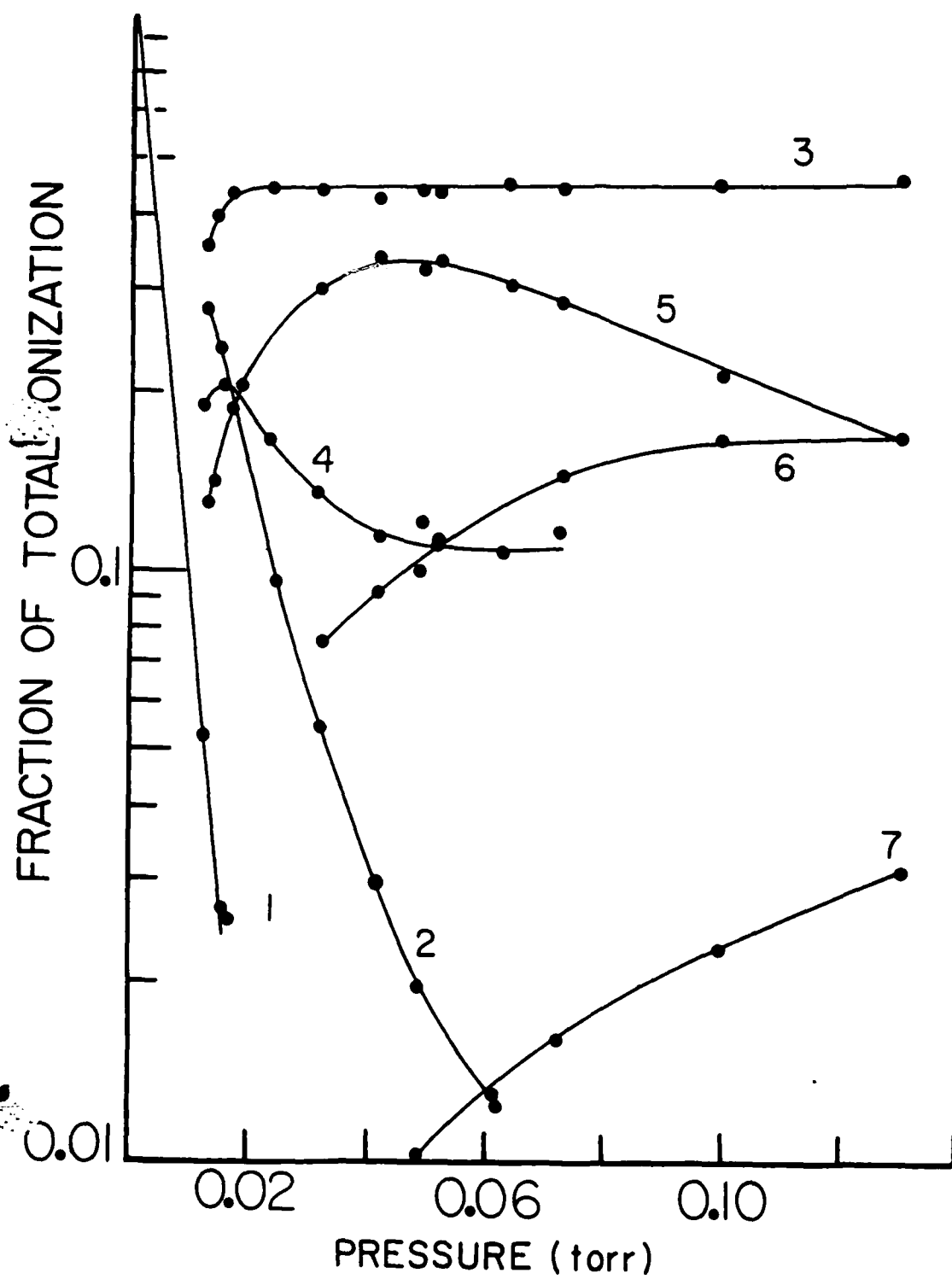
Sharon G. Lias and P. Ausloos  
Center for Chemical Physics  
National Bureau of Standards  
Washington, D. C. 20234

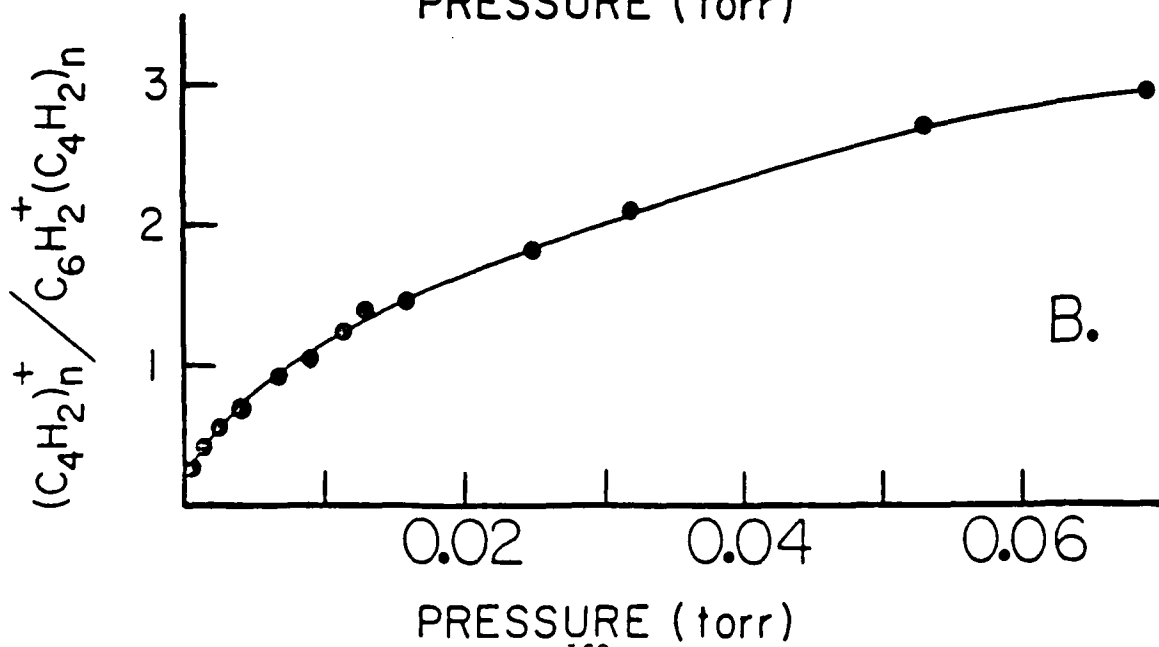
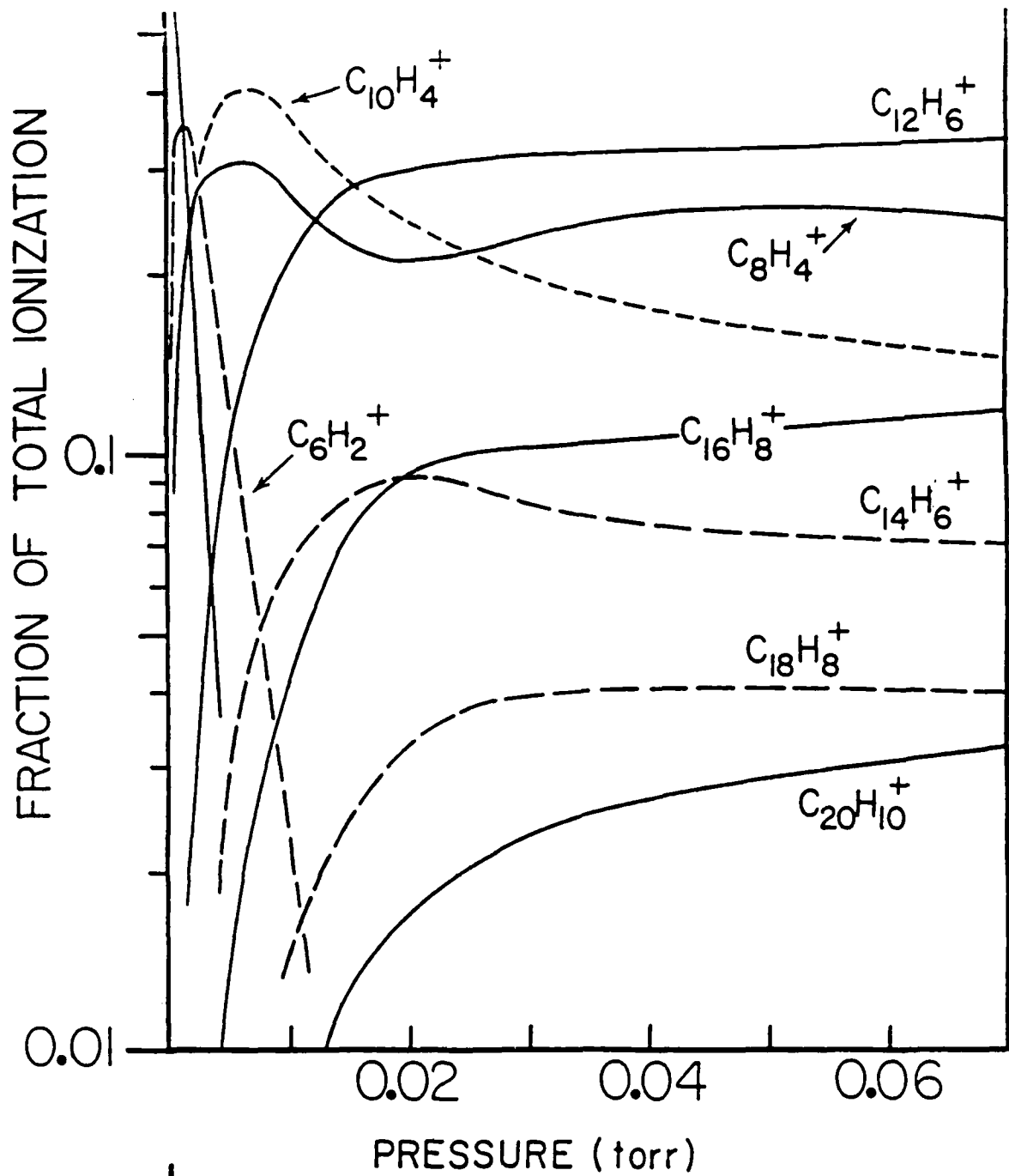
**Abstract**

The structures, isomerization mechanisms, and reaction kinetics of  $C_6H_7^+$  ions formed in a variety of systems have been studied. The ions formed in the reactions ( $H_2C=C=CH_2^+ + H_2C=C=CH_2$ ) and ( $HC\equiv CCH_3^+ + HC\equiv CCH_3$ ), as well as the fragment  $C_6H_7^+$  ions in 1,3-cyclohexadiene, 1,4-cyclohexadiene, trans-1,3,5-hexatriene, 1-methylcyclopentene, 3-methylcyclopentene, and 4-methylcyclopentene exhibit at least two structures under the conditions of an ICR experiment. In each case, one isomer transfers a proton to bases with proton affinity higher than that of benzene demonstrating that this species has the benzenium (protonated benzene) structure. The remaining  $C_6H_7^+$  ions have in some systems (e.g. allene<sup>+</sup> + allene, 1- and 4-methylcyclopentene) a conjugate base with a proton affinity of 202 kcal/mol, while in other systems (e.g. 3-methylcyclopentene, trans-1,3,5-hexatriene) the conjugate base of the non-benzenium isomer has a proton affinity of 205 kcal/mol. When the  $C_6H_7^+$  ions are formed by fragmentation of a  $C_6H_8^+$  ion (in the cyclohexadienes or trans-1,3,5-hexatriene) which has a well-defined internal energy, it is seen that the fraction of  $C_6H_7^+$  ions exhibiting the benzenium structure decreases with increasing energy. The fraction of ions with the benzenium structure also decreases with increasing internal energy of the ( $C_3H_4^+ + C_3H_4$ ) reaction complex from 0.72 in allene (energy level of separated reactants: 315 kcal/mol) to 0.62 in propyne (energy level of separated reactants: 327 kcal/mol).

The energetics of the fragmentation process leading to  $C_6H_7^+$  formation have been examined in a photoelectron-photoion coincidence spectrometer for trans-1,3,5-hexatriene, and 1,3- and 1,4-cyclohexadiene. It is found that the transition state for the fragmentation process [ $C_6H_8^+ \rightarrow C_6H_7^+ + H$ ] is effectively the same in all three systems but lies at an energy level higher than (benzenium ion + H) products.

Rate constants for reactions of benzenium ions with a variety of organic and inorganic compounds have been determined.





### Figure Legends

Figure 1. A. Normalized abundances of ions observed in diacetylene in the high pressure mass spectrometer, plotted as a function of pressure (300 K). B. Stabilization/decomposition ratio in diacetylene as a function of pressure. See text for meaning of ordinate scale.

Figure 2. Normalized abundances of ions observed in cyanoacetylene in the high pressure mass spectrometer, plotted as a function of pressure (300 K). The ions are  $(C_3HN)^+_n$ , and the displayed numbers identify n.



Table 5. Ion-molecule reactions in cyanogen: Thermochemistry, rate constants, and reaction efficiencies.

Reaction	$\Delta H^a$ kcal/mol	$k_{Rn}^b$	$k_{Rn}/Z^c$
$C_2N_2^+ + C_2N_2 \rightarrow C_4N_4^+$	-54	0.35	0.032
$C_4N_4^+ + C_2N_2 \rightarrow C_6N_6^+$		0.22	0.023
$C_6N_6^+ + C_2N_2 \rightarrow C_8N_8^+$		0.08	0.009

<sup>a</sup>See Table 2.

<sup>b</sup>Rate constants in  $cm^3/molecule-s \times 10^{-10}$  determined in the ICR.

<sup>c</sup>Probability that a collision results in observable reaction; collision rate constants,  $Z$ , calculated from AQO formulation in reference 13a. The quadrupole moment of  $C_2N_2$  taken as  $-9.0 \times 10^{-26}$  esu  $cm^2$  (see ref. 18).

Table 4. Ion-molecule reactions in cyanoacetylene: Rate constants, and reaction efficiencies.

Reaction	$k_{Rn}^a$	$k_{Rn}/Z^b$
$HC\equiv C-C\equiv N^+ + HC\equiv C-C\equiv N \rightarrow C_6H_2N_2^+$	7.4	0.28
$HC\equiv C-C\equiv N^+ + HC\equiv C-C\equiv N \rightarrow [C_6H_2N_2^+]^* \rightarrow C_6HN_2^+ + H$		
$C_6H_2N_2^+ + HC\equiv C-C\equiv N \rightarrow H_3C_9N_3^+$	1.2	0.054
$C_3H_3N_3^+ + HC\equiv C-C\equiv N \rightarrow H_4C_{12}N_4^+$		
$C_4H_4N_4^+ + HC\equiv C-C\equiv N \rightarrow H_5C_{15}N_5^+$		
$C_5H_5N_5^+ + HC\equiv C-C\equiv N \rightarrow H_6C_{18}N_6^+$		
$C_6H_6N_6^+ + HC\equiv C-C\equiv N \rightarrow H_7C_{21}N_7^+$		

<sup>a</sup>Rate constants in  $cm^3/molecule-s \times 10^{-10}$  determined in the ICR.

<sup>b</sup>Probability that a collision results in observable reaction; collision rate constants,  $Z$ , calculated from A.D.O. formulations in reference 13b.

<sup>c</sup>Observed in high pressure mass spectrometer only.

the transition state for all three systems is probably the same for most dissociating ions.

If one accepts that the differences obtained for the energy levels of the transition states in the two cyclohexadiene systems (Table 1) are not significant, it follows that the mechanism for the dissociation involves a rearrangement of both ions to a common transition state structure, which is apparently more readily accessible to the 1,3-c-C<sub>6</sub>H<sub>8</sub><sup>+</sup> ion than to the 1,4-c-C<sub>6</sub>H<sub>8</sub><sup>+</sup> (see Table 2).

It can finally be pointed out that although Allan, Dannacher, and Maier<sup>3</sup> established that in the trans-1,3,5-hexatriene system, a fraction of the ions excited to the  $\tilde{A}$  state (onset at 10.26 eV) decay by photon emission, there is no obvious distortion of the shapes of the normalized decay curves shown in Figure 2. (There was an observed increase in the abundance of the parent C<sub>6</sub>H<sub>8</sub><sup>+</sup> ions at energies above 10.6 eV observed at 6.20 us, but this result has not been included in the Figure because of the likelihood that it results from an artifact, such as a dissociation of a polymer impurity.)

#### Structures of C<sub>6</sub>H<sub>7</sub><sup>+</sup> Ions Determined through Kinetic Behavior

Figures 5, 6, and 7 show the abundances of C<sub>6</sub>H<sub>7</sub><sup>+</sup> ions generated in trans-1,3,5-hexatriene, and 1,3- and 1,4-cyclohexadiene as a function of time, under conditions (in the ICR) such that the ions undergo collisions with neutral molecules. In the cyclohexadienes, it is evident (Figures 6 and 7) that there are at least two populations of C<sub>6</sub>H<sub>7</sub><sup>+</sup> ions present, one which undergoes an efficient reaction with the parent compound, and one which does not. Because in pure trans-1,3,5-hexatriene, the reaction of the C<sub>6</sub>H<sub>7</sub><sup>+</sup> ions with the precursor compound is relatively slow, the presence

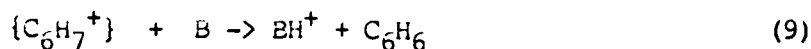
of two populations of ions is not obvious; however, when  $\text{CH}_3\text{OH}$  is added, it becomes clear that some of the  $\text{C}_6\text{H}_7^+$  ions react with this molecule by proton transfer, while a fraction do not react with methanol or with the precursor  $\text{C}_6\text{H}_8$  species. From plots such as those shown in Figure 5, it is possible to estimate the relative abundances of the two populations of  $\text{C}_6\text{H}_7^+$  ions in these and other systems. Figures 8 and 9 show the abundances of  $\text{C}_6\text{H}_7^+$  ions formed through reactions 4 and 5 in allene and propyne, respectively, as a function of time. Here even in the absence of added methanol, it is clear that in both systems, there are two distinct populations of product  $\text{C}_6\text{H}_7^+$  ions, one of which reacts with the precursor  $\text{C}_3\text{H}_4$  species and one of which does not.

#### Identities of $\text{C}_6\text{H}_7^+$ Isomers

Because the more reactive  $\text{C}_6\text{H}_7^+$  ions in all of these systems only transfer protons to bases with proton affinities higher than that of benzene, we can assume that these ions are actually benzenium ions. In order to further confirm the identity of this ion, the rate constants for reaction of authentic benzenium ions (prepared by proton transfer from  $\text{CH}_5^+$  to benzene<sup>18</sup>) were compared with rate constants for analogous reactions of the more reactive  $\text{C}_6\text{H}_7^+$  populations generated in the systems under consideration here (Table 3). The point of interest is that within experimental error the same values for the rate constants ( $k = 2.0 \pm 0.5 \times 10^{-10} \text{ cm}^3/\text{molecule-s}$ ) were obtained for reactions of the  $\text{C}_6\text{H}_7^+$  isomer with  $\text{CH}_3\text{OH}$  in every system; the only reaction channel observed was proton transfer, which is slightly exothermic (by 0.6 kcal/mol) for benzenium ions. (As will be shown below, other  $\text{C}_6\text{H}_7^+$  isomers have conjugate bases with higher proton affinities.) Also, the rate constants for reaction of benzenium ions with allene and propyne are within experimental error the

same as those ascribed to the reactive  $C_6H_7^+$  product ion (reactions 1 and 2) in pure allene and propyne, respectively (Table 3).

Some information about the identities of the non-benzenium isomers,  $\{C_6H_7^+\}$ , formed in the various systems can be obtained from experiments in which other bases of known proton affinity are added to the systems, and the occurrence or non-occurrence of the reaction:



is noted.

Table 4 gives the details of the bracketing experiments performed in the different systems studied here. In these various systems, the  $C_6H_6$  conjugate bases of the  $\{C_6H_7^+\}$  ions exhibit three different proton affinities (or possibly "apparent" proton affinities if the structure of the ion and that of the corresponding conjugate base are very different, i.e. if an isomerization is involved in the deprotonation). For instance, in a number of systems (allene, 1,3- and 1,4-cyclohexadiene, 1- and 4-methylcyclopentene) the  $\{C_6H_7^+\}$  species transfers a proton to tert- $C_4H_9OCH_3$  (proton affinity, 202.2 kcal/mol)<sup>6</sup> but not to  $(C_2H_5)_2CO$  (proton affinity, 201.4 kcal/mol)<sup>6</sup> demonstrating that the  $C_6H_6$  conjugate base corresponding to the  $\{C_6H_7^+\}$  generated in the system has a proton affinity of  $201.8 \pm 0.4$  kcal/mol. In other systems (trans-1,3,5-hexatriene, 3-methylcyclopentene) the  $\{C_6H_7^+\}$  species transfers a proton to (iso- $C_3H_7$ )O (proton affinity, 205.6 kcal/mol)<sup>6</sup> but not to hydrazine (proton affinity, 204.7 kcal/mol)<sup>6</sup>, pinpointing the proton affinity of the conjugate base as  $205.2 \pm 0.5$  kcal/mol. In propyne, one or both of these isomers may be present, but there is formed, in addition, a  $C_6H_7^+$  ion which does not transfer a proton to molecules having a proton affinity as high as 226 kcal/mol.

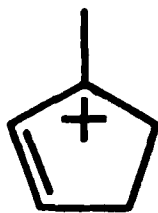
In order to address the question of the structures of the three non-

benzenium  $\{C_6H_7^+\}$  species formed in these systems, it is necessary first to consider the heats of formation of possible isomeric structures, along with the heats of formation of the conjugate  $C_6H_6$  bases which would result upon deprotonation. Table 5 summarizes experimental heats of formation of  $C_6H_7^+$  ions, and estimated heats of formation of certain other isomers for which experimental data are not available. The Table also gives estimated or experimental heats of formation of the  $C_6H_6$  conjugate bases, and the proton affinities of the conjugate bases. The proton affinities of 1,5- and 2,4-hexadiyne were determined by bracketing experiments to be in both cases  $196 \pm 3$  kcal/mol, leading to values for the heats of formation of the corresponding protonated molecules of 269 and 260 kcal/mol, respectively.

Of the  $C_6H_7^+$  ions listed in the Table, those which apparently most closely match the thermochemistry of the  $\{C_6H_7^+\}$  ions formed in most of these systems are the two protonated fulvenes II and III (Table 5). In addition, 3,4-dimethylenecyclobutene is predicted to be associated with two proton affinity values (corresponding to  $C_6H_7^+$  ions IV and V in Table V) which are also estimated to be close to 202 or 205 kcal/mol. The vinylcyclobutenyl ion (VI) might be expected to deprotonate to yield an acyclic  $C_6H_6$  product since a substituted cyclobutadiene product would be highly strained; depending on the identity of the  $C_6H_6$  isomer formed, the "apparent" proton affinity which would be manifested in the deprotonation of this ion might also lie in the vicinity of 202 or 205 kcal/mol (Table 5). The energy levels corresponding to formation of these  $C_6H_7^+$  ions are shown on the composite potential energy diagram given in Figure 1, where it is seen that, of the possible structures which can be assigned to the  $\{C_6H_7^+\}$  ions, the protonated fulvenes are predicted to be favored on energetic grounds. On the other hand, Bowers et al.<sup>19</sup> examined the isotopic labelling of product ions formed by the loss of ethylene from the

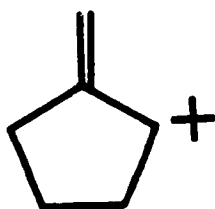
condensation ion formed from  $(\text{CD}_2=\text{C}=\text{CD}_2^+ + \text{CH}_2=\text{C}=\text{CH}_2)$ , and concluded that the results could best be explained by a  $\text{C}_6(\text{H},\text{D})_8^+$  precursor having a dimethylenecyclobutane structure. If H loss proceeded from the same precursor structure, then structures IV or V would be implicated.

The dissociation to form  $\text{C}_6\text{H}_7^+$  in the methylcyclopentenenes occurs on the  $\text{C}_6\text{H}_9^+$  potential surface rather than on that of  $\text{C}_6\text{H}_8^+$ , but it may be possible to use the differences in the identities of the non-benzenium products formed in these compounds as a clue to their structures. If one surmises that the loss of an H-atom from the 3-methylcyclopentene ion will lead to the  $\text{C}_6\text{H}_9^+$  species:

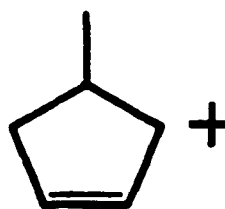


IX

while 1-methyl- and 4-methylcyclopentene ions will most likely form allylic  $\text{C}_6\text{H}_9^+$  product ions, such as X or XI:



X



XI

then one would readily identify the expected product of further dissociation of IX as II, and that of X and XI as III.

In the case of the propyne system, the energy level with which the  $\text{C}_6\text{H}_8^+$  condensation ions originate is sufficiently high (Figure 1) that a

dissociation channel is available which is unavailable in the other systems studied here when ionization is effected by electron impact on the parent molecules. As shown in Table 4,  $C_6H_7^+$  ions are present in the propyne system which do not transfer a proton to bases having a proton affinity of 226 kcal/mol. The thermochemical considerations summarized in Table 5 indicate that isomeric ions containing three-membered rings might possibly deprotonate to give  $C_6H_6$  species with proton affinities higher than 226 kcal/mol, but the formation of these ions is predicted to be energetically accessible to the  $C_6H_8^+$  species formed in allene as well as in propyne, and thus would not be consistent with the opening of this channel for  $C_6H_8^+$  ions in propyne but not in allene. The energy levels of many of the acyclic  $C_6H_7^+$  ions are sufficiently high that the structures would only be accessible to ions formed in reaction 2, but the proton affinities of the conjugate  $C_6H_6$  bases lie in the range 195-200 kcal/mol.

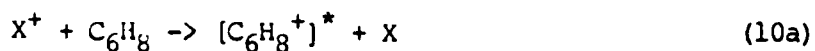
It would appear from the information summarized in Tables 2 and 4 that the identity of the particular non-benzenium  $C_6H_7^+$  isomer which is formed is dictated more by the structure of the precursor species than by the energy level. For example, both the 1,3- and 1,4-cyclohexadiene ions form the same non-benzenium isomer (proton affinity of conjugate base, 202 kcal/mol). This is the same isomer as that formed in the allene system (reaction 1) with a probability of 0.30. On the other hand, the trans-1,3,5-hexatriene ion (which might be expected to undergo ring closure to form an excited 1,3-cyclohexadiene ion) does not dissociate to give that non-benzenium isomer but the alternate species (proton affinity of conjugate base, 205 kcal/mol), and with a probability of only 0.13. Since the identity of the non-benzenium isomer formed in trans-1,3,5-hexatriene is different from that in the cyclohexadienes, one must assume that this



dissociation involves a different transition state, possibly ring closure to directly form a five-membered (or a four-membered) ring. This is in accord the conclusions reached by Allan, Dannacher, and Maier<sup>3</sup>, who interpreted their results in terms of two competing slow ring closure processes.

#### Relative Abundances of $C_6H_7^+$ Isomers as a Function of Energy

More information about the energy dependence of the processes leading to the formation of different  $C_6H_7^+$  isomers was obtained in experiments in which the parent radical cations which are the precursors of the fragment ions of interest have been generated in the ICR with known amounts of internal energy through charge transfer reactions:



where  $X^+$  is a xenon, krypton, or argon ion with a recombination energy of, respectively 12.1, 14.0 or 15.75 eV. Figure 10 shows the relative abundances of  $c-C_6H_7^+$  and  $\{C_6H_7^+\}$  ions generated in trans-1,3,5-hexatriene and in 1,3- and 1,4-cyclohexadiene as a function of energy (where  $\{C_6H_7^+\}$  is the non-benzenium isomer). In both 1,3,5-hexatriene where considerable rearrangement is necessary to form the benzenium ion, and in the cyclonexadienes, where a simple C-H bond cleavage can lead to a benzenium ion, the relative abundance of benzenium decreases with an increase in energy imparted to  $[C_6H_8^+]^*$ .

#### Conclusions

The  $C_6H_8^+$  ions generated in propyne and allene, as well as the parent ions of trans-1,3,5-hexatriene, 1,3- and 1,4-cyclohexadiene, each undergo at least two fragmentation processes leading to different  $C_6H_7^+$  species,

with the process leading to non-benzenium isomers increasing in importance with increasing energy. The loss of an H-atom from 1,3- and 1,4-cyclohexadiene radical cations is a slow process, associated with a transition state which lies at an energy level about half an eV higher than that of the lowest energy products, ( $c\text{-C}_6\text{H}_7^+ + \text{H}$ ). In the cyclohexadienes, the dissociation mechanism leading to the benzenium ion apparently can not be described as a simple lengthening of a C-H bond.

At least three different non-benzenium  $\text{C}_6\text{H}_7^+$  isomers are observed in the systems studied here. From an examination of the energetics of proton transfer from these non-benzenium isomers, and estimations of the proton affinities of possible  $\text{C}_6\text{H}_6$  conjugate bases, it is concluded that the most likely structures are the two protonated fulvenes, II and III, although the protonated dimethylenecyclobutenes, IV and V, can not be ruled out on the basis of the proton transfer "bracketing" experiments.

## Acknowledgements

The photoelectron-photoion coincidence experiments were carried out using the apparatus and associated computer programs for interpretation originally put together by Drs. Henry M. Rosenstock, Roger Stockbauer, and Albert Parr. We would like to thank Drs. Stockbauer and Parr for graciously acceding to our use of this instrument. One of us (S. G. L.) gratefully acknowledges being tutored in the use of the apparatus and programs by Dr. James Butler. The late Henry M. Rosenstock also contributed greatly to our education in the interpretation of results from photoelectron-photoion coincidence experiments.

A detailed critical reading of a preliminary draft of the manuscript by Dr. Josef Dannacher was invaluable to the authors, particularly in arriving at a correct presentation of the photoelectron-photoion coincidence results. Dr. Dannacher's comments prompted a detailed re-evaluation of the relative contributions of the parent and daughter ions to the composite  $m/e$  79- $m/e$  80 time-of-flight peaks; he also suggested the inclusion of a sentence pointing out the apparent lack of an effect on the shape of the decay curves of the radiative decay from the 1,3,5-hexatriene cation A state.

Discussions with Dr. Joel Liebman and Dr. Stephen E. Stein provided useful insights in the estimations of thermochemical quantities presented in Table 5.

This work was supported by the Air Force Office of Scientific Research.

Table 1. Appearance Energies of  $C_6H_7^+$  Ions in  $C_6H_8$  Isomers

$C_6H_8$	$\Delta H_f(C_6H_8)^a$ kcal/mol	IP( $C_6H_8$ ) <sup>b</sup> eV	TSC	Factor <sup>d</sup>	$E_{Act}^e$ eV	$\Delta S_{Act}$ cal/deg-mol	AP( $C_6H_7^+$ ) eV	Energy Level Transition St. kcal/mol
trans-CH <sub>2</sub> =CHCH=CHCH=CH <sub>2</sub>	40. (298 K) <sup>f</sup> 46. (0 K)	8.28±0.02	B F	1.023 1.083	1.665 1.675	-5.3 -3.8	9.945 9.955	275 (0 K), 269 (298 K) 275 (0 K), 269 (298 K)
1,3-c-C <sub>6</sub> H <sub>8</sub>	25. (298 K) <sup>g</sup> 31. (0 K)	8.25±0.02	B F	0.848 0.926	2.20 2.19	+6.4 +6.7	10.45 10.45	272 (0 K), 266 (298 K) 272 (0 K), 266 (298 K)
1,4-c-C <sub>6</sub> H <sub>8</sub>	26. (298 K) <sup>h</sup> 32. (0 K)	8.82±0.02	B F	0.932 1.000	1.735 1.735	-1.7 -1.2	10.557 10.555	275 (0 K), 269 (298 K) 275 (0 K), 269 (298 K)

<sup>a</sup>Corrections from 298 to 0 K values made using vibrational frequencies from references 12, 13, 14 and 15.

<sup>b</sup>From H. M. Rosenstock, K. Draxl, B. W. Steiner, and J. T. Herron, J. Phys. Chem. Ref. Data 6, Suppl. 1 (1977).

<sup>c</sup>Transition state model: B - Transition state frequencies derived from vibrational frequencies of benzene (reference 15b); F - Transition state frequencies derived from vibrational frequencies of fulvene (reference 15a).

<sup>d</sup>Factor by which vibrational frequencies of transition state model must be multiplied in order to correctly predict experimentally-observed cross-over energy.

<sup>e</sup>This is the quantity actually predicted by the QET calculations (see Discussion); this is added to literature values for the ionization potentials to obtain the cited appearance potentials, which correspond to zero Kelvin onsets for  $C_6H_7^+$  formation.

<sup>f</sup>Estimated (J. F. Liebman, personal communication).

<sup>g</sup>From J. B. Pedley and J. Rylance, "Sussex - N. P. L. Computer Analysed Thermochemical Data: Organic and Organometallic Compounds", University of Sussex (1977).

<sup>h</sup>From R. Shaw, D. M. Golden, and S. W. Benson, J. Phys. Chem. 81, 1716 (1977).

Table 2. Probabilities of Formation of  $C_6H_7^+$  Isomers in Allene and Propyne, and through Electron Impact<sup>a</sup> or Charge Transfer in  $C_6H_8$  and  $C_6H_{10}$  Compounds.

Precursor	Per Cent of $C_6H_7^+$		Proton Affinity of Conjugate Base, Non-Benzenium Isomer kcal/mol
	Benzenium Ion	Non-Benzenium Ion	
$CH_3C\equiv CH^+ + CH_3C\equiv CH$	44	56	>226
$CH_2=C=CH_2^+ + CH_2=C=CH_2$	70	30	202
$CH_2=CHCH=CHCH=CH_2^+$	87	13	205
$Xe^+ + M$	91	9	
$Kr^+ + M$	83	17	
$Ar^+ + M$	80	20	
$1,3-c-C_6H_8^+$	91	9	202
$Xe^+ + M$	94	6	
$Kr^+ + M$	77	23	
$Ar^+ + M$	73	27	
$1,4-c-C_6H_8^+$	46	54	202
$Xe^+ + M$	75	25	
$Kr^+ + M$	43	57	
$Ar^+ + M$	37	63	
$1-CH_3-c-C_5H_7^+$	91	9	202
$3-CH_3-c-C_5H_7^+$	88	12	205
$4-CH_3-c-C_5H_7^+$	85	15	202

<sup>a</sup>Electron impact results: ionization of precursor molecule effected with 40 eV electrons.

Table 3. Rate Constants for Reactions:  $C_6H_7^+ + M \rightarrow$  Products

Source of $C_6H_7^+$	M	$k_{Rn} \times 10^{10} \text{ cm}^3/\text{molecule-sec}$	$k_{Rn}/Z$	$\Delta H$ kcal/mol	Reaction <sup>a</sup>
$CH_5^+ + \text{Benzene}^b$	$CH_3OH$	2.5 (326 K)	0.16	-0.6	PT
	$CH_3C\equiv CH$	1.6	-0.7		PT
	$CH_2=C=CH_2$	0.44	-5.0		PT
	$CH_3CHO$	13.5	0.66	-5.3	PT
	$CH_3SH$	6.6	0.54	-6.1	PT
	$PH_3$	2.6	0.24	-7.3	PT
	$HCOOCH_3$	8.5	0.58	-7.6	PT
	$CH_3OCH_3$	11.6	0.84	-10.8	PT
	$HCOO(n-C_4H_9)$	14.3	0.92	-13.5	PT
	$i-C_4H_8$	5.8	0.48	-14.6	PT
	$CH_3COCH_3$	21.8	1.0	-15.4	PT
	$CH_2=CHCH=CHCH=CH_2$	4.5			C
$CH_2=CHCH=CHCH=CH_2^c$	$CH_2=CHCH=CHCH=CH_2$	4.2			C
	$CH_3OH$	2.3			PT
$1,3-C_6H_8^c$	$CH_3OH$	2.0			PT
	$CH_3CHO$	14.2			PT
	$CH_3OCH_3$	10.7			PT
$1,4-C_6H_8^c$	$CH_3OH$	1.9			PT
	$CH_3CHO$	12.7			PT
	$CH_3OCH_3$	11.0			PT

Table 3. Continued.

Source of $C_6H_7^+$	M	$k_{Rn} \times 10^{10} \text{ cm}^3/\text{molecule-sec}$	$k_{Rn}/Z$	$\Delta H$ kcal/mol	Reaction <sup>a</sup>
$CH_3C\equiv CH^C$	$CH_3C\equiv CH$	1.5			C
$CH_2=C=CH_2^C$	$CH_2=C=CH_2$	0.5			C

<sup>a</sup>PT = Proton transfer; C = Condensation

<sup>b</sup>Error limits,  $\pm 10\%$

<sup>c</sup>Rate constants determined after subtracting out abundance of non-benzenium isomer; error limits,  $\pm 25\%$

Table 4. Proton Affinities of Non-Benzenium  $C_6H_7^+$  Isomers through Bracketing<sup>a</sup>.

Precursor of $C_6H_7^+$	Reactant Molecule			
	$(C_2H_5)_2CO$	$(t-C_4H_9)OCH_3$	$H_2NNH_2$	$(i-C_3H_7)_2O$
Proton Affinity <sup>b</sup> (kcal/mol):	<u>201.4</u>	<u>202.2</u>	<u>204.7</u>	<u>205.6</u>
$[HC\equiv CCH_3^+ + HC\equiv CCH_3]^c$	0	0	0	0
$[CH_2=C=CH_2^+ + CH_2=C=CH_2]$	0	PT	PT	PT
1,3-c- $C_6H_8$	0	PT	PT	PT
1,4-c- $C_6H_8$	0	PT	PT	PT
trans- $CH_2=CH-CH=CH-CH=CH_2$	0	0	0	PT
c- $C_5H_7$ -1- $CH_3$	0	PT	PT	PT
c- $C_5H_7$ -3- $CH_3$	0	0	0	PT
c- $C_5H_7$ -4- $CH_3$	0	PT	PT	PT

<sup>a</sup><sub>0</sub> = No reaction; PT = Proton transfer from  $C_6H_7^+$  to M was observed.

<sup>b</sup>Proton affinity data from reference 6.

<sup>c</sup>The non-benzenium  $C_6H_7^+$  isomer formed in propyne does not undergo proton transfer with 2-methyltetrahydrofuran (proton affinity 205.6), niline (proton affinity, 209.5 kcal/mol) methylamine (proton affinity, 214.1 kcal/mol), or diethylamine (proton affinity, 225.9 kcal/mol).



AD-A154 269

THERMODYNAMICS OF HIGH TEMPERATURE MATERIALS(U)  
NATIONAL BUREAU OF STANDARDS GAITHERSBURG MD CENTER FOR  
CHEMICAL PHYSICS S ABRAMOWITZ 15 MAR 85

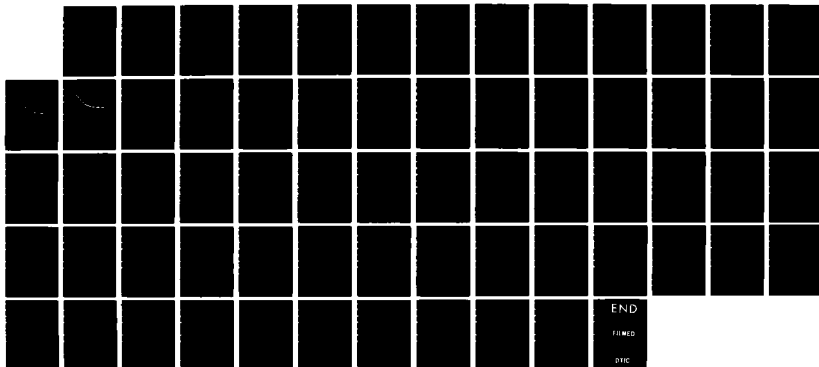
3/3

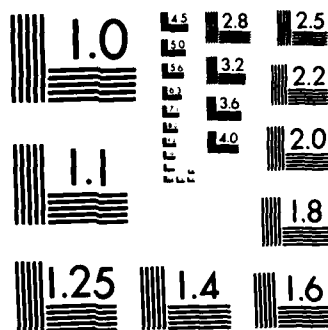
UNCLASSIFIED

AFOSR-TR-85-0394 AFOSR-ISSA-84-00034

F/G 11/2

NL





MICROCOPY RESOLUTION TEST CHART  
NATIONAL BUREAU OF STANDARDS-1963-A

Table 5. Thermochemistry of  $C_6H_7^+$  Ions and Conjugate  $C_6H_6$  Bases.




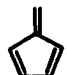
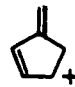
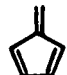





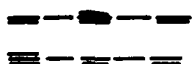




Ion	$\Delta H_f(298\text{ K})$ kcal/mol	Ref.	Conjugate Base	$\Delta H_f(298\text{ K})$ kcal/mol	Ref.	Proton Affinity kcal/mol
I 	204	6		19.8	20,22	181.3
II 	213 228 242	Est <sup>a</sup> Est <sup>a</sup> 23 <sup>a</sup>		53.8	21	206 191 177
III 	214	Est <sup>b</sup>		53.8	21	205
IV 	234	Est <sup>c</sup>		80.2	21	212
V 	245	Est <sup>d</sup>		80.2	21	201
VI 	259	Est <sup>e</sup>		99.1 or 87	22 22	206 194
VII 	222 237	Est <sup>f</sup> 23		114	Est <sup>g</sup>	258 243
VIII 	222	Est <sup>h</sup>		127	Est <sup>i</sup>	272
$HC\equiv OCH_2CH_2C=CH_2^+$ 260	This work	$HC\equiv OCH_2CH_2C\equiv CH$	99	22	196	
$CH_3CH=C-C\equiv OCH_3^+$ 260	This work	$CH_3C\equiv C-C\equiv OCH_3$	90	22	196	

Table 5. Continued.

<u>Ion</u>	<u><math>\Delta H_f</math> (298 K)</u> <u>kcal/mol</u>	<u>Ref.</u>	<u>Conjugate</u> <u>Base</u>	<u><math>\Delta H_f</math> (298 K)</u> <u>kcal/mol</u>	<u>Ref.</u>	<u>Proton</u> <u>Affinity</u>
$H_2C=C-C\equiv C-C_2H_5^+$	271	Est	$HC\equiv C-C\equiv C-C_2H_5$	103	22	198
$H_2C=CCH_2C\equiv CCH_3^+$	276	Est	$HC\equiv CCH_2C\equiv CCH_3$	106	22	196

<sup>a</sup>(1) Value of 213 kcal/mol: Estimated assuming that the hydrogen affinity of the  $C_6H_6^+$  radical cation will be similar to hydrogen affinities of species with similar structural features which add H to give product cations which are structurally similar to the relevant  $C_6H_7^+$  ions (Ref. 22). Taking the hydrogen affinity (HA) of methylene cyclopentane ion as 84 kcal/mol and HA of 2-methyl-1,3-butadiene ion as 91 kcal/mol, one estimates a hydrogen affinity associated with the formation of this ion as  $87 \pm 3$  kcal/mol leading to an estimated heat of formation of the ion of 211 kcal/mol; the heat of formation of the fulvene cation is 246 kcal/mol. An estimation based on the hydride affinity (i.e. based on the heats of formation of methylenecyclopentadienes) leads to a value of -213 kcal/mol. Both of these approaches neglect the destabilizing effect of the "anti-aromaticity" of the five-membered conjugated ring. The magnitude of this effect can be estimated by examining the differences between the heats of formation of  $C_6H_5C^+HCH=CH_2$  (-242 kcal/mol) and the ion formed by loss of an H atom from indene (-276 kcal/mol), or between  $CH_2=C=C^+HCH=CH_2$  (-216 kcal/mol) and  $C-C_5H_5^+$  (252 kcal/mol); on this basis, if we take a value of -178 kcal/mol for the heat of formation of  $(CH_2=CH)_2C^+CH_3$ , then ring closure would lead to a  $C-C_5H_4CH_3^+$  ion with a heat of formation of 213 kcal/mol. (2) Value of 228 kcal/mol: Another approach to this heat of formation is to examine the stabilization effected by replacing an H atom by a methyl group in other cyclic  $C_6H_n^+$  ions; in  $C_3H_3^+$  (aromatic case) and in  $C_6H_6^+$  (non-aromatic case), such a substitution leads to a lowering of the heat of formation by 20 kcal/mol. Substitution of a methyl group for an H-atom in  $C-C_5H_5^+$ , then would give a  $C-C_5H_4CH_3^+$  ion with a heat of formation of <232 kcal/mol (since the stabilizing effect of methyl should be greater in the anti-aromatic case). If we assume that the heats of formation estimated from H-atom affinities or from hydride affinities must be corrected for the destabilizing effect of anti-aromaticity (+35 kcal/mol) in a methyl-bearing ring (-20 kcal/mol), then the value of 213 kcal/mol estimated above should be increased to approximately 228 kcal/mol. All thermochemical data from references 6 and 20. (3) Stein (reference 23) estimated a value of 242 kcal/mol for the ion. On the basis of the considerations presented here, it seems that the heat of formation lies between -213 kcal/mol and -232 kcal/mol (i.e. the proton affinity of the conjugate base is bracketed between 187 and 206 kcal/mol).

<sup>b</sup>Estimated assuming that the hydrogen affinity of the  $C_6H_6^+$  radical cation will be similar to hydrogen affinities of species with similar structural features which add H to give product cations which are structurally similar to the relevant  $C_6H_7^+$  ions. HA of 1,3-pentadiene ion = 85 kcal/mol; HA of cyclopentadiene ion = 84 kcal/mol (thermochemical data from references 6 and 20); taking a value for the heat of formation of fulvene of 53.5 kcal/mol (reference 21), the heat of formation of the fulvene cation is 246 kcal/mol (ref. 20).

<sup>c</sup>Estimated assuming that the proton affinity of  $C_6H_6$  will be similar to that of 1-methyl-3-methylenecyclobutene (reference 6).

<sup>d</sup>Estimated assuming that the proton affinity of  $C_6H_6$  will be similar to that of dimethylcyclobutene (reference 6).

<sup>e</sup>Estimated using "macroincrementation" (ref. 22). Taking  $\Delta H_f(C-C_4H_4CH_3^+)$  = 234 kcal/mol,  $\Delta H_f(CH_3CH=CH_2)$  = 4.8 kcal/mol;  $\Delta H_f(C_2H_6)$  = -20 kcal/mol. (Thermochemical data from ref. 20).

<sup>f</sup>Estimated using "macroincrementation" (ref. 22). Taking  $\Delta H_f(C-C_3H_3^+)$  = 257 kcal/mol;  $\Delta H_f(C-C_3H_2CH_3^+)$  = 237 kcal/mol;  $\Delta H_f(C-C_3H_2CH=CH_2^+)$  = 242 kcal/mol (ref. 20), then  $(237 + 242 - 257)$  kcal/mol = 222 kcal/mol.

<sup>g</sup>Estimated using "macroincrementation" (ref. 22). Taking  $\Delta H_f(C-C_3H_4=CH_2)$  = 48 kcal/mol;  $\Delta H_f(C-C_3H_6)$  = 12.7 kcal/mol;  $\Delta H_f(1,3-C_4H_6)$  = 26 kcal/mol;  $\Delta H_f(CH_3CH=CH_2)$  = 4.8 kcal/mol; then  $(48 + 58 + 26 - 13 - 5)$  kcal/mol = 114 kcal/mol. (Thermochemical data from ref. 20).

<sup>h</sup>Estimated using "macroincrementation" (ref. 22). Taking  $\Delta H_f(C-C_3H_2CH=CH_2^+)$  = 242 kcal/mol;  $\Delta H_f(1,3-C_4H_6^+)$  = 235 kcal/mol;  $\Delta H_f(1,3-C_5H_8^+)$  = 215 kcal/mol; then  $(242 + 215 - 235)$  kcal/mol = 222 kcal/mol. (Thermochemical data from ref. 20).

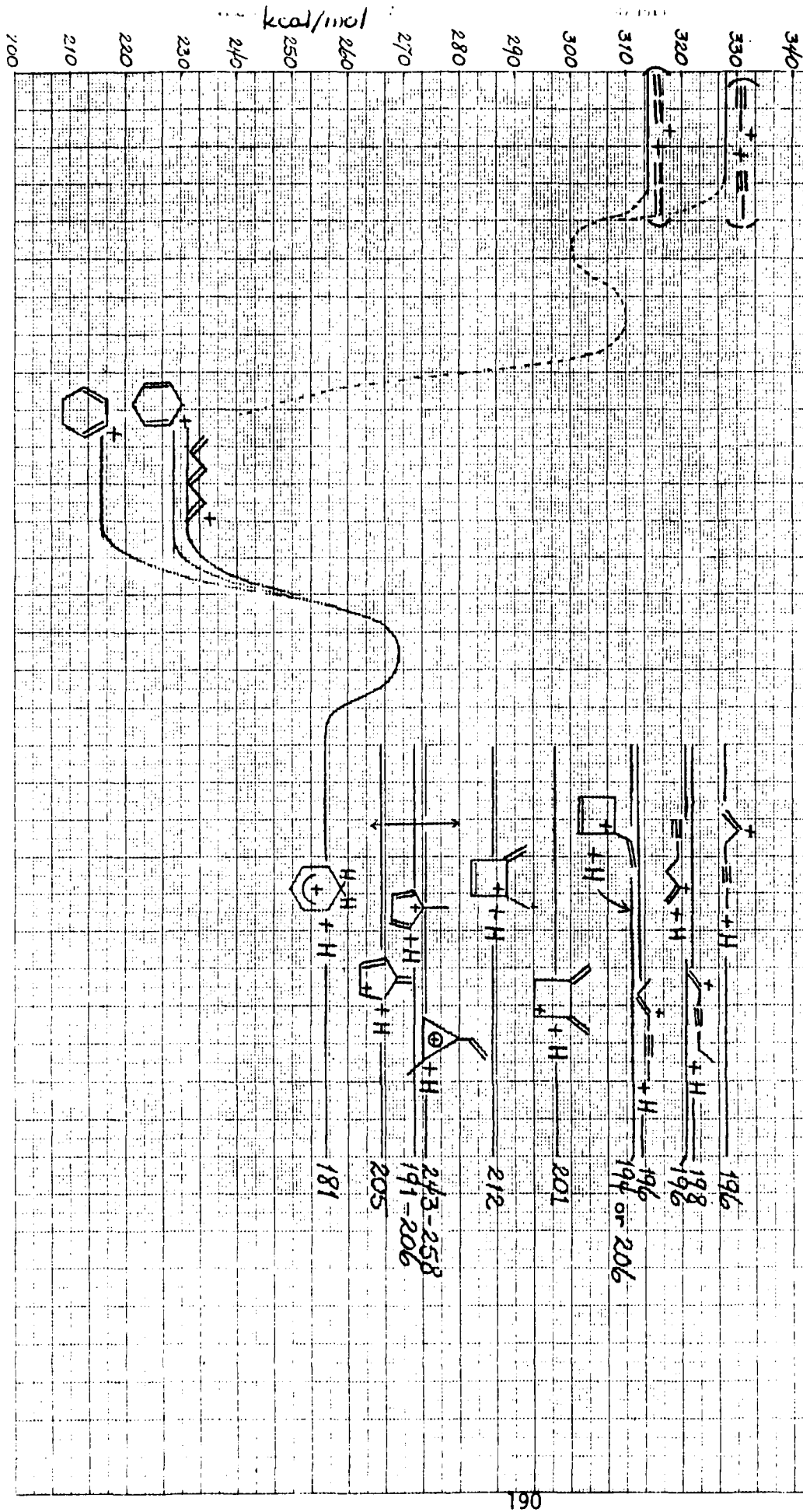
<sup>i</sup>Estimated using "macroincrementation" (ref. 22). Taking  $\Delta H_f(C-C_3H_4)$  = 66 kcal/mol;  $\Delta H_f(C-C_3H_4=CH_2)$  = 48 kcal/mol;  $\Delta H_f(C-C_3H_6)$  = 12.7 kcal/mol;  $\Delta H_f(1,2-C_4H_6)$  = 39 kcal/mol;  $\Delta H_f(C_2H_4)$  = 12.5 kcal/mol; then  $(66 + 48 - 13 + 39 - 12.5)$  kcal/mol = 127 kcal/mol. (Thermochemical data from reference 20).

## Figure Legends

- Figure 1. Approximate potential surface (at 298 K) for  $[C_6H_8^+ \rightarrow C_6H_7^+ + H]$  dissociations in 1,3,5-hexatriene, 1,3-cyclohexadiene, and 1,4-cyclohexadiene; the energy level of the transition state relative to those of the parent radical cations is derived from experimental results reported here. The energy levels of the parent ions and the [benzenium ion + H] products are from the literature (references 6 and 20); energy levels of the protonated hexadiynes are from this work, and of other product ions are estimated in Table 5. The dotted line represents the potential surface reported for the  $[CH_2=C=CH_2^+ + CH_2=C=CH_2]$  and  $[CH_3C=CH^+ + CH_3C=CH]$  systems in reference 1.
- Figure 2. Normalized relative abundances of  $C_6H_8^+$  (○) and  $C_6H_7^+$  (Δ) ions in 1,3,5-hexatriene as a function of photon energy in the photoelectron-photoion coincidence apparatus. The circle and triangle symbols denote results obtained using a detailed analysis of the shapes of the overlapping time-of-flight peaks; associated horizontal dashes indicate relative abundances based on peak maxima only, as described in the Experimental section. Results are given for ions having residence times in the source of 1.22 μs and 6.20 μs. The dotted line is the breakdown curve derived from the rate-energy curve calculated using the parameters given in Table 1. Curves based on the assumption of a "benzene-like" transition state or a "fulvene-like" transition state are effectively the same.
- Figure 3. Normalized relative abundances of  $C_6H_8^+$  (○) and  $C_6H_7^+$  (Δ) ions in 1,3-cyclohexadiene as a function of photon energy in the photoelectron-photoion coincidence apparatus. The circle and triangle symbols denote results obtained using a detailed analysis of the shapes of the overlapping time-of-flight peaks; associated horizontal dashes indicate relative abundances based on peak maxima only, as described in the Experimental section. Results are given for ions having residence times in the source of 1.22 μs and 6.20 μs. The dotted line is the breakdown curve derived from the rate-energy curve calculated using the parameters given in Table 1. Curves based on the assumption of a "benzene-like" transition state or a "fulvene-like" transition state are effectively the same.
- Figure 4. Normalized relative abundances of  $C_6H_8^+$  (○) and  $C_6H_7^+$  (Δ) ions in 1,4-cyclohexadiene as a function of photon energy in the photoelectron-photoion coincidence apparatus. The circle and triangle symbols denote results obtained using a detailed analysis of the shapes of the overlapping time-of-flight peaks; associated horizontal dashes indicate relative abundances based on peak maxima only, as described in the Experimental section. Results are given for ions having residence times in the source of 1.22 μs and 6.20 μs. The dotted line is the breakdown curve derived from the rate-energy curve calculated using the parameters given in Table 1. Curves based on the assumption of a "benzene-like" transition state or a "fulvene-like" transition state are effectively the same.

- Figure 5. Abundance of  $C_6H_7^+$  generated in 1,3,5-hexatriene in the ICR, plotted as a function of time in the presence (a) and absence (b) of added  $CH_3OH$ .
- Figure 6. Abundance of  $C_6H_7^+$  generated in 1,3-cyclohexadiene in the ICR, plotted as a function of time.
- Figure 7. Abundance of  $C_6H_7^+$  generated in 1,4-cyclohexadiene in the ICR, plotted as a function of time.
- Figure 8. Abundance of  $C_6H_7^+$  formed in the reaction  $[CH_2=C=CH_2^+ + CH_2=C=CH_2 \rightarrow C_6H_7^+ + H]$ , plotted as a function of time in the ICR.
- Figure 9. Abundance of  $C_6H_7^+$  formed in the reaction  $[CH_3C=CH^+ + CH_3C=CH \rightarrow C_6H_7^+ + H]$ , plotted as a function of time in the ICR.
- Figure 10. Relative fractions of non-benzenium  $C_6H_7^+$  isomers generated in  $C_6H_8$  isomers (trans-1,3,5-hexatriene, 1,3-cyclohexadiene, and 1,4-cyclohexatriene) in the reaction  $[X^+ + C_6H_8 \rightarrow C_6H_7^+ + H + X]$ , where X is Xe (ionization potential 12.1 eV), Kr (ionization potential, 14.0 eV), or Ar (ionization potential, 15.75 eV).

ESTIMATED  
PROTON AFFINITY  
OF CONJUGATE BASE



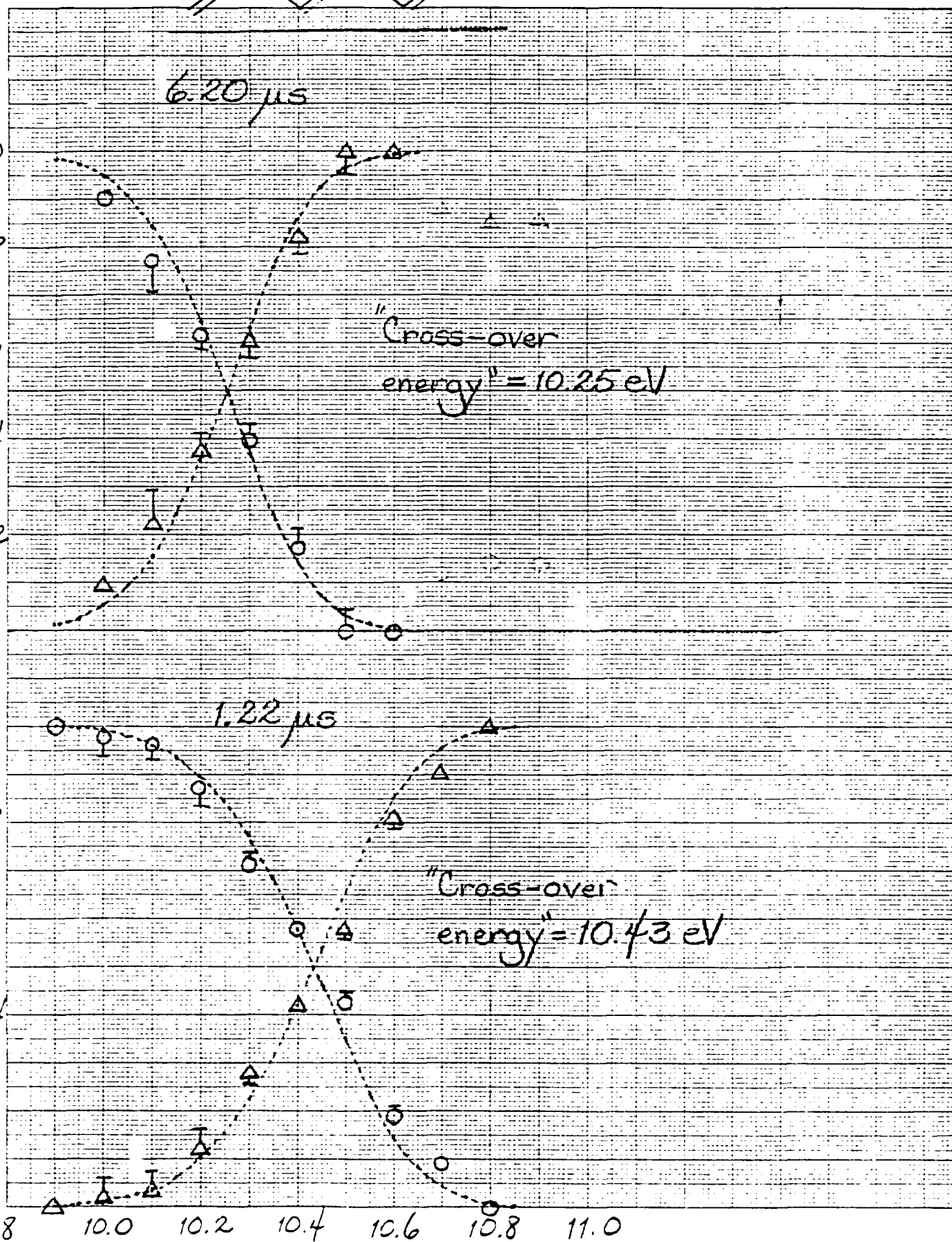


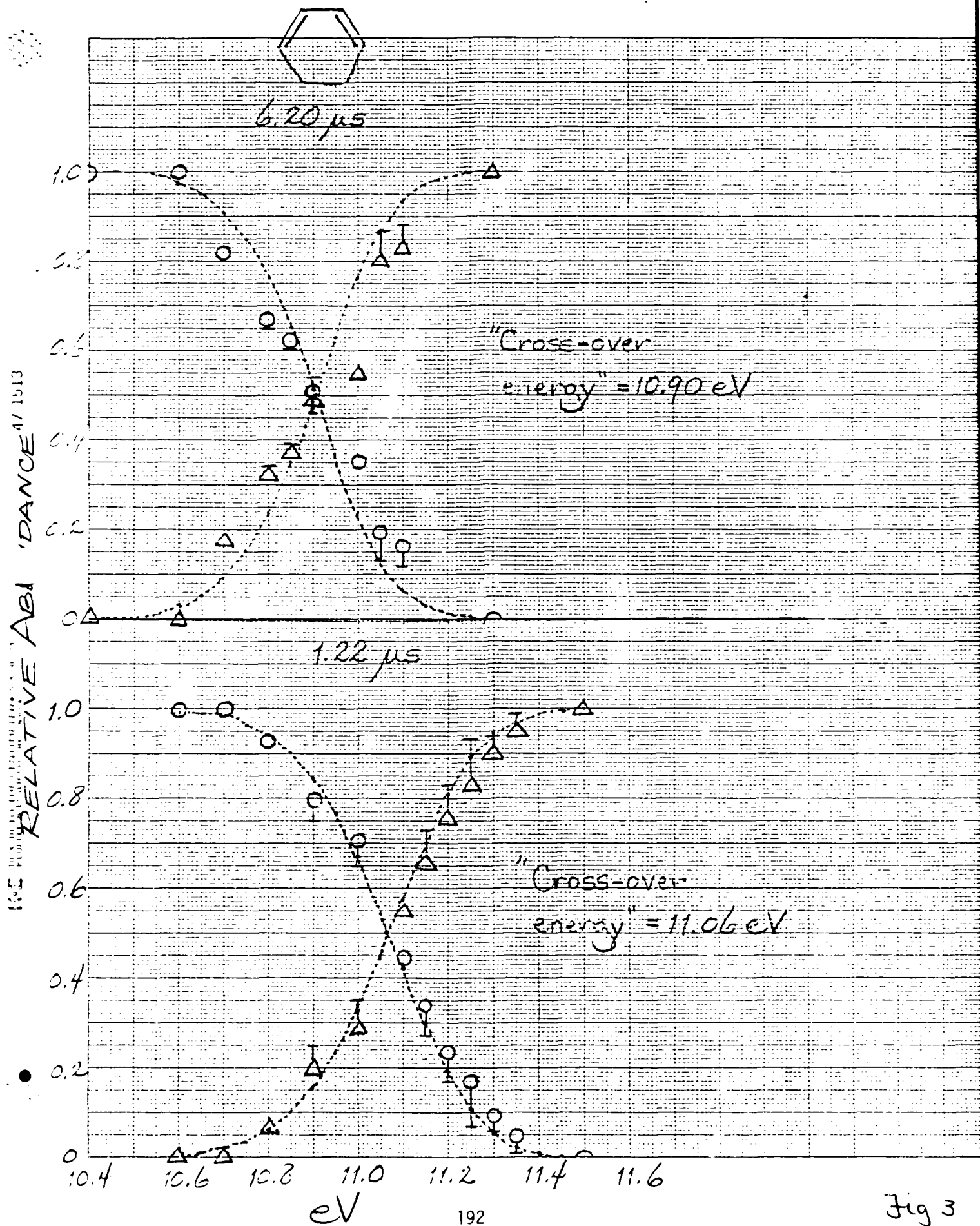
4/1513

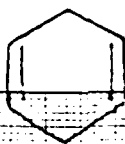
RELATIVE ABUNDANCE

6.20  $\mu$ s"Cross-over  
energy" = 10.25 eV1.22  $\mu$ s"Cross-over  
energy" = 10.43 eV

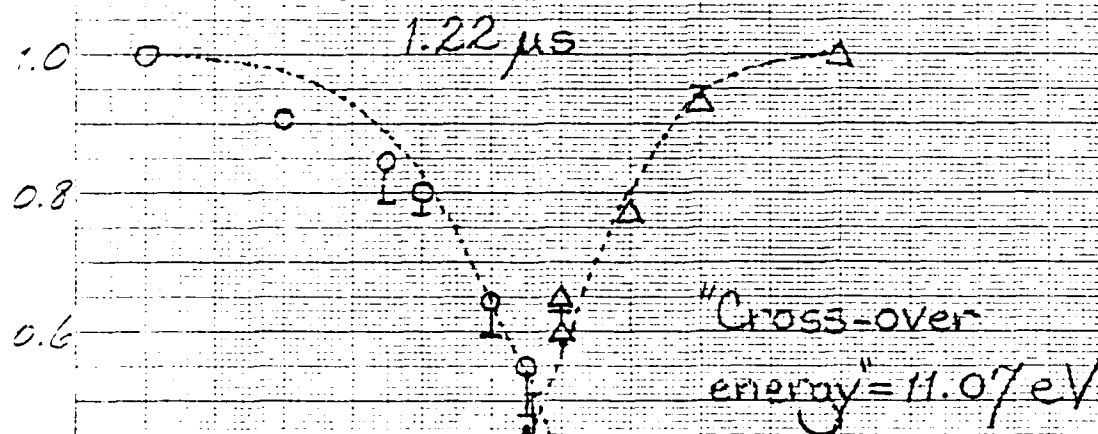
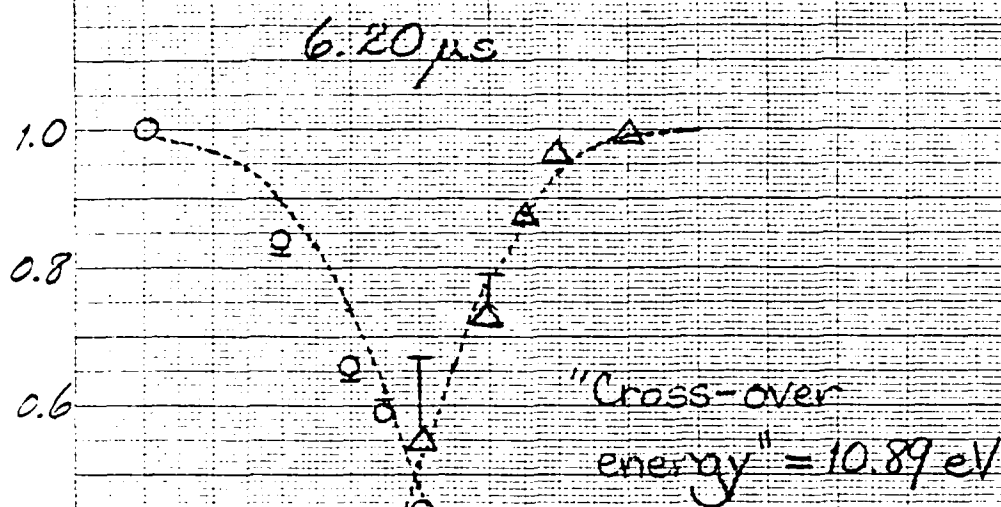
eV







RELATIVE ABUNDANCE



eV

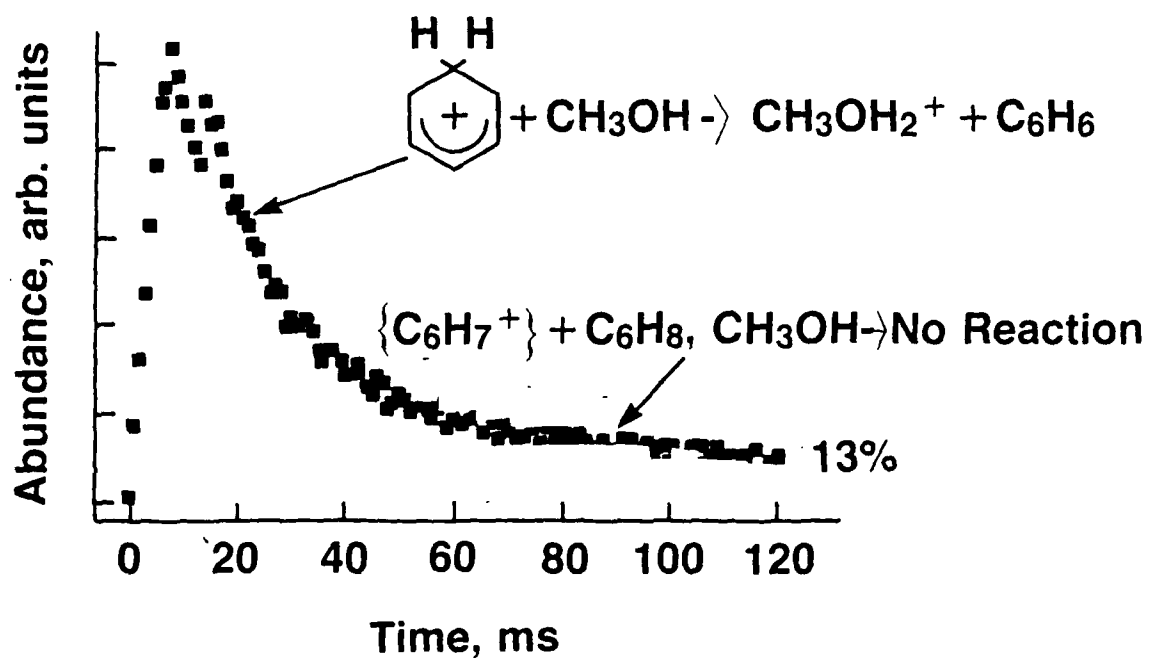
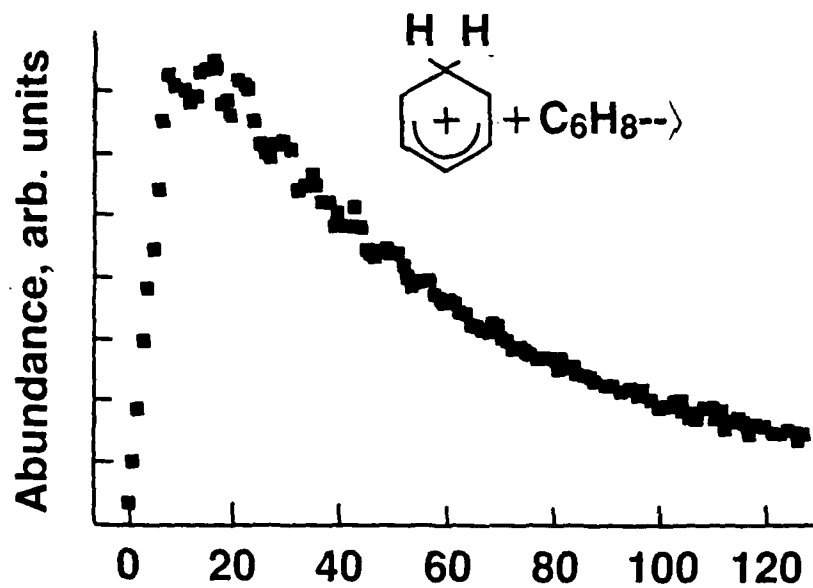
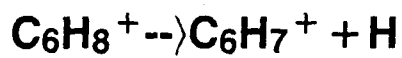
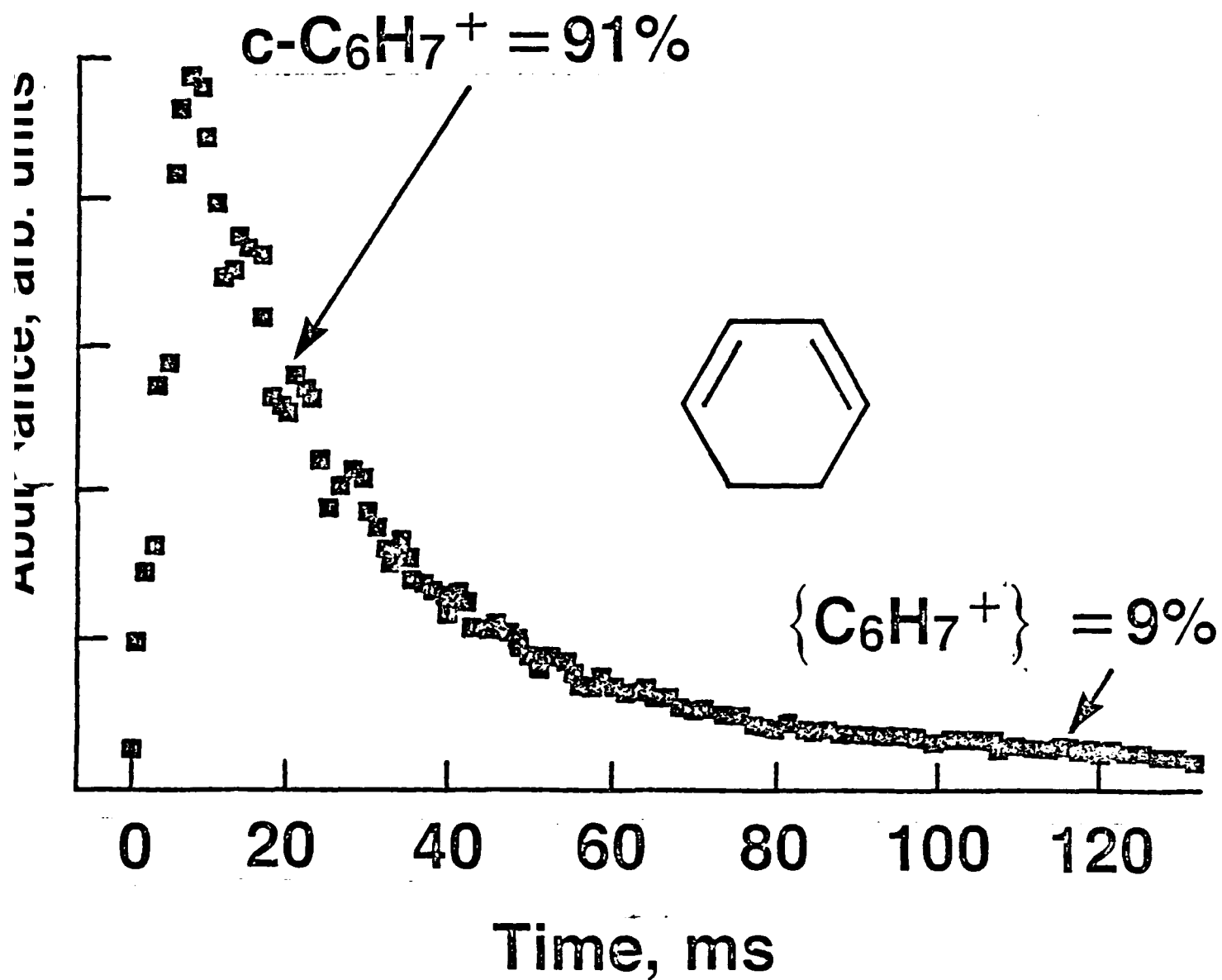


Fig 5



Arbitrary units

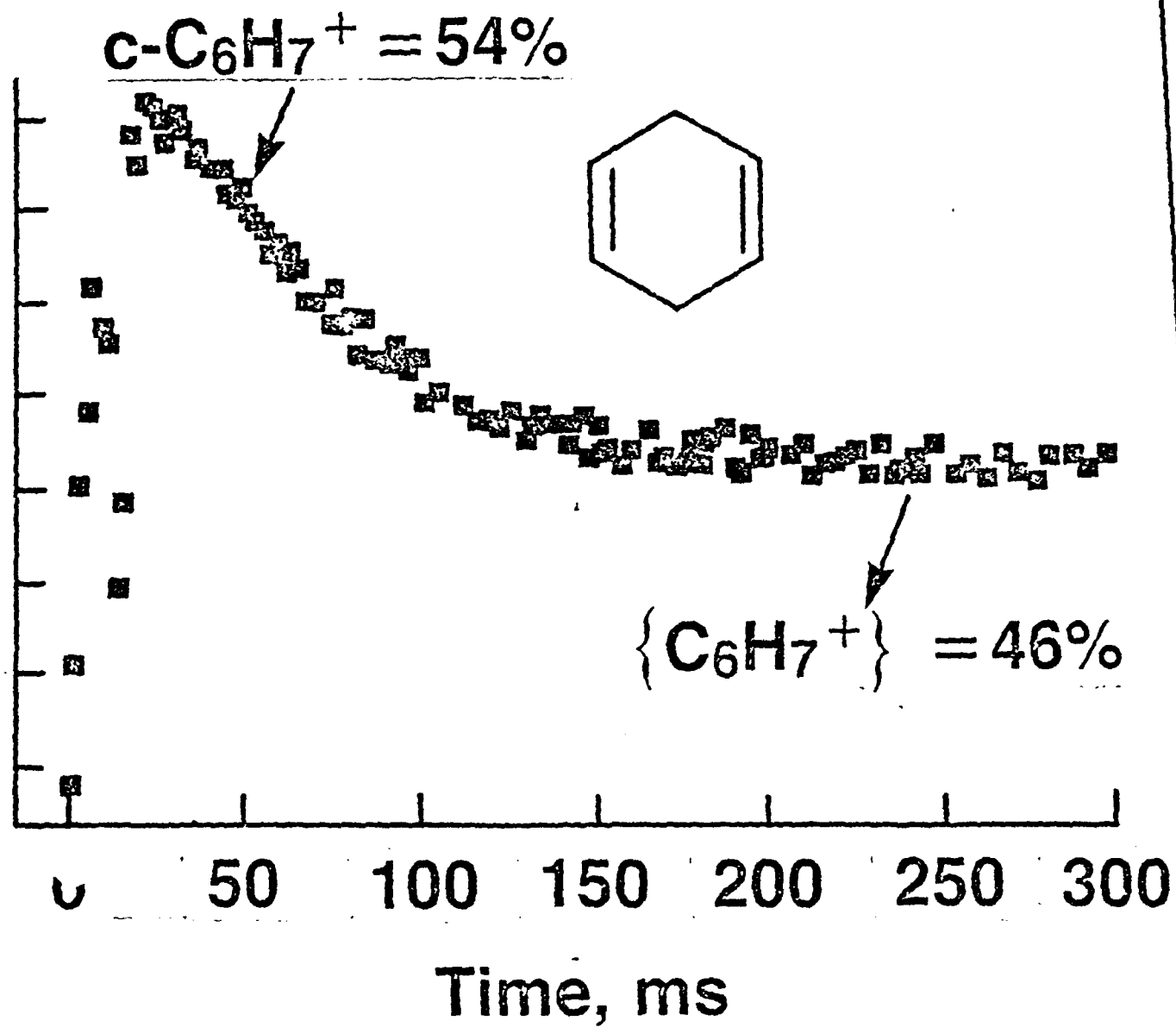


Fig 7

produced by the initial pulse. For this reason, each series of intensity-time profiles (for individual masses) were collected after a pre-conditioning period, and successive series were taken from a new spot on the surface. To check the amount of signal loss, with the number of laser shots, the major peak ( $C_3$ ) was sampled both at the beginning and end of a series.

### 3.2 Results:

Figures 3-5 show time-resolved, averaged intensity-profiles for the 36 ( $C_3^+$ ), 12 ( $C_1^+$ ), and 24 ( $C_2^+$ ) amu ions, respectively. Similar data were collected for the ions  $C_4^+$  and  $C_5^+$ . As has been noted in previous studies, during initial heating hydrocarbon impurities are released from even high purity graphite (e.g., see Zavitsanos and Carlson, [1973]). In the present study, this effect was observed primarily in the form of  $C_2H^+$  (25 amu),  $C_2H_2^+$  (26 amu), and  $C_4H_2^+$  (50 amu) mass spectral ions during the initial first few laser shots onto a given surface position. These signals tended to vanish more rapidly than those for the  $C_n$  species, suggesting the presence of surface hydrocarbon contamination. Of particular note was the long time delay for the 26 amu ( $C_2H_2$ ) species, as compared with the  $C_n$  ions. A similar effect may be noted in the results of Lincoln [1969]. For comparison, both our data and Lincoln's show a time difference between 26 and 36 amu of 150 to 200  $\mu$  sec. We attribute this time delay either to the  $C_2H_2^+$  arising from electron impact fragmentation of a heavier polyacetylene precursor (e.g.,  $C_4H_9$ ) or, to a reaction time such as diffusion in the substrate. The 57 amu ( $C_4H_9^+$ ) ion showed an even larger delay time and the intensity-time profile was exceptionally wide.

From post-run examination of deposit patterns around vacuum chamber apertures, the vaporization process was shown to be approximately independent of the laser incidence angle and the plume was normal to the surface to within a few ( $\sim \pm 5$ ) degrees for sample-surface to mount angles from 45 to 15 degrees.

In a typical laser-induced vaporization experiment, a 7 nsec 10 mJ laser pulse was focused at the sample surface by a 500 mm focal length f/10 lens which produced a spot size of 250 microns. The 20 J/cm<sup>2</sup> of deposited energy is converted into thermal excitation at the surface and penetrates to a depth of only a few tens of atomic diameters. Rapid vaporization occurs, leading at peak-temperature to the formation of a gas-dynamically stabilized plume which yields a molecular beam. The beam is collimated by three circular differentially pumped apertures, and travels a distance of 26 cm between the sample and ion chamber. Each aperture is sized to just allow clear passage of the beam through the 4.8 mm diameter entrance aperture of the mass filter ion source, and also through the larger ion source exit. Species are ionized by electron impact at adjustable voltages, and mass analyzed by a quadrupole mass filter. These filtered ions are then collected and amplified by an electron multiplier. The signals are averaged, with 0.5 usec/channel time resolution, and the sweep synchronized by a trigger generated from the onset of the laser beam. This data collection process gives a time resolved intensity-profile of an individual mass peak. Sufficient signal time-sweeps are collected (typically between 100 and 1000) to provide reasonably good statistics in the leading edge and peak centroid area. The process is repeated for each individual mass peak. It was observed that, dependent on laser beam to surface angle, the initial signal intensity would decay during the first few tens of pulses and then stabilize at a value about half that



Figure 2 shows details of the VHPMS vacuum system. The viewpoint (normal to the page) is that of the entering laser beam. For the present study, the chopper, in stage III, has been anchored with an open aperture centered on the beam line. The blade apertures are much larger than the diameter of the collimated beam. In the vacuum system, the mean free path of gas is always much greater than the local geometry. And, in the sample region, the pumping speed is calculated to be at least 1500 l/s. This pump conductance has been confirmed by pressure measurements at known gas loads. Although the laser pulse and vaporization time scale is too short for the pressure gauges to respond, the local pressure outside the gas-dynamic shock boundaries should be in the molecular flow regime. Thus we can eliminate from consideration any possible perturbation by post-expansion collisions.

The sample was mounted on a stainless steel bar. Graphite samples were taken from a rod of spectroscopic grade graphite selected by the NBS Analytical Chemistry Division for spectrographic analyses on the basis of its freedom from contaminants. The hydrogen content is unknown but probably insignificant, although weak mass spectrometric signals were observed corresponding to  $C_2H_2$  and other low hydrogen-containing species. Possible hydrocarbon contributions to the  $C_n$  ( $n = 1 - 5$ ) ion signals are estimated to be less than a few percent and can be neglected. Sample preparation consisted of parting-off a short section of 1/4 inch (~ 6.4 mm) rod, and milling a flat of the desired angle using carefully cleaned steel cutting tools. The angle between sample surface and mount (or laser beam, see figure 1) was chosen as 15 degrees for the data reported here. This geometry represented a compromise between the laser-entrance and mass spectrometer sampling angles. The reduced mass flux for the slightly off-axis sampling was not expected to be significant, as shown by the earlier study of Covington et al., [1977].

## 2. Subtask A: Laser Vaporization Kinetics of Carbon-Containing Refractories

### --Results and Discussion

#### 2.1 Apparatus and Experimental Approach

The basic apparatus, developed especially for this subtask, is shown schematically in figure 1. Note that the laser, molecular beam orifices, and mass spectrometer are configured to reduce the possibility of laser interaction with the portion of vapor plume directed toward the mass spectrometer. Such an interaction could lead to ionization and plasma effects not characteristic of the vaporization process, as noted in earlier studies, e.g., see Lincoln and Covington [1975]. The laser beam enters the first pumping stage of the Vertical High Pressure Sampling Mass Spectrometer (VHPMS) at right angles to the mass spectrometer beam line, as shown in figure 1.

The laser system basically consists of an externally mounted 10 Hz Nd/YAG laser (very recently upgraded to 20 Hz), operating at wavelengths from 1060 nm to 350 nm. To allow for ready visual alignment of the beam, the 532 nm doubled line of the laser fundamental has been chosen as the working wavelength. The laser pulse time used was about 7 nsec, which is negligible on the time scale of the vaporization process. This process required about 0.5-1  $\mu$ sec for a 10 percent change on the leading edge of the ion intensity-versus-time signal profile. Earlier studies, such as those of Ohse, et al., [1979], have indicated the utility of short pulse time, high power lasers (e.g., Nd/YAG) for controlled surface vaporization studies. The laser beam was focused onto the sample by a 500 mm focal length lens, mounted on a movable stage. A spot size of 250 microns was used. The laser was operated near threshold and adjusted to deliver the same power for each pulse in a data-averaging series.

crystals and the beam collimation telescopes, necessary to proper propagation of the beam, has been delayed (~ 6 months) by the vendor, and the new system is not expected to be fully operational until early in FY85.

Under subtask B, attempts to produce molecular clusters by non-equilibrium adiabatic expansion of NaCl, KCl, and  $C_n$  ( $n = 1 - 5$ ) molecular species showed no evidence of clustering at source vapor pressures to one atmosphere. Apparently, higher pressures and longer expansion times (e.g., larger nozzles and lower expansion pressure-ratios) are needed to remove the excess energy produced in the initial aggregation process. It is also possible, though unlikely in the present case, that a small amount of clustering may remain undetected due to destruction of the clusters during the electron impact ionization process in the mass spectrometer. Additional studies are planned to determine the conditions needed for cluster formation and detection.

With regard to subtask C, we have found that the ionization cross-section ( $\sigma$ ) can vary quite significantly with temperature, particularly for species exhibiting a large geometry change on ionization. Data obtained for the test cases, NaCl and KCl, exhibited large changes in  $\sigma$  (25:1) between high temperature (~ 1000 K) species and translationally cooled low temperature (~ 50 K) molecules. A quantitative potential energy curve model has been developed to account for this initially unexpected effect. The model has also been extended, on a qualitative basis, to allow for predictions of temperature dependent electron impact fragmentation with other high temperature species, including  $C_n$  ( $n = 1 - 5$ ). Future studies will attempt to validate and improve the model.

establishment of local thermodynamic equilibrium at the sample "surface."

The "surface" in these studies was actually slightly cratered by the focused laser beam, with a typical crater having dimensions of about 0.03 cm width and 0.01 cm depth. For minimum laser power (10 mJ) conditions, the surface temperature was determined indirectly from the mass spectral data to be  $4100 \pm 300$  K at a total species pressure of one atmosphere (1 atm = 101,325 Pa). A beam-velocity analysis of the  $C_n$  species indicated an appreciable cooling effect (to 2500 K) in the vapor plume by an adiabatic expansion process. Additional studies are needed to identify the processes occurring at a smooth surface, in comparison with those resulting from the shallow craters formed under the present experimental conditions. Planned experiments include:

- o Traversing the sample surface between successive laser shots--to avoid crater-formation.
- o Use of a rod-like sample geometry, with cross section dimension matching that of the hot-spot--to provide for a complete surface regression as opposed to cratering.
- o Data collection, at a fixed sample position, as a function of number of laser shots and, hence, crater size--to follow the transition between free ( $\alpha \leq 1$ ) and Knudsen-like (equilibrium,  $\alpha \approx 1$ ) vaporization conditions.

Based on these initial results, obtained with the 10 Hz Nd/YAG laser system, and also earlier tests with a CW  $CO_2$  laser, a new laser was selected (and procured by NBS) for permanent coupling with the mass spectrometric system. This 20 Hz Nd/YAG laser has been received and optically coupled with the mass spectrometer. However, delivery and installation of the doubling

o Subtask C: Ionization Processes.

Objective: To determine the influence of high temperature on molecular ionization processes, with emphasis on both partial and total electron-impact ionization cross-sections. A temperature dependence of these cross-sections would manifest itself in the electron impact fragmentation patterns of the  $C_n$  ( $n = 1 - 5$ ) species, for instance, and could account for some of the disparate literature results.

Of these areas, subtask A is the primary effort, with subtask C providing important information regarding mass spectral interpretation and particularly for high temperature systems. Subtask B deals with the link between the molecular-level initial vapor-forming process and the macroscopic process of aerosol formation. The principal research carried out under these subtasks, during FY84, is summarized as follows with additional details given in Section 2.

For subtask A, a Laser-Induced Vaporization facility has been constructed and tested. The apparatus consists of a 10 Hz, pulsed Nd/YAG laser coupled to a specially designed high pressure sampling mass spectrometer. In principle, the mass spectrometer can detect both charged and neutral species arising from the laser vaporization process. However, under the conditions of the present study, where laser-vapor plume interaction was avoided as far as possible, only neutral species were observed. Thus the ions referred to here are those resulting from electron impact ionization of molecular species in the mass spectrometer ion-source. Initial studies on an ultra-pure spectroscopic grade graphite sample, provided quantitative time-resolved mass spectral peaks of  $C_n$  ( $n = 1 - 5$ ) molecular ions with excellent signal-to-noise ratios and reproducibility. The absolute and relative concentrations of the corresponding neutral species were consistent with the

6. Molecular Basis for Laser-Induced Vaporization  
of Refractory Materials

J. W. Hastie, D. W. Bonnell, and P. K. Schenck  
High Temperature Processes Group  
Inorganic Materials Division  
Gaithersburg, MD 20899

1. Introduction and Summary

The interaction of high power lasers with refractory materials has been studied by a number of workers during the last two decades. Most of these studies have concentrated on the macroscopic, non-molecular, processes such as: crater formation, material removal rate, and plume dynamics. The objective of the present study is to provide a molecular-level description of the vaporization processes, and to provide a fundamental link to smoke and aerosol formation. These processes are central to the interaction of high power lasers with graphitic or other refractory materials. This report describes the results of research carried out during FY84. The effort is divided into three interlinked subtasks, as follows:

o Subtask A: Laser Vaporization Kinetics of Carbon-Containing Refractories.

Objective: To determine molecular specific mechanisms of laser-induced vaporization using high energy laser heating of surfaces, and time-resolved, high pressure sampling mass spectrometry of the vapor species produced.

o Subtask B: Mechanisms of Formation for Submicron Metal-Containing Particulates.

Objective: To follow aerosol formation from expanding high temperature vapors in a vacuum environment. Particular emphasis is given to the mechanism for homogeneous nucleation which results from aggregation of molecular species to form cluster intermediates and macroscopic particulates.

PROTON AFFINITIES OF  $\text{HC}\equiv\text{C}-\text{C}\equiv\text{CH}$ ,  $\text{HC}\equiv\text{C}-\text{C}\equiv\text{N}$  and  $\text{N}\equiv\text{C}-\text{C}\equiv\text{N}$ :  
EXPERIMENTAL AND AB INITIO STUDIES

by

Michael Meot-Ner (Mautner) and Thomas J. Buckley

Center for Chemical Physics  
National Bureau of Standards  
Gaithersburg, Maryland 20899

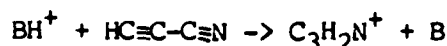
and

Carol A. Deakyne

Department of Chemistry  
College of the Holy Cross  
Worcester, Massachusetts 01610

Abstract

The proton affinity of  $\text{HC}\equiv\text{C}-\text{C}\equiv\text{N}$  was determined in the NBS pulsed high pressure mass spectrometer through measurements of equilibrium constants for proton transfer reactions with bases of known gas basicity:



The proton affinity was determined to be 180 kcal/mol. Since protonated diacetylene,  $\text{C}_4\text{H}_3^+$ , and protonated cyanoacetylene,  $\text{C}_3\text{H}_2\text{N}^+$ , undergo fast reactions with the respective precursor molecules, proton transfer equilibria could not be established in these systems. Therefore, the proton affinities of  $\text{HC}\equiv\text{C}-\text{C}\equiv\text{CH}$  and  $\text{N}\equiv\text{C}-\text{C}\equiv\text{N}$  have been determined in the NBS pulsed ion cyclotron resonance spectrometer (ICR) using the technique known as "bracketing", in which one determines the occurrence or non-occurrence (and in the former case, the efficiency) of the reactions:



for a series of bases, B, of known gas basicity. From these results one can estimate the energy at which the protonation of the compound of interest is thermoneutral, and thereby obtain the proton affinity value. The results led to a value of 180 kcal/mol for the proton affinity of diacetylene, and 154 kcal/mol for cyanogen.

The proton affinities of these molecules reflect the stabilizing or destabilizing effects of the multiple triple bonds and the highly polar  $-\text{C}\equiv\text{N}$  groups in the relevant molecules and ions; these interactions are studied through ab initio calculations presented here.

17. K. Kimura, S. Katsumata, Y. Achiba, T. Yamazaki, and S. Iwata, "Handbook of HeI Photoelectron Spectra of Fundamental Organic Molecules", Japan Scientific Societies Press, Tokyo (1981).
18. The  $C_6H_7^+$  ions, which may be produced with as much as 49 kcal/mol excess energy in this reaction, are deactivated by collisions with methane before undergoing reaction in these systems. This is substantiated by the observation that proton transfer rate constants for  $C_6H_7^+$  ions formed by protonation of benzene by  $H_3S^+$  (maximum excess energy of  $C_6H_7^+$ , 11 kcal/mol) are identical to those measured in the methane mixtures.
19. M. T. Bowers, D. D. Elleman, R. M. O'Malley and K. R. Jennings, J. Phys. Chem. 74, 2583 (1970).
20. (a) J. B. Pedley and J. Rylance, "Sussex-NPL Computer Analysed Thermocchemical Data: Organic and Organometallic Compounds", Univ. of Sussex (1977); (b) H. M. Rosenstock, K. Draxl, B. W. Steiner, and J. T. Herron, J. Phys. Chem. Ref. Data 6, Suppl. 1 (1977); (c) R. D. Levin and S. G. Lias, Natl. Stand. Ref. Data Ser., Natl. Bur. Stand. (U. S.), 71 (1982).
21. wolfgang Rotn, personal communication.
22. H. M. Rosenstock, J. Dannacher, and J. F. Liebman, Radiat. Phys. Chem. 29, 7 (1982).
23. S. E. Stein, Combustion and Flame 51, 357 (1983).



## References

1. (a) C. Lifshitz, Y. Gleitman, S. Gefen, and U. Shainok, *Int. J. Mass Spectrom. Ion Phys.* 40, 1 (1981); (b) C. Lifshitz and Y. Gleitman, *Int. J. Mass Spectrom. Ion Phys.* 40, 17 (1981); (c) C. Lifshitz and Y. Gleitman, *J. Chem. Phys.* 77, 2383 (1982); and references cited therein.
2. J. L. Franklin and S. R. Carroll, *J. Am. Chem. Soc.* 91, 6564 (1969).
3. M. Allan, J. Dannacher, and J. P. Maier, *J. Chem. Phys.* 73, 3114 (1980).
4. H. Schwarz, Wolfschutz, and Levsen, quoted in reference 1(b).
5. G. S. Groenewold and M. L. Gross in "Ionic Processes in the Gas Phase" (M. A. Almoester Ferreira, Editor) D. Reidel Publ. Co., Dordrecht (1984).
6. S. G. Lias, J. F. Liebman, and R. D. Levin, *J. Phys. Chem. Ref. Data*, in press (1984).
7. (a) R. E. Winters and J. H. Collins, *Org. Mass Spectrom.* 2, 299 (1969); (b) A. G. Harrison, P. Haynes, S. McLean, and F. Meyer, *J. Am. Chem. Soc.* 87, 5099 (1965).
8. (a) S. G. Lias, J. R. Eyler, and P. Ausloos, *Int. J. Mass Spectrom. Ion Phys.* 19, 219 (1976); (b) S. G. Lias and T. J. Buckley, *Int. J. Mass Spectrom. Ion Proc.* 56, 123 (1984).
9. (a) R. L. Stockbauer, *Int. J. Mass Spectrom. Ion Phys.* 27, 185 (1977); (b) R. L. Stockbauer and H. M. Rosenstock, *Int. J. Mass Spectrom. Ion Phys.* 27, 185 (1978); (c) H. M. Rosenstock, R. L. Stockbauer, and A. C. Parr, *J. Chem. Phys.* 71, 3708 (1979); (d) H. M. Rosenstock, R. Stockbauer, and A. C. Parr, *J. Chem. Phys.* 73, 773 (1980).
10. R. T. McIver, Jr., R. L. Hunter, E. B. Ledford, Jr., M. L. Locke, and T. J. Franck, *Int. J. Mass Spectrom. Ion Phys.*, 39, 65 (1981).
11. (a) M. Allan and J. P. Maier, *Chem. Phys. Lett.* 43, 94 (1976); (b) V. E. Bondybey, J. H. English, and T. A. Miller, *J. Mol. Spectrosc.* 80, 200 (1980).
12. E. M. Popov and G. A. Kogan, *Opt. Spectrosc.* 17, 362 (1964).
13. C. Di Lauro, N. Neto, and S. Califano, *J. Molec. Str.* 3, 219 (1969).
14. (a) S. J. Cyvin and O. Gebhardt, *J. Molec. Str.* 27, 435 (1975); (b) O. Gebhardt and S. J. Cyvin, *J. Molec. Str.* 27, 345 (1975).
15. P. J. Domaille, J. E. Kent, and M. F. O'Dwyer, *Aust. J. Chem.* 27, 2463 (1974).
16. T. Shimanouchi, "Tables of Molecular Vibrational Frequencies. Consolidated Volume I", *Nat. Stand. Ref. Data Ser.*, Nat. Bur. Stand. (U.S.), 39 (1972).

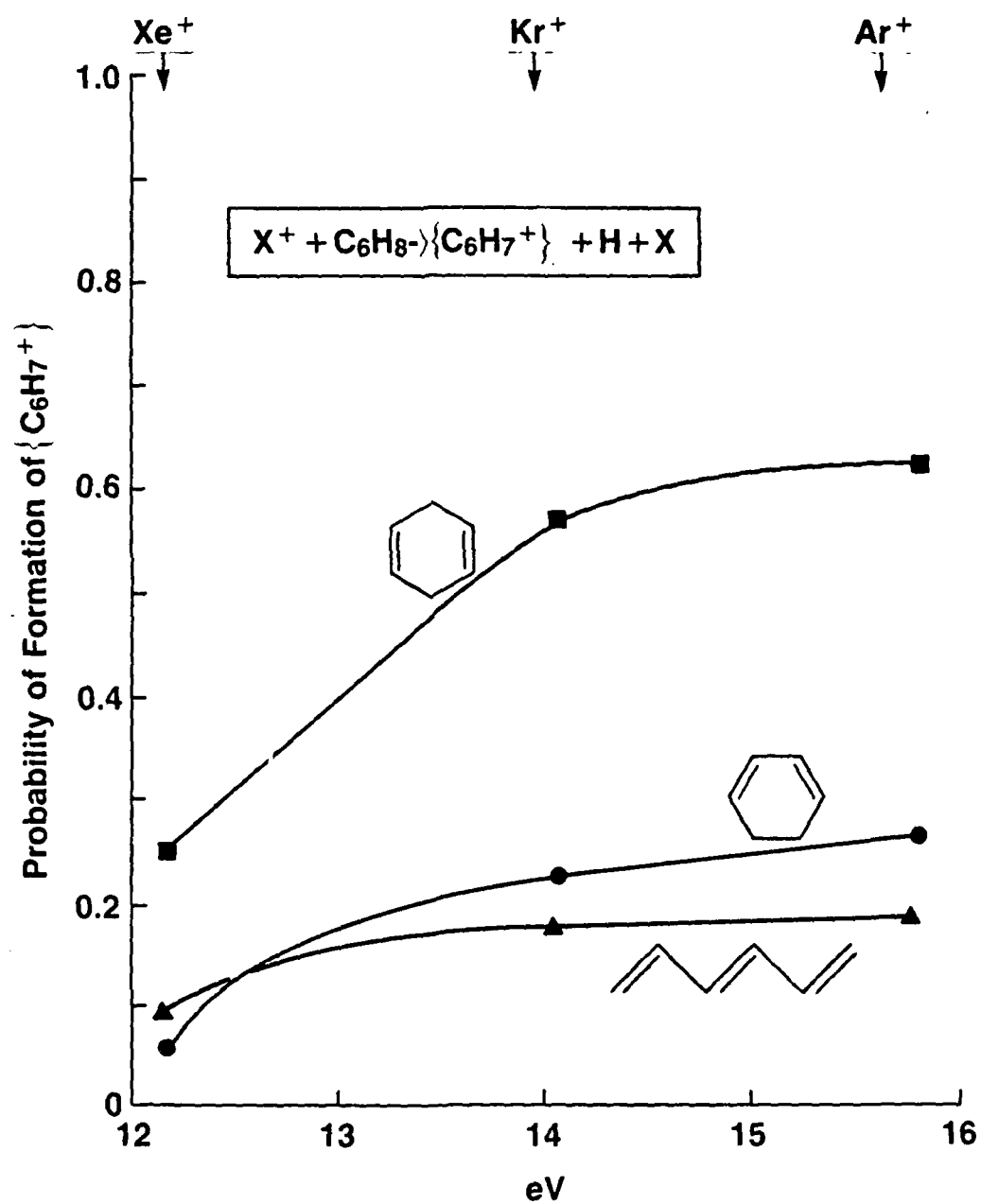
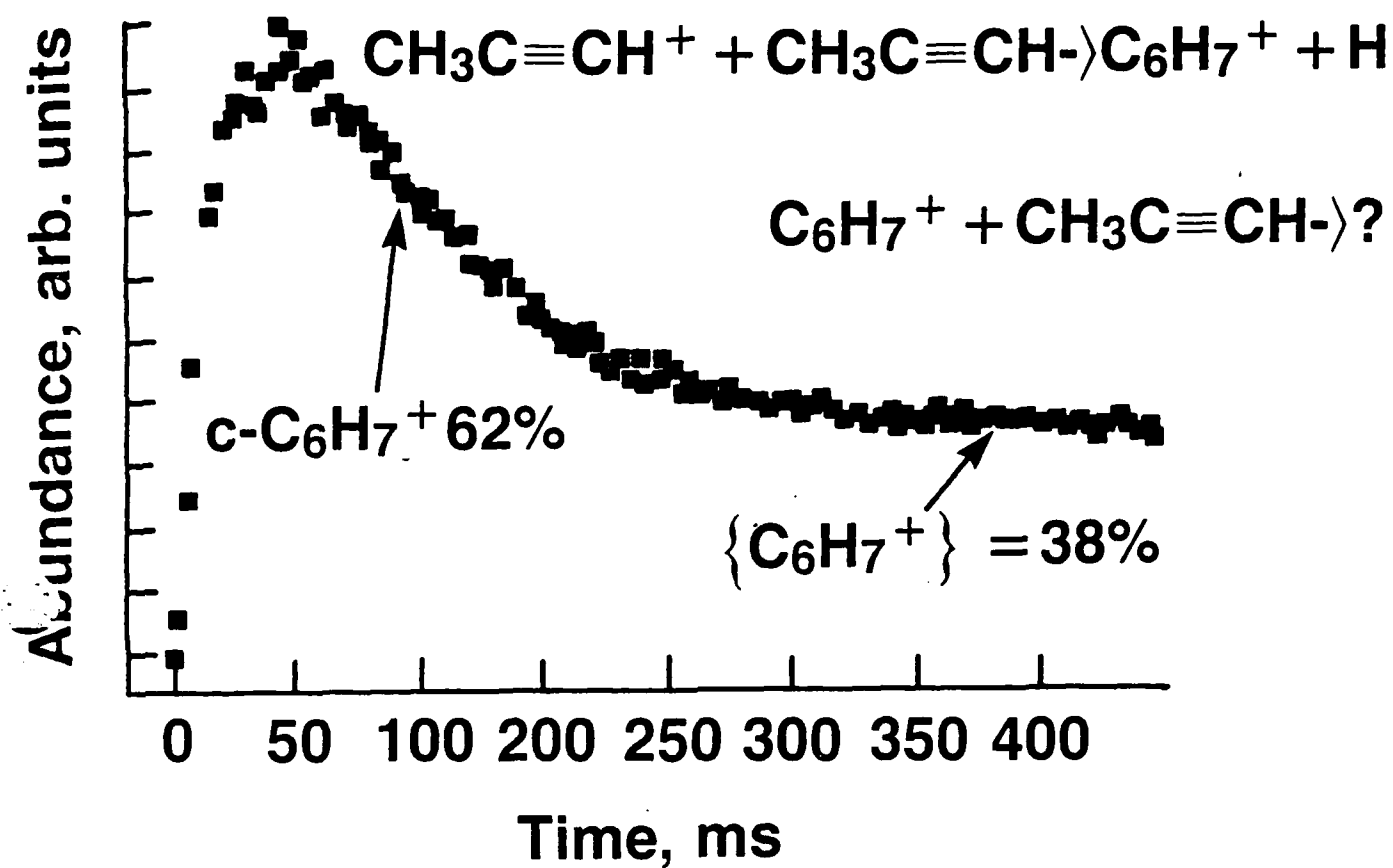
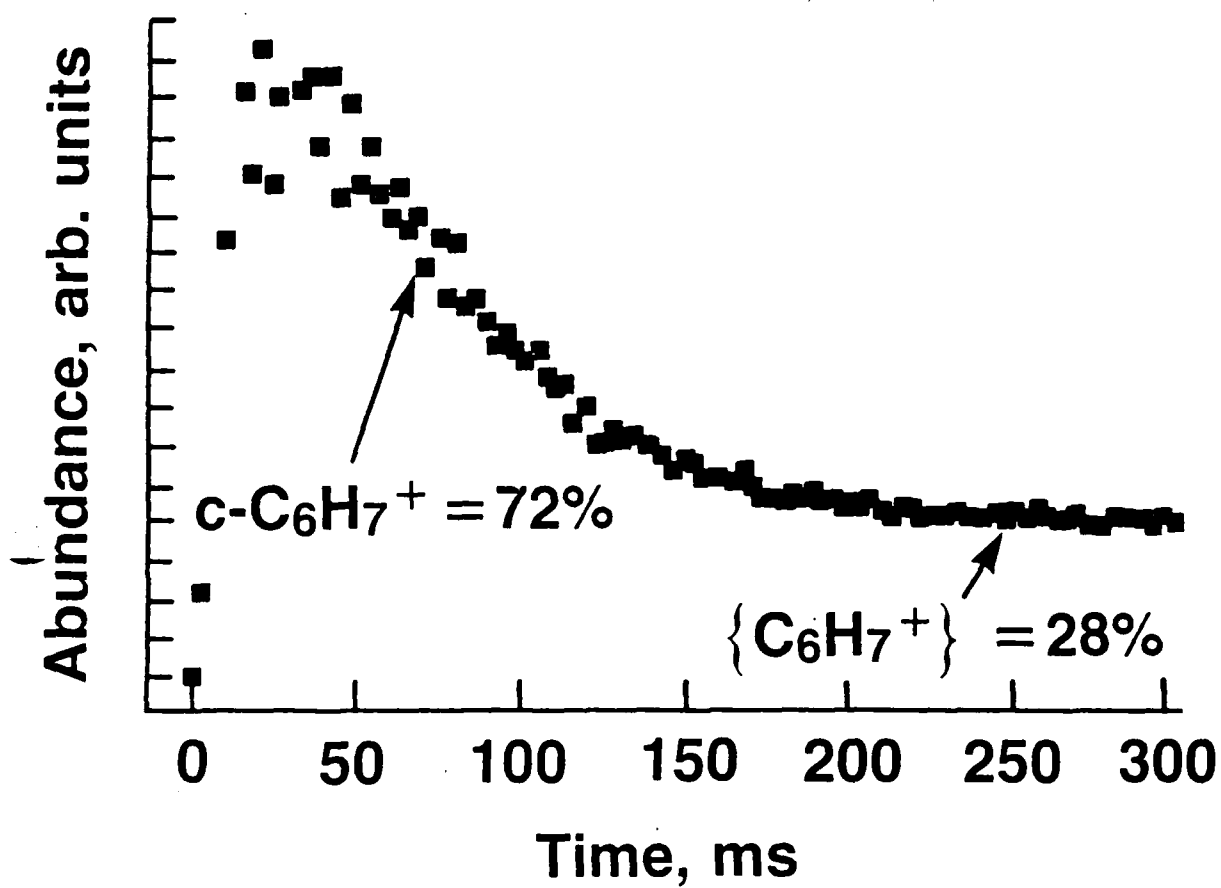
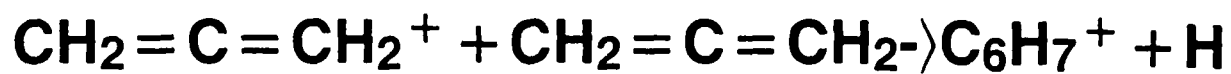


Fig 10





The intensity-time profiles from  $C_n$  are quite similar to those observed in analogous measurements by Olstad and Olander [1975] for  $Fe_n$  species. These authors provide a theoretical analysis of the atom density pulses in terms of an equilibrium vaporization model with known laser pulse energy-time profiles. A similar analysis should be possible for the  $C_n$  system.

Table 1 gives results from two runs at widely differing ionizing electron energy. The validity of the assignment of ions to neutral precursors is borne out by the insignificant changes in ion ratios from 26 eV to 96 eV ionizing electron energy. Ion intensities, proportional to neutral gas concentrations, were computed from the intensity-time profiles in two ways; (1) peak maximum at peak centroid, and (2) integrated peak intensity. Both techniques gave consistent results which were almost independent of ionizing energy. However, the peak maximum results indicated the presence either of a slight excess of atomic-carbon, or of an unknown sampling artifact which affects only the lowest mass  $C_n$  species (see also Section 2.3).

The results of Table 1 may be interpreted to indicate that the graphite species vaporization coefficients appear to be very close to unity, contrary to the results of earlier work. This observation may result from the effect of signal-averaging several hundred vaporization events from a crater which could serve as a crude Knudsen cell. Other significant causes of data differences between this and earlier work may arise from our avoidance of laser/plume interaction and the use of relatively short laser pulses to reduce perturbation of the gas-dynamic process. Also, as the present study was performed off the central plume axis, it is possible that if non-equilibrium effects occurred only along the perpendicular axis they would

not have been observed in the present work. As the plume is highly forward-peaked in the perpendicular direction, this possibility needs further study.

### 2.3 Temperature Determination

For these initial studies, several indirect methods have been used to derive the temperature ( $T_0$ ) of the laser heated spot. Application of potentially more accurate optical pyrometric methods have been deferred due to uncertain emissivity data and the difficulty of accounting for plume contributions to the emission signals. Under the laser pulse conditions used, it is likely that only the surface layer (a few wavelengths, i.e., ~ 2000 to 5000 nm) is heated and the total extent of vaporization is confined to an area nearly equal to that of the laser spot [Hall, 1984]. The initial tests used a laser spot intensity profile which is roughly "donut-shaped." The effect of such a spot geometry, relative to a gaussian profile, should be to level-out the temperature profile of the heated area.

#### 2.3.1 Beam Velocity Analysis

The time-of-arrival,  $\Delta t$ , of the beam-species may be used as a measure of the plume temperature. Regardless of the exact model of the vaporization and beam-forming process, if a collection of gas molecules are in thermal equilibrium their velocity function is proportional to  $(T_0/M)^{1/2}$ , where  $M$  is the individual species molecular weight. As  $\Delta t$  is inversely proportional to velocity, a linear plot of  $\Delta t$  versus  $(M)^{1/2}$  is indicative of thermal equilibrium. Figure 6 shows that the various  $C_n$  species exhibit such behavior. Using the assumption of the equipartition of translational energy, one has

$$Mv^2/2 = 3kT/2 \quad (2.1)$$

where  $v$  is the most probable velocity, i.e., the peak of the velocity distribution, and  $T$  is the beam temperature ( $\langle T_0 \rangle$ ). Because peaking of the ion intensity-time-profile is caused by cooling of the sample, the arrival times were selected at the half-height position of the leading edge of the profile. Correlating this time with the most probable velocity yields the time-of-arrival function

$$\Delta t = (d/3kT)^{1/2} \cdot M^{1/2} \quad (2.2)$$

where  $d$  is the flight distance, 26 cm. Note, in figure 6, that the zero mass intercept, a measure of the inherent delay in the quadrupole filter, is quite small. From these arguments, and the slope of the 100 eV curve of figure 6, we obtain a beam temperature estimate of  $2500 \pm 300$  K. This temperature is much lower than is reasonable for the degree of vaporization observed and may be taken as evidence of expansion-cooling, followed by translational equilibration as the vapor species pass through a shock-front stagnation zone. Ohse, et al., [1979] have noted that for free vaporization from a surface, gas-dynamic models predict a rapid temperature drop to the sonic point such that  $T \sim 2T_0/3$ . This prediction, together with the above velocity model, suggests a pre-expansion temperature ( $\sim T_0$ ) of  $3800 \pm 300$  K, which is quite consistent with the thermodynamic arguments given below. Although this temperature analysis is not yet rigorous, our experimental results (not given here) for the thermochemically more-established BN system provide excellent confirmation, as we obtain  $4000 \pm 300$  K by comparing the  $C_2^+$  arrival time relative to that for  $B^+$  at  $T_0 = 2900$  K (see table 2). Other supporting arguments are also summarized in table 2.

### 2.3.2 Species Intensity Analysis

The time-of-arrival evidence for thermal equilibrium suggests that the "known"  $C_n$  species distribution with temperature can be used to derive the sample temperature ( $T_0$ ) from the measured species concentration ratios. Also, the beam-formation process is quite similar to that for more usual supersonic expansions, where the beam composition represents a "frozen equilibrium" and corresponds to the pre-expansion temperature/pressure conditions [Bonnell and Hastie, 1979]. The high pumping speed of the vacuum system used for the present studies, and the pulsed nature of the gas evolution process, further ensures high expansion ratios and "frozen equilibrium" in the gas-dynamic process.

Values of "known"  $C_n$  species concentration ratios were calculated as a function of temperature using the JANAF [1971] thermochemical tables. While other sources of thermodynamic data exist (see discussion in section 2.4), these tables still provide the most widely accepted critically evaluated thermodynamic functions for  $C_n$  species. Table 1 gives temperatures calculated from the listed  $C_n/C_3$  ratio data. Note that although the temperature from the  $C_1/C_3$  ratio fortuitously agrees with the post-expansion temperature (time-of-arrival data), such a temperature is unrealistically low for the observed species pressures. The corresponding ratios for the  $C_4$  and  $C_5$  species yield temperatures that are more consistent with those expected and also with those indicated by the above beam velocity analysis.

The anomalous low temperature result could be interpreted as being due to an apparent excess of  $C_1$ . Arguments for and against additional sources of  $C_1^+$  include:



- o Electron impact fragmentation of higher mass  $C_n$  species or contaminants such as CO. In this connection, it should be noted that the literature data were usually obtained at lower electron energies than for the present study. However, the present results are consistent with the lower eV data of Berkowitz and Chupka [1964] and Drowart, et al., [1959].
- o A compelling argument against significant fragmentation in the present study is the time-of-arrival result which indicates that  $C_1^+$  arises from a 12 amu neutral, i.e.,  $C_1$ .
- o Analysis of the  $C_n^+$  ion-stabilities (bond dissociation energies) indicates no loss of stability on ionization of  $C_n$ ; hence no major fragmentation effect is likely.
- o The constancy of ion-ratios over the range 26 to 96 eV is consistent with an absence of fragmentation and the existence of a single ion-precursor for all ions.
- o The  $C_1^+$  appearance potential curve indicates  $C_1$  as the major precursor.
- o From the  $C_1^+$  ion intensity, the carbon-atom pressure ( $P_C$ ) is calculated to be equal that obtained from JANAF [1971]. For this calculation  $k_C$ , the mass spectrometer proportionality constant, was obtained from our established boron ion intensity data (not given here).

Wachi and Gilmartin [1970] found  $C_1/C_n$  to decrease with time, and to depend on sample preparation and surface morphology. Also, considerable literature controversy exists concerning the entropy and hence absolute partial pressure of  $C_3$ . Thus, the use of observed  $C_1/C_3$  ratios together with JANAF [1971] calculated ratios to infer temperatures, etc., seems : sky. In

this connection, literature more recent than JANAF [1971], as reviewed by Meyer and Lynch [1973], indicates  $C_1/C_3 < \text{JANAF}$ , with  $C_3$  being more significant than JANAF; e.g., at 4000 K, with pressures indicated in atm,

$$C_1/C_3 (\text{JANAF}) = (7.9 \times 10^{-2}) / (5.0 \times 10^{-1}) = 0.16, \text{ whereas}$$

$$C_1/C_3 (\text{M \& L}) = (7.9 \times 10^{-2}) / (1.2) = 0.066$$

$$\text{i.e., JANAF is too high by factor of } 0.16/0.066 = 2.4,$$

$$\text{i.e., } C_3 (\text{M\&L}) = 2.4 \times \text{JANAF}.$$

This difference is comparable with the uncertainty in cross sections used to translate ion intensity to partial pressure data. However, use of the Meyer and Lynch [1973] or Meyer, et al., [1973] data and our  $C_1/C_3$  results gives an even lower  $T_0$  than the JANAF value of 2600 K, which is impossible. Hence the  $C_1^+$  data do not appear to have thermodynamic significance for  $C_1$  concentration measurement.

Another, less-likely, argument as to why  $C_1/C_3$  gives a lower  $T_0$  than  $C_n/C_3$  ( $n > 1$ ) is based on the higher sublimation enthalpies for  $C_n$  ( $n > 1$ ), as compared with  $C_1$ . This means that  $C_1$  becomes a relatively more important species at lower temperatures and, as the hot spot cools,  $C_1$  could become more significant than  $C_n$  ( $n > 1$ ). However, this would require  $T_0$ , as calculated from the crater size, to be less than from the  $C_n/C_3$  ratio data. No crater size data have been obtained to test this hypothesis. However, for our analogous study of BN (results not given here), the crater size measurements gave a high value for  $T_0$ . This explanation would also require our observation of  $B/B_2$  to yield a lower  $T_0$  which was not the case.

For the case of the  $C_2/C_3$  ratio (see table 1), if the relative cross-sections were 1/1.5, which is quite reasonable based on empirical trends in other systems, the calculated temperature would be 4200 K, in agreement with the values obtained using the  $C_4$  and  $C_5$  species. This cross-section ratio agrees favorably with the estimate of 1/1.23 given by Meyer and Lynch [1973]. The higher polymeric  $C_n$  species should have cross-section ratios close to unity, which we have assumed in the present analysis.

#### 2.4 Literature Studies of Laser-Induced Vaporization of Graphite

Since the JANAF evaluation, dated December, 1969 [in JANAF, 1971], a number of studies of the graphite vaporization system have been reported over the period 1968 to 1983. Analysis of the results of these studies indicates that the equilibrium distribution of various carbon species at temperatures greater than 2800 K is still uncertain.

##### 2.4.1 Literature Survey for the Period 1968-1983

###### o Zavitsanos [1968]

Zavitsanos [1968] carried out laser vaporization mass spectrometric studies using conditions similar to those of the present work. However, only the  $C_1/C_3$  ion intensity ratios are comparable between the two studies, as shown in table 3. The crater dimensions observed by Zavitsanos [1968], and found in the present study, are notably similar for various graphite-types at 4100 K with similar laser energy conditions.

###### o Clarke and Fox [1969]

The vaporization data from graphite filaments at temperatures to 3400 K were analyzed in terms of  $C_2$  as the principal species with a vaporization coefficient,  $\alpha = 1$ . For this analysis, the JANAF  $\Delta H_{rn}(298)$  (i.e., for  $2C(s) = C_2$ ) was assumed to be correct and equal to 832.6 kJ/mol. Assumptions

of  $C_1$ ,  $C_2$ , and  $C_3$  as the principal species with  $\alpha = 1$ , or with the Thorn and Winslow [1957]  $\alpha$  values, do not fit the data. Later workers have apparently not attempted to rationalize the results of Clarke and Fox [1969] with the prevailing viewpoint of  $C_3$ , rather than  $C_2$ , as the dominant species. These authors also cite all pertinent earlier literature work.

o Wachi and Gilmartin [1970]

These workers studied the free vaporization (Langmuir) behavior of various graphites using both double-focusing magnetic sector and time-of-flight mass spectrometric detection of the  $C_1$  to  $C_5$  species. A relatively low ionizing electron energy of 17 eV was used. Above 17.5 eV, the appearance potential curve for  $C_3$  showed a pronounced upward curvature, indicating possible fragmentation of higher molecular weight species. Ion molecule reactions in the ion source were also suggested as a possible additional source of  $C_3^+$ . Apparent activation energies were basically in agreement with those reported earlier by Zavitsanos [1968]. No attempt to convert the ion intensity data to absolute species concentrations was made in this study. Thus, these results cast little light on the equilibrium thermodynamic vaporization behavior of the various  $C_n$  species. It is pertinent, however, to note the close similarity between the activation energies and equilibrium enthalpies (literature data) of vaporization. This similarity suggests local equilibrium conditions may be present under free vaporization conditions for graphite. Another important observation from this study was the pronounced time-dependency of the relative ion intensities, with  $C_3^+$  showing a strong increase relative to  $C_1$  and  $C_2$ . This effect was tentatively attributed to changes in surface morphology and the possible formation of an allotropic form of carbon.

o Milne et al. [1972]

Using Knudsen effusion mass spectrometry, these workers obtained relative ion intensity mass spectral data for  $C_1^+$  -  $C_7^+$  at temperatures to 3300 K and with 17 eV electron energy. The ion ratios between  $C_1$ ,  $C_2$ ,  $C_3$  and  $C_5$  agree well with the extrapolated data of Drowart et al. [1959], and hence JANAF [1971]. The  $C_4$  partial pressures were lower than those indicated by JANAF [1971] and the  $C_6$  and  $C_7$  values were lower than theoretical predictions, including those of Leider et al., [1973]. Useful second law data were obtained only for the relatively abundant  $C_3$  and  $C_1$  species. During initial heating,  $C_4$  (48 amu) was anomalously high due to presence of a Ti impurity at the same amu. A comparison between the extrapolated results of Milne et al., [1972] and the present work is given in Table 4. Note that  $C_2/C_3$  is the only ion ratio in agreement for the two studies.

The Milne et al., [1972] intensity-time profiles showed multiple peaks from each ion, which they attributed to possible ion trapping in the ion source. The positions and shapes for  $C_1^+$ ,  $C_2^+$  and  $C_3^+$  suggested substantial  $C_3$  fragmentation at 50 eV and none at 17 eV. There was also some indication of  $C_3^+$  fragment-ion formation at the higher temperatures. The narrow  $C_3^+$  peak shape was indicative of non-effusive expansion conditions. Note, however, that their pressures did not exceed  $\sim 10^{-3}$  atm for a 1/8 in. diameter cell orifice size and these conditions, while outside of molecular effusion, would not lead to excessive gas-dynamic cooling.

o Zavitsanos and Carlson [1973]

Knudsen effusion mass spectrometry to 3000 K indicated good agreement with the JANAF [1971]  $C_1$  -  $C_4$  partial pressures. But the JANAF  $C_1$  pressures were used to calibrate the pressure scale. These workers also used the newer  $C_3$  thermodynamic functions of Strauss and Thiele [1967] but this did not

improve the poor agreement between second and third law  $C_3$  vaporization enthalpies. The possibility (also suggested by others) of a temperature-dependent  $C_3$  ionization cross section was mentioned as a possible source of error with the second law enthalpy. Heavier species than  $C_4$  were not significant in this study. This observation does not conflict with the analysis of Leider, et al., [1973] since they predict  $C_5 - C_7$  as significant species at higher temperatures ( $> 4000$  K) than the  $< 3000$  K achieved by Zavitsanos and Carlson [1973]. The appearance potential data of these latter authors was considered evidence of negligible fragmentation at ionizing electron energies to 20 eV. However, the structure of their curves could also be interpreted to indicate fragmentation. More precise appearance potential measurements of  $C_3$  [Wachi and Gilmartin, 1970] over pyrolytic graphite at 2788 K, showed a pronounced break at 17.5 eV, indicative (but not proof) of fragmentation of a higher polymer or other carbon-containing species. Extrapolation of these data to 26 eV suggests about 30 percent of  $C_3^+$  could arise from fragmentation in the present studies.

o Meyer et al., [1973]

Pulse laser vaporization of pyrolytic graphite with mass spectrometric (time-of-flight) analysis indicated  $C_n$  integrated ion intensities (relative) of:  $C_1$  (1.0),  $C_2$  (1.3), and  $C_3$  (18), at 18.6 eV, with higher n-species being negligible. Note that our corresponding values are:  $C_1$  (1.0),  $C_2$  (0.35), and  $C_3$  (3.1), at 26 eV. Using estimated ionization cross sections and other ion intensity conversion factors, the corresponding relative partial pressures for the Meyer et al., [1973] data are:  $C_1$  (1.0),  $C_2$  (0.32), and  $C_3$  (35). Based on the Palmer and Shelef [1968]  $C_3/C_1$  pressure ratio data, the temperature is indicated as 4500 K. Pulsed laser vaporization studies of graphite generally indicate surface temperatures in the range 4000 to 4500 K.

From their analogous studies on TaC, where only  $C_1$  and  $C_3$  were significant, we can argue that the fragmentation,  $C_1^+(C_3)$  or  $C_2^+(C_3)$  is not a significant factor in the graphite mass spectra, at least to 18.6 eV.

Note that a significant difference between the Meyer et al., [1973] experiments and ours is their use of a single laser pulse and hence the need to consider vaporization coefficients in their conversion of ion intensities to partial pressures. Their intensity-time results are similar to ours and do not show the anomalous secondary peaks characteristic of the Milne et al., [1972] observations. However, their laser-plume geometry was coaxial, giving rise to possible laser perturbation of the plume species.

Hydrocarbon species noted by Meyer et al., [1973] over pyrolytic graphite included,  $C_2H_2$ ,  $C_4H_2$ , and  $C_6H_2$ , in addition to  $H_2$  and  $CO$ ;  $C_2H_2$  and  $CO$  were also noted over TaC.

o Meyer and Lynch [1973]

Their analysis of literature results is closer to that of Palmer and Shelef [1968], and also of Zavitsanos [1968] and Leider et al., [1973] than that of JANAF [1971]. The main result is that the  $C_3$  partial pressures are predicted to be about three times greater than for the JANAF [1971] data. At temperatures in the region of 4000 K, the following differences are found between the Meyer and Lynch [1973] and JANAF [1971] evaluations:

$\frac{C_1/C_3 \text{ (ML)}}{C_1/C_3 \text{ (JANAF)}}$	=	0.309	$\frac{C_2/C_3 \text{ (ML)}}{C_2/C_3 \text{ (JANAF)}}$	=	1.06
$\frac{C_4/C_3 \text{ (ML)}}{C_4/C_3 \text{ (JANAF)}}$	=	2.54	$\frac{C_5/C_3 \text{ (ML)}}{C_5/C_3 \text{ (JANAF)}}$	=	2.35.

Table 5 gives a comparison of temperatures calculated using the ion intensities of the present work together with the Meyer and Lynch [1973] and JANAF [1971] partial pressure ratios. Note that the comparison using the JANAF data gives the more realistic temperatures.

o Lundell and Dickey [1977]

The graphite rate-of-mass-loss data of Lundell and Dickey [1977] agree well with JANAF [1971] provided unit vaporization coefficients are assumed for the temperature range of 4000 - 4500 K. Under the CW -CO<sub>2</sub> laser heating conditions used, the vapor plume was supersonic. Temperatures were determined by pyrometry of the surface using an estimated emissivity. This is one of the few graphite vaporization studies where controllable CW laser radiation was used and direct surface temperature measurements were made.

o Covington et al., [1977]

These workers have analyzed the gas dynamic behavior of free-jet expansions from laser-vaporized carbon surfaces at temperatures to 4500 K. Their results are consistent with the JANAF [1971] tables, indicating equilibrium conditions and a species-averaged vaporization coefficient and emissivity of 0.9. The data agreement with JANAF [1971] assumes C<sub>1</sub>, C<sub>2</sub> and C<sub>3</sub> as the major species with the latter predominant. These workers also concluded that the vaporization process was independent of microscopic surface roughness.

o Gupta and Gingerich [1979]

These workers report Knudsen effusion data for C<sub>1</sub>, C<sub>2</sub>, and C<sub>3</sub> at temperatures to 2700 K. For the third law enthalpies, fair agreement with JANAF [1971] was obtained for C<sub>1</sub> and C<sub>2</sub>; for C<sub>3</sub>,  $\Delta H_{\text{atom}}(298) = 1313 \pm 6.6$  kJ/mol, as compared with the JANAF [1971] value of  $1321 \pm 21$  kJ/mol.



o Wulfson et al., [1980]

These workers determined a maximum laser plume temperature of  $3600 \pm 300$  K from the CN-impurity vibrational temperature for a pulsed laser graphite vapor plume. We believe that the conditions used would have yielded a total carbon-species pressure of about an atmosphere, similar to the present work.

o Lundell [1982]

From a review of earlier work, Lundell [1982] concluded that at relatively low temperatures (1400 to 2400 K) the vaporization coefficients are not well known but are considerably less than unity and differ between the various  $C_n$  species. At higher temperatures (3500 to 4500 K), the vaporization coefficients approach unity. Note that for the best available vaporization coefficient estimates and the JANAF [1971] data,  $C_1$  is predicted to be the predominant species at the lower temperature range and  $C_3$  at the higher range, with  $C_7$  or other higher molecular weight species becoming significant above the boiling point.

o Baker et al., [1983]

The recent work of Baker et al., [1983], using similar methodology as for the study of Covington et al., [1977], provides an alternative analysis to that of Lundell [1982]. The results differed significantly from JANAF [1971] and were more consistent with the re-evaluation of Leider, et al., [1973]. However, the analysis depends to some extent on assumed emissivity, species distribution, and vaporization coefficient behavior. Their analysis indicates an average  $\alpha = 0.4 - 0.7$ , based on JANAF [1971], but that extrapolating to the melting point would require  $\alpha > 1$ , which is the primary basis for disagreement with JANAF. However, the linearity of the

temperature-pressure extrapolation process is by no means assured. Comparison with the Livermore thermochemical tables [Leider, et al., 1973] indicates  $\alpha = 0.2 - 0.6$  over the data range and  $\sim 0.8$  at the melting point. Based on the physical reasonableness of  $\alpha$  approaching unity at the melting point, the authors preferred the Livermore to the JANAF analysis. The differences in Livermore and JANAF pressures are primarily only significant at temperatures higher than about 4200 K, which is the region most dependent on extrapolations and spectroscopically-based thermodynamic functions. The results of Baker et al., [1983] suggest  $\alpha$  to be strongly temperature dependent. In this connection, it is pertinent to note that their carbon surface morphologies were relatively flat, as opposed to the cratered condition in the present studies.

#### 2.4.2 Literature Summary, for the Period 1968-1983

##### Clarke and Fox [1969]

- o Indirect evidence of  $C_2$  as the major species and  $\alpha = 1$  (3400 K).

##### Wachi and Gilmartin [1970]

- o Relative intensities of  $C_n^+$  ( $n = 1$  to 5) strongly dependent on time and sample form.
- o Possible evidence for  $C_3^+$  fragment ion formation above 17.6 eV.
- o Data insufficient to compare with JANAF [1971].

##### Milne et al., [1972]

- o Basically in agreement with JANAF [1971] (to 3300 K).
- o Time-of-arrival data suggests some fragmentation of  $C_3$ .

##### Meyer et al., [1973]

- o  $C_3/C_1$  ion ratios are consistent with a laser plume temperature of 4500 K.
- o No evidence of  $C_1^+$  or  $C_2^+$  fragment ions from  $C_3$  at 18.6 eV.

Table 3. Comparison of Present Results with Zavitsanos [1968] Ion Intensities, Normalized to  $C_3$  at 4100 K

<u>Ion</u>	<u>Zavitsanos (20 eV)</u>	<u>This Work (26 eV)</u>
$C_1$	0.48	0.47
$C_2$	1.00	0.14
$C_3$	1.00	1.0
$C_4$	0.24	0.014
$C_5$	0.39	0.027
$C_6$	0.15	<0.01
$C_7$	0.16	---

Table 4. Comparison of Present Ion Intensity Results with the Milne et al., [1972] Extrapolated Ion Ratios at 4200 K, Normalized to  $C_3$

	<u>JANAF [1971] Pressure (atm)</u>	<u>Milne, et al. [1972]</u>	<u>This Work (26eV)</u>
$C_3$	2.5	1.0	1.0
$C_1$	0.2	0.08 (= JANAF)	0.32
$C_2$	0.3	0.12 (= JANAF)	0.11
$C_4$	0.3	0.12	0.013
$C_5$	0.3	0.12	0.027
$C_6 - C_7$	0.001	0.0004	<0.01

Table 1.  $C_n$  Ion Intensities and Corresponding Calculated Equilibrium Surface Temperatures<sup>a</sup>

Ionizing electron energy = 96 eV				
Mass (amu)	Species	Peak Signal	Integrated Signal	Temperature (K) <sup>b</sup>
12	$C_1$	0.51	0.32	2600
24	$C_2$	0.16	0.12	3450
36	$C_3$	1.0	1.0	---
48	$C_4$	0.015	0.018	4400
50	$C_5$	0.04	0.04	4300

Ionizing electron energy = 26 eV				
Mass (amu)	Species	Peak Signal	Integrated Signal	Temperature (K) <sup>b</sup>
12	$C_1$	0.47	0.32	2600
24	$C_2$	0.14	0.11	3200
36	$C_3$	1.0	1.0	---
48	$C_4$	0.014	0.013	4100
50	$C_5$	0.027	0.027	4000

<sup>a</sup>The accuracy of the  $C_1$  and  $C_2$  ratios to  $C_3$  is about 30 and 10 percent, respectively; for  $C_4$  and  $C_5$  the accuracy is about 25 percent. Typical  $C_3$  signals are 100 to 200 mv peak.

<sup>b</sup>Obtained by comparison of observed Integrated Signal intensities, relative to  $C_3$ , with the JANAF [1971] thermochemical partial pressure data.

Table 2. Surface Temperature Results in the Graphite System

Method	Temperature (K)
$C_2^+$ arrival time relative to $B^+$ (at 2900 K)	4000 $\pm$ 300
$P_C$ from $P = k I(C^+) T$ , with JANAF [1971]	4200 $\pm$ 300
$C^+/B^+$ intensity ratio (for B at 2900 K)	4100 $\pm$ 300
$C_4$ (or $C_5$ )/ $C_3$ , with JANAF [1971]	4100 $\pm$ 300
Average	4100 $\pm$ (300)

Meyer, R. T., and Lynch, A. W. [1973]. High Temp. Science 5, 192.

Meyer, R. T., Lynch, A. W., and Freese, J. M. [1973]. J. Phys. Chem. 77, 1083.

Milne, T. A., Beachey, J. E., and Greene, F. T. [1972]. In "Vaporization Kinetics and Thermodynamics of Graphite Using the High Pressure Mass Spectrometer," AFML-TR-72-227 (AD 753713).

Nikolaev, E. N. [1972]. Khim. Vys. Energii, 3, 49.

Ohse, R. W., Babelot, J. F., Cercignani, C., Kinsman, P. J., Long, K. A., Magill, J., and Scotti, A., [1979]. P. 83 in Characterization of High Temperature Vapors and Gases, J. W. Hastie, ed., NBS SP 561, U.S. Govt. Printing Office, Washington, DC.

Olstad, R. A., and Olander, D. R. [1975]. J. Appl. Phys. 46, 1509.

Oppenheimer, M., and Berry, R. S. [1971]. J. Chem. Phys., 54, 5058.

Palmer, H. B., and Shelef, M. [1968]. Carbon 4, 85.

Sterns, C. A., Kohl, F. J., Fryburg, G. C., and Miller [1979]. P. 303 in Characterization of High Temperature Vapors and Gases, J. W. Hastie, ed., NBS SP 561, U. S. Govt. Printing Office, Washington, DC

Strauss, H. L., and Thiele, E. [1967]. J. Chem. Phys., 46, 2473.

Thorn, R. J., and Winslow, G. H. [1957]. J. Chem. Phys. 26, 186.

Wachi, F. M., and Gilmartin, D. E. [1970]. Carbon 8, 141.

Wulfson, E.K., Dworkin, W.I., and Karjakin, A. W. [1980]. Spectrochim. Acta 35B, 11.

Zavitsanos, P. D., [1968]. Carbon 6, 731.

Zavitsanos, P. D., and Carlson, G. A. [1973]. J. Chem. Phys. 59, 2966.

## 5.0 References

- Akishin, P. A., Gorokov, L. N., and Sidorov, L. N. [1960]. Proc. Acad. Sci. USSR. (Dok. Phys. Chem.) 135, 1001.
- Baker, R. L., Covington, M.A., and Rosenblatt, G. M. [1983]. "The Determination of Carbon Thermochemical Properties by Laser Vaporization". P. 143 in High Temperature Materials Chemistry, Eds. Munir, Z. A., and Cubicciotti, D., Electrochem. Soc., Pennington, NJ.
- Berkowitz, J., and Chupka, W. [1964]. J. Chem. Phys. 40, 2735.
- Bonnell, D. W., and Hastie, J. W. [1979]. P. 357 in Characterization of High Temperature Vapors and Gases, J. W. Hastie, ed., NBS SP 561, U.S. Govt. Printing Office, Washington, DC.
- Bonnell, D. W., and Hastie, J. W. [1983]. A Theoretical Analysis of Temperature Dependent Electron Impact Fragmentation, 31st Ann. Meeting, Amer. Soc. Mass Spec., Boston.
- Clarke, J. J., and Fox, B. R. [1969]. J. Chem. Phys. 51, 3231.
- Covington, M. A., Liu, G. N., and Lincoln, K. A. [1977]. AIAA J. 15, 1174.
- Dronin, A. A., and Gorokov, L. N. [1972]. Teplofiz. Vys. Temp. 10, 49.
- Drowart, J., Burns, R. P., De Maria, G., and Inghram, M. G. [1959]. J. Chem. Phys. 31, 1131.
- Fesenko, V. V., and Bolgar, A. S. [1969]. Teplofiz. Vys. Temp. 7, 244.
- Gupta, S. K., and Gingerich, K. A. [1979]. J. Chem. Phys. 71, 3072.
- Hall, [1984] R. Private Communication.
- Hastie, J. W., Zmbov, K. F., and Bonnell, D. W., [1984]. "Transpiration Mass Spectrometric Analysis of Liquid KCl and KOH Vaporization," High Temp. Science, in press.
- "JANAF Thermochemical Tables", 2nd ed., NSRDS-NBS 37 (Washington, DC, 1971).
- Leider, H. R., Krikorian, O. H., and Young, D. A. [1973]. Carbon 1, 555.
- Lincoln, K. A. [1969]. P. 323 in "High Temperature Technology," Butterworths and Co., London.
- Lincoln, K. A., and Covington, M. A. [1975]. Int. J. Mass Spec. Ion Phys. 16, 191.
- Lundell, J. H., and Dickey, R. R. [1977]. Progr. Astron. and Aeron. 56, 405.
- Lundell, J. H. [1982]. Progr. Astron. and Aeron. 83, 472.

- o Centrifugal broadening of the potential-well and high rotational level occupation may be important in the calculation--at  $T > 800$  K,  $J(\text{max})$  is of the order of 60; the effect on  $f_v(T)$  and  $Y_v$  may be significant, the effect on the potential is less likely to be a problem.
- o Avoided-crossing distortions of the potential-well may be important at high temperatures although Oppenheimer and Berry [1971] calculate that point for NaCl to be at  $r = 0.94$  nm, where no significant thermal occupation would exist.
- o The actual form of the potential may not be accurate enough above  $v = 2-3$ .
- o The separation of the two states of the ion, expected to exist, may cause the simple overlap model to fail at higher temperatures.

An ab-initio calculation for this problem is now possible and probably warranted. However, many important systems are not yet calculable, and fragmentation at a single bond is a very important case. The sensitivity shown by this model also points to the possibility of directly using this effect to test existing ab-initio calculations at the higher energy levels.

temperature (EXPANSION) data. This difference indicates the impossibility of successfully modeling temperature dependent fragmentation based only on high temperature data. Also, the extreme sensitivity of the model prediction on the value of  $r_c$  is demonstrated by comparison of the high temperature fit and low temperature anharmonic oscillator results in figure 9. This sensitivity indicates that low temperature ion-intensity data can provide a stringent test of ground state potential well shape, particularly for levels above the ground vibrational state.

The basis for the anharmonic model used is as follows. The potential well was computed by the Rydberg-Klein-Rees method from the spectroscopic data selected by JANAF [1971]:  $\omega_e = 363.62$ ,  $\omega_e x_e = 1.72$ ,  $B_e = 0.21691$ , all in  $\text{cm}^{-1}$ . These values imply  $r_e = 0.23671$  nm. The function,  $f_v(T)$  was summed directly from the anharmonic eigenvalues

$$E_v = \omega_e(v + 1/2) - \omega_e x_e(v + 1/2)^2,$$

normalized by summing to  $v = 15$  where the population, even at 1200 K, was insignificant. The anharmonic eigenfunctions were approximated by mapping harmonic oscillator eigenfunctions onto the actual potential well. Figure 9 shows the resulting model behavior for  $R$  with  $T$ , given as the Anharmonic Oscillator curve ( $r_c = 0.2445 \pm 0.0001$  nm). The model agreement with the TMS data is now excellent; however, the model still fails to predict the effusive KMS data. Possible explanations are:

- o Harmonic oscillator eigenfunctions are not a good model at high temperature--the "true" eigenfunctions do exhibit higher amplitude toward the right wall of an anharmonic potential than toward the left.



system pressure. At high temperatures, the vibrational levels are significantly populated, up to  $v = 10$  or more. For the NaCl case, considered in detail here, less than half of the molecules at 800 K are in the  $v = 0$  state (harmonic oscillator assumption), and 1 percent, or more, occupancy is found up to the level  $v = 8$ . This makes empirical interpretation based on the observed high temperature ratio so insensitive to small changes in the value of  $r_c$  that almost no information can be obtained from hot beams.

Figure 9 shows a low temperature limit near  $R = 27$  for the NaCl case (TMS data). For the harmonic oscillator fit, values of  $\omega_e = 363.62 \text{ cm}^{-1}$  and  $r_e = 0.23606 \text{ nm}$  were used. Equation 4.1 was evaluated by numerical integration of  $Y_v$  and direct summation over  $v$  from 0 to 12. The evaluation was iterated on  $r_c$  with  $T = 10 \text{ K}$  until the experimental value,  $R = 27 \pm 0.5$  was obtained and the corresponding value of  $r_c$  was  $0.24648 \pm 0.0001 \text{ nm}$ . Note that the high precision obtained for  $r_c$  is indicative of the high sensitivity of this model approach. The temperature-dependence results based on this fit are plotted in figure 9 as the Harmonic Oscillator curve. It is clear that the qualitative shape of the data (including effusive measurements taken from the literature [Bonnell and Hastie, 1979]) is adequately modeled by the harmonic oscillator approximation. But even with a possible error of a factor of two in beam temperature (which has been applied to the data), the model does not quantitatively fit either the TMS or KMS effusive data. A likely explanation of the models' deficiency is that the ground state well is anharmonic, and the harmonic oscillator eigenvalues of the levels underestimate upper level participation.

The curve labeled High Temp. Fit in figure 9 is based on a harmonic oscillator-model calculation, made using only the high temperature effusion data. Note the disagreement of this model approach with that using the low

state to the ion-state region to the right of the internuclear distance where the ion dissociation limit intersects the ion-state repulsive wall. The population fractions  $f_v(T)$  of the various vibrational states can be determined, from which the fragmentation ratio can be calculated using the relationship:

$$R = M^+/MC1^+ = \left( \sum_{v=0}^{\infty} \left[ \int_{r_c}^{\infty} \{ Y_v^* Y_v dr \} \cdot f_v(T) \right] - 1 \right)^{-1}, \quad (4.1)$$

where  $Y_v$  is the vibrational eigenfunction for vibrational state  $v$ . From this expression, transitions from the ground state to the right of  $r_c$  lead to parent ion formation, and transitions to the left of  $r_c$  produce dissociation to fragments (see fig. 8). Although Nikolaev [1972] presented calculations of  $r_c$ , based on a model of the ion-state, he found it necessary to compute  $r_c$  for CsCl empirically from the experimental fragmentation ratio, obtaining  $r_c = 0.342$  nm, compared to his calculated value of 0.323 nm.

A more definitive, generally applicable model for this relatively novel process (for high temperature species) has been obtained under the present subtask using the TMS system. The isentropic expansion used to form a representative non-interacting beam from a high temperature region provides extreme rotational and vibrational cooling of the molecules. This cooling effect has led to observation of anomalously high ratios of  $M^+/MX^+$  in alkali halide species [Bonnell and Hastie, 1983]. The above model provides a basis for interpreting these experimental data since the proper temperature describing molecules in the beam is given by the isentropic temperature of the expansion rather than the source temperature. For suitable orifice dimensions, the temperature can be altered over a wide range by varying the

One possible explanation for these results could be that higher molecular weight clusters fragment, thereby contributing to ion signals for the lower polymers. Our analysis indicates, however, that such effects must be less than about 10 percent, as neither phase (time-of-flight) data nor appearance potentials show any evidence for unexplained contributions to assigned precursors. Similar arguments pertain to the  $C_n$  system which also showed no evidence for cluster formation.

#### 4. Subtask C: Results on Ionization Processes

In order to identify gaseous species, a mass spectrometer must be used to ionize and detect the neutrals. However, the electron impact ionization process frequently produces fragment ions. A universal assumption in high temperature mass spectrometry is that intensity ratios of fragment to parent ion are temperature independent, as might be argued from the thermal energy being negligible with respect to the ionizing energy. One known exception for high temperature species has been reported by Askishin et al., [1960] for the CsCl system, where a 20 percent variation in the ratio  $Cs^+/CsCl^+$  was observed over the temperature interval 800 to 900 K. These authors argued that temperature-dependence in the Franck-Condon factors was the result of poor overlap between the ground state of CsCl with the bound ion state. Changes in the thermal population of the higher vibrational states with temperature would then influence the Franck-Condon factors.

A relatively simple model of the temperature-dependent ionization process has been discussed by Dronin and Gorokov [1972], and Nikolaev [1972]. Figure 8 shows a harmonic oscillator potential model for the ground state, located such that only a small overlap occurs with the stable region ( $r > r_0$ ) of the bound-ion state. The stable region is defined by vertical transitions (the Franck-Condon assumption for electron impact excitation) from the ground

independently controlled, and from which expansions into a vacuum chamber can be monitored with mass spectrometric detection [Bonnell and Hastie, 1979]. Alkali halides have been selected as test cases for monitoring cluster formation processes.

The apparatus, termed Transpiration Mass Spectrometer (TMS), consists of an initial chamber for vapor transpiration and molecular beam production, and a second chamber where modulation of the molecular beam and mass analysis are performed. Figure 7 shows the transpiration inlet system, located in a vacuum chamber. The entire system is heated by a tantalum foil furnace (not shown), and the beam is directed to a quadrupole mass spectrometer which is operated in a cross-beam configuration. The unit is laser aligned with the beam axis directed toward the ion source. Differentially pumped apertures collimate the beam and a mechanical chopper modulates the beam to allow phase sensitive lock-in amplification. The two-stage vacuum system used is similar in concept to the LIV system (shown in fig. 2) but with a horizontal beam-path geometry.

Vapor expansion experiments were conducted with KCl and NaCl vapor, in a  $N_2$  carrier gas, at source pressures of  $\sim 0.04$  MPa (0.4 atm) and temperatures to 1300 K. The data have been discussed in detail elsewhere [Hastie, et al., 1984], including a complete thermochemical analysis. Studies with variable pressure of nitrogen and orifice size were conducted to identify excess dimer/trimer formation due to clustering by expansion cooling. For the smaller orifice, (lower final beam temperature), the ion intensity ratio of dimer to monomer species decreased with increased  $N_2$  pressure (ie, decreased beam temperature), which indicated an absence of clustering. Similar results were found for the NaCl system.

These observations do not necessarily conflict with the lower temperature studies of Fesenko and Bolgar [1969] owing to the large temperature differences together with the strong  $C_3/C_1$  temperature dependence.

Meyer et al., [1973] argue that the carbide vapor composition may reflect the molecular structure of the solid phase and that different carbides may produce different  $C_n$  distributions. A higher laser energy (18 J of focused energy versus 0.1 J for graphite) was needed for TaC owing to its greater reflectivity. The results could not be quantified because of the non-congruent vaporization. Also, no direct indication of the TaC temperature was obtained in these experiments, but the signals were approximately an order of magnitude weaker than for graphite.

In view of the incomplete and disparate nature of the literature studies, further examination of the molecular composition in laser plumes over tantalum carbide samples is needed and planned.

### 3. Subtask B: Cluster Formation Studies

Laser vaporization processes can result in relatively high pressures of vapor species, as shown by the results for  $C_n$  given in Section 2. When a high pressure vapor expands adiabatically into a vacuum environment the temperature can fall markedly, leading to a supersaturated vapor state. Such a condition tends to favor homogeneous nucleation, with the formation of cluster intermediate, aerosol, and particulate states. While the laser vaporization studies of graphite, described in Section 2, showed evidence of expansion-cooling there was no indication of cluster formation. Independent control of the source pressure and temperature, which was not possible with the graphite studies, is required to understand the mechanistic details of the vapor to cluster to aerosol transformation. For this purpose, we have developed a chamber in which the total pressure and temperature can be

Langmuir vaporization studies of refractory metal carbides, including those of Ta, Nb, Hf, Zr, and Ti have been reported by Fesenko and Bolgar [1969]. Vaporization rates increased in the above order, Ta to Ti. The data were also consistent with vaporization to metal plus atomic-carbon. However, this assignment may not be definitive owing to the non-molecular-specific approach used. At the highest temperature of 3373 K, the total pressure over the congruent vaporizing composition,  $\text{TaC}_{0.71}$ , was  $4.5 \times 10^{-5}$  atm. From this pressure, and the condition of congruency, we can compute the thermodynamic activity of  $\text{C}_3$  as  $1.56 \times 10^{-3}$ . This reduced activity of  $\text{C}_3$  in  $\text{TaC}_{0.71}$ , as compared with graphite (1.0 by definition), favors dissociation to  $\text{C}_1$ . At 3373 K the ratio  $P_{\text{C}_1}/P_{\text{C}_3} \sim 10$ , whereas for graphite the ratio is 0.17, i.e., the atomic-carbon-enhancement factor is 58.8 for the carbide.

More recent vaporization studies of TaC using laser vaporization mass spectrometry (at 18.6 eV) indicate  $\text{C}_3$  as the predominant species [Meyer et al., 1973]. However, the substrate composition is unspecified in these studies and could well be closer to TaC than  $\text{TaC}_{0.71}$ . This situation would tend to favor a higher  $\text{C}_3/\text{C}_1$  ratio than for the work of Fesenko and Bolgar [1969]. Using the measured relative partial pressures of  $\text{C}_3/\text{C}_1$ , in comparison with values calculated from the Palmer and Shelef [1968] evaluation for graphite, a surface temperature of 4500 K was indicated. The JANAF [1971] derived temperatures would be greater, but vaporization coefficient and ionization cross section uncertainties probably contribute to this difference. A comparison of the observed TaC and C vapor species abundances (integrated ion intensities) indicates  $\text{C}_1 : \text{C}_2 : \text{C}_3$  values of 1.0 : 0.06 : 2.2 and 1.0 : 0.32 : 35, respectively, and presumably at 4500 K in both cases.

The principal conclusions are:

- o  $P_{\text{total}} \sim 10 \times P_{\text{JANAF}}$  (at  $T \sim 4000$  K).
- o  $T_{\text{boiling}} \sim 3850$  K vs. 4150 K for JANAF [1971].
- o The carbon-atom may be used as a reference point as its properties are well established.
- o Entropy of  $C_3$  is about 21 J/mol·K greater than JANAF at [1971] 4000 K.

#### 2.4.4 Conclusions From the Literature Survey

Despite recent indications to the contrary, the JANAF [1971] tables still appear to be the most consistent with the available data. However, a re-evaluation of all the thermodynamic functions is warranted as the JANAF [1971] data-consistency may result from offsetting errors, particularly for the  $C_3$  species.

#### 2.5 Carbon Vaporization from Carbides

For spacecraft survivability under laser irradiation, the development of ablative coatings is a promising approach. An important coating requirement is to maximize energy absorption, which implies minimizing the energy stored as chemical bonds in the vaporized protectant. In the case of carbon, the fact that  $C_3$  is the predominant vapor species at high temperatures makes carbon a less favorable ablator than if carbon atoms were the preferred vaporizing species. Over pure carbon, it is thermodynamically unreasonable to significantly modify the vapor species distribution. However, with refractory metal carbides, the reduced thermodynamic activity of carbon species should favor release of lower molecular weight  $C_n$ -species, in comparison with graphite. Carbides can also improve the refractory properties of ablative coatings. Tantalum carbide (TaC) is a promising ablation material and is a suitable test case for a detailed analysis of vaporization kinetics. A limited understanding of TaC vaporization processes is available from several earlier studies, described as follows.

Meyer and Lynch [1973]

- o  $P_{C_3} \sim 3 \times \text{JANAF [1971]}$

Zavitsanos and Carlson [1973]

- o Knudsen mass spectrometry results to 3000 K, agree with JANAF [1971].

Lundell and Dickey [1977]

- o Results agree with JANAF [1971] at  $T = 4000\text{--}4500$  K.
- o Conditions similar to the present study but mass-loss method used instead of mass spectrometry.

Covington et al., [1977]

- o Laser vapor-plume analysis to 4500 K.
- o  $\alpha \sim 0.9$ .
- o  $C_3$  is indirectly indicated the major species.
- o Results are consistent with JANAF [1971].

Wulfson et al., [1980]

- o Laser vapor-plume temperature  $3600 \pm 300$  K.

Baker et al., [1983]

- o Data more consistent with analysis of Leider et al., [1973] than for JANAF [1971].
- o  $\alpha = 0.2 - 0.6$ ;  $\sim 1$  at melting point
- o  $\alpha$  strongly temperature dependent.
- o Data depart from JANAF [1971] mainly at  $T > 4200$  K.
- o  $P$  total  $\leq 2 \times \text{JANAF}$  up to 4200 K,  $\sim 3 \times [\text{JANAF}]$  at 4500 K.

2.4.3 Literature Summary, for the Pre-1968 Period

The JANAF [1971] evaluation is based on data available prior to 1968. An independent critical analysis of results from this period has also been made by Palmer and Shelef [1968], using theoretical  $C_3$  entropy results not available to JANAF [1971].



Table 5. Temperatures Calculated from Partial Pressure Ratios, Relative to  $C_3$

<u>Species</u>	<u>Ion Intensities</u> <u>[This Work, 96 eV]</u>	<u>Temp. K</u> <u>[JANAF]</u>	<u>Relative Pressures</u> <u>[Meyer and Lynch]</u>	<u>Temp. K</u> <u>[Meyer and Lynch]</u>
$C_1$	0.32	2600	0.1	>5000
$C_2$	0.12	3450	0.13	3500
$C_3$	1.0	---	1.0	---
$C_4$	0.018	4400	0.046	>5000
$C_5$	0.04	4300	0.094	>5000

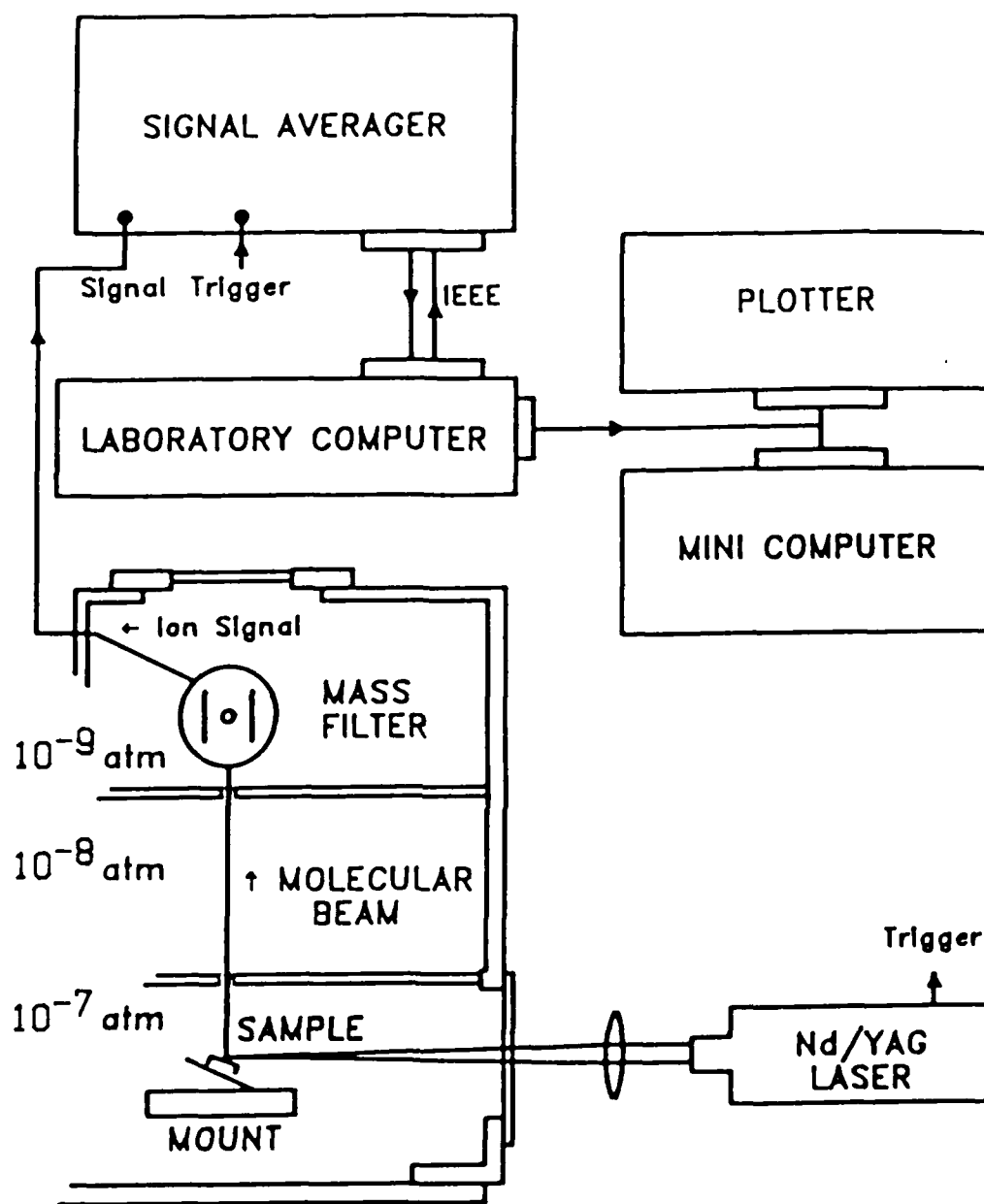


Figure 1. Schematic of laser-induced vaporization mass spectrometric facility (side view), showing laser-sample-molecular beam geometries. The microcomputer system shown controls the signal averager and records completed scans.

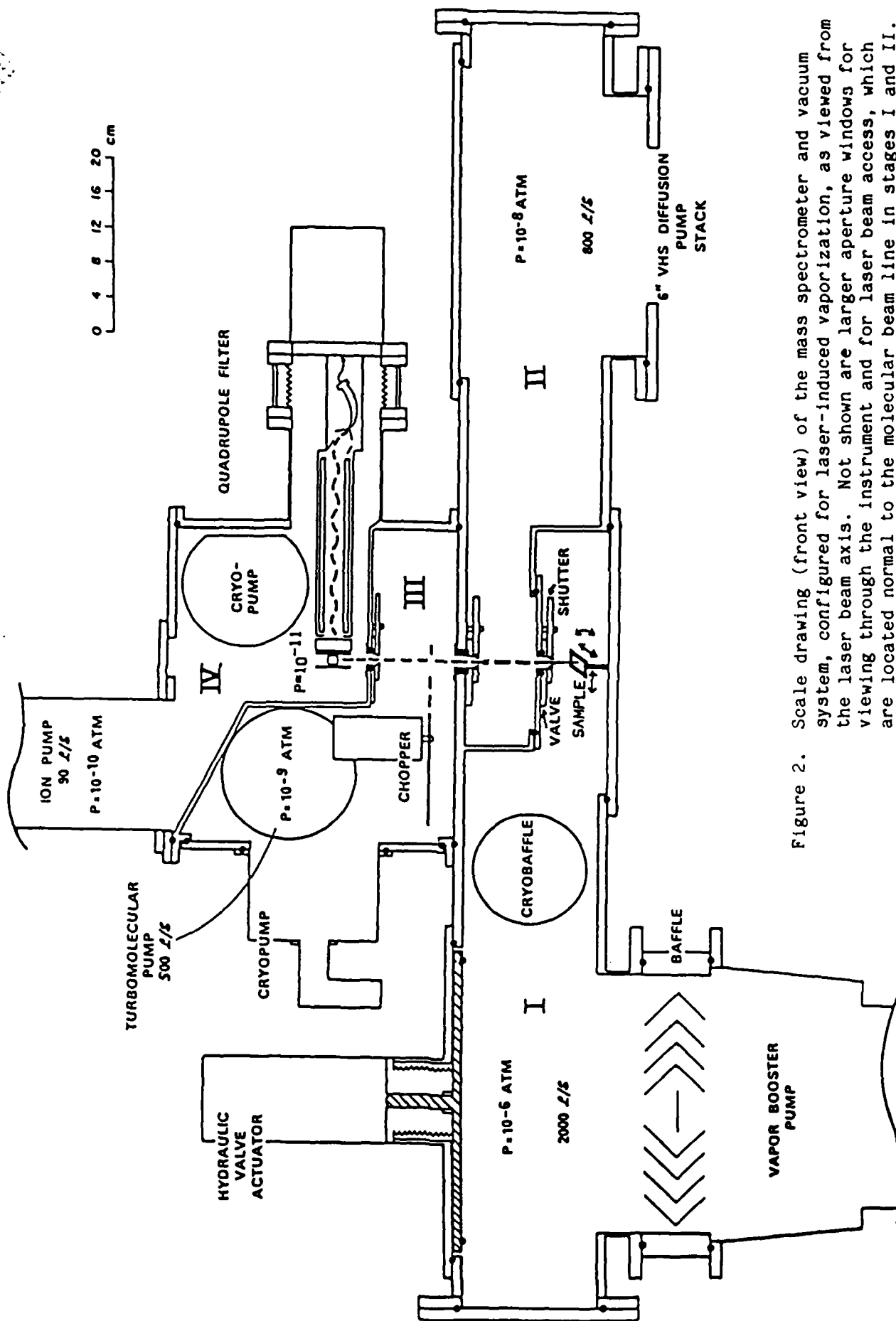


Figure 2. Scale drawing (front view) of the mass spectrometer and vacuum system, configured for laser-induced vaporization, as viewed from the laser beam axis. Not shown are larger aperture windows for viewing through the instrument and for laser beam access, which are located normal to the molecular beam line in stages I and II. There is also a smaller pair of viewports centered on the beamline at the mass spectrometer ion source level (stage IV).

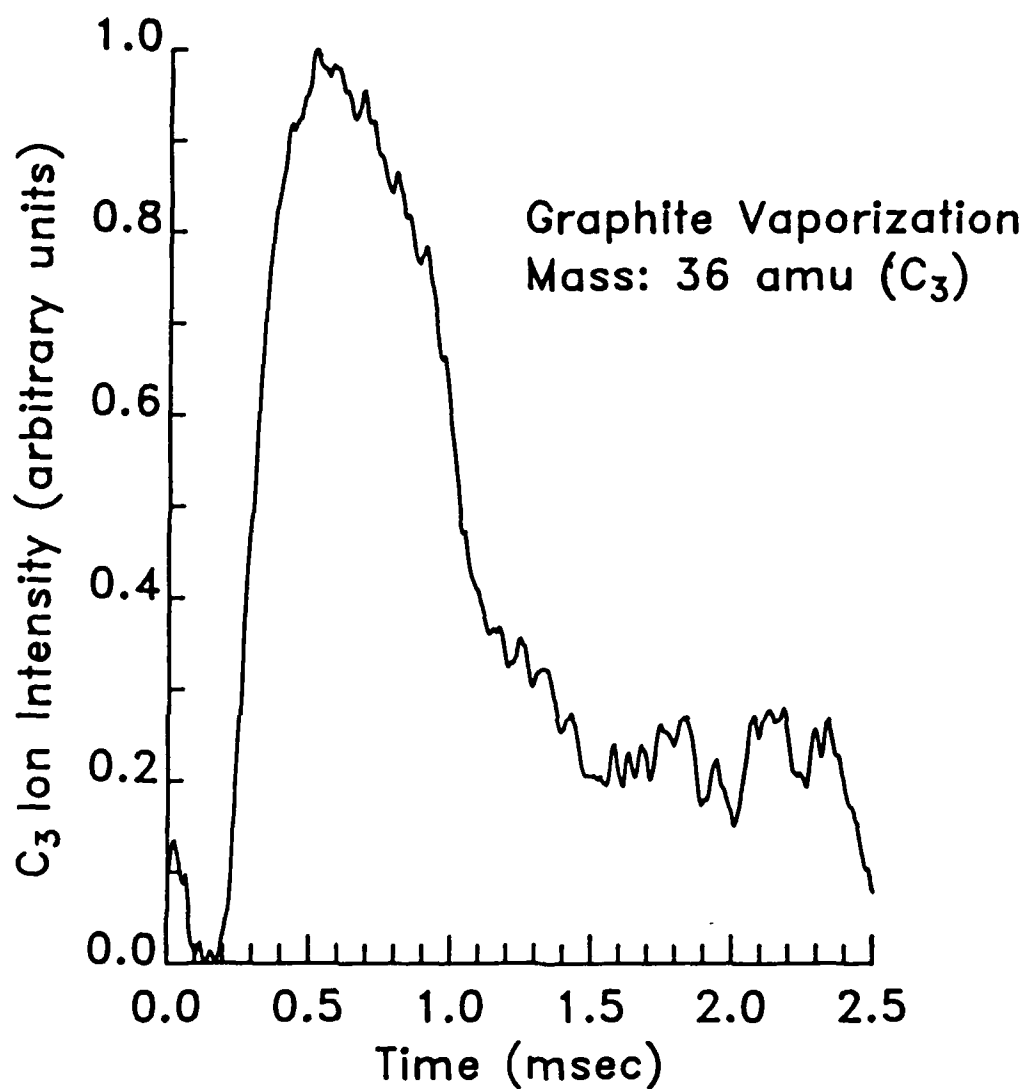


Figure 3. Mass spectral ion intensity-versus-time profile for the 36 amu ( $C_3^+$ ) ion at 30 eV nominal (26 eV actual) ionizing electron energy. Unit peak-ion-intensity equals 27336 counts.

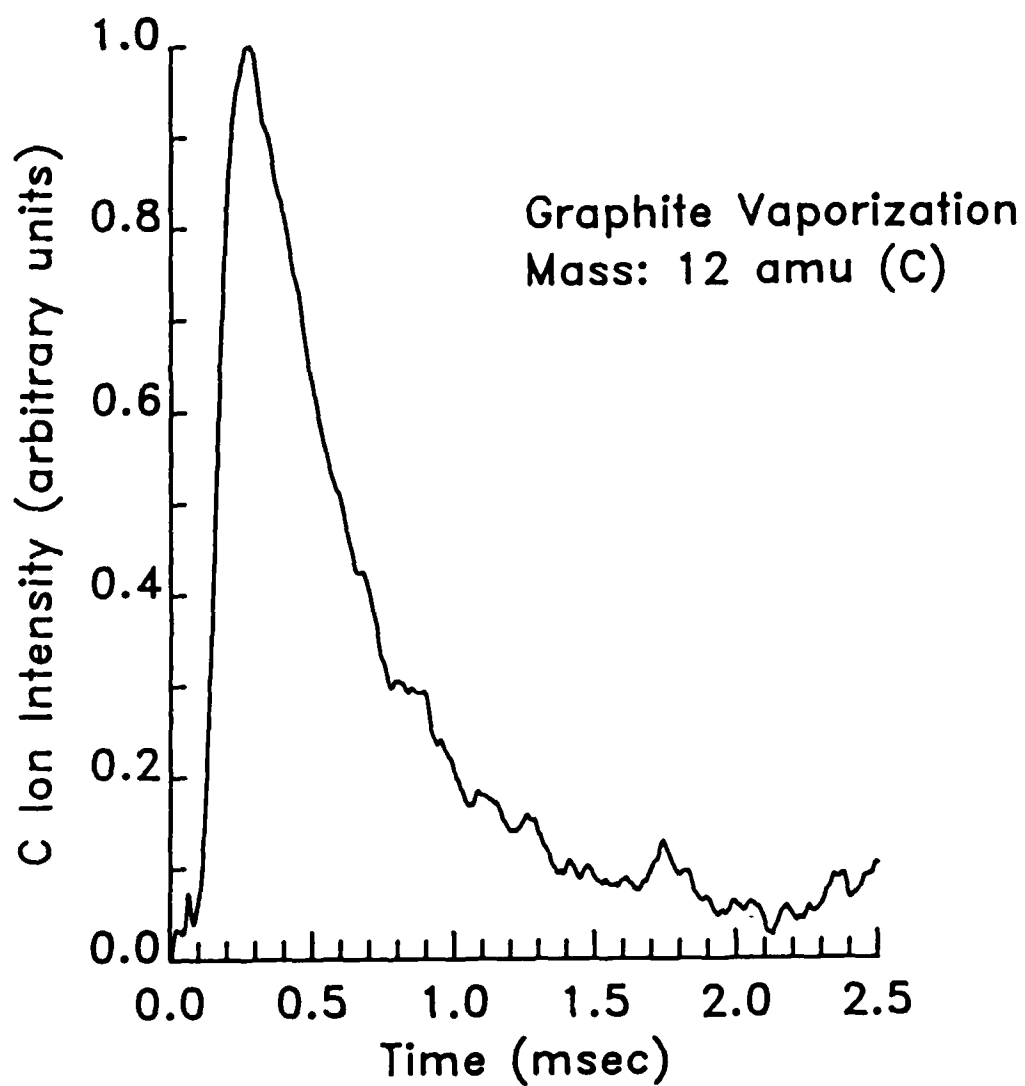


Figure 4. Mass spectral ion intensity-versus-time profile for the 12 amu ( $C_1^+$ ) ion at 30 eV nominal (26 eV actual) ionizing electron energy. Unit peak-ion-intensity equals 30551 counts.

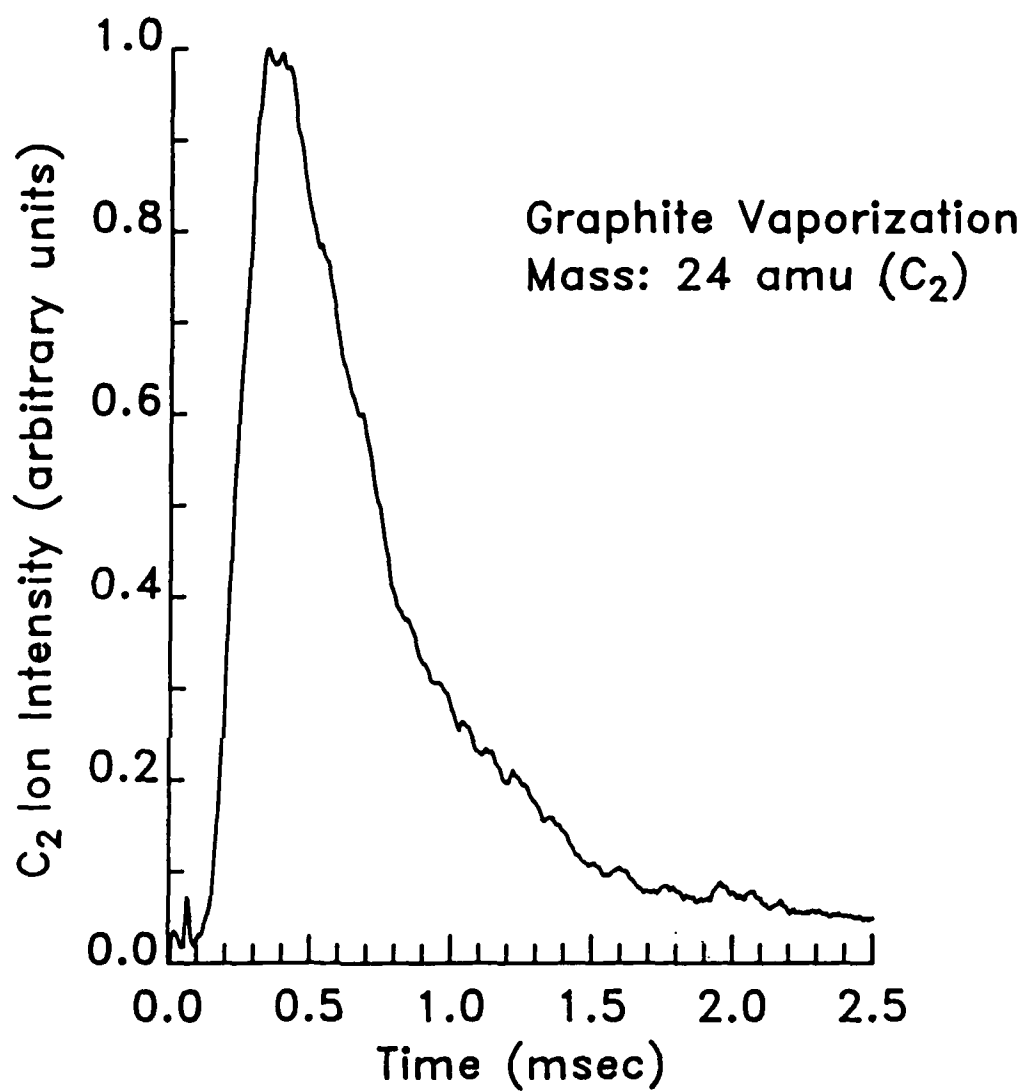


Figure 5. Mass spectral ion intensity-versus-time profile for the 24 amu ( $C_2^+$ ) ion at 30 eV nominal (26 eV actual) ionizing electron energy. Unit peak-ion-intensity equals 20337 counts.

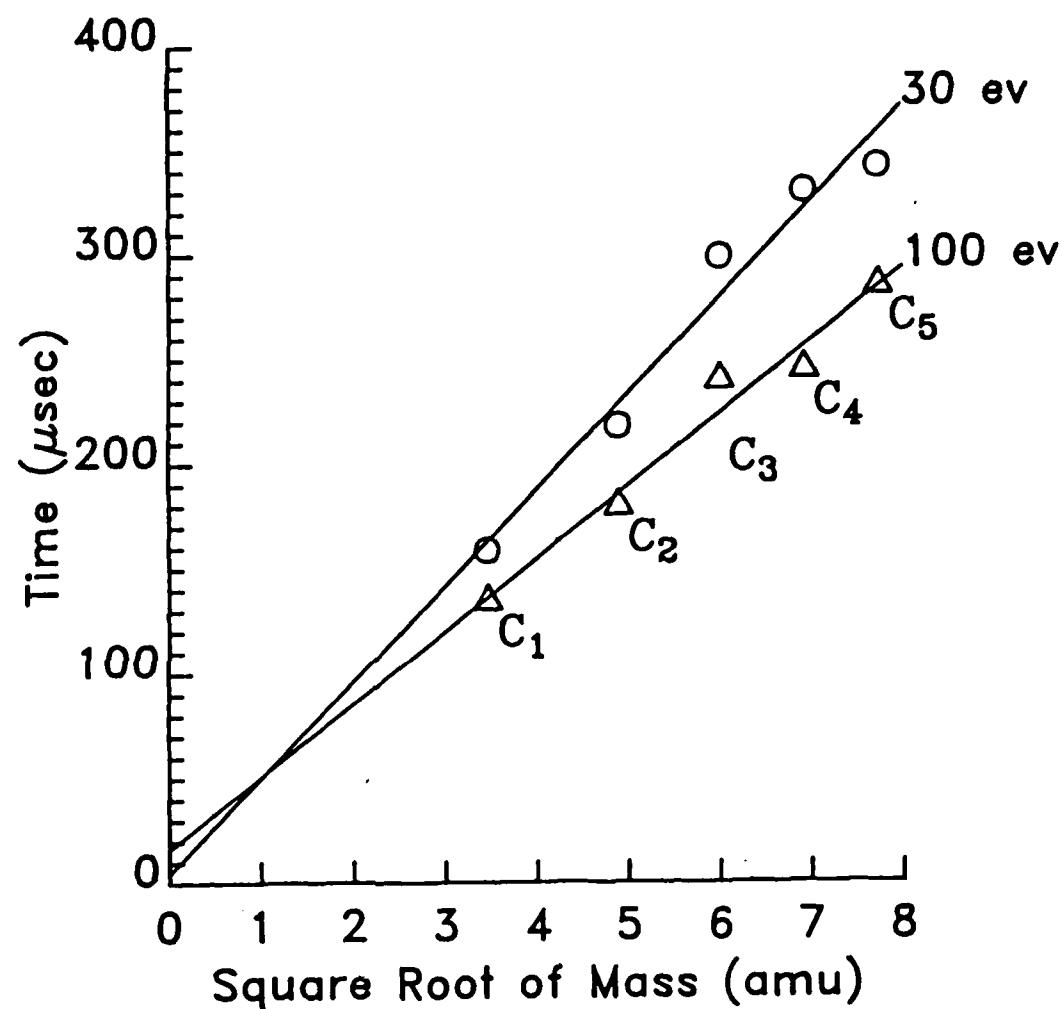


Figure 6. Dependence of the time-of-arrival for  $C_n^+$  ( $n = 1$  to 5) ions as a function of molecular weight from laser vaporized graphite. The linear dependence confirms the assignment of neutral precursors, and indicates a common thermal source and local thermal equilibrium. The two curves shown are for 30 eV and 100 eV data sets.

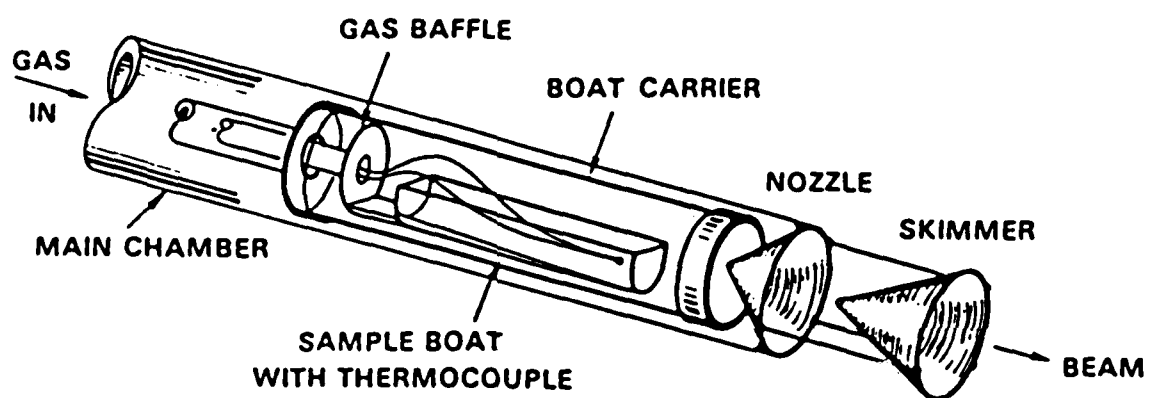


Figure 7. The Transpiration Mass Spectrometer Inlet System.



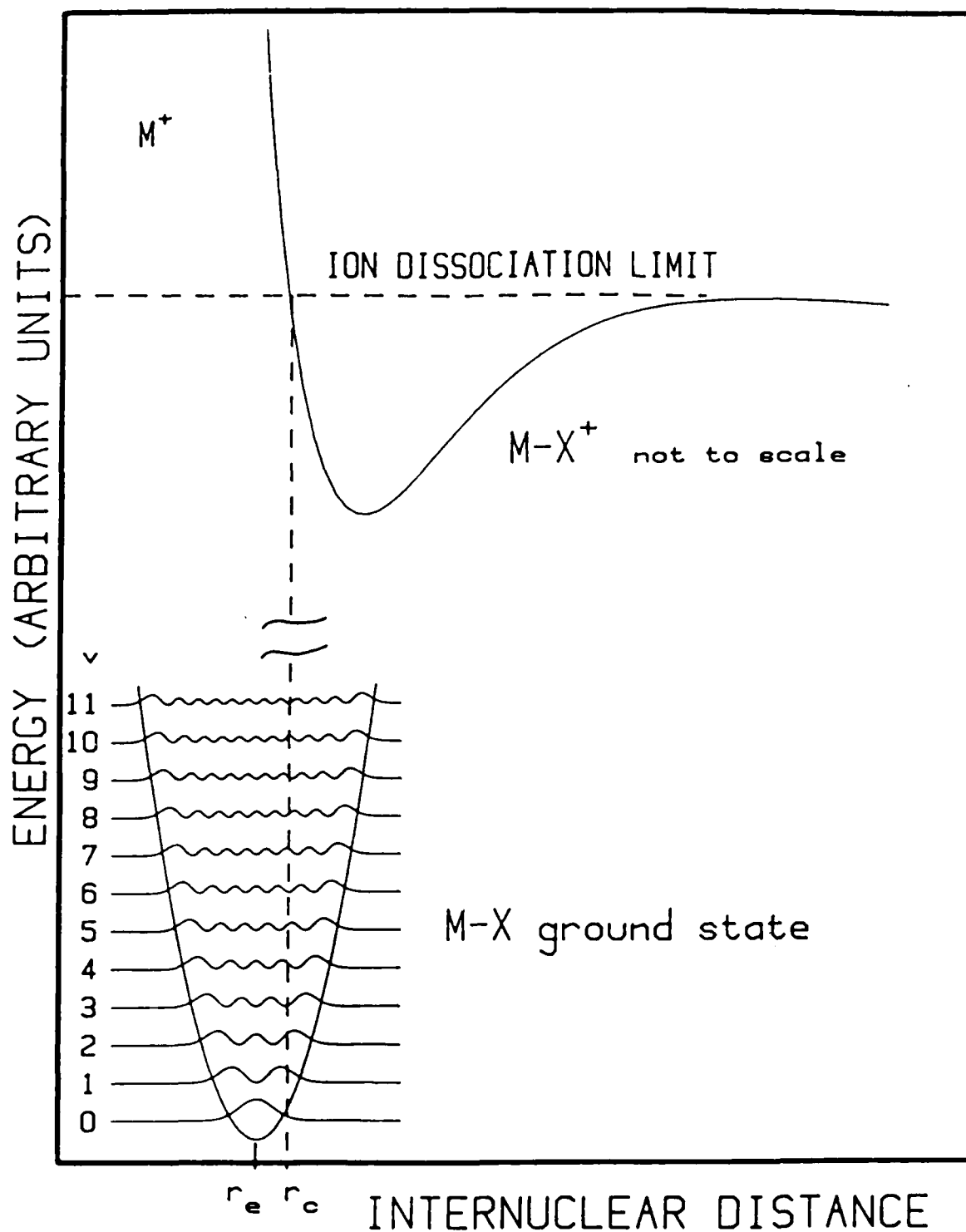


Figure 8. Temperature-dependent electron impact fragmentation model. The lower potential well is for a harmonic oscillator with the probability density functions (square of harmonic oscillator eigen-functions) drawn to scale;  $r_e$  is the equilibrium internuclear distance, and  $r_c$  represents the dividing line between vertical (Franck-Condon) transitions to a bound molecular ion (at  $r > r_c$ ) and to an unstable condition (at  $r < r_c$ ) giving fragmentation.

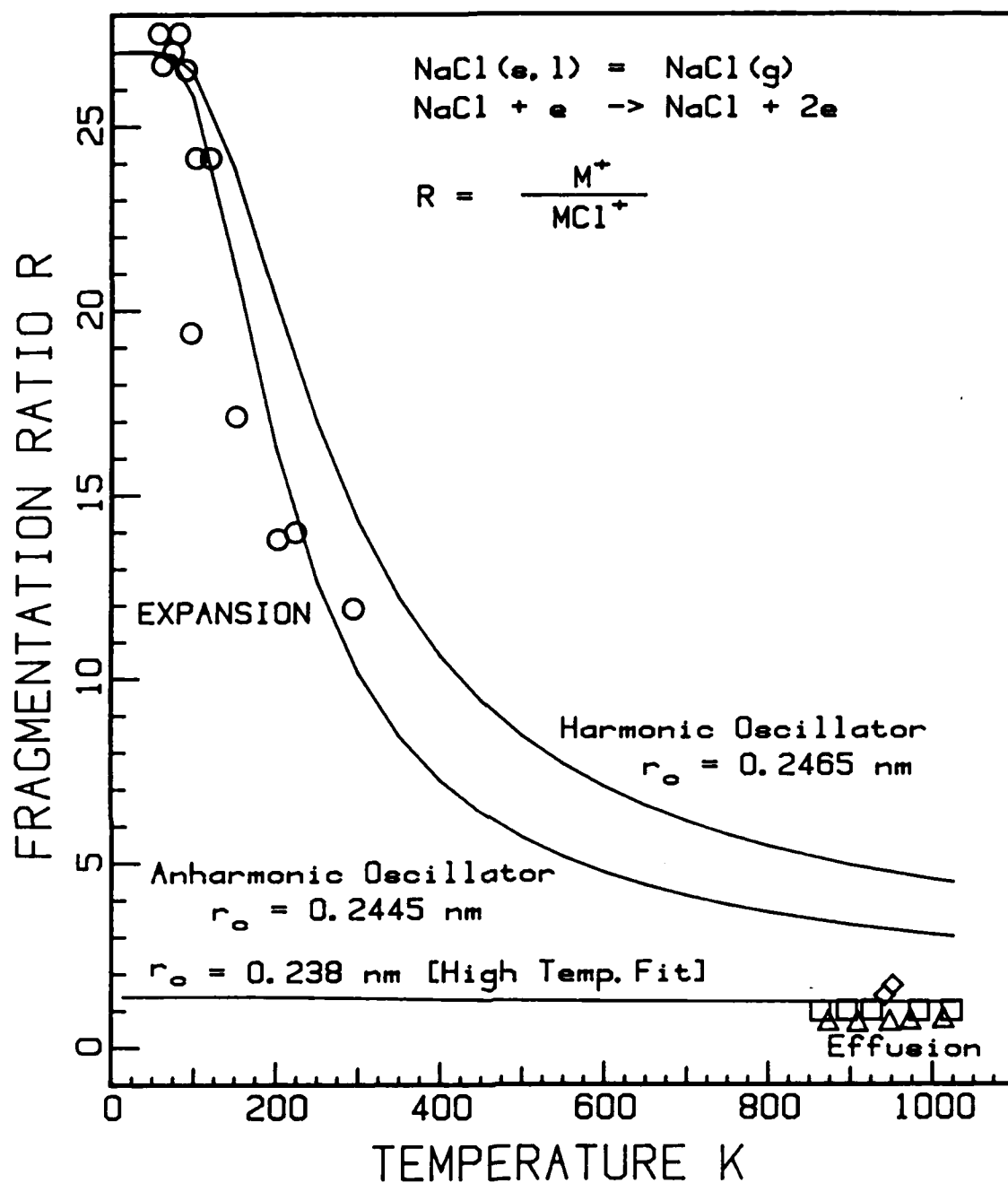


Figure 9. Comparison of experimental and model fragmentation ratios in high pressure expansions of NaCl vapor-N<sub>2</sub> gas mixtures. The temperature axis was derived from the source pressure using an isentropic expansion/sudden-freeze model (see for instance, Stearns, et al., 1979). An expansion effectiveness parameter of 0.5 has been applied to the derived T/T<sub>0</sub>. The r<sub>0</sub> value labeled High Temp. Fit is for a harmonic oscillator calculation, using only experimental high temperature R-data (see text).

**END**

**FILMED**

**7-85**

**DTIC**